UNIVERSITY OF CALIFORNIA

Los Angeles

Buckling of Columns and Films: from Fundamental Mechanics to Functional Materials

A dissertation submitted in partial satisfaction of the

requirements for the degree Doctor of Philosophy

in Mechanical Engineering

by

Yuzhen Chen

2021

ABSTRACT OF THE DISSERTATION

Buckling of Columns and Films: from Fundamental Mechanics to Functional Materials

by

Yuzhen Chen

Doctor of Philosophy in Mechanical Engineering

University of California, Los Angeles, 2021

Professor Lihua Jin, Chair

Buckling instabilities are traditionally regarded as failure modes. However, they can also be exploited to design functional materials. This dissertation focuses on investigating the buckling of columns and films, and on harnessing these buckling instabilities to design pneumatically actuated pattern-transforming metamaterials, design reusable energy-absorbing architected materials, and achieve complex 3D morphing of LCE thin films. Four major contributions are made:

First, we propose a pneumatically actuated pattern-transforming metamaterials and reveal the mechanism of the pattern transformation. Metamaterials are carefully structured materials that exhibit unusual properties relying primarily on their geometries rather than their constitutive

materials. The proposed metamaterial is composed of an elastomer with periodic circular holes sealed by elastomeric membranes. Subjected to negative pressures, it can undergo pattern transformation, yielding large transformation strains. Such pattern transformation is triggered by a buckling instability and can be broadly tuned by the geometry of the metamaterial. Here we numerically, analytically and experimentally investigate the effects of geometry on the pattern transformation. Our finite element simulations indicate that the thickness of the slenderest wall and the pattern of the holes play key roles in determining the critical load for the pattern transformation, the transformation strain, and the transformation type. To quantify the effects of these geometric parameters, we further analytically model the pattern transformation of the metamaterial by simplifying it to a network of rigid rectangles linked by deformable beams. Finally, we experimentally characterize the pattern transformation of the metamaterials with different geometric parameters. The experimental, numerical, and analytical results are in good agreement. Our work provides design guidelines for this metamaterial.

Secondly, we numerically show that a straight hyperelastic column under axial compression exhibits complex buckling behavior. As its width-to-length ratio increases, the column can undergo transitions from continuous buckling, like the Euler buckling, to snapping-through buckling, and eventually to snapping-back buckling. In particular, we numerically and experimentally identify a new snapping-back mode of column buckling. We develop an analytical discrete model to reveal that snapping-back buckling results from strong coupling between stretching and bending. Besides, we analytically determine the critical width-to-length ratios for the transitions of buckling modes using a general continuum mechanics-based asymptotic post-buckling analysis in the framework of finite elasticity. A phase diagram is constructed to demarcate the different buckling modes of axially compressed columns.

Thirdly, by harnessing the newly discovered snapping-back buckling, we design a new class of reusable energy-absorbing architected material. Subjected to an axial compression, a wide hyperelastic column can discontinuously buckle, snapping from one stable equilibrium state to another, leading to energy dissipation, while upon unloading, it can completely recover its undeformed state. Making use of this property, we design an energy-absorbing architected material by stacking layers of wide hyperelastic columns, and fabricating it by multi-material 3D printing and sacrificial molding. Characterized by quasi-static and drop tests, the material shows the capability of energy dissipation and impact force mitigation in a reusable, self-recoverable, and rate-independent manner. A theory is established to predict the energy-absorbing performance of the material and the influence of the column geometry and layer number. Wide tunability of the peak force, energy dissipation and stability of the material is further demonstrated. Our work provides new design strategies for developing reusable energy-absorbing materials and opens new opportunities for improving their energy dissipation capacities.

Finally, we achieve well-defined 3D shapes by buckling flat liquid crystal elastomer (LCE) thin sheets subjected to in-plane nonuniform stresses. Shape morphing of flat thin sheets to well-defined 3D shapes is an effective method of fabricating complex 3D structures, and LCEs are an attractive platform for shape morphing due to their ability to rapidly undergo large deformations. Here we model the buckling-induced 3D shape formation from a thin LCE sheet with prescribed in-plane stretch profiles. The sheet is modeled as a non-Euclidean plate, in which the prescribed metric tensor cannot be realized in a flat configuration and thus no stress-free configuration exists even in the absence of external loads or constraints. Under the thin plate limit, when the stretching energy dominates, we solve both the forward and inverse problems, i.e. determine the 3D shapes under prescribed stretch profiles, and determine the stretch profiles for desired 3D shapes,

respectively. In the condition of a finite thickness of the sheet, the resulting 3D shapes are determined by the interplay between both the stretching and the bending energies. For a sheet with a small but finite thickness, we predict the 3D shapes for prescribed stretch profiles, and identify the critical thicknesses at which the transition from the flat to buckled configurations occurs. The theoretical predicted 3D shapes agree closely with the ones from both finite element simulations and experiments. Our analysis sheds light on the design of the shape morphing of LCE sheets, and provide quantitative predictions on the 3D shapes of programmed LCE sheets upon stimuli for various applications.

The dissertation of Yuzhen Chen is approved.

Ajit Mal

Vijay Gupta

Mohammed Khalid Jawed

Lihua Jin, Committee Chair

University of California, Los Angeles

2021

TABLE OF CONTENTS

LIST OF FIGURES

ACKNOWLEDGMENTS

I would like to express my sincere gratitude to all the people who provide support to me for finishing my PhD thesis.

First and foremost, I would like to express my deepest and heartiest gratitude to my PhD advisor, Prof. Lihua Jin, for her tremendous support throughout my PhD program. Her guidance is always helpful and inspiring. Her excellent insight, very deep understanding, and great passion in mechanics field influenced me profoundly. I am feeling extremely lucky being her PhD student.

Second, I would like to thank my other committee members, Prof. Ajit Mal, Prof. Vijay Gupta, and Prof. M. Khalid Jawed, for their valuable suggestions and comments to my PhD thesis.

Third, I would like to thank my collaborators, Prof. Ryan Hayward, Prof. Sihong Wang, and Dr. Alexa Kuenstler.

Then I also want to thank my previous and current group members for supporting and helping me during my PhD program. They are Masato Koizumi, Yu Zhou, Ashley F. Stein-Merlob, Boliang Wu, Shivam Agarwal, Chen Wei, Tianzhen Liu, Dr. Chen Xuan, Dr. Kangjia Fu, and Weikang Xian.

Finally, I would like to thank my parents and my friends for giving me all the unconditional love and understanding.

VITA

2008-2012 B. Eng. in Mechanical Engineering, Dalian University of Technology, Dalian, China.

2012-2015 MS in Mechanical Engineering, Tsinghua University, Beijing, China.

PUBLICATIONS

[1] **Y. Chen**, L. Jin, Reusable Energy-Absorbing Architected Materials Harnessing Snapping-Back Buckling of Wide Hyperelastic Columns, Adv. Funct. Mater. (2021) 2102113.

[2] A.S. Kuenstler*, **Y. Chen***, P. Bui, H. Kim, A. DeSimone, L. Jin, R.C. Hayward, Blueprinting Photothermal Shape-Morphing of Liquid Crystal Elastomers, Adv. Mater. 32 (2020) 2000609. (*Equal Contribution)

[3] **Y. Chen**, L. Jin, Snapping-back buckling of wide hyperelastic columns, Extreme Mechanics Letters. 34 (2020) 100600.

[4] **Y. Chen**, L. Jin, From continuous to snapping-back buckling: A post-buckling analysis for hyperelastic columns under axial compression, International Journal of Non-Linear Mechanics. 125 (2020) 103532.

[5] **Y. Chen**, L. Jin, Geometric role in designing pneumatically actuated pattern-transforming metamaterials, Extreme Mechanics Letters. 23 (2018) 55–66.

Chapter 1 Background

Buckling instability is traditionally regarded as failure mode. However, they can also be harnessed to design functional materials. Researchers have incorporated buckling instabilities into soft materials capable of large deformations to achieve advanced functionalities. By harnessing the sudden and repeatable deformations triggered by buckling instabilities, fast locomotion in soft robotics, tunability in mechanical metamaterials, and complex shape morphing have been achieved. Herein, we first introduce the buckling instabilities of flexible structures such as columns and thin films, which play a key role in functional materials. Then we review the different applications exploiting buckling instabilities in soft robotics, mechanical metamaterials, and shape morphing.

1.1 Buckling Instability

Buckling instability is the sudden change in deformations of a structure under loads. It is regarded as failure modes for many engineering structures made of rigid materials, since the buckling-induced large strains usually exceed the yielding limit of the constitutive materials, leading to plastic deformations or even fractures. However, soft elastomeric materials can undergo large deformations, which enables the buckling instability to be exploited for new functionalities. In general, the buckling instability is governed primarily by the structural geometry rather than the material properties. Based on the force-displacement relations, the buckling instability can be of three types: continuous (Figure 1.1a), snapping-through (Figure 1.1b), and snapping-back (Figure 1.1c) buckling.

Figure 1.1a shows the schematic of the force-displacement relation for continuous buckling, in which the force increases with the displacement after the buckling occurs at a rate much lower than that prior to the buckling. Thus, it allows for large deformations with a slight increase in

external loads. However, the structures exhibiting the continuous buckling have no snap motion when loaded under either force or displacement controls, since the stable equilibrium paths are continuous. This buckling type can be seen in axially-loaded slender elastic beams with various end constraints [1].

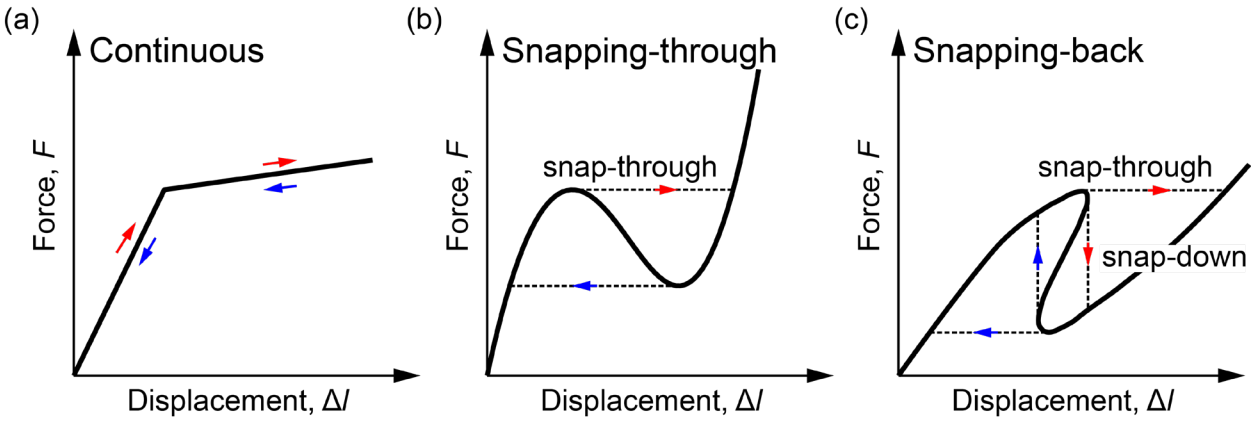

Figure 1.1 Buckling instabilities of different types : (a) continuous buckling, (b) snapping-through buckling, and (c) snapping-back buckling. Unlike the continuous buckling exhibiting a monotonic force-displacement relation, the snapping-through buckling has a force-displacement curve featuring a negative stiffness regime lying between two positive stiffness regimes, as shown in Figure 1.1b. When loaded in a force-controlled manner, the structures exhibiting snapping-through buckling will snap rapidly between two stable equilibrium states after the buckling point, leading to a sudden change in deformations while keeping its prescribed force constant. This snap motion enables very high actuation speeds, and the hysteresis area in a complete loading cycle enables energy dissipations. Many structures can exhibit this snapping-through buckling, such as tilted or curved beams [2–5], shallow shells [6–8], and von Mises trusses [1]. The judicious design of these structures can lead to bistable systems.

The third type of buckling instability is snapping-back buckling, which exhibits more complex force-displacement relation than the first two types. Figure 1.1c shows a schematic of the force-displacement curve for snapping-back buckling, in which both force and displacement decrease after the buckling point, forming a post-buckling regime with a positive stiffness. This type of buckling instability can result in snap motion when loaded under either force or displacement control, which enables fast actuation and energy dissipation under more types of loading conditions compared to snapping-through buckling. This snapping-back buckling is commonly observed in perfect cylindrical shells [9] and shallow arches [10].

1.2 Buckling of Thin Films Induced by Residual Stresses

The buckling instability is usually induced by external forces or confinements. However, natural bodies often undergo buckling instability without any external forces or confinements, leading to a wide range of 3D shapes, such as Acetabularia acetabulum [11], blooming lily [12], chiral seed pods [13,14], and aquatic plant leaves [15] (Figure 1.2). This buckling instability is induced by residual stress, which is caused by in-plane differential growth due to nonuniform cell elongation and proliferation. Inspired by nature, researchers have developed many synthetic materials [16–21] which can generate controllable distribution of residual stresses upon activation and buckle into well-designed 3D shapes (Figure 1.3).

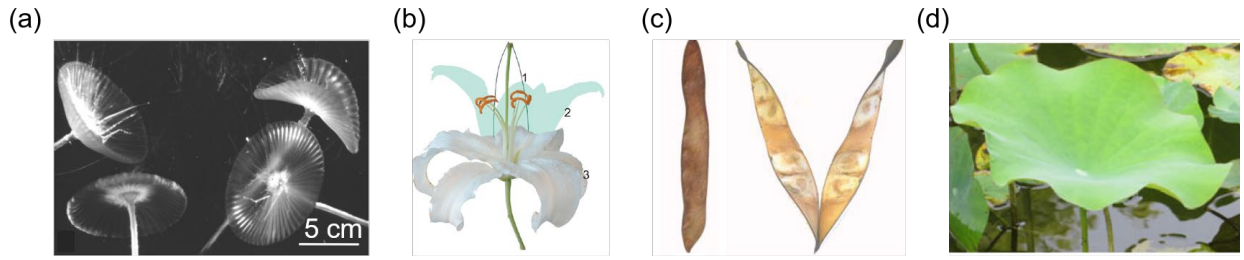

Figure 1.2 Buckling-driven morphogenesis of natural bodies. (a) Acetabularia acetabulum [11], (b) blooming lily [12], (c) chiral seed pods [13,14], (d) aquatic plant leaves [15].

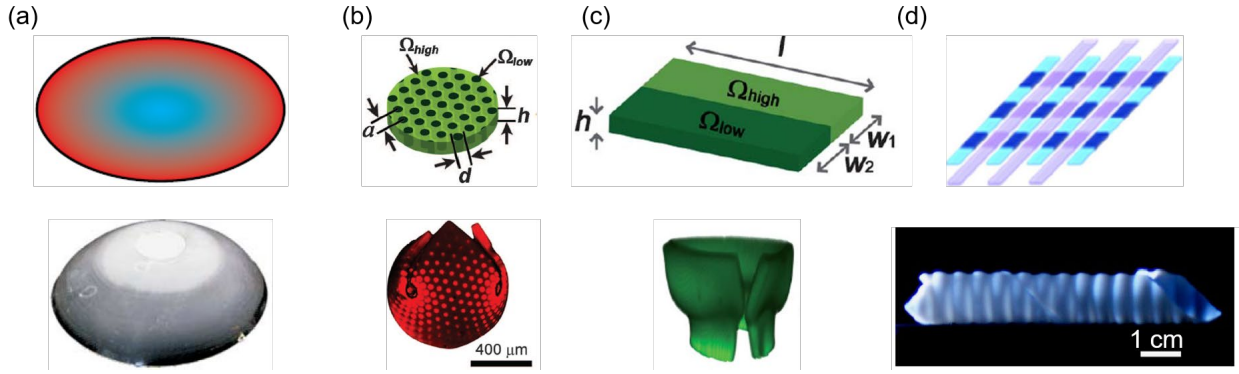

Figure 1.3 Buckling of synthetic materials induced by residual stresses. (a) A gel disk with in-plane radial gradient in swelling ratios buckles into a dome-like shape [16]. (b) A gel disk with complex patterns of in-plane swelling ratios buckles into a spherical shape [17]. (c) A bistrip composed of two strips with different swelling ratios adopts a rolling shape [18]. (d) A sheet composed of different responsive materials can buckle into different 3D shapes in response to applied stimuli [19].

The residual stress-induced buckling shapes can be captured by non-Euclidean plate theory [22–25], which addresses the modeling of elastic plates with residual stresses. Since no stress-free configuration can be used as a reference configuration, the strains are defined by metric tensors rather than by configurations. The metric tensor g of a sheet quantifies the local distances between

the adjacent points on the surface of the sheet. By prescribing the in-plane stretch profiles, a reference metric tensor $\bar{g}$ can be programmed, which may not be immersible into a flat configuration. The actual metric tensor g of the sheet deviates from the prescribed reference metric $\bar{g}$, generating residual stresses that buckle the sheet. The deviation of the actual metric from the reference metric costs stretching energy, and the nonzero curvature metric costs bending energy. The total elastic energy [22–25] is the combination of the stretching and the bending energies

$$w = \frac{1}{8}Eh(g - \bar{g})^2 + \frac{1}{2}Eh^3\kappa^2, \tag{1.1}$$

where E represents the Young's modulus, h denotes the thickness of the sheet, and κ is the curvature tensor. The buckled shapes triggered by residual stresses can be determined by minimizing the total elastic energy.

1.3 Mechanical Metamaterials

Metamaterials are man-made materials with a tailored, architected structure, designed to achieve properties that cannot be realized in conventional materials. They derive their properties not from their constitutive materials, but from their carefully designed structures. They are usually arranged in repeating pattern and are fabricated at scales that are smaller than the wavelength of the phenomena they influence. Some novel but unusual photonic [26] and acoustic [27] properties have been achieved, and possible applications such as phononic transistor-like device [27] have been demonstrated.

As a more recent branch of metamaterials, mechanical metamaterials exhibit some unique mechanical properties. An early example [28] of mechanical metamaterials is auxetic materials that feature negative Poisson's ratio. Figure 1.4 shows the auxetic behaviors of a rubber sheet patterned with a square array of circular holes under uniaxial loads. Although individual rubber

filaments become thicker when subjected to compression, the overall structure does not expand laterally, achieving negative Poisson's ratio. This example illustrates how the behavior of mechanical metamaterials is controlled by their structure rather than their composition. More recently, the developments in the field of mechanical metamaterials involves elastic instabilities and large deformations to create soft mechanical metamaterials, which have achieved more complex functionalities such as pattern and shape transformation [2,29–41], programmable mechanical responses [2,5,42,43] and reproduction of phenomena seen in crystallographic systems [41,44].

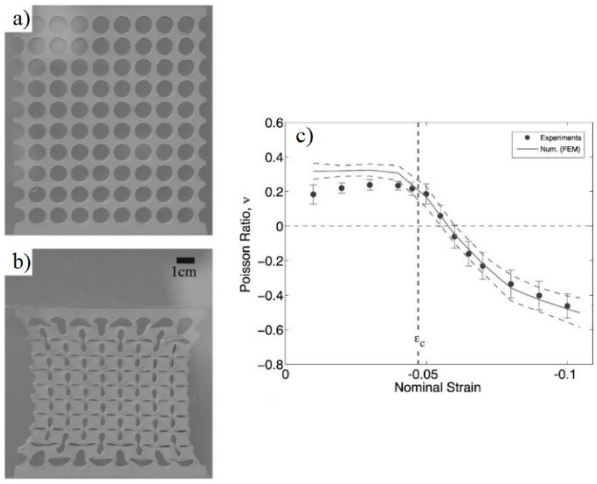

Figure 1.4 Auxetic metamaterials. (a) Sample in the initial unstrained configuration. (b) Sample under uniaxial compression of ε = -0.25. (c) Poisson's ratio as a function of the applied axial nominal strain [28].

1.3.1 Pattern and shape transformation

Some soft mechanical metamaterials can undergo sudden but well-controlled pattern switch shape shifting ranging from 2D [2,30–38,40,41,45] to 3D [29,39,46]. Their functionality depends on their special structures consisting of stiffer elements linked by slender and flexible

elements as hinges. Under precisely designable loading conditions, the slender elements can undergo buckling instabilities, which trigger reversible pattern transformations. The simplest example of such metamaterials [31,33–36,40,41,45] is a square array of circular holes patterned in an elastomeric sheet [28,35]. When the structure is subjected to uniaxial compression, buckling of the beam-like ligaments creates large deformations and triggers a sudden pattern transformation. As shown in Figure 1.5, the circular holes pattern is replaced by a strikingly different pattern of alternating mutually orthogonal ellipses. Moreover, it has been proved that both the symmetry of the lattices [34] and the shape of the voids [31] play important roles in determining pattern transformations (Figure 1.6 and Figure 1.7).

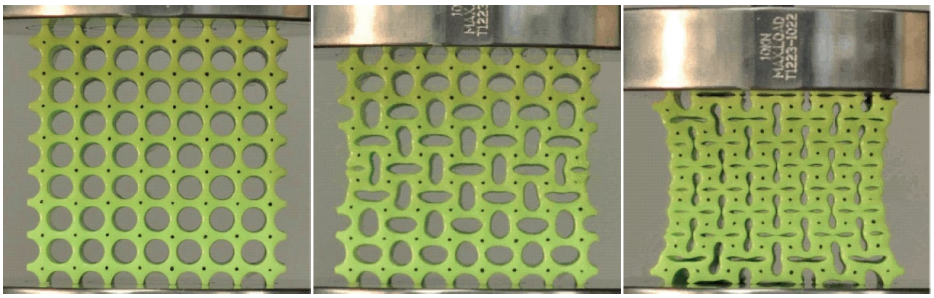

Figure 1.5 A mechanical metamaterials patterned with circular holes undergoes a reversible pattern transformation triggered by buckling instabilities [28,35].

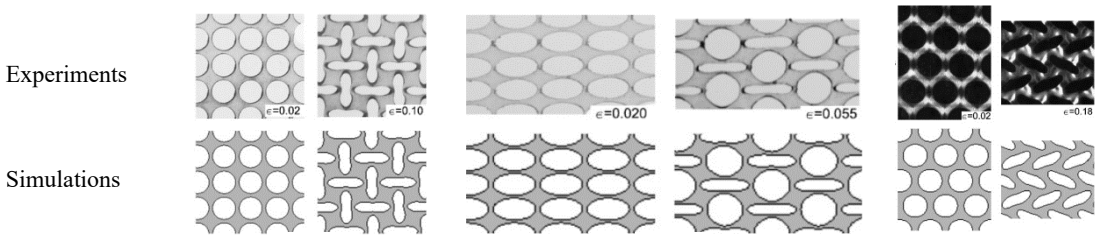

Figure 1.6 Experimental (top) and numerical (bottom) deformed images for (a) square lattices of circular voids, (b) rectangular lattices of elliptical voids, and (c) oblique lattices of circular voids [34].

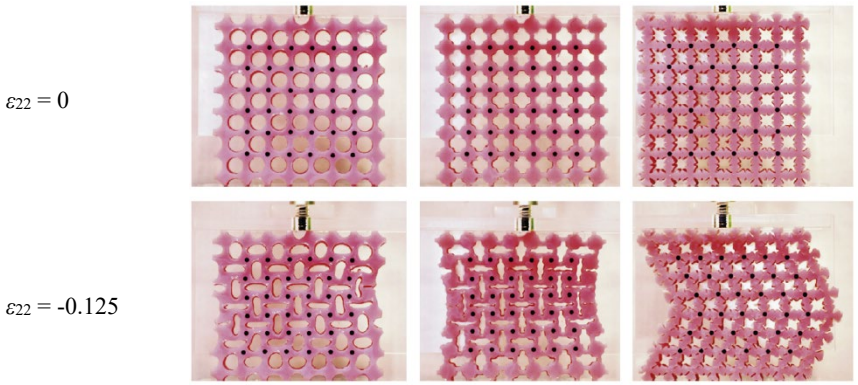

Figure 1.7 Experimental images of three periodic structures with different pore shapes under uniaxial compression [31].

The development of fabrication techniques broadens the structural complexity of soft mechanical metamaterials. Additive manufacturing makes it possible to fabricate various unit cells and mix them to achieve aperiodic structures, which exhibit inhomogeneous pattern transformations. One example [40] of such hybrid structure is porous elastomeric surfaces whose perforations feature varying shape and spacing (Figure 1.8). Another example [39] is so called Voxelated mechanical metamaterials (Figure 1.19), where the cubicle unit cell can deform into two different shapes that fit together in several ways. The sample shown in Figure 1.9 is composed of 10x10x10 unit cells, arranged differently in such a way that a smiley patterned texture appears on one of the faces under uniaxial compression.

All these examples mentioned above illustrate that the architecture of the mechanical metamaterials is crucial for their properties and functionalities, and that pattern switch can be "programmed" into their structural design. Furthermore, the structures recover their initial shape when unloaded.

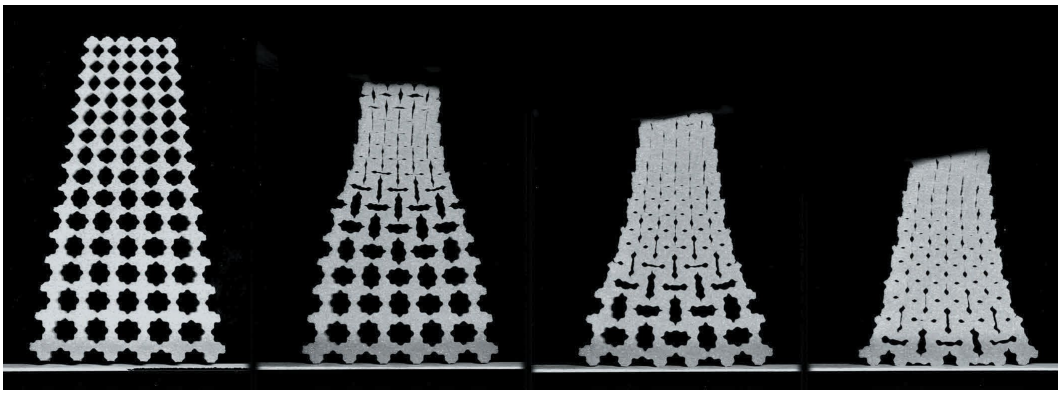

Figure 1.8 Inhomogeneous pattern transformation exhibited by the hybrid structures. From top to bottom, both the shape and spacing of the perforations are proportionally varied [40].

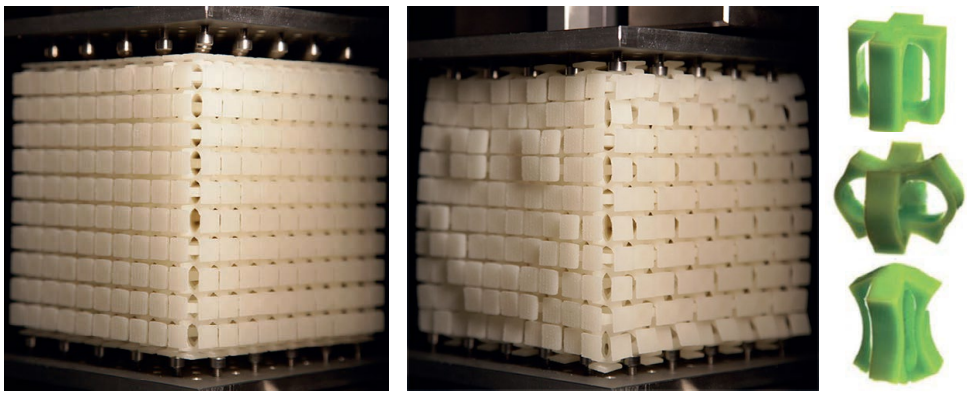

Figure 1.9 A metacube consisting of 10x10x10 unit cells reveals smiley texture under uniaxial compression [39].

1.3.2 Programmable mechanical responses

The mechanical responses under uniaxial load can also be programmed by structural design. One example [42,43] exhibiting such programmable mechanical responses is a quasi-2D elastic sheet patterned by a regular array of large and small holes, as shown in Figure 1.10. The inequality in hole sizes creates two different polarizations of the hole pattern, determined by whether *x* compression or y compression is dominant. By constraining this metamaterial in the x direction, and then compressing it in the *y* direction, the material undergoes a polarization switch from an *x*-polarized to a *y* polarized state, as illustrated in Figure 1.10(a). Depending on the magnitude of the *x* confinement, this polarization switch can be either smooth or discontinuous, and the force-displacement curves can be tuned from monotonic to nonmonotonic and eventually display hysteresis, as shown in Figure 1.10(b).

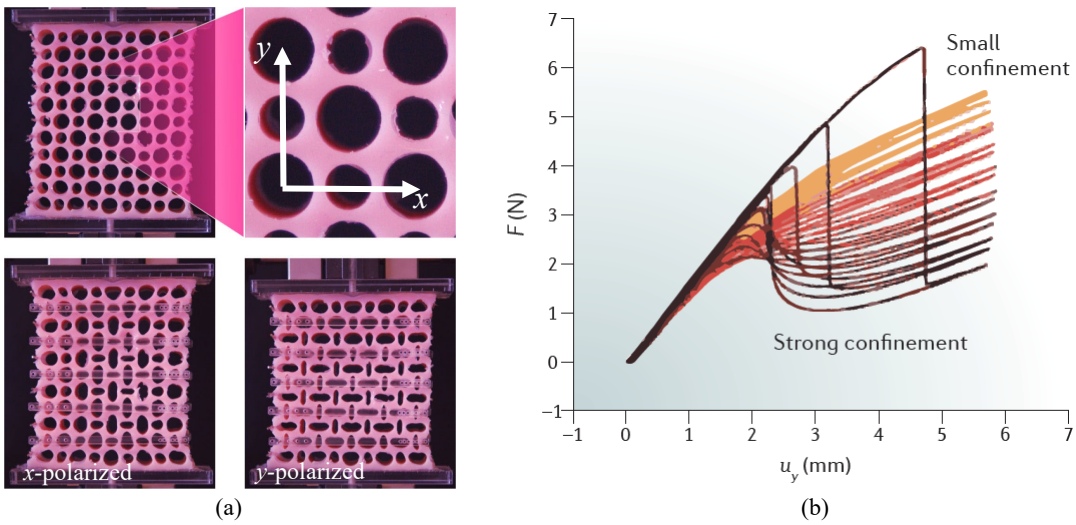

(a) (b)

Figure 1.10 Mechanical metamaterials exhibiting tunable mechanical response under uniaxial compression [42,43]. (a) The structure characterized by alternating large and small holes, and polarizations switch caused by the competition between x confinement and y compression. (b) The vertical force F as a function of the vertical compression.

Another example [5] is a snapping metamaterial composed of a periodic arrangement of snapping units, as shown in Figure 1.11(b). Their design is inspired by a bistable mechanism, where two curved beams are centrally clamped, as illustrated in Figure 1.11(a). A normal force applied in the middle of the double-beam mechanism can prompt it to snap through to its second stable state (shown as dashed line in Figure 1.11(a)). When compressed along its axis of symmetry, each row of the entire structure snaps through, and exhibits a pattern switch from a wavy-shaped structure to a diamond-like configuration. Depending on the geometries of the curved segments, this transition can be either smooth or discontinuous, and the mechanical responses can be tuned to be monotonic, S-shaped, plateau, and non-monotonic. As illustrated in Figure 1.11(c)~(e), for small a/l, the response is smooth without snap-through instabilities, whereas for larger values of a/l, the metamaterial snaps sequentially and exhibits a long-serrated plateau.

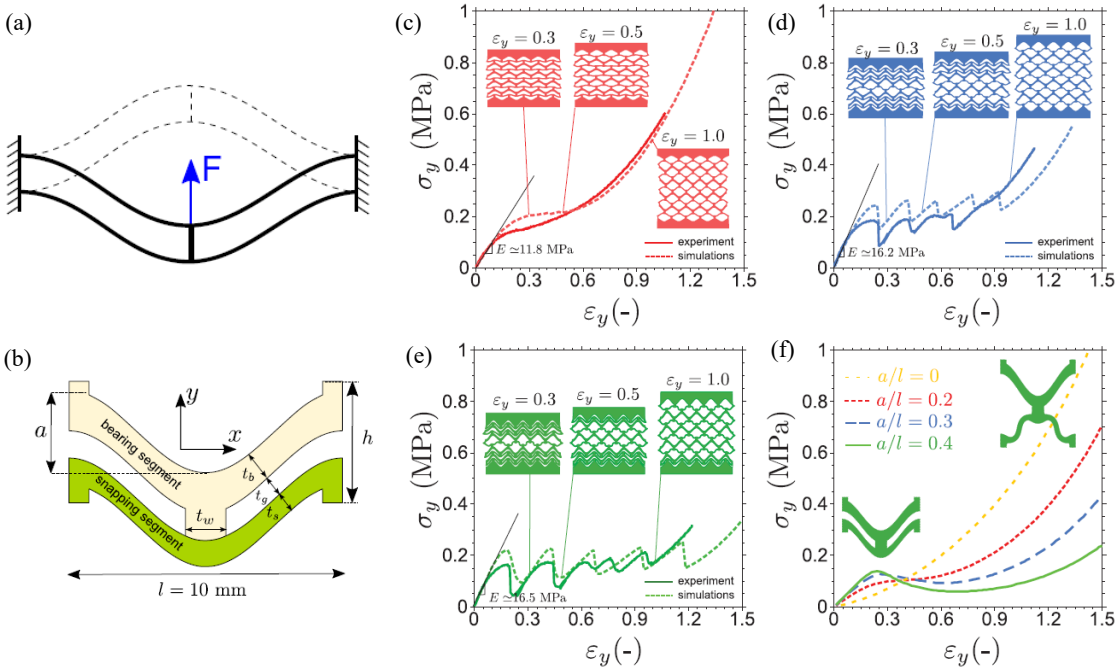

Figure 1.11 Snapping metamaterials under tension. (a) Bistable mechanism of double curved beams under a vertical force applied in the middle. (b) The geometries of the unit cell composed

of load bearing and snapping segments. (c)~(e) Nominal stress-strain responses from experiments and FEA simulations for different geometries: (c) a/l = 0.2, (d) a/l = 0.3, and (e) a/l = 0.4. (f) Mechanical response of a single unit cell for selected a/l ratios [5].

In both examples mentioned above, the mechanical behavior in response to uniaxial load can be precisely programmed by structural designs. By varying boundary conditions or geometries or both, the mechanical metamaterials exhibit monotonic, nonmonotonic, and hysteretic behaviors, which underlie their programmability.

1.3.3 Reproduction of phenomena seen in crystallographic systems

Some mechanical metamaterials [41,44] can macroscopically reproduce the phenomena that occur in crystallographic systems. One example [41] is phase-transforming and switchable metamaterials that can generate a shape-memory effect [47] similar to that exhibited by ferroelastic materials (Figure 1.12). The mechanism of shape-memory effects in ferroelastic materials is illustrated in Figure 1.12(a). When cooled below a certain temperature, the microscopic structures of ferroelastic materials are transformed from cubes into tetragonal unit cells whose long axis points at different directions. Here, different orientations refer to different "variants". The switch between variants can be triggered by macroscopic external stresses. As a result, the bulk material is molded into different macroscopic shapes depending on its history of loading. When heated above a certain temperature, the microscopic structures recover cubes, and the material returns to its original shape. Similarly, the phase-transforming and switchable metamaterials shown in Figure 1.12(b) can change its unit cell shape from square to rectangle by controlling the external pressures, reminiscent of microscopic structure transition under temperature changes in ferroelastic materials. Moreover, the switch between variants can also be achieved through a uniaxial compression (from

tall rectangle to wide rectangle, Figure 1.12(c)), like the variant switch in ferroelastic materials by external load. Finally, the shape-memory effect can be observed when the shapes of the unit cells recover square under initial external pressures.

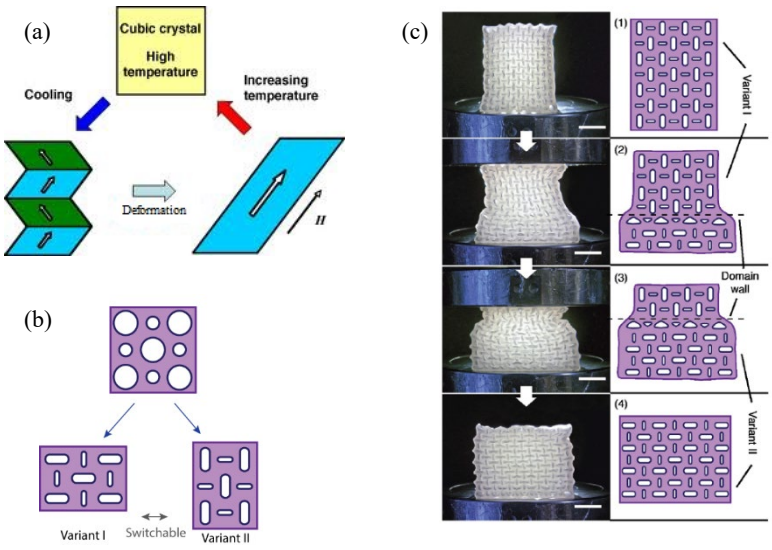

Figure 1.12 Phase-transforming and switchable metamaterials analogue to ferroelastic materials. (a) The mechanism of shape-memory effects in ferroelastic materials. (b) Schematic of the phase transition, variant switching and shape-memory effects in metamaterials. (c) By applying a compressive load in the long axis, the rectangular sample switches from a tall rectangle to a wide rectangle [41].

Another example is given by flexible origami metamaterials [44] (Figure 1.13). Each unit cell of the metamaterials is mechanically bistable. By switching between states, that is by "popping through" some of the folds, the metamaterials exhibit crystallographic structures, such as vacancies (Figure 1.13(a)), dislocations (Figure 1.13(b)), and grain boundaries (Figure 1.13(c)).

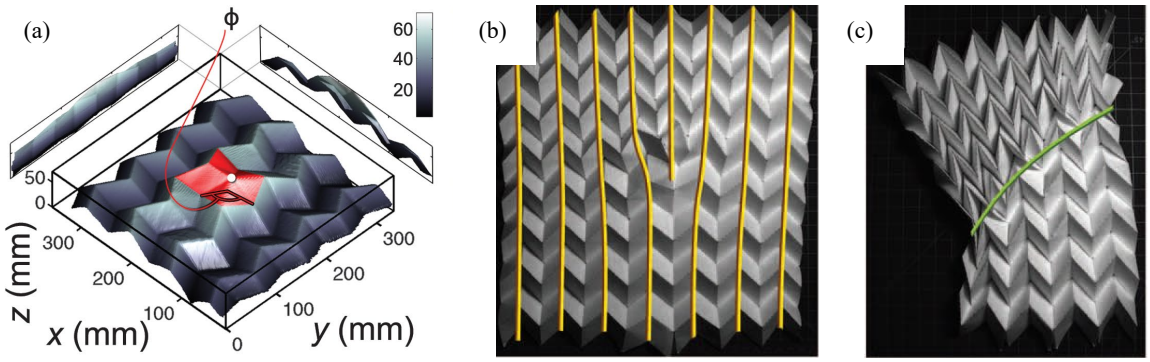

Figure 1.13 Flexible origami metamaterials exhibiting crystallographic structures. (a) 3D reconstruction with a centrally located pop-through defect. The red region can be recognized as a lattice vacancy. (b)~(c) Photographs with complex defect structures: (b) Column of lattice vacancies generate an edge dislocation; (c) Column of edge dislocations generate a grain boundary [44].

Given the scale-free geometric character in the two examples above, the ideas for metamaterial design can be directly transferred to milli-, micro-, and nanometer-size systems. This is of significance for two reasons. First, it provides an efficient way of preparing microstructured materials with targeted mechanical and optical properties. Secondly, it offers a new approach to study at a macroscopic scale the microscopic interactions in crystallographic systems.

1.4 Buckling-induced Functionalities

In this section, we will provide several representative examples of exploiting buckling instabilities in soft robotics, mechanical metamaterials, and shape morphing, illustrating how buckling instabilities can be harnessed to design functional materials.

1.4.1 Enhancing actuations in soft robotics

Compared to conventional rigid robots, soft robots have significant advantages on adaptability to uncertain environment, and safety to humans and fragile objects. However, soft materials of which soft robots are made lead to low actuation speed and small actuation forces, limiting the power that soft robots can output. To overcome these power limitations, people have developed many strategies by harnessing the snapping-through buckling, since this type of buckling can enable rapid and large movements with low energy inputs, which can effectively amplify the actuation forces in soft robotics.

Here we show three examples in which the snapping-through buckling are exploited to design soft actuators with fast actuations. Inspired from Venus flytrap, a soft gripper [48] (Figure 1.14a) is developed that can achieve very fast gripping speed. This gripper consists of a pneumatically actuated bistable trigger sandwiched by two bistable curved layers. Upon pneumatic actuations, each bistable curved layer can suddenly transition between its convex and concave states, leading to fast open or close of the gripper. Another example is a swimming soft robot [49] (Figure 1.14b) in which its proportion force comes from the snap motion of a bistable beam. This snap motion is triggered by the shape-memory polymer attached to the bistable beam in response to surrounding temperature changes. Depending on the number of bistable beams and how they are interconnected, the swimming soft robot can achieve different sequential motions. Using similar mechanisms, a crawling soft robot with bistable actuators can achieve relatively high speeds with low actuation frequencies [50] (Figure 1.14c). All the three examples above demonstrate how snapping-through instability provides soft robots with rapid and tunable motions.

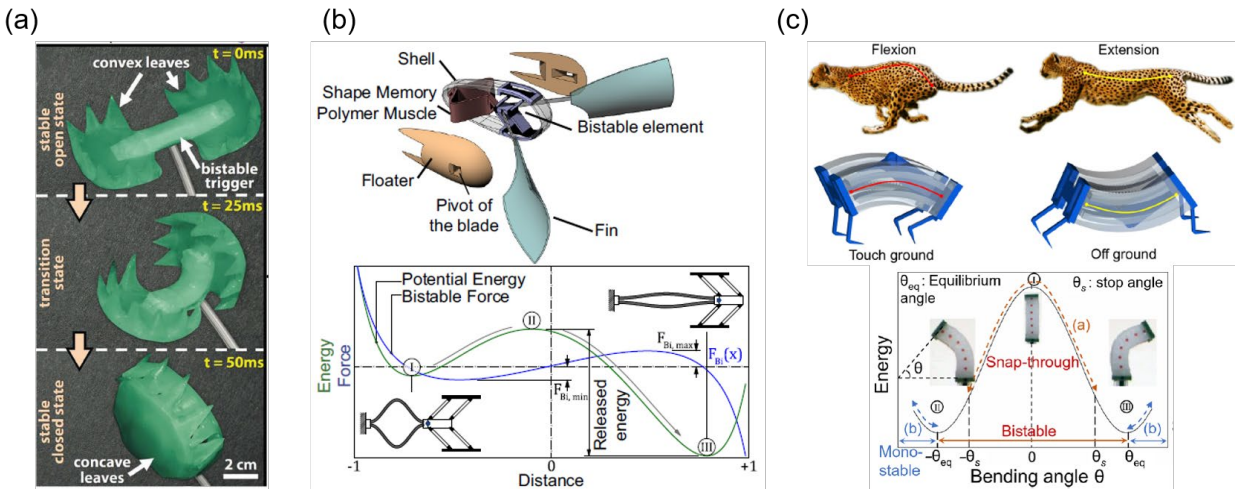

Figure 1.14 Fast motions leveraging snapping-through instability. (a) Venus flytrap-inspired soft gripper that can close in around 50ms [48]. (b) Swimming soft robot driven by bistable elements [49]. (c) Cheetah-like galloping crawler with bistable actuators that can achieve relatively high speeds with low actuation frequencies [50].

1.4.2 Reusable energy-absorbing architected materials

Energy-absorbing materials are ubiquitously used to protect humans and objects from impacts or collisions, examples including football helmets, car bumpers, and packaging of delicate goods. The essence of an energy-absorbing material is the capability of absorbing mechanical shock energy while keeping the peak force below the safety threshold. Besides, energy dissipation is required to mitigate rebounds [51]. Among various energy dissipation mechanisms, plastic deformation or fracture of metals, ceramics and composites [52,53] is often utilized to dissipate a large amount of energy by means of dislocation motion or bond breakage. However, these energy-absorbing materials are typically only good for one-time usage, since they undergo irreversible deformation or are permanently damaged during an impact. Materials with the energy dissipation mechanisms of viscous flow [54] and viscoelasticity [55–57] can be used repeatedly, but they are

highly rate-dependent with slow recovery to the undeformed states upon unloading. Friction [58–60] between particles in granular materials also permits reusability, but the collapsed materials are usually not self-recoverable.

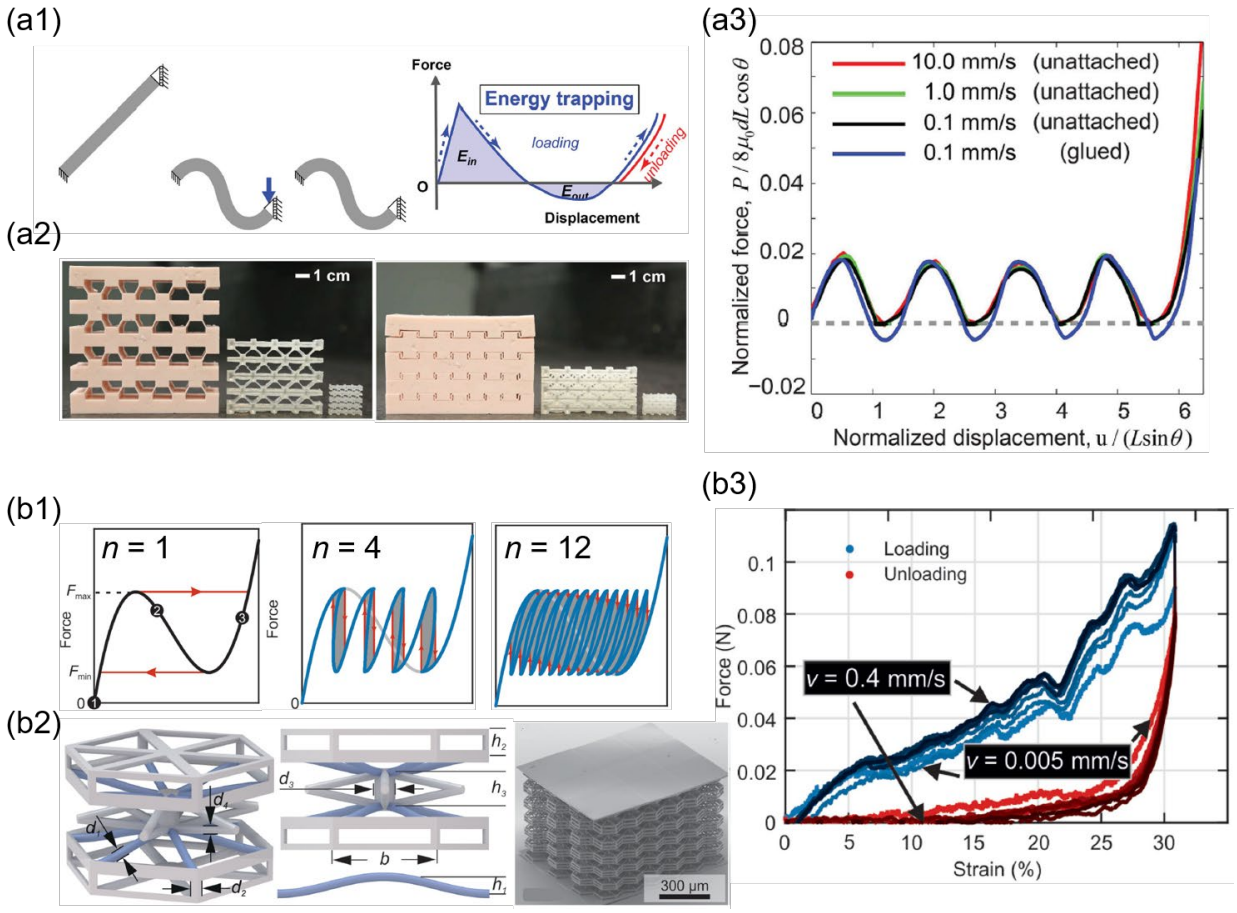

Figure 1.15 Reusable energy-absorbing architected materials harnessing snapping-through buckling. (a) Multistable architected materials for energy trapping [4]. (a1) A bistable tilted beam can trap part of input energy into the material. (a2) Samples with different scales before and after the impact. (a3) Mechanical response of the samples under different loading rates. (b) Light-weight microlattices shock absorbers [3]. (b1) Schematic force-displacement curve for a single (n = 1) monostable snapping-through element and for multiple (n = 2 and 12) elements connecting in series. The gray area is the energy dissipated in one loading and unloading cycle. (b2) Schematic

of a single element exhibiting monostable snapping-through buckling and the electron image of a sample. (b3) Force-displacement curves for different loading rates.

To achieve a reusable, rate-independent and self-recoverable energy-absorbing material, a novel design strategy of harnessing the snapping-through instability of tilted or curved beams in architected materials has been proposed [2–5,38,61–73] (Figure 1.15). These beams are stacked into a multi-layered structure, and buckle sequentially one layer after another under compression, resulting in a nearly constant force as the displacement proceeds. The impact energy can be either trapped in the material due to bistability (Figure 1.15a), or damped into heat due to snapping motions (Figure 1.15b). Since the material only deforms elastically, it is reusable and rate-independent. However, when the constituent beams are bistable [2,4,38,61–63,66,68,69] (Figure 1.15a), the architected material stays in the deformed configuration after compression, without self-recovering its undeformed state. On the other hand, when the constituent beams are monostable, although the formed energy-absorbing architected material is self-recoverable upon unloading, a large number of layers connecting in series are required to achieve energy dissipation [3,64,74] (Figure 1.15b), making the structure thick and heavy.

1.4.3 Shape morphing in Liquid Crystal Elastomers (LCEs)

Liquid Crystal Elastomer (LCE) [75] is combination between liquid crystals (mesogens) and lightly crosslinked polymer networks. Upon external activations such as heat [76] and light [77,78], these mesogens can undergo phase transitions between the nematic (aligned in the same direction which is the director direction) and isotropic (oriented randomly) phases, leading to fast, large, anisotropic and reversible deformations (Figure 1.16). Due to these special properties, LCE has been widely and deeply studied and shown great potentials in the applications of artificial

muscles [79,80] and soft robotics [81]. It is also an attractive platform for shape morphing [82–90].

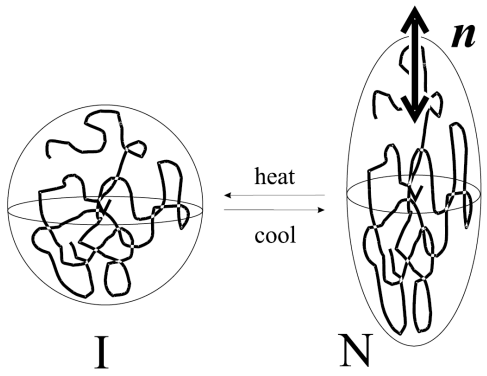

Figure 1.16 Spontaneous deformation of liquid crystal elastomers due to phase transition [75]. Polymers with mesogens on the main chains undergo spontaneous deformation in response to temperature changes as mesogens transition between the isotropic (I) and nematic (N) states.

To achieve desired target shapes, one needs to prescribe ununiform stretches within the LCE sheets. Recent work focuses on programming the director orientation to achieve the variations in stretches. Figure 1.17 illustrate an optical patterning system in which the polarization of laser is used to manipulate the alignment of mesogens on a local surface as small as 0.01 mm^2 [91]. Arbitrary and spatially complex patterns can be programmed using this method, leading to many complex 3D shapes upon activations. The director orientation can also be controlled by microchannels fabricated by photolithography [88,89] (Figure 1.18). Using this patterning method, a more complex 3D shapes such as a face are generated from flat LCE sheets. With recent development of additive manufacturing, the director orientation can be programmed through direct ink writing 3D printing techniques (Figure 1.19). As the ink is extruded from the nozzle, the mesogens are aligned along the printing paths due to the shear forces. By carefully patterning the printing pathway, complex 3D shapes can be easily achieved (Figure 1.19b-c).

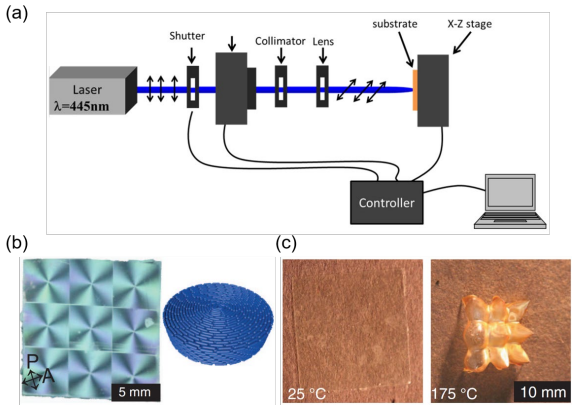

Figure 1.17 Patterns of director orientation controlled by an optical patterning system [91]. (a) Schematic of the optical patterning system. The local surface alignment of mesogens is controlled by the light polarization. (b) The LCE film with nine patches in which the director orientation varies azimuthally. (c) Upon heating, the flat LCE film reversibly transforms into the 3D shape with nine cones.

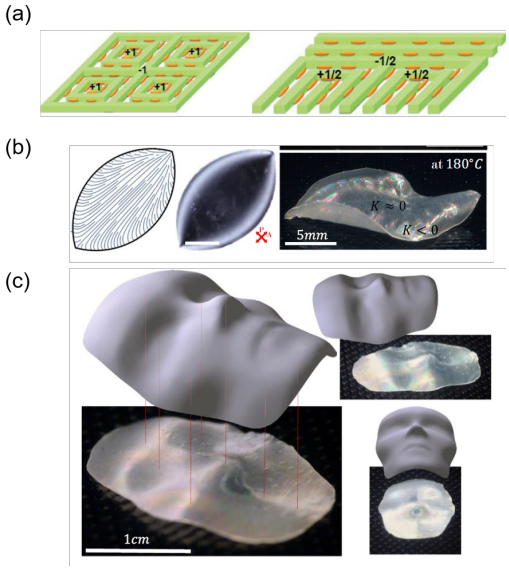

Figure 1.18 Patterns of director orientation programmed by the patterns of microchannels [88,89]. (a) Mesogens are aligned on patterned microchannels. (b) a leaf-shaped surface and (c) a face shape are obtained by programming the director fields.

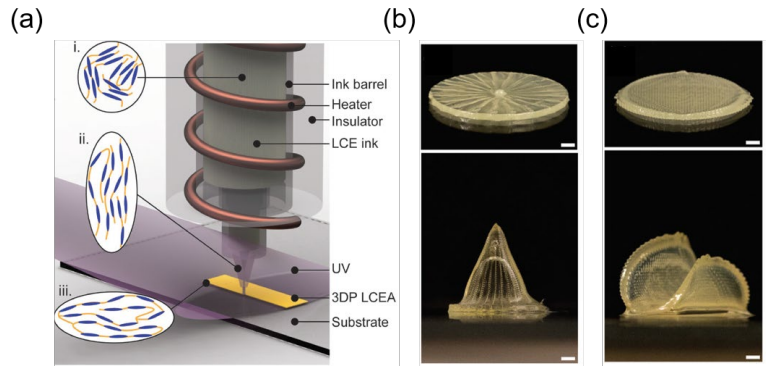

Figure 1.19 Patterning of direction orientation using direct ink writing [92]. (a) Schematic illustration of direct ink writing 3D print head for the LCE ink. Cone shape (b) and saddle shape (c) obtained by programming the alignment of mesogens in a circular disk.

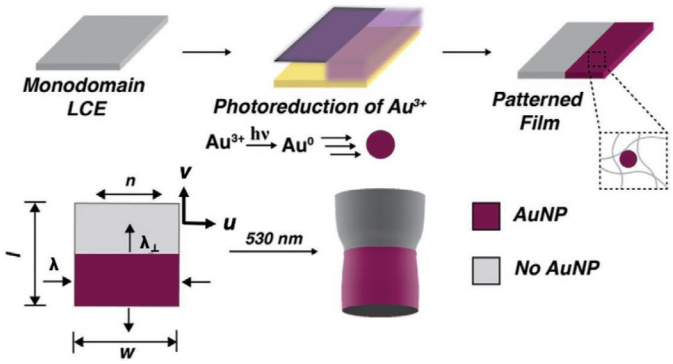

Figure 1.20 Photopatterning the in-plane stretch variations in a monodomain LCE sheet [93]. Gold nanoparticles are spatially embedded into the monodomain LCE sheet by photoreduction upon UV light. When visible light is shone on the surface, the ununiform heat generation leads to ununiform in-plane stretch gradients, which buckles the flat sheet into a prescribed 3D shape.

Other than spatially varying director orientation, another strategy of embedding stretch variations in the LCEs is programming the magnitude of deformation in a uniform director field. Figure 1.20 illustrates that arbitrary in-plane stretch profiles can be embedded into monodomain LCEs by programming the photothermal heat generations controlled by gold nanocomposite

distributions [93]. The spatially ununiform stretch profiles can trigger buckling of films, resulting in predictable 3D shapes. Compared to patterning the director orientations, this method has a simpler fabrication process, and can be widely generalized to all LCE systems.

1.5 Outline of the Dissertation

In this dissertation, we will focus on the buckling instabilities of columns and thin films, and on harnessing these buckling instabilities to design pneumatically actuated pattern-transforming metamaterials, design reusable energy-absorbing architected materials, and achieve complex 3D morphing of LCE thin films. The main points of each chapter are summarized as follows:

In Chapter 2, we propose a class of pneumatically actuated pattern-transforming metamaterials in which the pattern transformation is caused by beam buckling. We combine finite element method, analytical solutions, and experiments to reveal the mechanism of its pattern transformation and investigate the geometric effects on the pattern transformation. Our analytical model reveals the mechanics of the pattern transformation and shows good agreement with the finite element analysis. The experimental results confirm our theoretical predictions.

In Chapter 3, we numerically show that an axially loaded hyperelastic column can exhibit complex buckling behaviors, and discover a new buckling mode for straight columns with high width-to-length ratios under axial compression: snapping-back buckling mode. To understand the mechanism of snapping-back buckling, we have established an analytical discrete model, and unraveled that snapping-back buckling results from strong coupling between stretching and bending, similar to that of snapping-back buckling in shells. A phase diagram is constructed to demarcate the different buckling modes of axially compressed columns.

In Chapter 4, we analytically show that for a straight hyperelastic column, the increase of its width-to-length ratio can fundamentally alter its buckling mode, from continuous to snapping-through, and to snapping-back. Correspondingly, the initial post-buckling slope flips its sign from positive to negative, and eventually back to positive.

In Chapter 5, we develop a reusable energy-absorbing architected material harnessing the snapping-back buckling of wide hyperelastic columns. The quasi-static cyclic loading tests confirm that the proposed material is capable of dissipating energy while keeping the force nearly constant with a long working distance in a reusable, self-recoverable, and highly predictable manner, while the drop tests at high strain rates show the feature of rate-independency and the capability of force attenuation in a broad range of input energy.

In Chapter 6, we demonstrate a method combining experiments, FEM simulations, and analytical modeling to program photoactive shape morphing from monodomain LCE sheets with a unidirectional director by spatially controlling photothermal heat generation. Discontinuous metrics introduced via localized photothermal inclusions are shown to drive buckling into many complex 3D shapes. Furthermore, we established an analytical model based on the non-Euclidean plate theory to encode smoothly-varying stretch profiles to rationally approach the design of targeted shapes.

In Chapter 7, we summarize all the findings presented in this dissertation.

Chapter 2 Pneumatically Actuated Pattern-transforming Metamaterials

When a metamaterial, composed of an elastomer with periodic circular holes sealed by elastomeric membranes, is subject to a compressive load, it can undergo a pattern transformation, yielding a large transformation strain. Such pattern transformation is triggered by the buckling instabilities, and can be broadly tuned by changing the geometric parameters of the metamaterial. In this chapter, we numerically, analytically and experimentally reveal the mechanism of the pattern transformation in a pneumatically-actuated pattern-transforming metamaterial. Besides, we will survey the design space of the geometric parameters, and investigate their effects on the pattern transformation. Our finite element simulations indicate that the slenderest wall thickness and the pattern of the holes play key roles in determining the critical load for the pattern transformation, the transformation strain, and the transformation type. To quantify the effects of these geometric parameters, we further analytically model the pattern transformation of the metamaterial by simplifying it to a network of rigid rectangles linked by deformable beams. Finally, we experimentally characterize the pattern transformation of the metamaterials with different geometric parameters. The experimental, numerical, and analytical results are in good agreement with each other. Our work provides design guidelines for this metamaterial.

2.1 Introduction

Mechanical metamaterials are materials with micro-architectures, which bring in unusual mechanical properties that are difficult to achieve in conventional materials [94,95]. Mechanical metamaterials with micro-/nano- lattice structures have reached unprecedentedly high stiffness and strength at an extremely low density [96,97]. Pentamode lattices have shown vanishing shear

moduli [98–100]. Negative Poisson's ratio is found in auxetic metamaterials with various re-entrant structures [28,29,101–107]. In additional to the elastic constants, the whole nonlinear stress-strain relations of metamaterials are open to design. Introducing bistable structures into the micro-architectures enables pattern transformations of the metamaterials and non-monotonic stress-strain curves [2,5,38]. Making use of chiral lattice structures, a metamaterial can twist under a uniaxial compression [108].

Recently, a new class of mechanical metamaterials, each consisting of a rubber slab with periodic holes, has emerged [28,31,34–36,41–43,109–111]. These metamaterials can undergo a pattern transformation when subject to a compressive load. By harnessing the geometric nonlinearity and the pattern transformation of the metamaterials, researchers have shown a variety of unique functions of them, such as negative Poisson's ratio [28], tunable acoustic properties [111,112] and inducing torsional motions [110]. When the holes are alternatingly large and small, the stress-strain curves of the metamaterials change the monotonicity under different transverse constraints [42,43]. More interestingly, since the large and small holes collapse in two perpendicular directions, a high-symmetry square lattice of holes can transform into a low-symmetry rectangular lattice, with two energetically equivalent variants [41]. This phenomenon is analogue to the phase transformation in shape memory alloys. Indeed, the shape memory effort has been demonstrated in this kind of metamaterials [41].

The advantage of metamaterials is that their properties can be tuned by their micro-architectures [28,31,34,35,41–43]. In the metamaterials with periodic holes, the shape of the holes has been shown to tune the stiffness, Poisson's ratio, and critical condition for the pattern transformation [28,31]. The sizes of the large and small holes determine the transition between the monotonic and non-monotonic stress-strain responses [42,43]. To understand the effect of

geometry on the critical condition for the pattern transformation, finite element simulations [28,31,34–36,41,42,113,114]and analytical models [113,114] have been developed for the metamaterials with uniform-sized holes. These analytical models can predict the critical condition for the pattern transformation based on buckling analysis of the slender ligaments. However, they fail to predict the transformation strains due to the lack of post-buckling analysis. For the metamaterials with alternatingly large and small holes, an analytical model has been proposed to understand the programmable monotonicity of the stress-strain curves [43]. However, this model is simple and unable to capture the geometric effects.

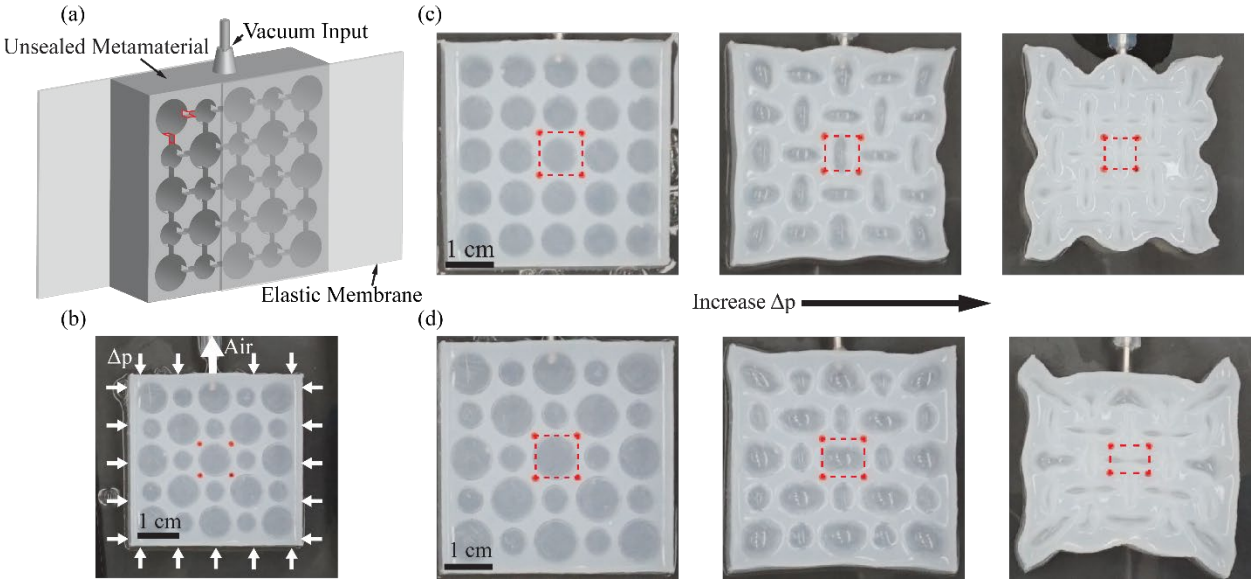

Figure 2.1 Overview of the pneumatically actuated pattern-transforming metamaterials. (a) A schematic of the fabrication. The metamaterial is an elastomeric slab containing an array of holes. All the holes are sealed by two elastic membranes, isolating the inner air from the atmosphere. The air chambers formed by the holes are connected via the grooves (two of which are outlined in red). The metamaterial is actuated by a source of vacuum, such as a syringe or a pump. (b) When actuated, the metamaterial is subjected to an external and internal pressure difference and

undergoes a pattern transformation. (c) When the holes are uniform-sized, the square lattice keeps square and the transformation strain is equibiaxial. (d) When the holes are alternatingly large and small, the square lattice transits to a rectangular shape and the transformation strain is non-equibiaxial.

In this chapter, combining finite element analysis, experiments and analytical modeling, we aim to establish quantitative understanding and a predictable theory to unravel the effects of geometry on the mechanical behavior of the metamaterials with arbitrary sizes of the alternatingly large and small holes. In experiments, to better control the deformation, we design and fabricate pneumatically actuated metamaterials, as illustrated in Figure 2.1a, where an elastomeric slab patterned with a square array of holes is sealed by two thin elastomeric membranes. Narrow and shallow grooves are used to connect all the holes so that air can flow freely throughout the whole structures. The holes are further linked to an external source of vacuum via a tube (Figure 2.1b). At a critical pressure Δp_{cr}, the metamaterial undergoes a pattern transformation with the circular holes altering their shapes into ellipses orthogonal to their neighbors, yielding a large transformation strain (Figure 2.1c-d). The pattern transformation, and therefore the corresponding transformation strain, is widely tunable: the pattern of uniform-sized holes leads to an equibiaxial contraction (Figure 2.1c), whereas the pattern of alternatingly large and small holes leads to a non-equibiaxial contraction (Figure 2.1d). We will numerically and experimentally characterize the pattern transformation as a function of the pressure Δp, and explore the effect of a wide range of geometric parameters. We will further provide an analytical model to explain how the geometry affects the pattern transformation of the metamaterials.

The chapter is organized as follows. In Sec. 2.2, we perform finite element simulations to investigate the tunable pattern transformation of the metamaterial by surveying the design space of the geometric parameters. In Sec. 2.3, we develop an analytical model to understand the effect of geometry on the critical condition for the pattern transformation, the transformation strain and the transformation type. Finally, we conduct experiments in Sec. 2.4 to demonstrate the tunable pattern transformation of the metamaterials and verify the results of the finite element simulations and the analytical model. Sec. 2.5 will conclude this chapter.

2.2 Finite Element Analysis

In this section, we systematically investigate the role of geometry in determining the critical pressure, transformation strain and the transformation type using finite element simulations in Abaqus (version 6.14).

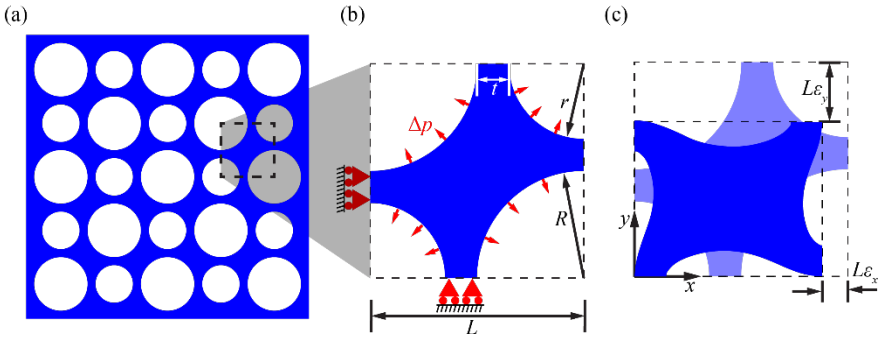

Figure 2.2 The setup of the finite element simulations. (a) A schematic of an elastomeric slab composed of an array of holes. (b) The unit cell used for the finite element simulations. A unit cell is identified here as the smallest geometric unit that can build up the whole system by mirroring and patterning itself. This unit cell is constrained by the symmetric boundary conditions, and is subjected to a pressure Δp, defined as the difference between the external pressure p_{ext} and the internal pressures p_{int} ($\Delta p = p_{ext} - p_{int}$). The geometric parameters include the two radii R and r, and

the lattice size L, which define two dimensionless geometric parameters. (c) The deformation of this unit cell is measured by changes in length of the lattice in the x and y directions between undeformed state (light blue) and deformed state (dark blue).

We perform simulations in a unit cell of an elastomeric slab (Figure 2.2a), which is selected as the smallest geometric unit that can build up the whole system by mirroring and patterning itself [115]. Symmetric boundary conditions are applied to the unit cell, i.e., on the bottom and left boundaries displacement is only allowed in the horizontal and vertical directions, respectively, and the top and right boundaries are constrained to maintain horizontal and vertical, respectively (Figure 2.2b). Although these boundary conditions are not periodic, the 2 x 2 cell, by mirroring the current unit cell horizontally and vertically, is equivalent to the smallest repeated structure for the periodic boundary condition. Besides, the unit cell is subjected to a pressure Δp, defined as the difference between the external and internal pressures, $\Delta p = p_{ext} - p_{int}$, on all the surfaces of the holes. The geometric parameters of the unit cell include the two radii R and r, and the lattice size L, the subtraction of which defines the thickness of the slenderest wall, $t = L - R - r$. We normalize the geometric parameters by the lattice size L and obtain two independent dimensionless parameters: R/L and r/L. We model the elastomer as an incompressible neo-Hookean continuum solid, whose strain energy density function W is given as [116,117]

$$W = \frac{\mu}{2}(tr(\mathbf{F}\mathbf{F}^{\mathrm{T}}) - 3), \tag{2.1}$$

where μ is the shear modulus, and $\mathbf{F}$ is the deformation gradient tensor with the constraint $\det(\mathbf{F}) = 1$. We use eight-node, quadratic, hybrid, plane strain elements (ABAQUS element type CPE8H), and perform mesh refinement study to ascertain the accuracy of simulations. To break the symmetry, small imperfections with amplitude ~t/1000 are introduced to the initial coordinates of

the nodes. We simulate the deformation of the unit cell under the pressure based on the Riks method, and calculate the strains ε_x and ε_y, defined as the changes in length of the lattice with respect to the original length in the x and y directions (Figure 2.2c).

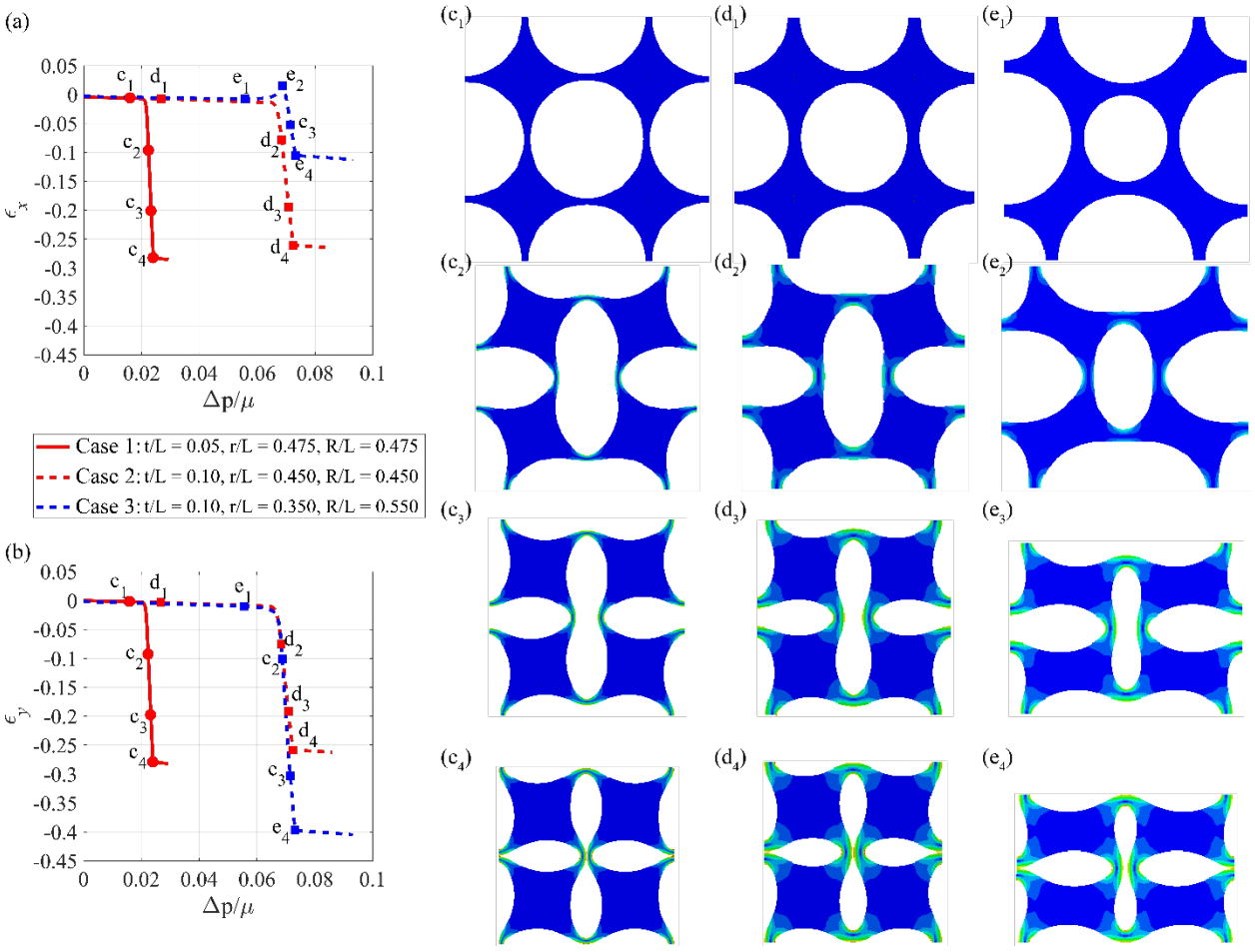

Figure 2.3 The results of the finite element simulations for three metamaterials with different geometric parameters. The dependence of the strains in the (a) x and (b) y directions on the pressure. (c) - (e) The deformed shapes of four unit cells of the three metamaterials: (c) uniformly large holes ($r/L = R/L = 0.475$, $t/L = 0.05$), (d) uniformly small holes ($r/L = R/L = 0.450$, $t/L = 0.10$), and (e) alternatingly large and small holes ($r/L = 0.350$, $R/L = 0.550$, $t/L = 0.10$). For each case, the states of the deformation correspond to the four selected points on its strain-pressure curves.

Figure 2.3 shows the simulation results of the strain-pressure relations (Figure 2.3a, b) and the shape evolution of four unit cells of the three metamaterials with different geometric parameters: uniformly large holes (Figure 2.3c), uniformly small holes (Figure 2.3d), and alternatingly large and small holes (Figure 2.3e). For all cases, when the pressure is small, both strains ε_x (Figure 2.3a) and ε_y (Figure 2.3b) only slightly decrease as the pressure increases. After the pressure reaches a critical value, the strains sharply drop, indicating a pattern transformation occurs. The deformed shapes of the metamaterials under different pressures shown in Figure 2.3c-e correspond to the points marked on the strain-pressure curves in Figure 2.3a, b. The strain-pressure curves reach another almost flat stage when the metamaterials form internal contact (Figure 2.3c_4-e_4).

Apart from these common features, we observe that the geometry can significantly affect the critical pressure and the transformation strains. Smaller holes, and therefore a larger wall thickness, lead to a higher critical pressure ($r/L = R/L = 0.475$, $t/L = 0.05$ for Figure 2.3c, and $r/L = R/L = 0.450$, $t/L = 0.10$ for Figure 2.3d). Interestingly, although the pattern of the holes in Figure 2.3e ($r/L = 0.350$, $R/L = 0.550$, $t/L = 0.10$) is different from that in Figure 2.3d, the two cases have the same critical pressure due to the same wall thickness. When the holes are uniform-sized ($r = R$), the transformation strain is equibiaxial, i.e. $\varepsilon_x = \varepsilon_y$, and the square lattice keeps a square shape. In contrast, when the holes are alternatingly large and small ($r \neq R$), the transformation strain is non-equibiaxial, i.e. ε_x and ε_y bifurcate from each other after the pressure reaches its critical value, and the square lattice transits to a rectangular shape. The three cases discussed have shown the fact that the pattern transformation of these metamaterials can be tuned by varying the wall thickness and the pattern of the holes.

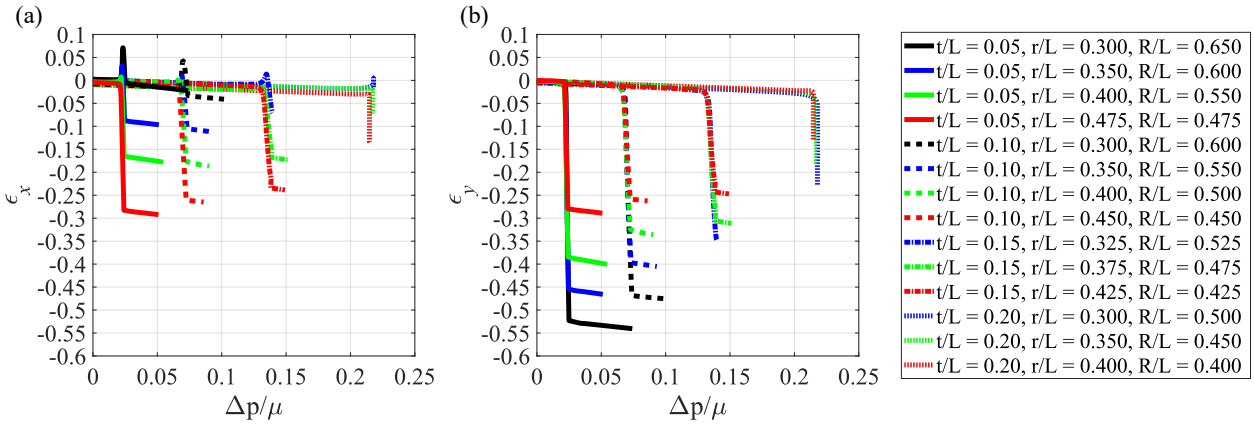

Figure 2.4 The dependence of the strainson the pressure for fourteen sets of geometric parameters in the (a) x and (b) y directions. The critical pressure for the onset of pattern transformation is shown to be governed by the wall thickness t/L.

Next, we survey the space of the geometric parameters and demonstrate the wide tunability of the pattern transformation. Figure 2.4 presents the strain-pressure curves for fourteen sets of geometric parameters. These sets can be sorted into four groups according to the value of the wall thickness: t/L = 0.05, t/L = 0.10, t/L = 0.15, and t/L = 0.20, represented by four different types of lines. These curves clearly show that the wall thickness determines the critical pressure, no matter whether the neighboring holes have the same size or not, and the critical pressure increases with the wall thickness. We also observe that the pattern of the holes determines the biaxiality of the transformation strain. As the ratio of the small radius to the large radius, r/R, decreases, the transformation strain deviates more from an equibiaxial contraction. When r/L = 0.3 and R/L = 0.65 (the black solid curve in Figure 2.4), the transformation strain is almost uniaxial with ε_y over 0.52 and ε_x less than 0.003 when the internal contact occurs. Note that the ε_x-pressure curves for metamaterials with alternatingly large and small holes always have overshoots (Figure 2.4a), i.e. ε_x becomes positive prior to the sharp drop during the pattern transformation, while these

overshoots do not occur for metamaterials with uniform holes. These overshoots are caused by the competition between the extension in the x direction when the unit cells tilt down and the contraction in the x direction in response to the pressure, occurring in metamaterials with unequal radii of neighboring holes. At the beginning of the pattern transformation, the extension caused by rotation of the unit cells dominates the change in strain ε_x. As the pressure increases, the contraction wins, and ε_x sharply decreases. For the metamaterials with uniform holes, however, no overshoot exists. This is because their unit cells are enclosed in the inscribed circle of the initial lattice, and thus the unit cells are unable to exceed the boundary of the initial lattice while tilting down. Instead, they are compressed into a smaller lattice under an increasing pressure, leading to a monotonic decrease in both strains ε_x and ε_y during the pattern transformation. Moreover, as the wall thickness t/L increases, the transformation type varies from a continuous second-order transition to a discontinuous first-order transition. When the wall thickness is small (t/L = 0.05, 0.10, or 0.15), the strains continuously, although sharply, drop with the pressure during the pattern transformation. However, when the wall thickness is large (t/L = 0.20), the slopes of the pressure-strain curves become positive (corresponding to negative slopes of the stress-strain curves) at the critical pressure, which indicates a discontinuous drop of the strains.

In this section, we have performed finite element simulations for a wide range of geometric parameters. From the results, we conclude that the pattern transformation of these metamaterials can be tuned by their geometry. To understand the role of the geometric parameters in governing the mechanics of the pattern transformation, an analytical model is proposed in the next section.

2.3 Analytical Model

2.3.1 Formulation of the analytical model

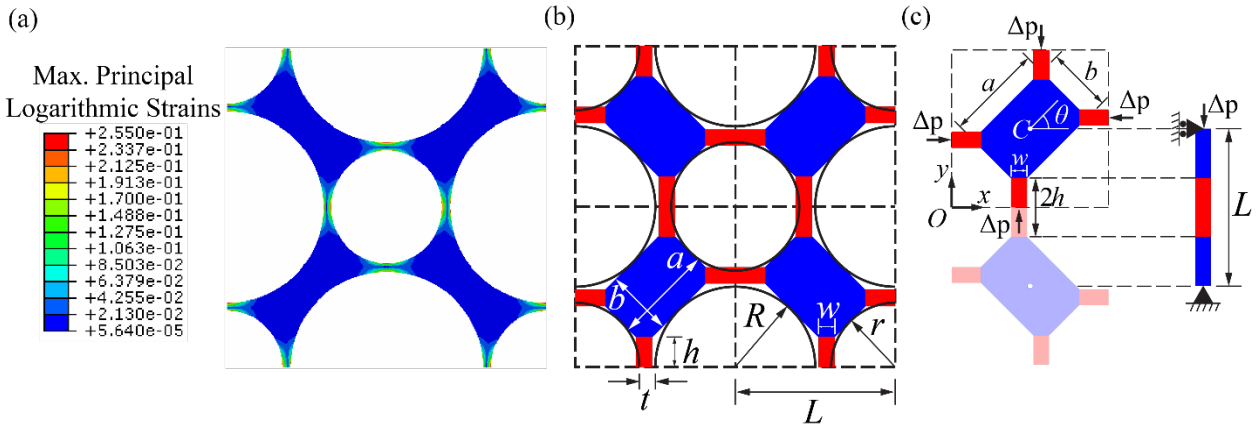

Figure 2.5 Sketches of the simplified structure and the equivalent one-dimensional beam model. The contour plot (a) of the maximal principal logarithmic strain for a metamaterial with geometric parameters t/L = 0.05, r/L = 0.350, and R/L = 0.600 at loading $\Delta p/\mu$ = 0.0246 shows that the deformation mainly concentrates in the slender regions. Thus, we proposed (b) a simplified structure consisting of rigid rectangles (blue) linked by deformable beams (red). The black solid line denotes the outlines of the holes, to which the edges of the blue parts are tangent. (c) To analytically determine the pattern transformation of this simplified structure, we solve the buckling and post-buckling behavior of an equivalent one-dimensional model composed of a deformable beam fixed to two rigid bars subject to an axial compressive stress Δp.

Figure 2.5a is a typical contour plot of the maximal principle logarithmic strain in four unit cells of a metamaterial (t/L = 0.05, r/L = 0.350, and R/L = 0.600) under a pressure $\Delta p/\mu$ = 0.0246 larger than the critical pressure for the pattern transformation. The result shows that the deformation is mainly concentrated in the slender regions, whereas the rest regions (shown in blue) only deform by less than 2%. Therefore, we propose to simplify the slender regions as deformable

beams, and the nearly undeformed regions as rigid rectangles [113], yielding a simplified structure as sketched in Figure 2.5b. By modeling the buckling and post-buckling of this simplified structure, we are able to analytically calculate the strain-pressure relations of the metamaterials.

The unit cell in the simplified structure is characterized by the dimension of the rigid rectangles ($a \times b$) and the dimension of the deformable beams ($2h \times w$) (Figure 2.5b). We set the boundaries of the rigid rectangles tangent to the neighboring circular holes, and set the thickness w of the deformable beams equal to the wall thickness t. To smoothly transit from the rigid rectangles to the deformable beams, the length of the deformable beams $2h$ is chosen to be longer than the distance between the two corners of the rigid rectangles by w, which takes into account the boundary effect of the bending of the slender regions on the rectangles (Figure 2.5b). As a result, we can relate the geometric parameters of the metamaterials to those of the simplified structures:

$$a = \sqrt{2}L - 2r, \tag{2.2}$$

$$b = \sqrt{2}L - 2R, \tag{2.3}$$

$$w = t, \tag{2.4}$$

$$h = \frac{L}{2} - \frac{\sqrt{2}}{4}a - \frac{\sqrt{2}}{4}b + \frac{t}{2} = \frac{\sqrt{2}-1}{2}(L - t), \tag{2.5}$$

where we have used $L = r + R + t$. Eq. (2.5) means that the length of the deformable beams, h/L, depends solely on the wall thickness t/L. With Eqs. (2.1)-(2.5), we can convert the metamaterial into a simplified structure, which maintain the main features of pattern transformation (See verification by finite element analysis in Appendix Figure 1.1).

Next, we will analytically quantify the pattern transformation of this simplified structure. We will solve its buckling condition, which gives rise to the critical pressure for the pattern

transformation. By further formulating its post-buckling process, we will analytically determine the strain-pressure relations during the pattern transformation.

The buckling and post-buckling of this simplified structure can be determined in an equivalent one-dimensional model composed of a beam with length $l_s = 2h$ fixed to two rigid bars with length $l_r = (L - l_s)/2$ subject to an axial compressive stress Δp, as shown in the right of Figure 2.5c. In a unit cell of a metamaterial with alternatingly large and small holes, although the two vertical loads offset by a distance, creating a moment about the center C of the rigid rectangle, the moment is balanced by that created by the two horizontal loads. Thus, shifting the deformable beams to the vertical and horizontal lines past the center C does not change their buckling and post-buckling behavior (Figure 2.5c). Moreover, since the rigid rectangles are free to rotate and translate during the pattern transformation, the equivalent beam model is restrained by a pin-roller support.

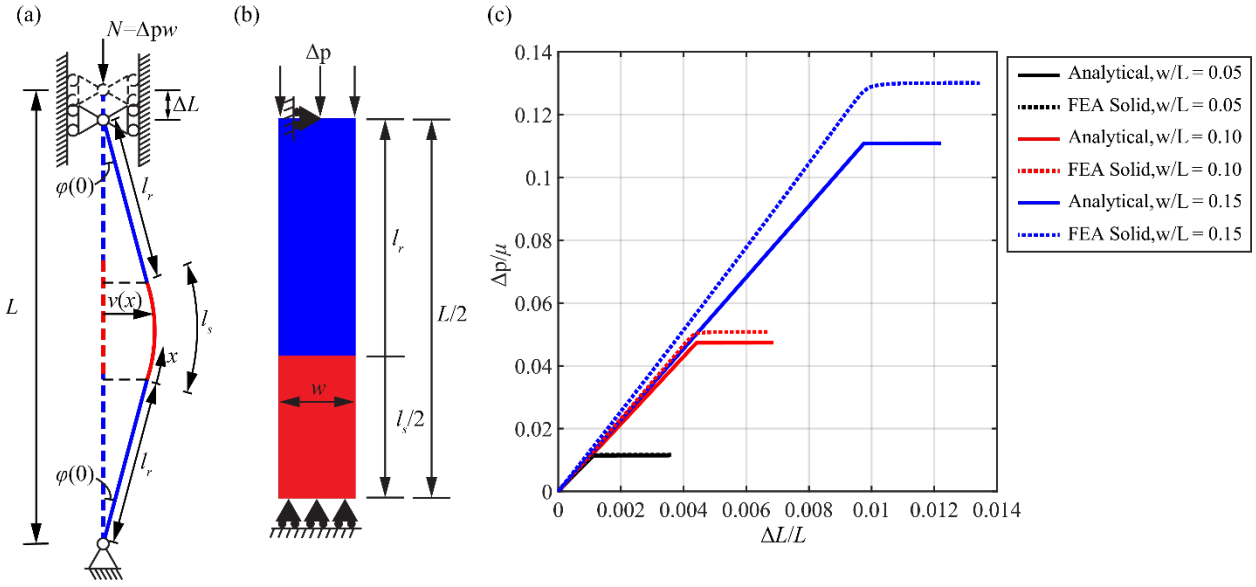

Figure 2.6 Buckling and post-buckling analysis of the one-dimensional beam model. (a) The model consists of a beam (red) of length $l_s = 2h$ fixed to two rigid bars (blue) of length $l_r = (L - l_s)/2$. The

whole structure is simply supported at the two ends, and is subject to an axial load *N*. When the load exceeds a critical value, the beam buckles, deviating from its initial straight position (dashed line), with the deflection $v(x)$ and bending angle $\varphi(x)$. (b) To verify our analytical buckling and post-buckling solutions, we perform finite element analysis (FEA) using solid elements. (c) The pressure-displacement relations for different width-to-length ratios *w*/*L* from the analytical solutions and the FEA using solid elements show good agreement.

The buckling and post-buckling behavior of this beam model (Figure 2.5c, Figure 2.6a) under the plane strain condition are solved analytically based on Euler's elastica and the theory of elastic stability [118] (see the derivation in Appendix A1.2). The beam is assumed to be linearly elastic with the Young's modulus *E*, Poisson's ratio $\tilde{\nu} = 0.5$, and shear modulus $\mu = E/3$. It is considered inextensible in the buckling and post-buckling analysis, because the compressive strain in response to the axial load is negligible compared to the displacement caused by the buckling. The beam buckles when the axial compressive force $N=\Delta p w$ reaches its critical value N_{cr}, which can be obtained by solving the following equation:

$$2k_{cr}l_r \cos kl_s = (k_{cr}^2 l_r^2 - 1) \sin k_{cr} l_s, \tag{2.6}$$

where $k_{cr} = \sqrt{N_{cr}/K}$ and $K = Ew^3/[12(1-\tilde{\nu}^2)]$ is the bending stiffness of the beam in the plain strain condition. Note that the critical force N_{cr} recovers that of a simply supported beam when l_r=0. The existence of the rigid bars (non-zero l_r) can significantly reduce the critical buckling force of this beam model with a beam fixed to two rigid bars.

As the load *N* slightly exceeds the critical value N_{cr}, the beam buckles, and its deflection *v* is given by

$$v(x) = a\sin(k_{cr}x + \gamma), \tag{2.7}$$

where the coordinate x is chosen to be along the tangential direction of the beam (Figure 2.6a), $\tan\gamma = k_{cr}l_r$, and the amplitude a as a function of N is given by

$$a = \frac{1}{2k_{cr}}\sqrt{\frac{N-N_{cr}}{N_{cr}}\frac{32l_s\left(1+k_{cr}^2l_r^2\right)^2+64l_r\left(1+k_{cr}^2l_r^2\right)}{l_s\left(1+k_{cr}^2l_r^2\right)^2+2l_r\left(1-k_{cr}^2l_r^2\right)}}. \tag{2.8}$$

The bending angle $\varphi(x)$ is solved as

$$\varphi(x) = \sin^{-1}\left(v'(x)\right) = \sin^{-1}(ak_{cr}\cos(k_{cr}x + \gamma)). \tag{2.9}$$

Using the assumption of the inextensible beam, we obtain the axial shortening of the beam Δl_s,

$$\Delta l_s = \int_0^{l_s}\left(1-\sqrt{1-v'^2}\right)dx \approx \int_0^{l_s}\frac{1}{2}v'^2dx = \frac{a^2k_{cr}^2\left(l_s+k_{cr}^2l_r^2l_s-2l_r\right)}{4\left(1+k_{cr}^2l_r^2\right)}. \tag{2.10}$$

The length change of the whole structure ΔL involves the contributions from the beam and the rigid bars, which yields

$$\Delta L = \Delta l_s + 2l_r\left(1-\sqrt{1-v'(0)^2}\right). \tag{2.11}$$

To verify the above analytical buckling and post-buckling solutions of the beam model, we perform finite element analysis using solid elements (Abaqus element type CPE8H) with the load and boundary conditions sketched in Figure 2.6b. The results are compared with the analytical solutions for different width-to-length ratios w/L (Figure 2.6c). Note that according to Eq. (2.5), w/L uniquely determines h/L, and therefore l_s/L and l_r/L. As a result, the critical displacements from the analytical solutions and the simulations are in good agreement, which verifies our analytical solutions. The critical load from the finite element simulations is slightly higher than that from the analytical solutions, because in the simulations the rigid bars constrain the lateral

expansion of the beam near their interfaces, increasing the effective stiffness of the beam, which is not accounted in the analytical beam model.

With this equivalent beam model, we are able to determine the pattern transformation of the simplified structure. The critical Δp_{cr} for the pattern transformation is given by

$$\Delta p_{cr} = \frac{N_{cr}}{w}, \tag{2.12}$$

where N_{cr} is the buckling load for the beam in Eq. (2.6). The critical pressure Δp_{cr} only depends on the thickness of the slenderest wall t/L, since t/L uniquely determines the lengths of the beam $l_s/L = 2h/L$ and the rigid bars l_r/L. When Δp is lower than the critical stress Δp_{cr}, the orientation of the rigid rectangle θ (Figure 2.5c) keeps 45° without a rotation, and the contraction of the unit cell is purely due to the deformation of the elastic beams. Consequently, the strains and the coordinates of the center point C (x_c, y_c) are given by

$$\begin{cases} \epsilon_x = -\dfrac{2(1-\tilde{\nu}^2)h}{3L}\dfrac{\Delta p}{\mu}, \\ \epsilon_y = -\dfrac{2(1-\tilde{\nu}^2)h}{3L}\dfrac{\Delta p}{\mu}, \end{cases} \quad \begin{cases} x_c = \dfrac{L}{2}(1+\epsilon_x), \\ y_c = \dfrac{L}{2}(1+\epsilon_y), \end{cases} \tag{2.13}$$

where the origin is taken as the bottom left corner point of the unit cell (Figure 2.5c). When Δp exceeds the critical stress Δp_{cr}, all the beams in a unit cell buckle clockwise (or counter-clockwise) due to the constraint of the rigid rectangle. The rigid rectangle rotates following the buckled beams with the orientation decreases (or increases) by $\Delta\theta$ equal to the bending angle of the beams at the ends $\varphi(0)$ determined in Eq. (2.9). Considering the current orientation angle of the rigid rectangle $\theta = 45° - \varphi(0)$, and the axial displacement of the beam Δl_s in Eq. (2.10), we can derive the strains of the unit cell and the coordinate of the center C (x_c, y_c) as functions of Δp as following

$$\begin{cases} x_c = h - \dfrac{\Delta l_s}{2} + \dfrac{a}{2}\cos\theta + \dfrac{b}{2}\sin\theta - \dfrac{w}{2}\cos\varphi(0), \\ y_c = h - \dfrac{\Delta l_s}{2} + \dfrac{a}{2}\sin\theta + \dfrac{b}{2}\cos\theta - \dfrac{w}{2}\cos\varphi(0), \end{cases} \quad \begin{cases} \varepsilon_x = \dfrac{2}{L}x_c - 1, \\ \varepsilon_y = \dfrac{2}{L}y_c - 1, \end{cases} \tag{2.14}$$

where the first two terms of the coordinate x_c or y_c represent the half length of a beam in the x or y direction respectively, and the last three terms of the coordinate x_c or y_c represent the contribution of the rigid rectangle in the x or y direction respectively (Figure 2.5c). The evolution of the pattern transformation slows down when the beams form contact with each other. The contact occurs when the bottom beam sketched in the unit cell in Figure 2.5c reaches the y axis or the right beam reaches the x axis, yielding correspondingly

$$\begin{cases} x_c - \dfrac{a}{2}\cos\theta + \dfrac{b}{2}\sin\theta + \dfrac{w}{2}\sin\varphi(0) - \big(v(h) - v(0)\big) - \dfrac{w}{2} = 0, \\ OR \\ y_c + \dfrac{a}{2}\sin\theta - \dfrac{b}{2}\cos\theta + \dfrac{w}{2}\sin\varphi(0) - \big(v(h) - v(0)\big) - \dfrac{w}{2} = 0, \end{cases} \tag{2.15}$$

where the first four terms in the first or second equation are the x or y coordinate of the end of the bottom or the right beam where it connects to the rigid rectangle, the fifth term in the parentheses is the relative deflection at the midpoint of the beam with respect to its end, and the last term defines the distances between the neutral axis and the surface of the beam. The deflections v of the buckled beam as a function of Δp is given by Eqs. (2.7) and (2.8). Eq. (2.15) determines the critical Δp when the contact forms, and the corresponding strains can be calculated by Eq. (2.14). Combining Eqs. (2.12)-(2.15), we can analytically obtain the pattern transformation of the simplified structure with different geometric parameters.

2.3.2 Results of the analytical model

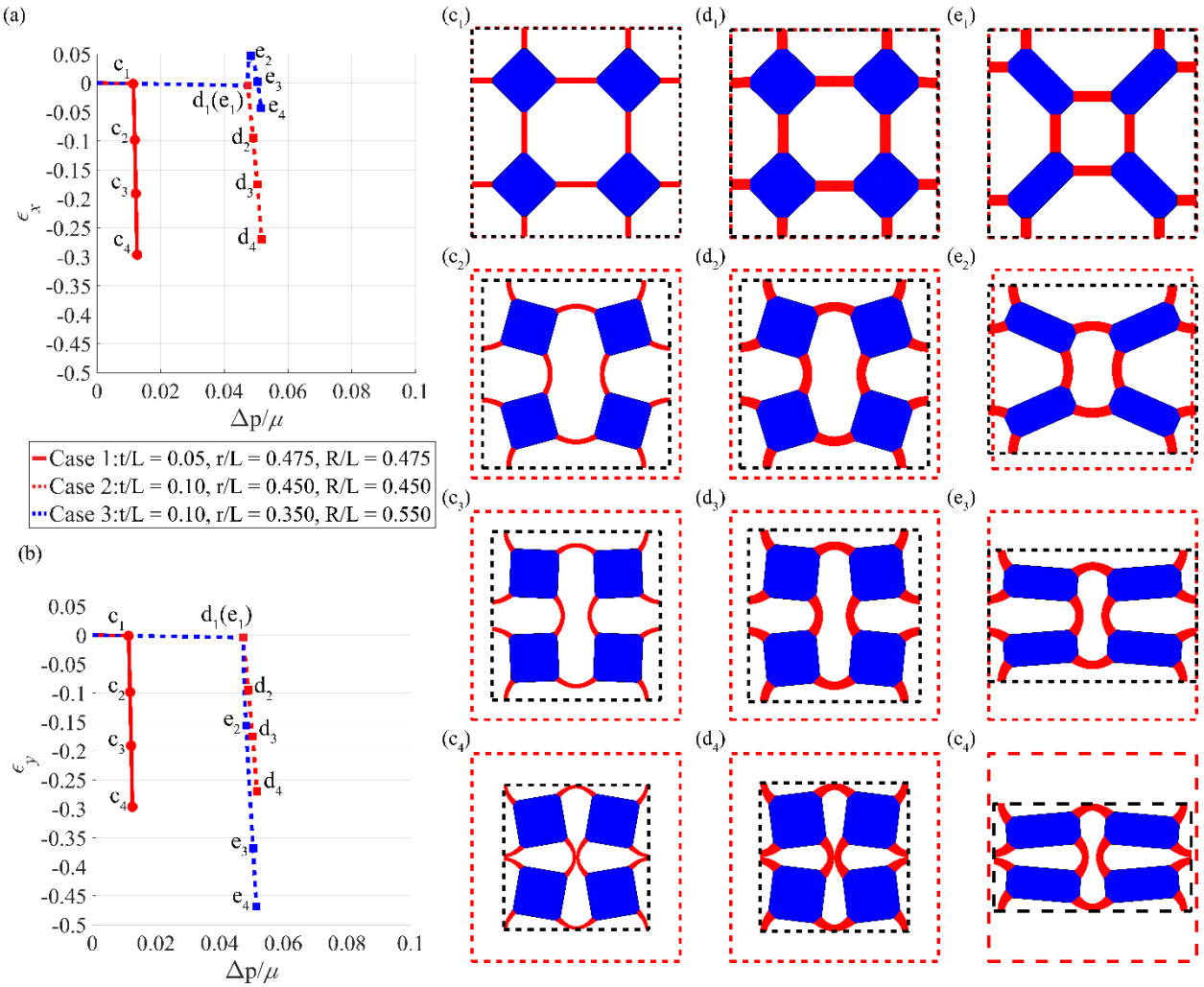

Figure 2.7 The prediction of the pattern transformation based on the analytical model for metamaterials with three different sets geometric parameters same as those in Fig. 3. The dependence of the strains in the (a) x and (b) y directions on the pressure. (c)-(e) The deformed shapes of four unit cells of the three metamaterials: (c) uniformly large holes ($r/L = R/L = 0.475$, $t/L = 0.05$), (d) uniformly small holes ($r/L = R/L = 0.450$, $t/L = 0.10$), and (e) alternatingly large and small holes ($r/L = 0.350$, $R/L = 0.550$, $t/L = 0.10$). For each case, the states of deformation correspond to the four selected points on its strain-pressure curves. The red dashed frames denote

the initial boundaries of the lattice, whereas the black dashed frames represent the current boundaries of the lattice.

Figure 2.7 shows the prediction of the pattern transformation based on the analytical model for metamaterials with three sets of geometric parameters same as those in Figure 2.3 (case 1, uniformly large holes; case 2, uniformly small holes; and case 3, alternatingly large and small holes). The results of our analytical model agree with those from the finite element simulations in Figure 2.3. When the pressure is small, the strains in the x and y directions, ε_x (Figure 2.7a) and ε_y (Figure 2.7b), do not change significantly as the pressure increases. When the pressure Δp reaches a critical value Δp_{cr}, the beams buckle and initiate the pattern transformation (Figure 2.7c_1-e_1). Since the case 1 has thinner beams, its pattern transformation initiates earlier than those of the cases 2 and 3. With the equal beam thickness, the pattern transformations in the cases 2 and 3 initiate at the same critical pressure, governed by the buckling condition of the beams. As the pressure further increases, the transformation strains sharply drop in all the three cases (Figure 2.7a, b). When the holes are uniform-sized ($r = R$), the transformation strain is equibiaxial (Figure 2.7a, b), and the square lattice remains a square shape (Figure 2.7c-d), whereas when the holes are alternatingly large and small ($r \neq R$), the transformation strain is non-equibiaxial (Figure 2.7a, b), and the square lattice transits to a rectangular shape (Figure 2.7e). (See Appendix Video 1.1-Appendix Video 1.3)

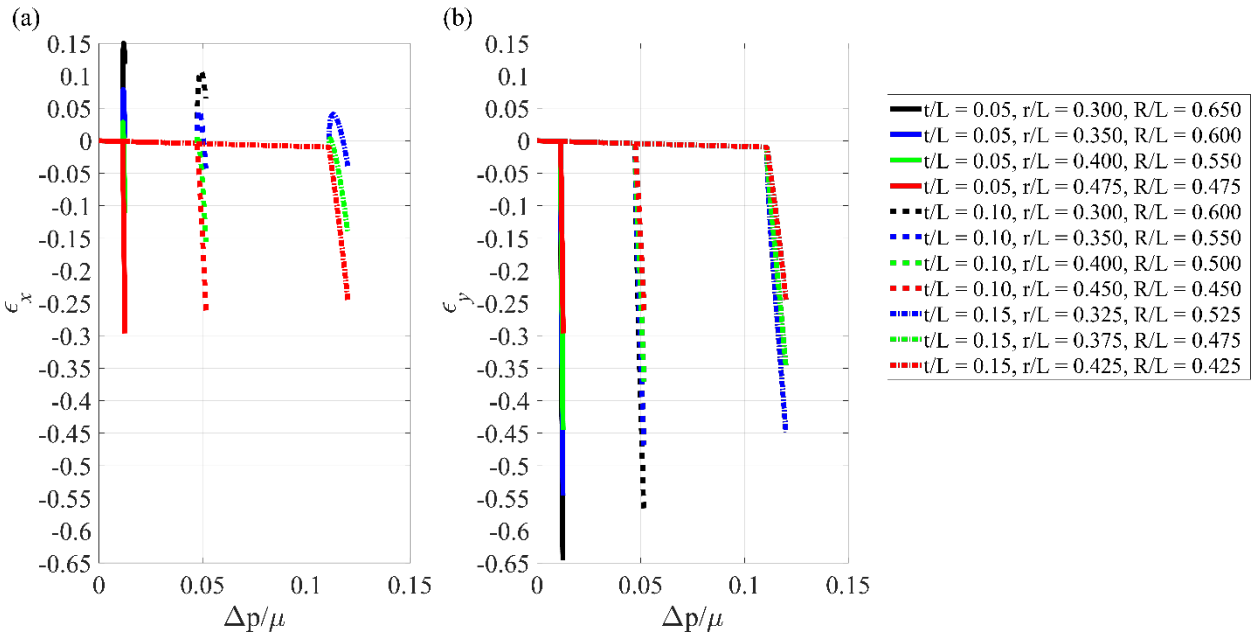

Figure 2.8 The dependence of the strains on the pressure in the (a) x and (b) y directions obtained by the analytical model for eleven sets of the geometric parameters. The critical pressure for the onset of the pattern transformation is shown to be governed by the wall thickness.

We now apply our analytical model to metamaterials with other geometric parameters. We restrict ourselves to thin beams ($t/L \leq 0.15$) because Euler's elastica fails to capture the post-buckling behavior for wide beams [119]. In particular, when the width-to-length ratio is high, the slope of the pressure-displacement curve (Figure 2.6c) has been shown to be negative, which is consistent with our finite element prediction that the pattern transformation becomes discontinuous when the wall thickness is large (Figure 2.4). In Figure 2.8, we plot the strain-pressure curves for eleven sets of geometric parameters. Our analytical model can capture all the features observed in the finite element simulations. (i) The critical pressure Δp_{cr} is governed by and increases with the wall thickness. (ii) The patterns of the holes control the biaxiality of the transformation strain. (iii) When the holes are alternatingly large and small, an overshoot exists in the ε_x - Δp curves, i.e. ε_x

first increases and then decreases as Δp increases at the onset of the pattern transformation, whereas no overshoot exists when the holes are uniform-sized.

2.4 Experimental Results

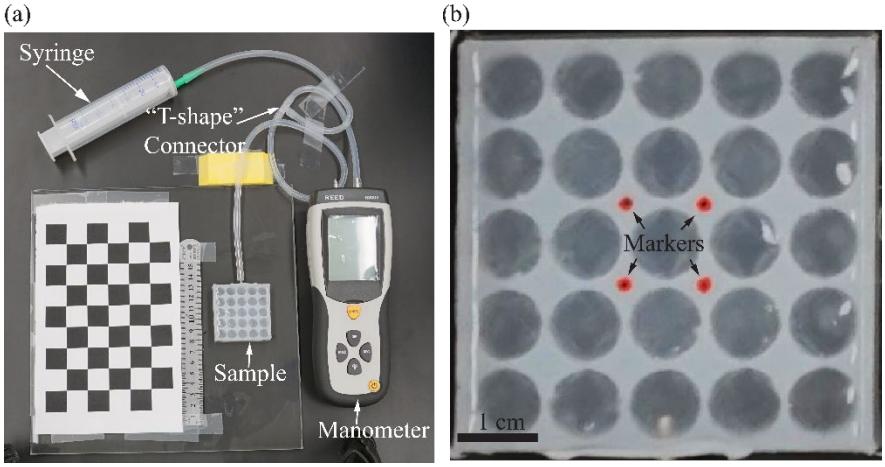

Figure 2.9 The setup of the experiments. (a) Top view of the experimental setup. By controlling the amount of air withdrawn from the metamaterials, the internal pressure of the metamaterial can be tuned continuously and measured by a manometer. (b) A camera records the displacement of the markers on the sample to acquire the strains of the metamaterial via imaging analysis. Markers are labeled far away from the boundaries to avoid the boundary effect.

To experimentally verify the role of the geometric parameters on the pattern transformation of the metamaterials, we fabricated metamaterials with different geometric parameters and measured the strains as functions of the external and internal pressure difference. The samples, each with lateral dimensions of 50 mm by 50 mm and thickness of 25 mm, were made of Ecoflex 00-30 (shear modulus μ = 30KPa [120]) and fabricated by casting the elastomer precursor into a 3D printed mold. We used the same Ecoflex as a glue to seal the holes with two thin membranes on the front and back sides of the slab (Figure 2.1a). Shallow groove structures were designed into

the metamaterials so that all the sealed holes are connected (Figure 2.1a). A syringe pump was further connected to the sample as a source of vacuum (Figure 2.9a). To measure the pressure in the metamaterials, a manometer (accuracy: ±0.01kPa) was linked to the syringe via a 'T-shape' connector (Figure 2.9a). The deformation of the metamaterials was recorded by a camera and the strains were measured (resolution: 0.01 mm) by tracking the position of the four markers via imaging analysis (Figure 2.9b) with the chessboard serving as a reference (Figure 2.9a). During the pressure loading, the samples was put on a glass sheet covered by soap water to reduce friction.

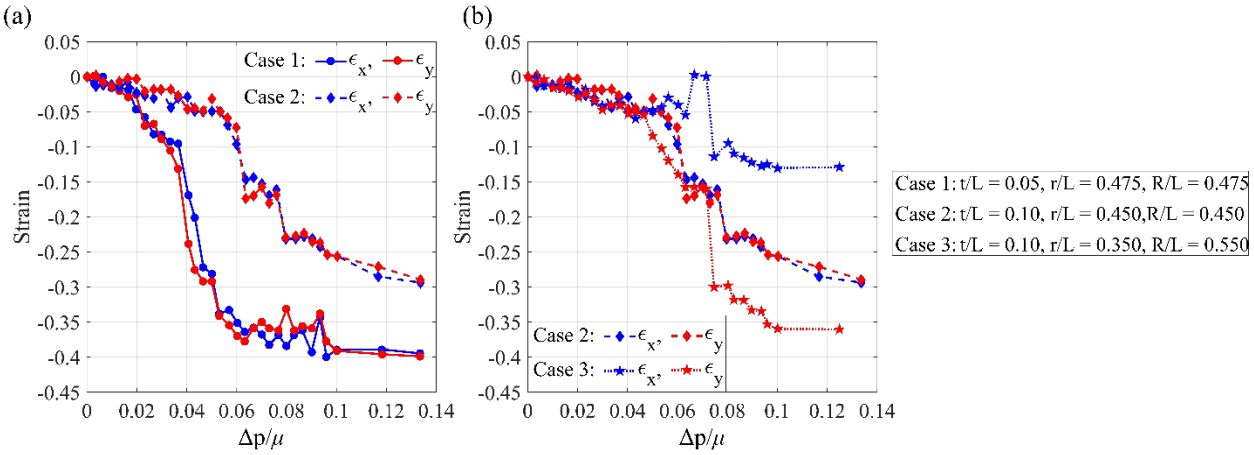

Figure 2.10 Experimental results for three metamaterials with geometric parameters exactly same as those shown in Fig. 3 and Fig. 7. (a) The strain-pressure curves for the case 1 and case 2. (b) The strain-pressure curves for the case 2 and case 3.

Figure 2.10 shows the strain-pressure relations for the metamaterials with three sets of geometric parameters same as those in both Figure 2.3 and Figure 2.7: $t/L = 0.05$, $r/L = 0.475$, $R/L = 0.475$ for the case 1, $t/L = 0.10$, $r/L = 0.450$, $R/L = 0.450$ for the case 2, and $t/L = 0.10$, $r/L = 0.35$, $R/L = 0.55$ for the case 3. The experimental results of the critical pressure and the transformation strains show good agreement with those of the simulations (Figure 2.3a and b) and the analytical model (Figure 2.7a and b). They verify the conclusion that the wall thickness governs

the critical pressure, and the critical pressure increases with the wall thickness. Although the case 3 has a different pattern of holes from that of the case 2, the critical pressures for the two cases are similar since the wall thicknesses are the same (Figure 2.10b). The experiments also confirm that the pattern of holes controls the transformation strain. The metamaterials with uniform-sized holes in the case 1 and 2 undergo an equibiaxial contraction (Figure 2.10a), while the metamaterial with alternatively large and small holes in the case 3 undergoes a non-equibiaxial contraction (Figure 2.10b). Moreover, an overshoot in ε_x - Δp curve was also observed in the experiment of the case 3 (Figure 2.10b), consistent with the simulation (Figure 2.3a) and analytical results (Figure 2.7a). Note that there are some discrepancies in the strain-pressure curves between the experiments and the simulations (Appendix Figure 1.3). Particularly, in the experiment the strain drops at a lower strain than the critical condition for the pattern transformation in the simulation, potentially due to imperfections in the samples, and the strain does not drop as sharply as that in the simulations during the pattern transformation, resulting from the frictions between the metamaterials and the glass sheet.

2.5 Summary

In summary, we numerically, analytically, and experimentally investigate the role of the geometric parameters on the pattern transformation of the metamaterials. We find that the critical pressure for the onset of the pattern transformation is governed by the slenderest wall thickness of the metamaterial, and that the transformation strain is controlled by the pattern of the holes. Our analytical model reveals the mechanics of the pattern transformation and shows good agreement with the finite element analysis. Experimentally, we have achieved pneumatic actuation of the metamaterials and characterized their pattern transformation. The experimental results confirm our

theoretical predictions. This study provides design guidelines for the metamaterial and facilitates its real-world applications.

Chapter 3 Snapping-back Buckling of Wide Hyperelastic Columns

The mechanical instability of columns with a low width-to-length ratio under axial compression has been studied for more than 260 years, known as the Euler buckling. Such columns buckle at a critical strain on the order of 1%, after which the compressive load continuously increases with the displacement. Recently, in the advance of soft robotics and mechanical metamaterials, researchers have harnessed buckling of high width-to-length ratio columns to achieve new functions. However, buckling and post-buckling of these columns are not well studied. In this chapter, we show hyperelastic columns, depending on their width-to-length ratio, can undergo continuous, snapping-through, or snapping-back buckling. In particular, we identify a new snapping-back mode of column buckling, in which beyond the onset of buckling, a column bends to form a sub-critical crease. Our analytical discrete model reveals that snapping-back buckling results from strong coupling between stretching and bending. A phase diagram is constructed to demarcate the different buckling modes of axially compressed columns.

3.1 Introduction

The widely exploited strategy of designing mechanical metamaterials [2,4,5,39,41,43,108,121–123] and soft robots [110,124,125] leverages hollowed structures, in which slender parts enable large deformation and buckling instability, leading to various advanced functions, such as pattern transformations [2,39,41,121–123], tunable nonlinear responses [43,108] and multi-stability [2,4,5]. Although buckling instabilities of slender structures have been well harnessed, post-buckling behavior of hyperelastic columns remains largely unexplored, especially for ones with high width-to-length ratios. It has been observed that columns with a width-to-length ratio greater than 0.12 exhibit a negative slope in the post-buckling regime of their force-

displacement curves [119,126]. However, columns with much higher width-to-length ratios, where the effect of the geometric nonlinearity becomes decisive, could show a distinctive buckling mode. Besides, post-buckling behavior of columns has mainly been studied in the vicinity of the buckling point, but the regimes far beyond the buckling point are still unknown.

When a column is bent, a crease [127–133], which is a localized self-contacting fold, can form on its compressed side where the critical compressive strain is reached. Thus, a crease can also form in a bent column due to buckling, and the post-buckling behavior will be inevitably affected by the crease. However, the influence of creasing on the post-buckling path remains unclear. It has been known that crease forming on a homogeneously compressed slab can be either a super-critical [131,133] or sub-critical [131] bifurcation, dependent on the lateral constraints. Here we show that varying the width-to-length ratio of a column can be another way to adjust a creasing bifurcation from super-critical to sub-critical in post-buckling. The formation of creases is scale-free. In an incompressible neo-Hookean material, creases form at a critical compressive strain of 0.354 [129], independent of geometries. In this study, we find that buckling facilitates formation of creases so that a crease sets in at an external compressive strain much lower than 0.354, and the crease onset strain varies with the width-to-length ratio of the column.

3.2 Four Post-buckling Modes

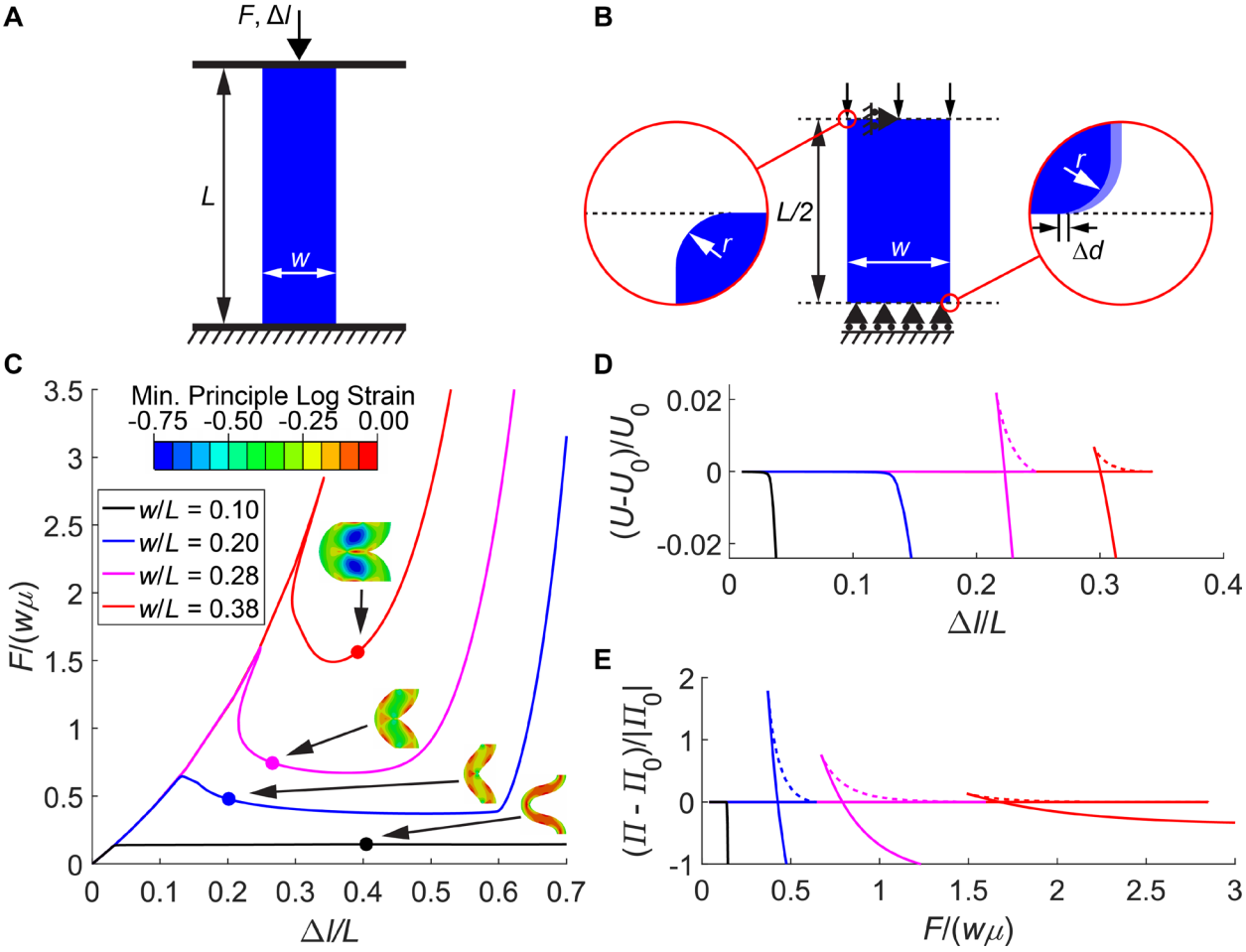

Figure 3.1 Four buckling modes of axially compressed columns with different width-to-length ratios. (**A**) A 2D hyperelastic column with width-to-length ratio w/L is subjected to a compressive force F or a displacement Δl that eventually results in buckling of the column. (**B**) Due to symmetry, only the top half of the column in (**A**) is selected for finite element simulations, where the bottom side is constrained by a symmetric boundary condition and the mid-point of the top side is restricted to moving vertically to eliminate rigid-body motions. A very small displacement defect Δd in the horizontal direction is introduced to the bottom side of the half column in its stress-free state (light blue) to trigger buckling. A quarter of a circle with a small radius r is introduced as a

defect to trigger the initiation of a crease at both the bottom right and top left corners of the half column. A rigid frictionless surface (dashed line) abuts one of the quarter-circle defects to form a self-contacting fold. (**C**) The relations between normalized compressive force $F/(w\mu)$ and displacement $\Delta l/L$ for columns with different w/L. Inset: the deformed shape of the columns in post-buckling from the finite element simulations. The color indicates the level of minimum principle logarithmic strain. (**D** and **E**) Normalized free energy difference between the buckled state and flat state (with subscript 0) as a function of applied displacement $\Delta l/L$ (**D**) and force $F/(w\mu)$ (**E**). The dashed lines indicate unstable equilibrium path. ((**C**-**E**) share the same legend).

We first identify four different post-buckling modes of axially compressed columns with different width-to-length ratios w/L (Figure 3.1) using finite element simulations (see Appendix A2.1 and Figure 3.1A). Due to symmetry, only half of a column is simulated. A horizontal perturbation Δd and a quarter of a circle with a very small radius r are introduced to trigger buckling and creasing instabilities (Figure 3.1B). The incompressible neo-Hookean model, with the shear modulus μ as the only material parameter, is adopted in the simulations to represent a generic hyperelastic material. When w/L is low (w/L = 0.10 in Figure 3.1C), the column exhibits continuous buckling: the force F increases with the displacement Δl after the onset of the buckling, which matches the prediction of Euler's elastica. As the column becomes thick (w/L = 0.20 in Figure 3.1C), the force-displacement curve first shows a negative slope in the post-buckling and then the force starts increasing significantly when the column is fully folded, forming snapping-through buckling. Besides, a crease appears on the compressed side of the thick column (w/L = 0.20) after the onset of the buckling, whereas the compressed side of the thin column (w/L = 0.10) remains smooth, even though the column has been compressed far beyond the onset of the buckling (See the insets of Figure 3.1C). For an even thicker column (w/L = 0.28 in Figure 3.1C),

a striking snapping-back buckling mode emerges, in which both the force and displacement decrease after the onset of the buckling, retaining a positive post-buckling slope of the force-displacement relation. Although snapping-back buckling is commonly observed in rods with kinematically controlled ends [134,135], perfect cylindrical shells [9] and shallow arches [10], it has neither been reported in column buckling, nor predicted by existing 1D beam models [126,136,137]. When w/L goes beyond a threshold at which the corresponding critical strain for buckling equals the critical strain for creasing (w/L = 0.38 in Figure 3.1C), although the column exhibits a snapping-back force-displacement curve, its post-bifurcation is solely determined by creasing instead of buckling. Under displacement-controlled loading, the buckled state of the snapping-back case has a higher free energy U than that of the flat state U_0 in certain displacement region, which corresponds to unstable equilibria (the dashed lines in Figure 3.1C). In contrast, under force-controlled loading, unstable equilibria exist in both the snapping-through and snapping-back cases, indicated by a higher free energy in the buckled state Π than that of the flat state Π_0 (the dashed lines in Figure 3.1E).

3.3 Transition from Snapping-through to Snapping-back Buckling

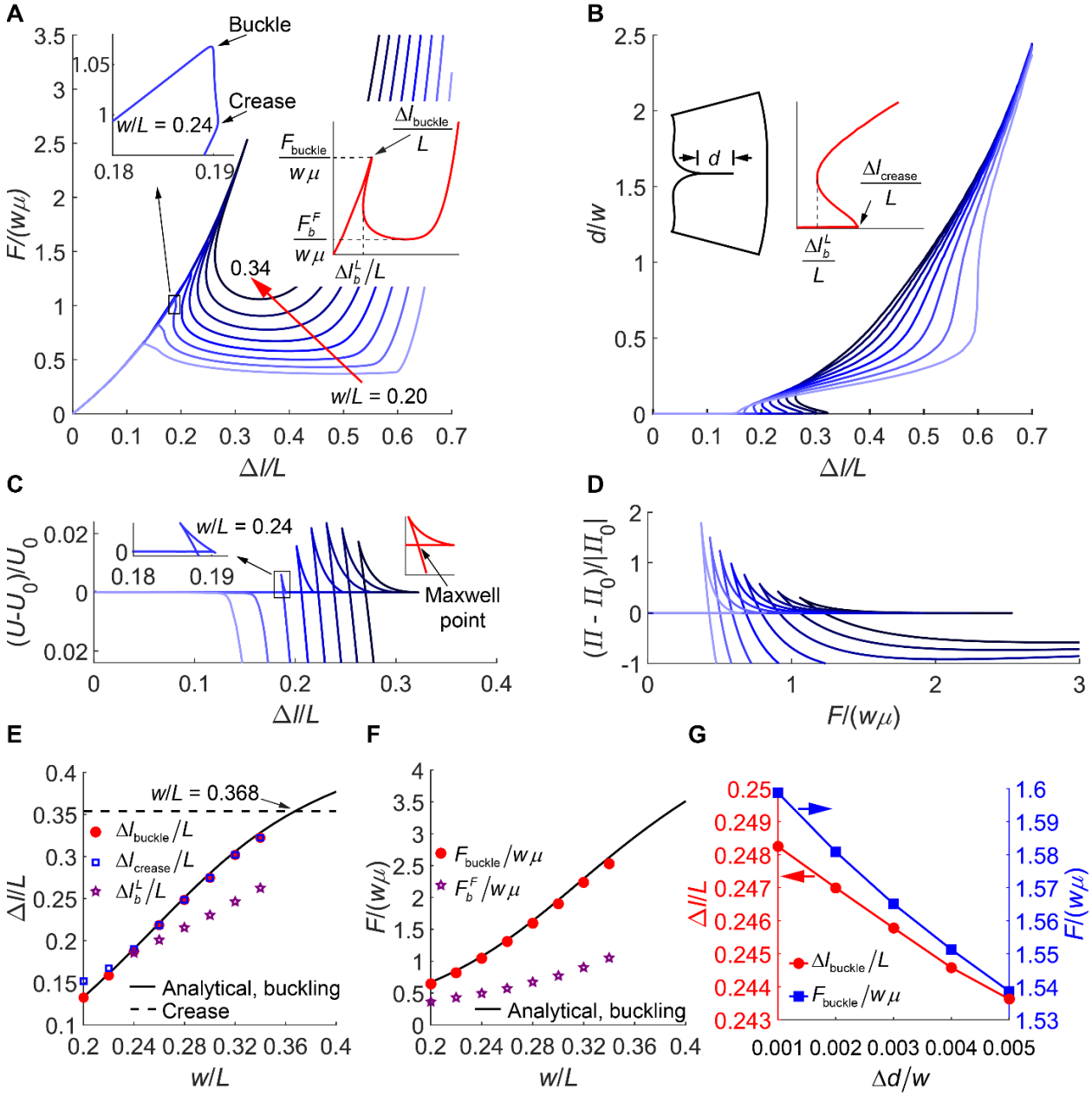

Figure 3.2 Transition from snapping-through buckling to snapping-back buckling mode as the width-to-length ratio w/L increases. (**A**) The normalized force-displacement relations as w/L increases from 0.20 to 0.34 with an increment 0.02. Inset (from left to right): the enlarged view in the vicinity of the buckling point when w/L = 0.24; a typical force-displacement curve for

snapping-back buckling that defines the critical strain $\Delta l_{\text{buckle}}/L$ and critical force $F_{\text{buckle}}/w\mu$ for buckling, snapping-backward force $F_b^F/w\mu$, and snapping-backward strain $\Delta l_b^L/L$. (**B**) The normalized crease depth as a function of displacement (the same color code as that in (**A**)). Inset (from left to right): the definition of the crease depth d, which is the length of the self-contact region when a crease forms; a typical depth-displacement curve for a subcritical crease that defines the critical strain for creasing $\Delta l_{\text{crease}}/L$ and snapping-backward strain $\Delta l_b^L/L$. (**C** and **D**) The normalized free energy difference between the buckled state and flat state (with subscript 0) as a function of the displacement (**C**) or force (**D**) (the same color code as that in (**A**)). Inset (from left to right): the enlarged view in the vicinity of the buckling point when $w/L = 0.24$; the Maxwell point. (**E**) The critical strain for buckling $\Delta l_{\text{buckle}}/L$ (red dots), critical strain for creasing $\Delta l_{\text{crease}}/L$ (blue squares) and snapping-backward strain $\Delta l_b^L/L$ (purple pentagons) as functions of w/L. The solid black line represents the analytical result of the critical strain for buckling, whereas the dashed black horizontal line denotes the critical strain for the onset of creasing on a homogeneously compressed slab. These two lines intersect at $w/L = 0.368$. (**F**) The critical force for buckling $F_{\text{buckle}}/w\mu$ (red dots) and snapping-backward force $F_b^F/w\mu$ (purple pentagons) as functions of w/L. The solid black line represents the analytical result of the critical force for buckling. (**G**) The critical strain $\Delta l_{\text{buckle}}/L$ and critical force $F_{\text{buckle}}/w\mu$ for buckling as functions of the imperfection $\Delta d/w$ when $w/L = 0.28$ and $r/w = 0.001$.

We then investigate the transition from snapping-through to snapping-back buckling with respect to the width-to-length ratio w/L, and identify the boundary between the two buckling modes. From the force-displacement curves for different w/L ranging from 0.20 to 0.34 (Figure 3.2A), we note that the buckling mode transitions smoothly from snapping-through to snapping-back as w/L

increases. Correspondingly, the bifurcation diagram of normalized crease depth (defined in the inset of Figure 3.2B) and displacement shows a transition from a super-critical to a sub-critical bifurcation (Figure 3.2B). When w/L equals 0.24, the force-displacement curve has a nearly infinite slope after the onset of the buckling (left inset in Figure 3.2A), which indicates $w/L = 0.24$ is the boundary between negative and positive post-buckling slopes in the vicinity of the buckling point. Soon after the onset of the buckling, a sub-critical crease sets in (left inset in Figure 3.2A), and the force-displacement curve starts to snap backward. Therefore, the boundary between snapping-through and snapping-back buckling is slightly lower than $w/L = 0.24$.

We can see the boundary between the snapping-through and snapping-back buckling modes clearer in energy diagrams. The snapping-back buckling mode occurs when a Maxwell point, where the free energy of the buckled state equals that of the flat state, can be identified in both the free energy-displacement diagram (Figure 3.2C) and the free energy-force diagram (Figure 3.2D), while the snapping-through buckling mode occurs when a Maxwell point can only be identified in the free energy-force diagram, but not the free energy-displacement diagram. We find the transition point from snapping-through to snapping-back mode is in the range of $w/L = 0.22$ to 0.24. One can also identify the boundary between the continuous and snapping-through buckling modes by checking when the Maxwell point appears in the free energy-force diagram (not shown here).

To quantitively describe the snapping-back buckling mode, we define some key instability conditions (inset in Figure 3.2A, B) and study how they vary with width-to-length ratio w/L. The critical strain for buckling $\Delta l_{\text{buckle}}/L$ (red dots in Figure 3.2E) and its corresponding force $F_{\text{buckle}}/w\mu$ (red dots in Figure 3.2F) increase with w/L and perfectly match the analytical results (solid black line in Figure 3.2E and F; see Appendix A2.2 for details). In Figure 3.2E, the analytical result of

the critical strain for buckling intersects a horizontal dashed line, which indicates the critical strain for crease forming on a homogeneously compressed slab $\Delta l/L = 0.354$, at $w/L = 0.368$. When $w/L < 0.368$, a crease sets in (blue squares in Figure 3.2E) on the compressed side of the column after the onset of buckling, which indicates bending induced by buckling facilitates the formation of creases. When w/L ranges from 0.26 to 0.368, the crease occurs immediately after the onset of buckling so that the blues squares almost overlap the red dots. When $w/L > 0.368$, a crease sets in first and no buckling occurs after the onset of the creasing. The increasing gap between the critical strain for buckling $\Delta l_{\text{buckle}}/L$ and snapping-backward strain $\Delta l_b^L/L$ (purple pentagons in Figure 3.2E) indicates $\Delta l/L$ snaps backward more as w/L increases. Likewise, $F/w\mu$ also snaps backward more as w/L increases, since the difference between the critical force for buckling $F_{\text{buckle}}/w\mu$ and snapping-backward force $F_b^F/w\mu$ (purple pentagons in Figure 3.2F) grows with w/L. Besides, we find the snapping-back buckling mode is very sensitive to the imperfection Δd (Figure 3.1B): the increase of Δd reduces $\Delta l_{\text{buckle}}/L$ and $F_{\text{buckle}}/w\mu$ dramatically (Figure 3.2G). However, the imperfection r used to trigger creases (Figure 3.1B) has a limited impact on the critical condition of buckling (see Appendix Figure 2.3).

3.4 Experimental Results

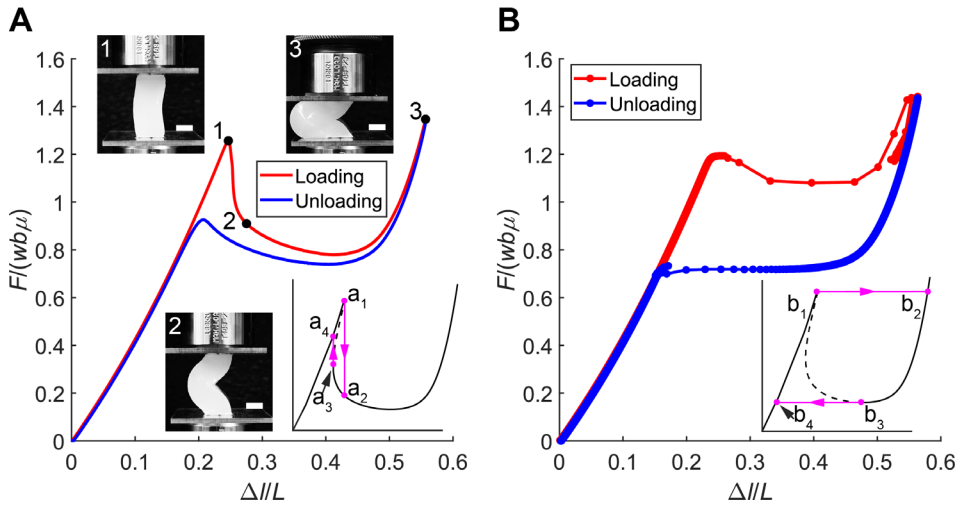

Figure 3.3 Experiment results to confirm the snapping-back buckling mode.Two identical columns with a width-to-length ratio w/L = 0.28 (width w = 14.6 mm, length L = 52.0 mm, depth b =30.0 mm) are loaded separately under (**A**) displacement control and (**B**) force control. (**A**) Relation between normalized force $F/(wb\mu)$ and displacement $\Delta l/L$ as $\Delta l/L$ varies at a ±0.1/min rate. The snapshots show the shapes of the column before snap-downward (1), after snap-downward (2) and at the end of the loading (3) (scale bar, 10.0 mm). (**B**) Normalized force-displacement relations as $F/(wb\mu)$ varies at a ±0.2/min rate. The dots on the curves are the measured data points. The small number of the data points during the snap-forward and snap-backward implies a rapid change in displacement. The insets in (**A**) and (**B**) show the expected loading and unloading paths for the snapping-back buckling mode. The dashed line represents unstable equilibrium paths that cannot be reached in the experiments (See Appendix A2.4, Appendix Video 2.1, and Appendix Video 2.2 for details).

We next conduct experiments to confirm the snapping-back buckling mode. We prepared two identical elastomeric columns with a width-to-length ratio w/L = 0.28, which are expected to exhibit snapping-back buckling. The depth of the columns was around two times of the width.

Although this dimension deviates from the plane strain condition assumed in the simulations, observation of snapping-back buckling in such columns can further show robustness of the phenomenon. These two columns were loaded separately under displacement and force control using an Instron machine, and the measured force-displacement relations after normalization are plotted in Figure 3.3 (see Appendix A2.4, Appendix Video 2.1, and Appendix Video 2.2 for details). Under displacement control, the measured force for snapping-back buckling is supposed to snap downward at the critical buckling strain from the bifurcation point a_1 to the point a_2 during loading, and to snap upward at the snapping-backward strain from the tangent point a_3 to the point a_4 during unloading (inset in Figure 3.3A). In the experiment (Figure 3.3A), we observed a sharp drop from point 1 to point 2, which meets the expectation of the snap-downward. The fact that the snap-upward is not obvious is mainly due to viscoelasticity of the elastomer and the adhesion between the self-contacting surfaces of the crease [138]. Under force control, the measured displacement for snapping-back buckling is expected to snap forward at the critical buckling force from the bifurcation point b_1 to the point b_2 during loading and snap backward at the snapping-backward force from the tangent point b_3 to the point b_4 during unloading (inset in Figure 3.3B). In the experiment (Figure 3.3B), we capture both the snap-forward and snap-backward, despite a slight drop in force during the snap-forward, which is because the motor of the machine reacts not fast enough to keep pace with the changes in force. As a comparison, a column with $w/L = 0.20$ was tested under displacement control. Instead of experiencing a sharp drop, the force decreases gently as the displacement increases, which implies a snapping-through buckling mode (see Appendix Figure 2.4 and Appendix Video 2.3).

3.5 Phase Diagram

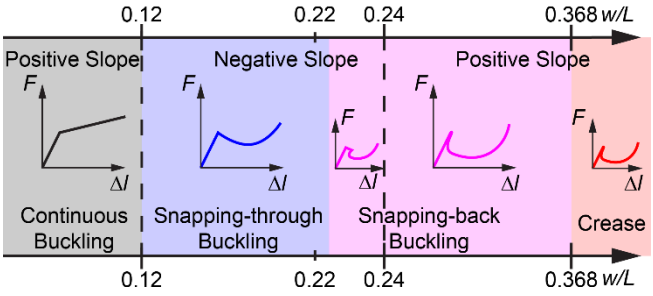

Figure 3.4 Phase diagram of buckling modes. Different colors separate continuous buckling (light gray), snapping-through buckling (light blue), snapping-back buckling (light magenta), and creasing (light red). Dashed lines mark the boundaries between positive and negative post-buckling slopes of the force-displacement curve in the vicinity of the buckling point.

Having numerically and experimentally explored the different buckling modes, we further construct a phase diagram to illustrate variation of the buckling modes across a wide range of width-to-length ratio w/L (Figure 3.4). When $w/L < 0.12$, the column exhibits continuous buckling (light gray in Figure 3.4) and its post-buckling slope of the force-displacement curve is positive. When w/L is above 0.12 but below 0.24, the post-buckling slope in the vicinity of the buckling point is negative. We have also analytically determined the boundary between the positive and negative post-buckling slopes as 0.237, based on post-buckling analysis [118,139,140], the details of which will be presented in the next chapter. The boundary between snapping-through (light blue in Figure 3.4) and snapping-back (light magenta in Figure 3.4) buckling occurs slightly earlier than $w/L = 0.24$, which is governed by a transition from super-critical to sub-critical creasing. When w/L exceeds 0.24, a column displays snapping-back buckling (light magenta in Figure 3.4) and its initial post-buckling slope turns into positive. After w/L crosses 0.368, the force-displacement

relation shows snapping-back features, which is purely determined by creasing [131] (light red in Figure 3.4).

3.6 Discrete Model

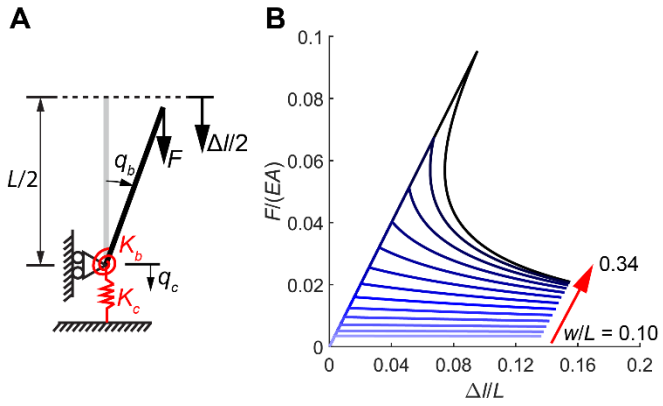

Figure 3.5 Discrete model that captures all three buckling modes. (**A**) The discrete model consists of a rigid bar of length $L/2$ supported by an extensional spring with a stiffness K_c and a rotational spring with a stiffness K_b. The rigid bar has two degrees of freedom: the vertical displacements q_c at its base and the inclination q_b, and is loaded vertically by a force F. (**B**) As w/L varies from 0.10 to 0.34 with an increment 0.02, the force-displacement curves show transitions from the continuous, snapping-through to snapping-back buckling modes.

To understand the transitions from the continuous, snapping-through to snapping-back buckling mode as the width-to-length ratio w/L rises, we develop a discrete model [1,141,142] (Figure 3.5A). We simplify half of a column as a rigid bar supported by an extensional spring and a rotational spring, which account for stretching and bending of the column, respectively, with q_c representing the vertical displacement at the base of the rigid bar, and q_b the inclination angle of the rigid bar. Since the compressive strain required for buckling is large when w/L is high (Figure 3.2E), the coupling effect between stretching and bending due to geometric nonlinearity cannot be

neglected [126]. The vertical displacement $\Delta l/2$ at the top of the rigid bar in response to a vertical load F can be solved by extremizing the following potential energy

$$\Pi = \frac{1}{2} K_c q_c^2 + \frac{1}{2} K_b \left(q_b + \xi q_b q_c \right)^2 - F \frac{\Delta l}{2}, \tag{3.1}$$

where the elastic energy due to stretching is stored in the linear extensional spring of stiffness $K_c = 2EA/L$, the elastic energy due to bending is stored in the rotational spring of stiffness $K_b = 2EI/L$, and ξ represents the coefficient of the coupling between stretching and bending (see Appendix A2.6 for details). The width-to-length ratio w/L affects the behavior of the discrete model through changing the stiffnesses of the two springs. As w/L varies from 0.10 to 0.34, the discrete model initially exhibits continuous buckling, then evolves into snapping-through buckling, and ends with snapping-back buckling (Figure 3.5B). The coefficient ξ is determined to be $12/L$, so that the critical w/L for the transitions between different buckling modes in the discrete model agree with those in the phase diagram shown in Figure 3.4. If ξ is set to be zero, meaning that no coupling exists between stretching and bending, the discrete model can only yield continuous buckling mode for any w/L, as predicted under the simplified assumption of Euler's elastica. By comparing the coupling energy with the other energy components in the discrete model for different w/L, we can conclude that the strong coupling between stretching and bending due to geometric nonlinearity is the dominant factor for snapping-back buckling (Appendix Figure 2.5).

3.7 Summary

Here we reveal post-buckling behavior of columns with different width-to-length ratios, and particularly identify a new buckling mode, snapping-back buckling, in wide columns. Column structures are widely adopted to design mechanical metamaterials and soft robots in the form of

flexible hinges or ligaments, where nonlinear responses of columns, such as buckling, are the foundation of functionalities. Our discovery of column buckling behavior can be exploited to achieve new and advanced functionalities in mechanical metamaterials and soft robotics. Utilizing the bistability of snapping-through and snapping-back buckling, we could create metamaterials with multi-stable states, and soft robots with fast snapping responses. The large hysteresis underneath the force-displacement curve in snapping-back buckling could be used to build energy-absorbing structures. To understand the mechanism of snapping-back buckling, we have established an analytical discrete model, and unraveled that snapping-back buckling results from strong coupling between stretching and bending, similar to that of snapping-back buckling in shells. However, different from a shell, where the initial curvature significantly contributes to large stretching, a wide column has a zero initial curvature, but buckles at a large compression due to its high width-to-length ratio. We believe snapping-back modes can also occur in other instabilities of soft materials, such as buckling of thick hyperelastic plates, and buckling of metamaterials.

Chapter 4 Post-buckling Analysis for Hyperelastic Columns under Axial Compression

In the last chapter, we numerically show that a straight hyperelastic column under axial compression exhibits complex buckling behavior. As its width-to-length ratio increases, the column can undergo transitions from continuous buckling, like the Euler buckling, to snapping-through buckling, and eventually to snapping-back buckling. In this chapter, we will analytically determine the critical width-to-length ratios for the transitions of buckling modes using a general continuum mechanics-based asymptotic post-buckling analysis in the framework of finite elasticity. The effect of material compressibility on the buckling modes and their transitions is further investigated. Our study provides new insights into column buckling.

4.1 Introduction

Column buckling is traditionally viewed as a way of material failure. However, it has recently been harnessed to design functional mechanical metamaterials [143], in which column buckling lays the foundation of many advanced functionalities, such as tunable Poisson's ratios [28], programmable nonlinear responses [43], shape morphing [5,21,29,35,39,41,121,122,144–146], and multi-stability [2,4,5]. The behaviors of these metamaterials are strongly influenced by the buckling and post-buckling of columns.

The simplest description of column buckling is Euler's elastica, in which columns are modeled as linear elastic rods undergoing small deformation. This model predicts that a straight column subjected to a compressive force F or strain ε buckles at a critical condition F_{cr} or $\varepsilon_{\mathrm{cr}}$, and that the post-buckling slope S defined in $(F - F_{\mathrm{cr}})/F_{\mathrm{cr}} = S(\varepsilon - \varepsilon_{\mathrm{cr}})$ is a positive constant 1/2, independent of geometries and boundary conditions [118,119]. This excellently predicts the

buckling behavior of slender columns. However, as columns become wide, their post-buckling behavior alters dramatically, since the critical strains for column buckling become large and thus both material and geometric nonlinearities start to play key roles in the post-buckling regimes. In the last chapter, we showed that as the width-to-length ratio increases, the buckling mode of a straight hyperelastic column under axial compression switches from continuous, snapping-through, to snapping-back. Correspondingly, the initial post-buckling slope changes from positive to negative and eventually back to positive. To predict bending and buckling behaviors of wide columns, various beam models have been proposed to extend Euler's elastica [126,136,137,147,148]. However, no existing one-dimensional beam models can capture the transition between snapping-through and snapping-back modes with respect to the width-to-length ratio. The beam models in refs. [136,147,148] consider axial and shear deformations but still keep the constitutive material linear. These beam models can predict that the initial post-buckling slope decreases from 1/2 as the width-to-length ratio increases, yet remains positive. A recent effort [126] was made to incorporate material nonlinearity while keep the beam extensible and shearable. The proposed beam model can capture that the initial post-buckling slope changes its sign from positive to negative as the width-to-length ratio increases, but never flips its sign back to positive if the width-to-length ratio further increases. This failure is because the high-order strain terms from geometric nonlinearity, which become non-trivial in the post-buckling regime of wide columns, are omitted in the model, as shown in the last chapter. Moreover, the kinematic assumption [149] adopted in these beam models, where the cross sections of beams are assumed to remain plane and undistorted in the deformed configuration, no longer holds for wide columns.

Compared to one-dimensional beam models, a two-dimensional continuum mechanics-based bifurcation analysis, which takes into account both material and geometric nonlinearities,

can accurately capture the buckling and post-buckling behavior of axially compressed columns. The onset of buckling for axially compressed columns has been thoroughly studied in the literature [150–155] by solving an incremental boundary value problem. To determine the post-buckling equilibrium paths and their stability, a general asymptotic technique is developed by Koiter [118], and is widely utilized to find the post-buckling solutions for a compressed half-space of neo-Hokkean material [156], for a thin hyperelastic layer under compression [157], for a hyperelastic tube under axial compression [158], and for a growing elastic rod attached to an elastic foundation [159]. In particular, Ref. [140] addresses the post-buckling problem using this asymptotic method for a two-dimensional rectangular block with various constitutive laws, and finds that a stubby column under displacement-controlled compression can exhibit an unstable post-buckling equilibrium path, which corresponds to the snapping-back buckling mode. However, the whole spectrum of buckling modes for axially compressed columns with respect to the width-to-length ratio has not been analytically determined, which motivates our current work.

In this chapter, we aim to analytically solve the initial post-buckling slope of a straight hyperelastic column under axial compression using a general asymptotic post-buckling analysis in the framework of finite elasticity, and capture the complete transitions of buckling modes from continuous, snapping-through, to snapping back with respect to the width-to-length ratio. Our results will be verified by finite element analysis (FEA). In Section 2, we expand our previous numerical findings to show that a two-dimensional hyperelastic column under axial compression can exhibit three different buckling modes as its width-to-length ratio varies. In Section 3, we conduct a continuum mechanics-based asymptotic analysis including both material and geometric nonlinearities in the model to determine the initial post-buckling slope as a function of the width-to-length ratio. Furthermore, the critical width-to-length ratios for the transitions of buckling

modes are determined, and the effect of material compressibility on the critical values is investigated. The prediction on post-buckling response is in excellent agreement with finite element simulations. Summary are presented in Section 4.

4.2 Transition of Buckling Modes

We first conduct FEA using the commercial software Abaqus/Standard to identify the three buckling modes of a straight hyperelastic column under axial compression as the width-to-length ratio varies. The constitutive relation used in FEA is the compressible neo-Hookean material law with the following elastic energy density

$$W = \frac{\mu}{2}\left[J^{-2/3}\mathrm{tr}(\mathbf{F}\mathbf{F}^{\mathrm{T}}) - 2\right] + \frac{K}{2}(J-1)^2, \tag{4.1}$$

where $\mathbf{F}$ is the deformation gradient ($\mathrm{F}_{ij} = \partial u_i/\partial X_j + \delta_{ij}$, u_i denotes the displacement in X_i direction and δ_{ij} denotes the Kronecker delta), J is the determinant of $\mathbf{F}$, μ and K are the shear and bulk moduli, respectively. With the factor $J^{-2/3}$, the first term in the strain energy W in Eq. (4.1) is due to deviatoric deformation, while the second term is due to volumetric deformation. When K approaches infinite, the model represents an incompressible neo-Hookean material, which is adopted in the simulations in Figure 4.2 to represent a generic hyperelastic material. We carry out two-dimensional plane strain simulations (Abaqus element type CPE8H) for columns with a width w and length L under an axial displacement Δl using the Riks method, and the compressive reaction force F is computed Figure 4.1. Both ends of the columns are allowed to slide freely along the horizontal direction but maintained flat. We assume reflection symmetry about the X_1 axis, and thus only half of this column is simulated. Imperfections are introduced into the initial geometry to trigger buckling and creasing instabilities (see Figure 3.1 for further details).

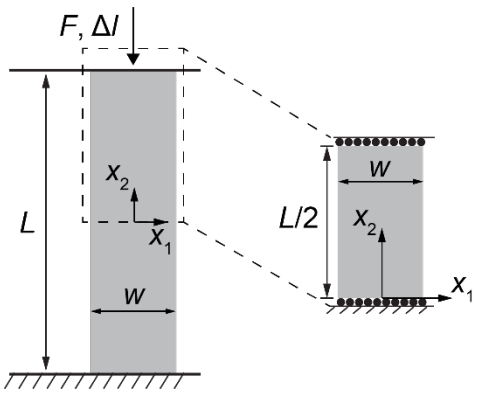

Figure 4.1 Schematic representation of a two-dimensional hyperelastic column (left) subjected to a compressive force F or a displacement Δl. Due to symmetry, only the top half of this column (right) is selected for simulations and modeling.

We summarize the numerical results in Figure 4.2 to show the three buckling modes for straight hyperelastic columns with different width-to-length ratios w/L under axial compression. We define the strain ε as $\Delta l/L$, which is the displacement Δl between the two ends of the column divided by the initial length L. We plot the normalized force-strain $F/w\mu$-ε curves along the equilibrium paths (the 2nd column of Figure 4.2), and show the deformed shapes at three representative positions on the $F/w\mu$-ε curves: the onset of column buckling (Point 1, the 3rd column of Figure 4.2), the onset of creasing [127–129,160], which is a scale-free, localized self-contacting fold, on the surface of the compressive side of the columns (Point 2, the 4th column of Figure 4.2), and the rebound of the reaction forces (Point 3, the 5th column of Figure 4.2). When w/L is low (w/L = 0.10, the 2nd row of Figure 4.2), although the slope of the $F/w\mu$ -ε curve decreases dramatically after buckling, it remains positive. We call this buckling mode as continuous buckling, since the post-buckling solution is stable, and the force and strain increase continuously. As w/L increases, the buckling behavior becomes discontinuous. When w/L = 0.20 (the 3rd row of Figure 4.2), the force decreases while the strain increases after the buckling point

(Point 1), leading to a negative initial post-buckling slope, which eventually increases sharply due to self-contact. This buckling mode with a negative initial post-buckling slope is called snapping-through buckling, which is commonly observed in shallow arches [1]. When $w/L = 0.28$ (the 4th row in Figure 4.2), both the force and strain decrease after the buckling point (Point 1), forming a positive initial post-buckling slope. This buckling mode with such a force-strain relation resembles shell buckling [9], and is called snapping-back buckling. In sum, as w/L increases, the buckling mode undergoes a transition from continuous to snapping-through, and eventually to snapping-back. Correspondingly, the initial post-buckling slope switches from positive to negative, and ends up with positive.

Our previous numerical results (Figure 3.2) show that the critical w/L for the buckling mode transition from snapping-through to snapping-back for an incompressible neo-Hookean material is around 0.24, which has not been predicted by any existing beam model [126,136,137,147,148]. In the next section, we will analytically determine the initial post-buckling slope as a function of w/L and capture the transitions of buckling modes.

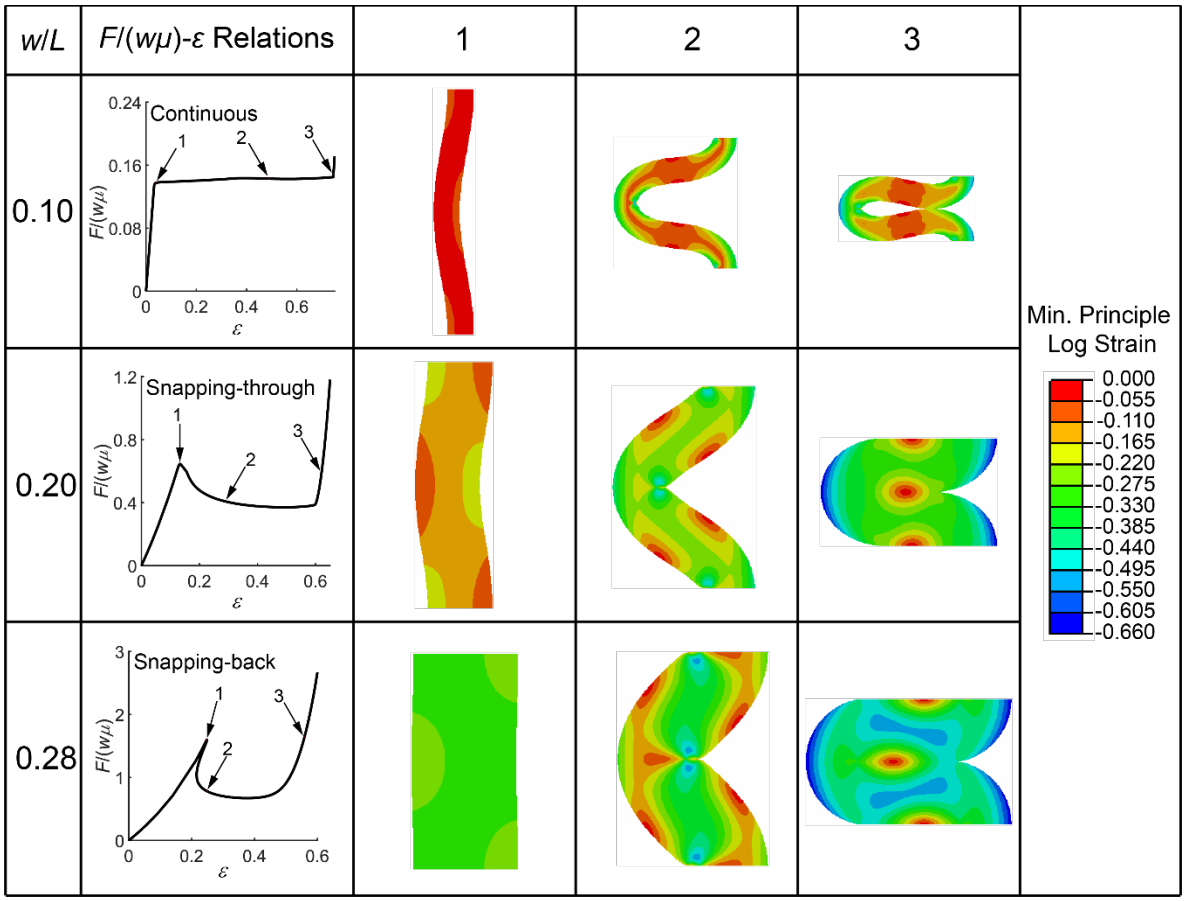

Figure 4.2 Three modes of column buckling under axial compression: continuous (the 2nd row), snapping-through (the 3rd row), and snapping-back (the 4th row). The normalized compressive force $F/(w\mu)$ and strain ε relations are plotted in the 2nd column. The 3rd to 5th columns show how the shapes of the columns evolve as the compressive strain increases. The color indicates the level of minimum principle logarithmic strain. The shear-to-bulk modulus ratio μ/K adopted in FEA is 0.

4.3 Continuum Mechanics-based Asymptotic Analysis

In this section, we conduct a continuum mechanics-based asymptotic analysis [118,139,140] to investigate the buckling and post-buckling behavior of axially compressed columns. Ref. [140] has studied the stability of the post-buckling path of axially compressed

columns. Here we further extend the analysis to determine the initial post-buckling slope, and investigate the transitions of buckling modes from continuous to snapping-back.

4.3.1 Bifurcation analysis

The potential energy for planar deformation of the half column shown in Figure 4.1 is

$$\Pi[\mathbf{u};\varepsilon] = \int_A W dA = \int_0^{\frac{L}{2}} \int_{-\frac{w}{2}}^{\frac{w}{2}} \left\{ \frac{\mu}{2}\left[J^{-2/3}\mathrm{tr}(\mathbf{F}\mathbf{F}^{\mathrm{T}}) - 2\right] + \frac{K}{2}(J-1)^2 \right\} dX_1 dX_2, \tag{4.2}$$

where $\mathbf{u}$ denotes the displacement field, W is the elastic energy density function given by Eq. (4.1). The variational equation of equilibrium can be obtained by applying the principle of stationary potential energy, i.e.

$$\Pi'[\mathbf{u};\varepsilon]\delta\mathbf{u} = 0, \tag{4.3}$$

where Π' denotes the first-order functional derivative of Π with respect to $\mathbf{u}$.

There exists a fundamental solution to Eq. (4.3), which is denoted as $\overset{0}{\mathbf{u}}$. This solution corresponds to homogeneous deformation and can be expressed in terms of the principle stretches

$$\overset{0}{\mathbf{u}} = \begin{bmatrix} \overset{0}{u}_1 \\ \overset{0}{u}_2 \end{bmatrix} = \begin{bmatrix} (\lambda_1 - 1)X_1 \\ (\lambda_2 - 1)X_2 \end{bmatrix}, \tag{4.4}$$

where λ_1 and λ_2 are the two principle stretches in the X_1 and X_2 directions, and can be determined by

$$\frac{\partial W}{\partial \lambda_1} = 0, \lambda_2 = 1 - \varepsilon. \tag{4.5}$$

The first equation in Eq. (4.5) indicates that the first Piola-Kirchhoff stress vanishes in the X_1 direction.

The fundamental solution $\overset{0}{\mathbf{u}}$ in Eq. (4.4) is stable until ε reaches $\varepsilon_{\mathrm{cr}}$, where another solution to Eq. (4.3) corresponding to column buckling emerges. The critical strain $\varepsilon_{\mathrm{cr}}$ for column buckling can be analytically determined by solving the following eigenvalue problem [118,139,140]

$$\Pi''\left[\overset{0}{\mathbf{u}}(\varepsilon_{\mathrm{cr}});\varepsilon_{\mathrm{cr}}\right]\overset{1}{\mathbf{u}}\delta\mathbf{u}=0 \tag{4.6}$$

for all admissible displacement fields $\delta\mathbf{u}$, where Π'' is the second-order functional derivative of Π with respect to $\mathbf{u}$, $\overset{0}{\mathbf{u}}(\varepsilon_{\mathrm{cr}})$ is the fundamental solution at $\varepsilon_{\mathrm{cr}}$, and $\overset{1}{\mathbf{u}}$ is the buckling mode.

Substituting Eq. (4.2) into Eq. (4.6), we have

$$\Pi''\left[\overset{0}{\mathbf{u}}(\varepsilon_{\mathrm{cr}});\varepsilon_{\mathrm{cr}}\right]\overset{1}{\mathbf{u}}\delta\mathbf{u}=\int_0^{\frac{L}{2}}\int_{-\frac{w}{2}}^{\frac{w}{2}}\frac{\partial^2 W\left[\overset{0}{\mathbf{u}}(\varepsilon_{\mathrm{cr}})\right]}{\partial u_{k,l}\partial u_{i,j}}\overset{1}{u}_{i,j}\delta u_{k,l}dX_1dX_2=0, \tag{4.7}$$

where u_i and $\overset{1}{u}_i$ are the components of $\mathbf{u}$ and $\overset{1}{\mathbf{u}}$ in the X_i direction, respectively, and $(\quad)_{,j}$ equals $\partial(\,)/\partial X_j$. Integration by parts yields the Euler-Lagrange differential equations for $\overset{1}{\mathbf{u}}$

$$\frac{\partial^2 W\left[\overset{0}{\mathbf{u}}(\varepsilon_{\mathrm{cr}})\right]}{\partial u_{k,l}\partial u_{i,j}}\overset{1}{u}_{i,jl}=0, \tag{4.8}$$

and the corresponding boundary conditions

$$\frac{\partial^2 W\left[\overset{0}{\mathbf{u}}(\varepsilon_{\mathrm{cr}})\right]}{\partial u_{k,1}\partial u_{i,j}}\overset{1}{u}_{i,j}=0 \text{ at } X_1=\pm\frac{w}{2}, \tag{4.9}$$

$$\delta u_2=0 \text{ and } \frac{\partial^2 W\left[\overset{0}{\mathbf{u}}(\varepsilon_{\mathrm{cr}})\right]}{\partial u_{1,2}\partial u_{i,j}}\overset{1}{u}_{i,j}=0 \text{ at } X_2=0 \text{ and } L/2, \tag{4.10}$$

where $(\quad)_{,jl}$ equals $\partial^2(\,)/\partial X_j\partial X_l$. Eq. (4.10) holds automatically. The solutions to Eq. (4.8) can be written in the following form

$$\begin{cases} \overset{1}{u}_1 = (\alpha_1 \cosh z_1 X_1 + \alpha_2 \cosh z_2 X_1) \cos \frac{2\pi X_2}{L} \\ \overset{1}{u}_2 = (\alpha_3 \sinh z_1 X_1 + \alpha_4 \sinh z_2 X_1) \sin \frac{2\pi X_2}{L} \end{cases}, \tag{4.11}$$

where z_1 and z_2 are the two positive roots of the characteristic polynomial for Eq. (4.8). Substituting Eq. (4.11) into Eqs. (4.8) and (4.9), we then obtain

$$\mathbf{A} \begin{bmatrix} \alpha_1 \\ \alpha_2 \\ \alpha_3 \\ \alpha_4 \end{bmatrix} = 0. \tag{4.12}$$

A nontrivial solution to Eq. (4.12) exists when the determinant of the coefficient matrix $\mathbf{A}$ vanishes, from which we can solve $\varepsilon_{\mathrm{cr}}$. With Eq. (4.12) and

$$\langle \overset{1}{\mathbf{u}}, \overset{1}{\mathbf{u}} \rangle = \frac{2}{Lw} \int_0^{\frac{L}{2}} \int_{-\frac{w}{2}}^{\frac{w}{2}} \overset{1}{u}_i \overset{1}{u}_i dX_1 dX_2 = 1, \tag{4.13}$$

we can determine the coefficients $\alpha_1 \sim \alpha_4$ that lead to the buckling mode $\overset{1}{\mathbf{u}}$ with a unit amplitude.

The critical strain for the onset of column buckling $\varepsilon_{\mathrm{cr}}$ depends on the shear-to-bulk modulus ratio μ/K and width-to-length ratio w/L. Figure 4.3 plots $\varepsilon_{\mathrm{cr}}$ for column buckling as a function of w/L under three different μ/K. Under a given μ/K, the critical strain $\varepsilon_{\mathrm{cr}}$ increases monotonically from zero with the increase of w/L. Similar results have been reported in ref. [140]. However, the dependence of $\varepsilon_{\mathrm{cr}}$ on μ/K is non-monotonic. For thick columns, $w/L > 0.35$, the case with an intermediate μ/K (the red curve in Figure 4.3) has the lowest $\varepsilon_{\mathrm{cr}}$. Once the critical strain for the onset of buckling surpasses that of creasing for sufficiently a high w/L, creasing occurs prior to buckling at a constant critical strain $\varepsilon_{\mathrm{cr}}$ (horizontal dotted lines) [129,160]. The critical strain for the onset of creasing under a plane strain condition is 0.354 for incompressible neo-Hookean material ($\mu/K = 0$) [129,160] and varies non-monotonically as μ/K increases [161]. The

intersection between the critical conditions of buckling and creasing determines the critical w/L, below which buckling occurs first and above which creasing occurs first.

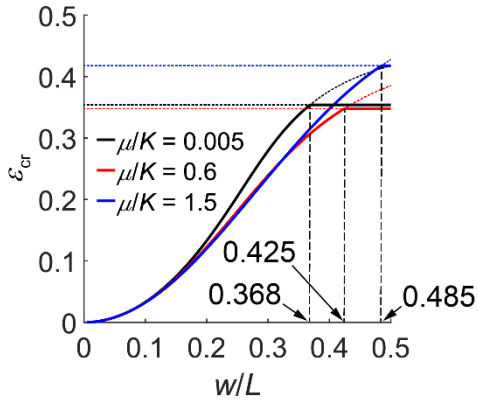

Figure 4.3 Critical strain ε_{cr} for the onset of column instability as a function of the width-to-length ratio w/L under different shear-to-bulk modulus ratios μ/K. The curves represent the critical strain for column buckling, while the horizontal dotted lines indicate the critical strain for creasing in a homogeneously compressed slab. They intersect at a critical w/L, below which buckling occurs first and above which creasing occurs first.

4.3.2 Post-buckling analysis

Having determined the critical strain ε_{cr} for the onset of buckling and the corresponding eigenmode $\overset{1}{\mathbf{u}}$, we asymptotically expand [118,139,140] the displacement field $\mathbf{u}$ and compressive strain ε in the vicinity of the buckling point along the equilibrium path of column buckling

$$\mathbf{u} = \overset{0}{\mathbf{u}}(\varepsilon) + \xi\overset{1}{\mathbf{u}} + \xi^2\overset{2}{\mathbf{u}} + o(\xi^3), \tag{4.14}$$

$$\varepsilon = \varepsilon_{cr} + \xi^2\varepsilon_2 + o(\xi^4), \tag{4.15}$$

where ξ represents the amplitude of the buckling mode $\overset{1}{\mathbf{u}}$. Due to symmetry, only even power terms of ξ are involved in Eq. (4.15) so that the sign of ξ has no effect on ε. Since $\mathbf{u}$ and ε given

by Eq. (4.14) and (4.15) must satisfy equilibrium $\Pi'[\mathbf{u};\varepsilon]\delta\mathbf{u}=0$, a Taylor-series expansion about the buckling point gives

$$\left(\Pi''_{\mathrm{cr}}\overset{2}{\mathbf{u}}+\frac{1}{2}\Pi'''_{\mathrm{cr}}\overset{1}{\mathbf{u}}^2\right)\delta\mathbf{u}\xi^2+\left(\varepsilon_2\dot{\Pi}''_{\mathrm{cr}}\overset{1}{\mathbf{u}}+\Pi'''_{\mathrm{cr}}\overset{1}{\mathbf{u}}\overset{2}{\mathbf{u}}+\frac{1}{6}\Pi^{(iv)}_{\mathrm{cr}}\overset{1}{\mathbf{u}}^3\right)\delta\mathbf{u}\xi^3+o(\xi^4)=0, \quad (4.16)$$

where $\Pi^{(n)}_{\mathrm{cr}}$ is the nth-order functional derivative of Π at the buckling point, i.e. $\Pi^{(n)}\left[\overset{0}{\mathbf{u}}(\varepsilon_{\mathrm{cr}});\varepsilon_{\mathrm{cr}}\right]$, and $\dot{(\,)}$ is the first derivative with respect to ε. The coefficients of ξ^2 and ξ^3 in Eq. (4.16) must vanish independently, which yields a variational equation for $\overset{2}{\mathbf{u}}$

$$\Pi''_{\mathrm{cr}}\overset{2}{\mathbf{u}}\delta\mathbf{u}+\frac{1}{2}\Pi'''_{\mathrm{cr}}\overset{1}{\mathbf{u}}^2\delta\mathbf{u}=0, \quad (4.17)$$

and an expression for ε_2 by setting $\delta\mathbf{u}=\overset{1}{\mathbf{u}}$

$$\varepsilon_2=-\frac{\Pi'''_{\mathrm{cr}}\overset{1}{\mathbf{u}}^2\overset{2}{\mathbf{u}}+\frac{1}{6}\Pi^{(iv)}_{\mathrm{cr}}\overset{1}{\mathbf{u}}^4}{\dot{\Pi}''_{\mathrm{cr}}\overset{1}{\mathbf{u}}^2}. \quad (4.18)$$

Substituting Eq. (4.2) into Eq. (4.17), we have

$$\int_0^{\frac{L}{2}}\int_{-\frac{w}{2}}^{\frac{w}{2}}\left[\frac{\partial^2 W\left[\overset{0}{\mathbf{u}}(\varepsilon_{\mathrm{cr}})\right]}{\partial u_{i,j}\partial u_{k,l}}\overset{2}{u}_{k,l}+\frac{1}{2}\frac{\partial^3 W\left[\overset{0}{\mathbf{u}}(\varepsilon_{\mathrm{cr}})\right]}{\partial u_{i,j}\partial u_{m,n}\partial u_{k,l}}\overset{1}{u}_{k,l}\overset{1}{u}_{m,n}\right]\delta u_{i,j}dX_1dX_2=0. \quad (4.19)$$

Integration by parts yields Euler-Lagrange differential equations for $\overset{2}{\mathbf{u}}$

$$\frac{\partial^2 W\left[\overset{0}{\mathbf{u}}(\varepsilon_{\mathrm{cr}})\right]}{\partial u_{i,j}\partial u_{k,l}}\overset{2}{u}_{k,lj}+\frac{1}{2}\frac{\partial^3 W\left[\overset{0}{\mathbf{u}}(\varepsilon_{\mathrm{cr}})\right]}{\partial u_{i,j}\partial u_{m,n}\partial u_{k,l}}\left(\overset{1}{u}_{k,lj}\overset{1}{u}_{m,n}+\overset{1}{u}_{k,l}\overset{1}{u}_{m,nj}\right)=0, \quad (4.20)$$

and the corresponding boundary conditions

$$\frac{\partial^2 W\left[\overset{0}{\mathbf{u}}(\varepsilon_{\mathrm{cr}})\right]}{\partial u_{i,1}\partial u_{k,l}}\overset{2}{u}_{k,l}+\frac{1}{2}\frac{\partial^3 W\left[\overset{0}{\mathbf{u}}(\varepsilon_{\mathrm{cr}})\right]}{\partial u_{i,1}\partial u_{m,n}\partial u_{k,l}}\overset{1}{u}_{k,l}\overset{1}{u}_{m,n}=0 \text{ at } X_1=\pm\frac{w}{2}, \quad (4.21)$$

$$\delta u_2 = 0 \text{ and } \frac{\partial^2 W\left[\overset{0}{\mathbf{u}}(\varepsilon_{\mathrm{cr}})\right]}{\partial u_{1,2}\partial u_{k,l}}\overset{2}{u}_{k,l} + \frac{1}{2}\frac{\partial^3 W\left[\overset{0}{\mathbf{u}}(\varepsilon_{\mathrm{cr}})\right]}{\partial u_{1,2}\partial u_{m,n}\partial u_{k,l}}\overset{1}{u}_{k,l}\overset{1}{u}_{m,n} = 0 \text{ at } X_2 = 0 \text{ and } L/2. \tag{4.22}$$

Eq. (4.22) is satisfied automatically. With the orthogonality between $\overset{1}{\mathbf{u}}$ and $\overset{2}{\mathbf{u}}$

$$\langle \overset{1}{\mathbf{u}}, \overset{2}{\mathbf{u}} \rangle = \frac{2}{Lw}\int_0^{\frac{L}{2}}\int_{-\frac{w}{2}}^{\frac{w}{2}} \overset{1}{u}_i \overset{2}{u}_i dX_1 dX_2 = 0, \tag{4.23}$$

the solutions to Eq. (4.20) can be written in the following form

$$\begin{cases} \overset{2}{u}_1 = B_1(X_1)\cos\frac{4\pi X_2}{L} + C_1(X_1) \\ \overset{2}{u}_2 = B_2(X_1)\sin\frac{4\pi X_2}{L} \end{cases}. \tag{4.24}$$

Substituting Eq. (4.24) into Eqs. (4.20) and (4.21) , we can obtain $\overset{2}{\mathbf{u}}$. Then ε_2 can be calculated by substituting $\overset{2}{\mathbf{u}}$ and Eq. (4.2) into Eq. (4.18)

$$\varepsilon_2 = -\frac{\int_0^{\frac{L}{2}}\int_{-\frac{w}{2}}^{\frac{w}{2}} \frac{\partial^3 W\left[\overset{0}{\mathbf{u}}(\varepsilon_{\mathrm{cr}})\right]}{\partial u_{i,j}\partial u_{k,l}\partial u_{m,n}}\overset{1}{u}_{m,n}\overset{1}{u}_{k,l}\overset{2}{u}_{i,j} dX_1 dX_2 + \frac{1}{6}\int_0^{\frac{L}{2}}\int_{-\frac{w}{2}}^{\frac{w}{2}} \frac{\partial^4 W\left[\overset{0}{\mathbf{u}}(\varepsilon_{\mathrm{cr}})\right]}{\partial u_{i,j}\partial u_{k,l}\partial u_{m,n}\partial u_{p,q}}\overset{1}{u}_{p,q}\overset{1}{u}_{m,n}\overset{1}{u}_{k,l}\overset{1}{u}_{i,j} dX_1 dX_2}{\int_0^{\frac{L}{2}}\int_{-\frac{w}{2}}^{\frac{w}{2}} \frac{d}{d\varepsilon}\left(\frac{\partial^2 W\left[\overset{0}{\mathbf{u}}(\varepsilon)\right]}{\partial u_{i,j}\partial u_{k,l}}\right)\Big|_{\varepsilon=\varepsilon_{\mathrm{cr}}} \overset{1}{u}_{k,l}\overset{1}{u}_{i,j} dX_1 dX_2}. \tag{4.25}$$

Given a specified compressive strain ε, we can obtain the displacement field $\mathbf{u}$ on the equilibrium path of column buckling using Eqs. (4.14) and (4.15). The applied force F corresponding to ε can then be calculated by

$$F = -\int_{-\frac{w}{2}}^{\frac{w}{2}} \frac{\partial W}{\partial u_{1,1}}\Big|_{X_2=L/2} dX_1 = F_{\mathrm{cr}} + \xi^2 F_2 + o(\xi^4), \tag{4.26}$$

where F_{cr} is the critical force for column buckling. Combining Eq. (4.15) and Eq. (4.26) and eliminating the intermediate variable ξ^2, we can write the relation between force F and strain ε in the following form

$$(F - F_{\mathrm{cr}})/F_{\mathrm{cr}} = S(\varepsilon - \varepsilon_{\mathrm{cr}}) + o[(\varepsilon - \varepsilon_{\mathrm{cr}})^2], \tag{4.27}$$

where S is the post-buckling slope in the vicinity of the buckling point

$$S = \frac{F_2}{\varepsilon_2 F_{\mathrm{cr}}}. \tag{4.28}$$

To verify this post-buckling analysis, we compare the post-buckling paths predicted by Eq. (4.27) with FEA under $\mu/K = 0.005$ (nearly incompressible neo-Hookean materials) (Figure 4.4). We select three values of w/L representing the three column buckling modes: $w/L = 0.10$ (continuous), $w/L = 0.20$ (snapping-through), and $w/L = 0.30$ (snapping-back). In each case, the strain ε in the post-buckling regime is restricted to 1% higher (continuous and snapping-through) or lower (snapping-back) than the corresponding critical strain $\varepsilon_{\mathrm{cr}}$ such that Eq. (4.27) with only linear order term of $(\varepsilon - \varepsilon_{\mathrm{cr}})$ can provide an accurate approximation of the force F. The post-buckling slope S defined in Eq. (4.27) for different w/L can be calculated using Eq. (4.28), yielding 0.02974 for $w/L = 0.10$, −5.788 for $w/L = 0.20$ and 12.06 for $w/L = 0.28$. As a result, the post-buckling paths predicted by Eq. (4.27) (the blue solid lines) and by FEA (the red circles) are in excellent agreement (percent error < 0.02%) (Figure 4.4). Even if the strain ε in the post-buckling regime increases (continuous and snapping-through) or decreases (snapping-back) from the critical strain $\varepsilon_{\mathrm{cr}}$ by 5%, the predictions made by Eq. (4.27) on the post-buckling paths are still reasonably accurate (percent error < 0.3%).

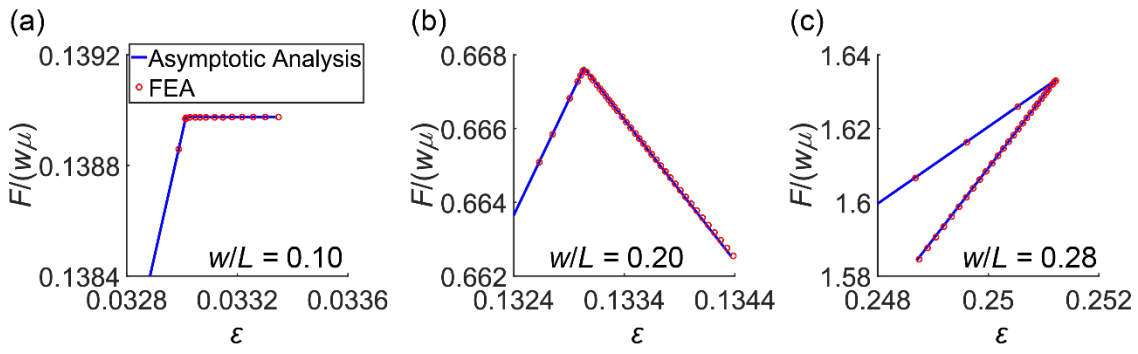

Figure 4.4 Comparison between the post-buckling paths predicted by the asymptotic analysis (the solid lines) and FEA (the dots) under $\mu/K = 0.005$ for the three column buckling modes: (a) continuous ($w/L = 0.10$), (b) snapping-through ($w/L = 0.20$), and (c) snapping-back ($w/L = 0.28$).

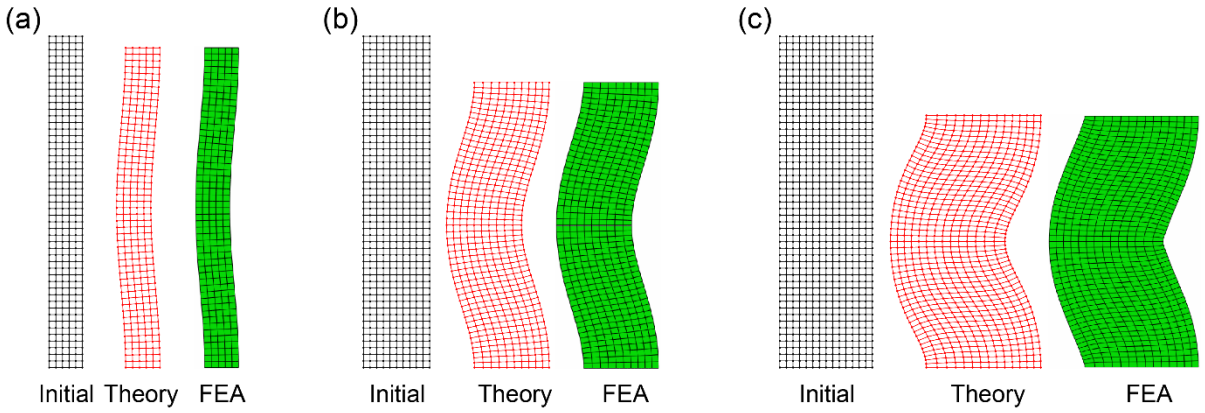

Figure 4.5 Comparison of the buckled shapes in the asymptotic analysis and FEA under $\mu/K = 0.005$ for the three column buckling modes: (a) continuous ($w/L = 0.10$), (b) snapping-through ($w/L = 0.20$), and (c) snapping-back ($w/L = 0.28$). The black lattices denote the initial shapes, whereas the red and green lattices denote the buckled shapes predicted by the asymptotic analysis and FEA, respectively, under a strain ε 5% higher (continuous and snapping-through) or lower (snapping-back) than the critical strain ε_{cr}.

We further compare the buckled shapes predicted by the asymptotic analysis and FEA when the strain ε in the post-buckling regime reaches $1.05\varepsilon_{cr}$ (continuous and snapping-through)

or $0.95\varepsilon_{cr}$ (snapping-back) (Figure 4.5). The buckled shapes predicted by our theory are in good agreement with FEA for all the three buckling modes. Note that when w/L is large, especially for the snapping-back case, the columns undergo large shear deformation, as assumed in the Timoshenko beam theory [136,147–149] Moreover, the initially flat cross sections do not remain flat after buckling, which is violated in the Timoshenko's assumption and the other existing beam models adopting the Timoshenko's assumption [126,136,137,147,148].

To study how the initial post-buckling slope S varies with w/L, we first investigate the two factors determining S in Eq. (4.28), F_2 and ε_2. We plot the normalized F_2/F_{cr} (Figure 4.6a) and $\varepsilon_2/\varepsilon_{cr}$ (Figure 4.6b) as a function of w/L under different μ/K, and find that both F_2 and ε_2 monotonically decrease with w/L from a positive value and pass zero at certain w/L. The condition $F_2 = 0$ given a positive ε_2 indicates that S changes its sign from positive to negative, whereas $\varepsilon_2 = 0$ given a negative F_2 indicates that S changes from negative infinite to positive infinite.

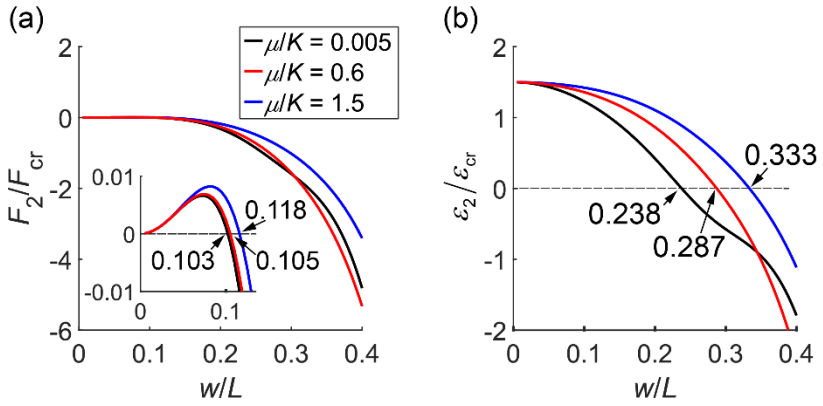

Figure 4.6 Normalized second-order terms in the asymptotic expansions of (a) the compressive force F and (b) compressive strain ε as a function of the width-to-length ratio w/L under different shear-to-bulk modulus ratios μ/K. The inset of (a) magnifies the region where the force changes from positive to negative.

We then plot S as a function of w/L under different μ/K (Figure 4.7). For all the μ/K values, the slope S starts with 0.5 when the column is extremely slender ($w/L \ll 1$), which agrees with the prediction of Euler's elastica. For an almost incompressible material with $\mu/K = 0.005$, as the column becomes thicker (w/L increases), the slope S decreases but remains positive until $w/L = 0.103$, at which the buckling mode transitions from continuous to snapping-through. The sign of S flips again at $w/L = 0.238$ from negative to positive, indicating the transition of the buckling mode from snapping-through to snapping-back. This critical $w/L = 0.238$ perfectly matches our previous numerical result in the last chapter. When μ/K is larger, corresponding to a more compressible material, the sign of S also flips twice, but the critical w/L for the transitions of buckling modes increase.

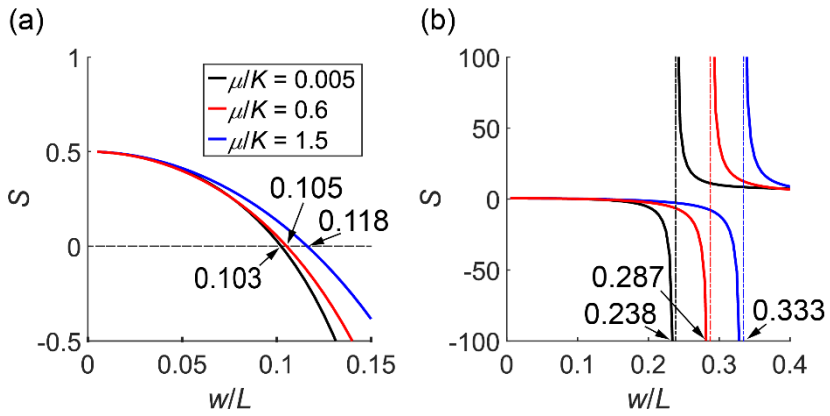

Figure 4.7 Post-buckling slope S as a function of the width-to-length ratio w/L under different shear-to-bulk modulus ratios μ/K. (a) is a zoom-in view of (b) in the region where S changes from positive to negative.

To thoroughly investigate the effect of shear-to-bulk modulus ratio μ/K on the transitions of buckling modes, we plot a phase diagram (Figure 4.8a) to demarcate the boundaries between the three buckling modes in the w/L-μ/K space. It is found that μ/K can significantly postpone the

transition between snapping-through and snapping-back to a higher w/L, whereas the transition between continuous and snapping-through is much less affected by μ/K. This increasingly strong influence of μ/K on the post-buckling paths as w/L increases can be seen more clearly in Figure 4.8b-d, in which the slopes of the $F/w\mu$-ε curves in the post-buckling regime under different μ/K are nearly equal under a low w/L (Figure 4.8b), whereas they differ markedly from each other under a high w/L (Figure 4.8c-d).

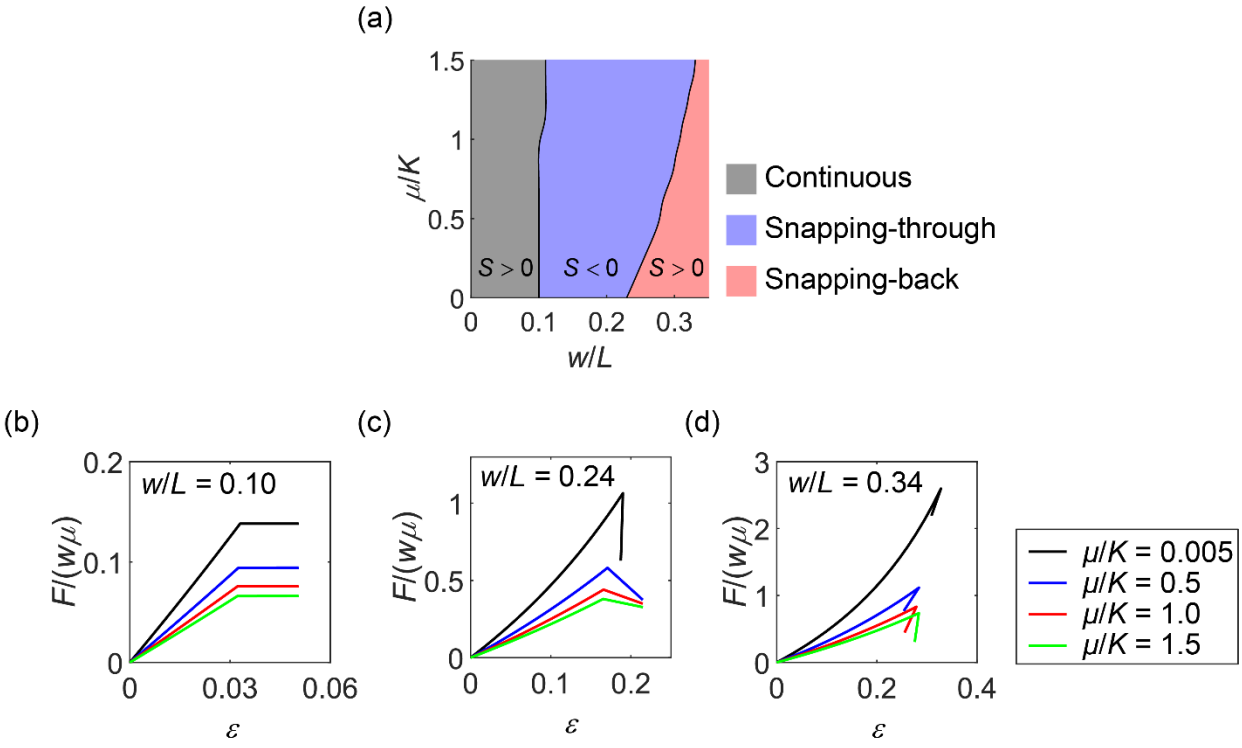

Figure 4.8 Effect of the shear-to-bulk modulus ratio μ/K on the transitions of buckling modes. (a) Phase diagram of the buckling modes with respect to the shear-to-bulk modulus ratio μ/K and width-to-length ratio w/L. The black solid lines denote the boundaries between the buckling modes. (b-d) Normalized force-strain $F/w\mu$-ε curves under different μ/K from the asymptotic analysis when (b) $w/L = 0.10$, (c) $w/L = 0.24$ and (d) $w/L = 0.34$.

4.4 Summary

Buckling of straight columns under axial compression has been extensively studied for centuries. Although the buckling behavior of slender columns are well predicted, the post-buckling response of wide columns with high width-to-length ratios, where material and geometric nonlinearities become crucial, remains largely unexplored. In this paper, we analytically show that for a straight hyperelastic column, the increase of its width-to-length ratio can fundamentally alter its buckling mode, from continuous to snapping-through, and to snapping-back. Correspondingly, the initial post-buckling slope flips its sign from positive to negative, and eventually back to positive. By applying a continuum mechanics-based asymptotic analysis, we determine the initial post-buckling slope as a function of the width-to-length ratio, and then identify the critical width-to-length ratios for the transitions of the buckling modes, which perfectly match the FEA results. Furthermore, we find that as the shear-to-bulk modulus ratio, which represents the material compressibility, increases, the transition between snapping-through and snapping-back buckling is postponed to a higher critical width-to-length ratio. A phase diagram of the buckling modes with respect to the width-to-length ratio and shear-to-bulk modulus ratio is constructed. Although our analysis is based on a specific neo-Hookean material model (Eq. (4.1)), other forms of neo-Hookean models yield similar results. The framework proposed in this paper can be applied to other constitutive laws to study the effect of different material nonlinearities on post-buckling behavior. We believe that our study provides new insights into column buckling and our findings could be of benefit to the design of mechanical metamaterials that rely on column buckling for their functionalities.

Chapter 5 Reusable Energy-absorbing Architected Materials Harnessing Snapping-back Buckling of Wide Hyperelastic Columns

In Chapter 3 and 4, we discover a new buckling mode for axially-loaded wide hyperelastic columns: snapping-back buckling mode, which can be used for energy dissipation. In this chapter, we propose a new class of reusable energy-absorbing architected material harnessing the snapping-back buckling of wide hyperelastic columns. Subjected to an axial compression, a wide hyperelastic column can discontinuously buckle, snapping from one stable equilibrium state to another, leading to energy dissipation, while upon unloading, it can completely recover its undeformed state. Making use of this property, we design an energy-absorbing architected material by stacking layers of wide hyperelastic columns, and fabricate it by multi-material 3D printing and sacrificial molding. Characterized by quasi-static and drop tests, the material shows the capability of energy dissipation and impact force mitigation in a reusable, self-recoverable, and rate-independent manner. A theory is established to predict the energy-absorbing performance of the material and the influence of the column geometry and layer number. Wide tunability of the peak force, energy dissipation and stability of the material is further demonstrated. Our work provides new design strategies for developing reusable energy-absorbing materials and opens new opportunities for improving their energy dissipation capacities.

5.1 Introduction

Energy-absorbing materials are ubiquitously used to protect humans and objects from impacts or collisions, examples including football helmets, car bumpers, and packaging of delicate goods. The essence of an energy-absorbing material is the capability of absorbing mechanical shock energy while keeping the peak force below the safety threshold. Besides, energy dissipation

is required to mitigate rebounds [51]. Among various energy dissipation mechanisms, plastic deformation or fracture of metals, ceramics and composites [52,53] is often utilized to dissipate a large amount of energy by means of dislocation motion or bond breakage. However, these energy-absorbing materials are typically only good for one-time usage, since they undergo irreversible deformation or are permanently damaged during an impact. Materials with the energy dissipation mechanisms of viscous flow [54] and viscoelasticity [55–57] can be used repeatedly, but they are highly rate-dependent with slow recovery to the undeformed states upon unloading. Friction [58–60] between particles in granular materials also permits reusability, but the collapsed materials are usually not self-recoverable.

To achieve a reusable, rate-independent and self-recoverable energy-absorbing material, a novel design strategy of harnessing the snapping-through instability of tilted or curved beams in architected materials has been proposed [2–5,38,61–73]. These beams are stacked into a multi-layered structure, and buckle sequentially one layer after another under compression, resulting in a nearly constant force as the displacement proceeds. The impact energy can be either trapped in the material due to bistability, or damped into heat due to snapping motions. Since the material only deforms elastically, it is reusable and rate-independent. However, when the constituent beams are bistable [2,4,38,61–63,66,68,69], the architected material stays in the deformed configuration after compression, without self-recovering its undeformed state. On the other hand, when the constituent beams are monostable, although the formed energy-absorbing architected material is self-recoverable upon unloading, a large number of layers connecting in series are required to achieve energy dissipation [3,64,74], making the structure thick and heavy. Connecting a single curved beam with a tailored elastic element allows energy dissipation without building a multi-

layered structure [162], but the complex design and the large volume of the elastic element make it unsuitable for practical applications.

In this chapter, we report a new class of reusable, rate-independent, and self-recoverable energy-absorbing architected material harnessing the snapping-back buckling of wide hyperelastic columns. The last two chapters show that an axially-loaded column (Figure 5.1A) can exhibit continuous, snapping-through and snapping-back buckling modes as the width-to-length ratio of the column increases (Figure 5.1B). In particular, the snapping-back buckling is a new mode of column buckling, where the force-displacement relation is discontinuous under not only force-controlled, but also displacement-controlled loading. When axially compressed, the column can snap between different stable equilibrium states, leading to energy dissipation. Upon unloading, the column instantaneously and completely recovers its undeformed state. Similar to tilted or curved beams that exhibiting the snapping-through buckling, the wide hyperelastic column is reusable and rate-independent. However, compared to a tilted or curved beam, the wide column of the same geometry has a higher critical strain for buckling, and thus has a higher energy-absorption capacity. Moreover, due to the nature of the snapping-back buckling mode, the dissipated energy for the wide column stacked in series increases faster with the layer number than that for the tilted or curved beam. The strategy of harnessing the snapping-back buckling of wide hyperelastic columns opens new opportunities for designing light-weight reusable energy-absorbing materials.

In this chapter, we first develop a theory to precisely predict the quasi-static force-displacement response of a multi-layered column structure, unveiling the influence of the geometry of the columns and the number of layers on the energy-absorbing performance, and highlighting the high energy dissipation capacity of a multi-layered structure composed of wide columns exhibiting the snapping-back buckling. Next, we fabricate the multi-layered energy-absorbing

architected materials by multi-material 3D printing and sacrificial molding. The wide columns are made of a silicone elastomer, a typical hyperelastic material that can undergo reversible large deformation in a rate-independent manner. We conduct static and drop tests to verify that the proposed architected materials are capable of absorbing impact energy while keeping the peak force below a safety threshold. Finally, we demonstrate that their mechanical responses can be widely tuned by the geometry and preloads.

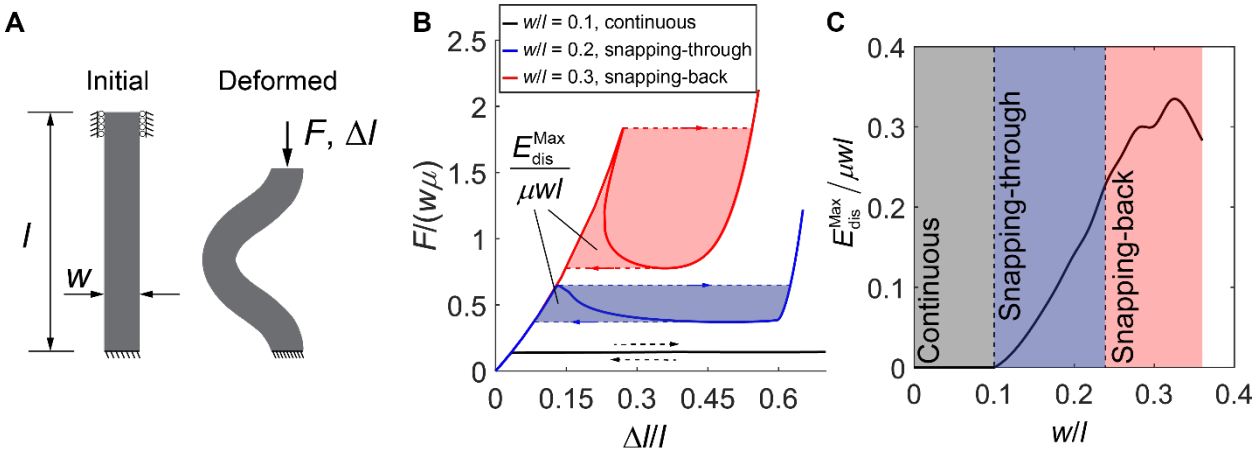

Figure 5.1 Energy dissipation mechanism of wide hyperelastic columns. (A) Schematic drawing of a straight hyperelastic column with a width-to-length ratio *w*/*l* subjected to axial compression and the clamped-clamped boundary condition. The column buckles under a critical load or displacement. (B) Normalized compressive force-displacement curves for three different values of *w*/*l*. The shaded areas indicate the normalized energy dissipation in one force-controlled loading and unloading cycle, which is also the maximum dissipated energy for the columns under displacement-controlled loading, $E_{\mathrm{dis}}^{\mathrm{Max}}/\mu wl$. (C) $E_{\mathrm{dis}}^{\mathrm{Max}}/\mu wl$ as a function of *w*/*l*. The regions of different colors indicate the different buckling modes of the column.

5.2 Theory

The energy-absorbing of our proposed architected material is based on the snapping-back buckling of wide hyperelastic columns (Figure 5.1), which ensures that the proposed material is reusable and its energy-absorbing performance is rate-independent. When subjected to an axial displacement Δl or force F (Figure 5.1A), a column of an initial shear modulus μ, a width-to-length ratio w/l, constrained by the clamped-clamped boundary condition buckles at a critical loading condition. Using finite element (FE) analysis, we found that the buckling mode transitions from continuous, snapping-through to snapping-back as w/l increases (Figure 5.1B) (for details on the FE modeling, see Appendix A3.1). For a column exhibiting the continuous buckling mode, both the force and displacement increase after the buckling point (the black curve in Figure 5.1B), so there is no hysteresis, and thus no energy dissipation, between the loading and unloading paths under both displacement-controlled and force-controlled loading. The columns exhibiting the snapping-through (the blue curve in Figure 5.1B) and snapping-back buckling modes (the red curve in Figure 5.1B) show a decreased and subsequently increased force after the buckling points, resulting in a hysteresis under force-controlled loading (shaded regions in Figure 5.1B). The enclosed area quantifies the normalized dissipated energy after a complete force-controlled loading and unloading cycle, which is also the maximum dissipated energy a column could achieve under displacement-controlled loading, $E_{\mathrm{dis}}^{\mathrm{Max}}$, when an infinite number of such columns are connected in series [2,3,74,162,163]. Clearly, $E_{\mathrm{dis}}^{\mathrm{Max}}$ depends on the width-to-length ratio, and thereby buckling mode (Figure 5.1C). Although $E_{\mathrm{dis}}^{\mathrm{Max}}$ changes non-monotonically as w/l increases, the snapping-back buckling mode ($0.24 < w/l < 0.36$) leads to a higher $E_{\mathrm{dis}}^{\mathrm{Max}}$ than the snapping-through buckling mode ($0.10 < w/l < 0.24$). The decrease in $E_{\mathrm{dis}}^{\mathrm{Max}}$ after $w/l = 0.32$ is due to the fact that the

increase in the height of the hysteresis area becomes slower than the decrease in its width (Appendix Figure 3.2).

We next establish a theory to quantitatively predict the dissipated energy E_{dis} of an architected material composed of n layers of axially-loaded columns exhibiting the snapping-through or snapping-back buckling mode, assuming that the structure can be simplified to n number of the same columns connected in series (Figure 5.2A). For such a column chain, the external force F equals the force F_i acting on each column, $F = F_i$, while the external displacement ΔL equals the sum of the displacement Δl_i of all the columns, $\Delta L = \sum_{i=1}^{n} \Delta l_i$. Each column can buckle independently, with the force F_i – displacement Δl_i relation predicted by FE analysis as shown in Figure 5.1B. For a given force F, a column exhibiting snapping-through or snapping-back mode has at most three possible displacements Δl_i. A column chain composed of n number of this identical column connected in series can thus have $\mathrm{C}_{n+2}^{2} = (n+1)(n+2)/2$ number of equilibrium F–ΔL branches (Appendix A3.5).

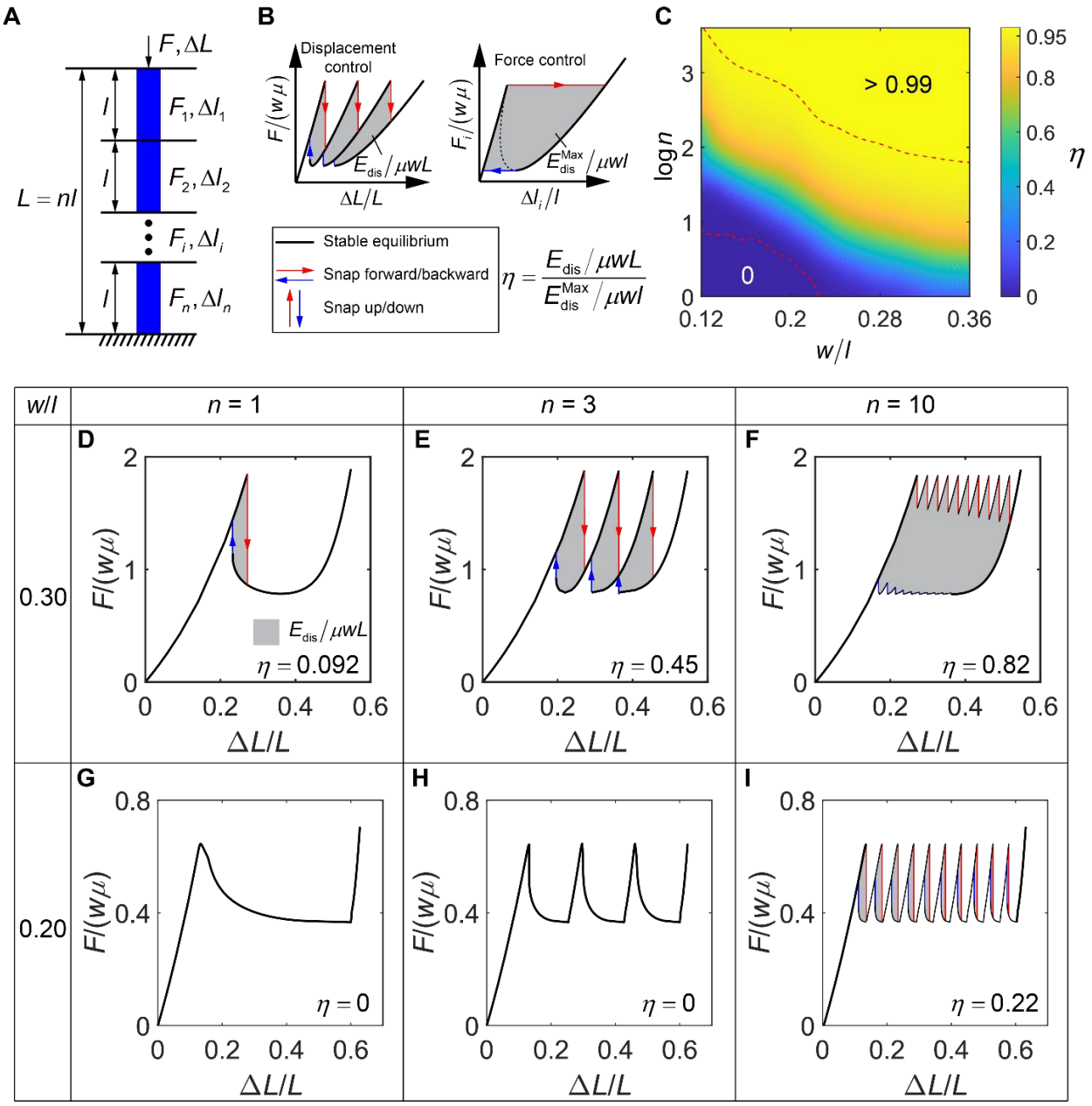

Figure 5.2 Energy dissipation of columns stacked in series. (A) Schematic of n number of identical columns stacked in series. The whole structure is subjected to a compressive force F or a displacement ΔL. The force and displacement of each individual column are F_i and Δl_i, respectively. (B) Definition of the energy dissipation efficiency η, as the ratio of the normalized dissipated energy for a n-column chain system under displacement control, $E_{\mathrm{dis}}/\mu wL$, to the

maximum normalized energy that the same single column can dissipate, $E_{\mathrm{dis}}^{\mathrm{Max}}/\mu wl$. (C) The contour plot of η with respect to the number of columns n and the width-to-length ratio w/l of the columns. The two red dashed lines indicate the boundaries between the regions $\eta = 0$ and $0 < \eta \leq 0.99$, and between the regions $0 < \eta \leq 0.99$ and $\eta > 0.99$, respectively. (D-I) The normalized force-displacement stable equilibrium paths (black), the snap-down (red) and snap-up (blue) paths under displacement control with the enclosed areas characterizing the dissipated energy (gray) for a n-column chain system containing columns with $w/l = 0.30$ (D, E and F) and 0.20 (G, H and I).

Note that not every equilibrium branch is stable when the displacement ΔL is controlled externally. For a column chain composed of columns exhibiting the snapping-through buckling mode, its equilibrium branches are stable if either (i) no column is in its negative-stiffness region (the negative slope part of its force-displacement curve), or (ii) there is exactly one column in its negative-stiffness region while the overall force-displacement curve of the column chain has a negative slope [74,163]. Otherwise, the equilibrium branches are unstable. For a column chain composed of columns exhibiting the snapping-back buckling mode, its stable equilibrium branches can be determined by the following steps. Because a force-displacement curve featuring the snapping-back buckling is equivalent to the superposition of a monotonic force-displacement curve and a force-displacement curve featuring the snapping-through buckling (Appendix Figure 3.4), we can view a column exhibiting the snapping-back buckling mode as a serial combination of a nonlinear elastic spring and a snapping-through element. we can then conceptually reorganize the column chain containing n snapping-back columns into n elastic springs and n snapping-through elements connected in series. We further replace the n elastic springs by a single spring with the equivalent force-displacement behavior. Therefore, the original column chain can be represented by a snapping-through element chain connected in series to a nonlinear elastic spring.

Since the spring does not affect the stability, the stable equilibrium branches of this column chain can be identified using the same way as the column chain composed of columns exhibiting the snapping-through buckling mode (Appendix A3.5).

After the stable equilibrium branches are identified, the quasi-static loading and unloading F–ΔL relation under displacement control can be constructed. We plot the stable equilibrium F–ΔL paths of column chains composed of columns with $w/l = 0.30$ (Figure 5.2D-F) and 0.20 (Figure 5.2G-I), which exhibit the snapping-back and snapping-through buckling modes, respectively, and find that the paths are not always continuous. When the stable equilibrium paths are discontinuous (Figure 5.2D-F and I), i.e. neighboring stable branches do not intersect, the column chain must snap rapidly down (red lines) or up (blue lines) to the neighboring stable equilibrium branch as one branch ends. The energy dissipated during a cycle of displacement-controlled loading is equal to the hysteresis area enclosed by the loading and unloading paths (grey areas), which is denoted by E_{dis}. If the stable equilibrium paths F–ΔL are continuous (Figure 5.2G and H), the force F varies smoothly along the paths as the column chain is loaded or unloaded under controlled ΔL, leading to zero energy dissipation.

To evaluate the performance of the energy dissipation for a column chain containing n number of columns under displacement-controlled loading, we define the energy dissipation efficiency η as the ratio of its normalized energy dissipation $E_{\mathrm{dis}}/\mu wL$ (Figure 5.2B left) to the normalized maximum energy dissipation that one column in this column chain can achieve $E_{\mathrm{dis}}^{\mathrm{Max}}/\mu wl$ (Figure 5.2B right) such that η ranges from 0 to 1. We plot the contour of η with respect to the number n and the width-to-length ratio w/l of the columns (Figure 5.2C**)**. When w/l is low (corresponding to the snapping-through buckling mode), η equals zero before n reaches a threshold

value (the lower red dashed line in Figure 5.2C), increases slowly with n beyond the threshold, and approaches 1 as n increases to a very large number (upper red dashed line in Figure 5.2C). To achieve a given η value, the number of layers n needed dramatically decreases with w/l. In particular, when w/l is high (corresponding to the snapping-back buckling mode), only less than 10 layers are needed to achieve η above 0.8, while tens of or even hundreds of layers are needed to reach the same η when w/l is low and in the snapping-through region. For example, η is nonzero when $n = 1$ (Figure 5.2D), equals 0.45 when $n = 3$ (Figure 5.2E), and reaches 0.82 when $n = 10$ (Figure 5.2F) for $w/l = 0.30$, whereas η remains zero when $n = 1$ (Figure 5.2G) and $n = 3$ (Figure 5.2H), and reaches merely 0.22 when $n = 10$ (Figure 5.2I) for $w/l = 0.20$. We further compare the energy dissipation of our material composed of wide columns to that of curved beams. We find that a wide column with $w/l = 0.30$ has maximum normalized dissipated energy $E_{\mathrm{dis}}^{\mathrm{Max}}/\mu A l$ one order of magnitude higher than that of a curved beam with the optimal geometry [3] (0.3015 for the wide beam shown in Appendix Figure 3.2A, and 0.0266 for the curved beam shown in Appendix Figure 3.5A, B). Moreover, the energy dissipation efficiency of a multi-layered structure composed of the wide columns is higher than that of the curved beam with the same number of layers (Appendix Figure 3.5C). Therefore, compared to both the columns and the curved beams exhibiting a snapping-through buckling mode, those wide columns exhibiting the snapping-back buckling mode are better candidates for energy-absorbing elements, since not only a single column has a higher maximum energy dissipation, but also less layers are needed to achieve the maximum energy dissipation.

5.3 Experiment

5.3.1 Fabrication and characterization

We fabricated the multi-layered energy-absorbing architected materials composed of wide columns with required constraints to prevent shearing of the columns using multi-material 3D printing and sacrificial molding (Figure 5.3A). We 3D printed a mold, which consists of a stiff frame made of polylactic acid (PLA) and sacrificial parts made of polyvinyl alcohol (PVA) by using a dual-extruder fused deposition modeling (FDM) printer (Ultimaker S5). A pre-cured silicone elastomer was poured into the mold for curing, yielding elastomeric columns with an initial shear modulus μ = 16.46 KPa (Appendix A3.2 and A3.6). To maintain the integrity of the material subjected to large compression, the columns are designed to be interconnected by wide flanges embedded into the frames (see the cross-section view in Figure 5.3A). Subsequently, the mold was placed in water to dissolve the sacrificial parts. 3D printed hinges made of PLA were assembled to the structure to ensure that the columns exhibit the desired buckling mode when the material is loaded axially. Figure 5.3B shows a sample of an 8-layered architected material with 5 × 5 identical columns of a width-to-length ratio w/l = 0.30 in each layer. Each column has a width w = 3 mm, length l = 10 mm, and the out-of-plane thickness b = 9 mm. Upon a critical compression, the columns buckle and bend toward the width direction, exhibiting the snapping-back buckling modes (Figure 5.3C).

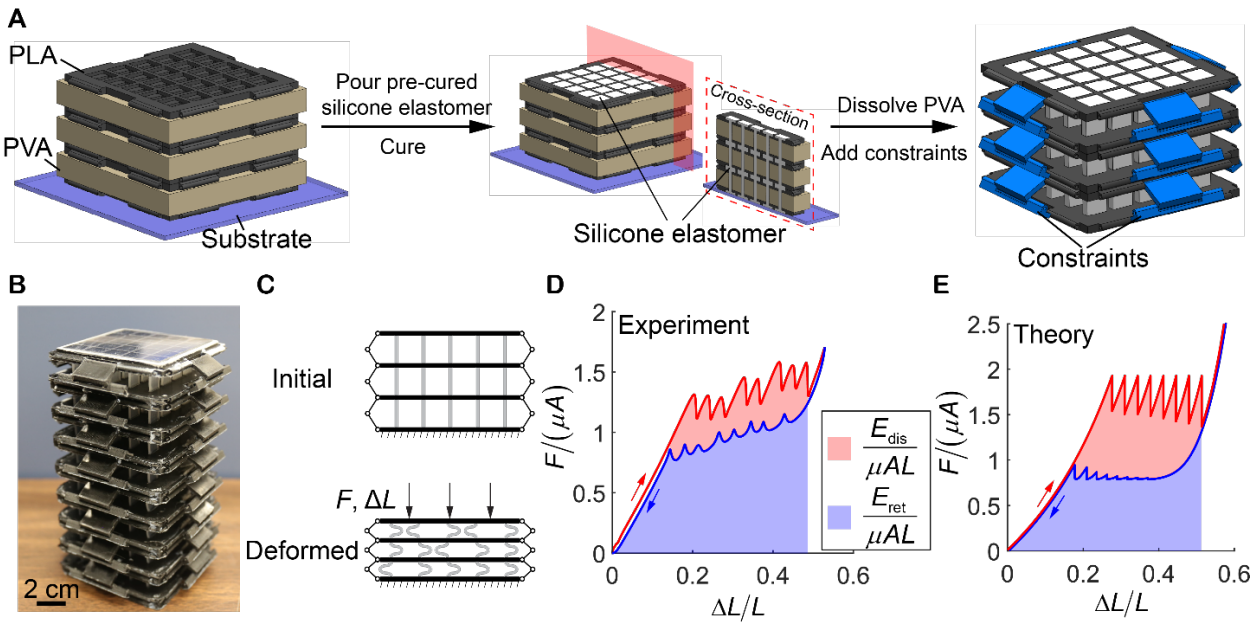

Figure 5.3 Fabrication process and mechanical responses of the proposed architected materials. (A) Fabrication process of the proposed architected materials through multi-material 3D printing and sacrificial molding. (B) A fabricated 8-layered architected material with 5 × 5 identical wide columns of a width-to-length ratio $w/l = 0.30$ in each layer. Each column has a width $w = 3$ mm, length $l = 10$ mm and out-of-plane thickness $b = 9$ mm. (C) Schematics of the initial and buckled states of the architected material when subjected to a compressive force F or a displacement ΔL. (D and E) The displacement-controlled force-displacement response of the sample shown in (B) from the experiment (D) with the loading/unloading strain rate ±0.2/min and the theory (E). The force is normalized by μA, with A the total area of all the columns $25wb$, while the displacement is normalized by L. The red curve denotes the loading path, whereas the blue curve denotes the unloading curve. The shaded area enclosed by the loading and unloading curves equals the normalized dissipated energy $E_{\text{dis}}/\mu AL$, while the shaded area underneath the unloading curve equals the normalized energy returned to the load head $E_{\text{ret}}/\mu AL$.

We conducted displacement-controlled loading and unloading tests (Appendix A3.3) for the sample shown in Figure 5.3B, and plotted the normalized loading and unloading force-displacement curves (Figure 5.3D). During loading, the layers buckle sequentially, which results in eight peaks in the loading path (the red curve in Figure 5.3D), each corresponding to the onset of buckling of one layer (Appendix Video 3.1). The force at each peak is the critical force for buckling of each layer F_{cr}. These peaks form a long and flat plateau of force, indicating large energy absorption at a near-constant load. Upon unloading, the layers recover sequentially, leading to eight peaks on the unloading path (the blue curve in Figure 5.3D, Appendix Video 3.1), prior to fully recovering its initial configuration. The area enclosed by the loading and unloading curves in Figure 5.3D is the normalized dissipated energy $E_{\mathrm{dis}}/\mu AL$, with A the total area of all the columns $25wb$, while the area underneath the unloading curve is the normalized energy returned to the load head $E_{\mathrm{ret}}/\mu AL$. We also found that the loading rates and the number of loading cycles have negligible effects on the energy dissipation due to the hyperelastic nature of the constitutive material (Appendix Figure 3.7). Hence, the proposed architected material is reusable, rate-independent, and self-recoverable. The experimental result agrees well with the theoretical prediction on the number of force peaks and the width of the force plateau on both the loading and unloading curves, the normalized plateau force on the unloading curve, and the returned energy (Figure 5.3E). However, the experimental result shows a lower F_{cr} for each layer, which is caused by unavoidable imperfections in the architected material. Besides, the bottom layers buckle at slightly lower F_{cr} than those of the top layers due to the preloads caused by gravity, leading to a slight increase in the force across the plateau as the displacement increases. The good agreement between the experiment (Figure 5.3D) and theory (Figure 5.3E) indicates that the behavior of the proposed material is highly predictable.

We further examined the performance of the proposed architected material during an impact by drop tests (Appendix A3.4). We simulate the situations where the protected object is placed at the top of the material whereas the impact occurs at its bottom. The peak force acting on the protected object is expected to be restrained below the safety threshold when certain level of impact energy is applied. We dropped an 8-layered sample containing columns of a width-to-length ratio w/l = 0.30, same as shown in Figure 5.3B, from different heights h, while measured the acceleration at its top surface using a piezoelectric accelerometer, and converted it to the force by multiplying the acceleration a by the mass of the top plate (m = 0.156 kg). To achieve a high input energy E_{inp} with a small height, we increased the total dropped weight by attaching some steel plates to the bottom of the sample (Appendix Figure 3.8). As a result, we obtained E_{inp} up to 2.5 J within a height of 20 cm. We find that the peak force F_{peak} acting on the top plate remains almost a plateau in a broad range of E_{inp}, forming a force mitigation regime (Figure 5.4A). The force at this plateau matches the critical force measured in the static compression test, F_{cr} (ranging from 15.65 N at the first peak to 18.37 N at the eighth peak in Figure 5.3D), even though the strain rate in the drop test is 2×10^4 times higher than that in the static test (Appendix A3.3). This remarkable agreement indicates that the proposed energy-absorbing mechanism is rate-independent. Besides, the force plateau occurs in the range of E_{inp} from 0.6 J to 1.8 J, which is on the same order of magnitude as the absorbed energy underneath the plateau of the force-displacement loading path in the static test (0.45 J, Figure 5.3D). The level of the force plateau and the corresponding range of E_{inp} can be scaled up by increasing the modulus of the elastomer and the number of columns in each layer. Figure 5.4B shows the acceleration-time relation when an impact energy of E_{inp} = 1.8 J (upper limit of the mitigation regime) is applied. During the impact, the columns buckle sequentially from the bottom layer to the top layer (Figure 5.4C1-C3 and

Appendix Video 3.2), limiting the impact force acting on the top layer to the critical force for column buckling. The drop tests confirm that the proposed architected materials are capable of restraining the impact force from exceeding the safety threshold for a wide scope of input energy at high strain rates by harnessing the snapping-back buckling.

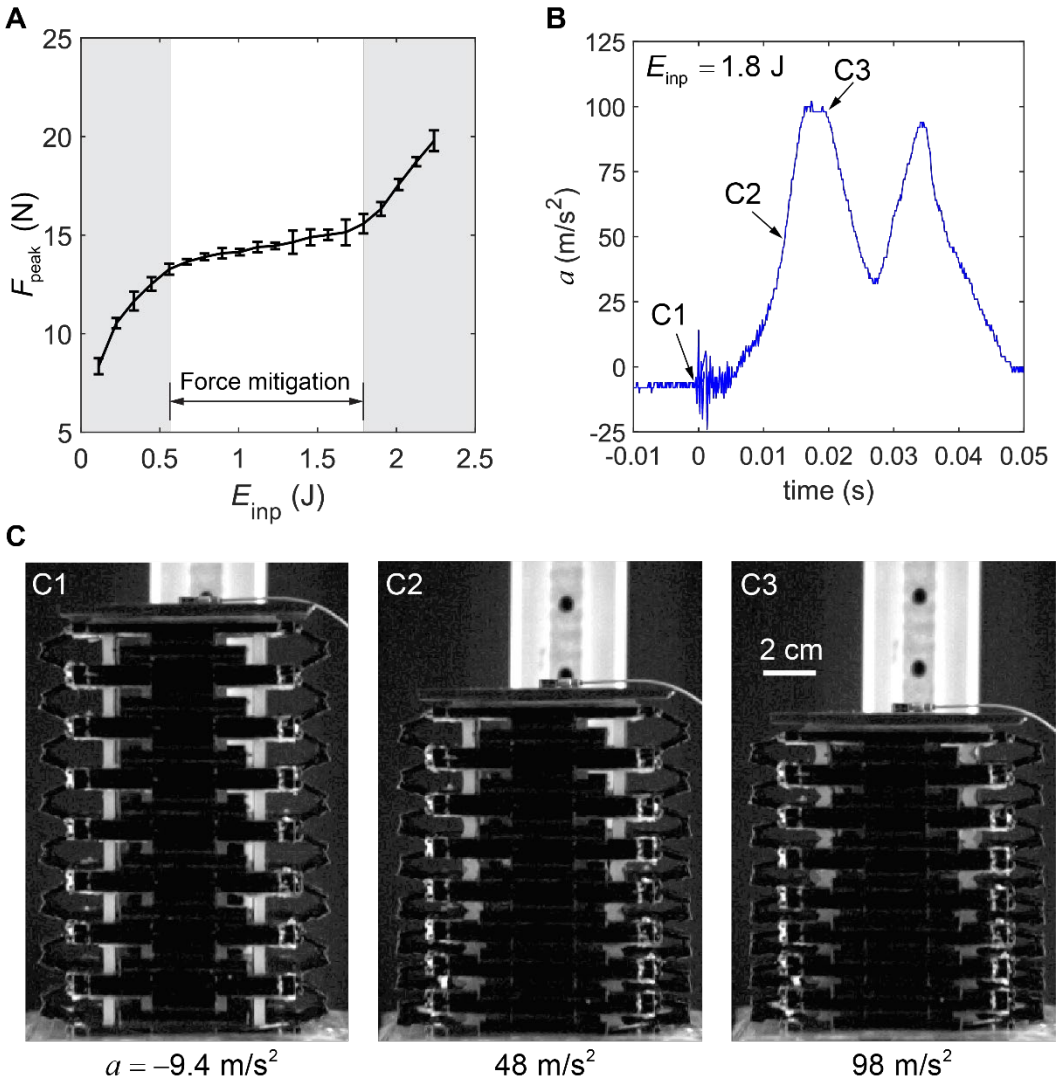

Figure 5.4 Drop tests for the proposed architected material. (A) The peak reaction force F_{peak} on the top surface as a function of the input energy E_{inp} from the bottom. The error bars indicate the standard deviations of 5 tests for a given E_{inp}. The force remains nearly constant in a wide range

of E_{inp} in the force mitigation regime. (B) Acceleration-time relation during the impact when E_{inp} = 1.8 J. (C) Snapshots of the sample corresponding to the three time points in (B). C1 records the moment when the impact occurs. C2 shows that the lower layers have buckled whereas the upper layers remain unbuckled. C3 shows the deformation at the peak acceleration, where all layers have buckled. The measured accelerations at the top surface are labeled at the bottom of all the snapshots. The negative sign indicates that the direction of the acceleration is vertically downward.

5.3.2 Programmable behavior of the architected material

The performance of the proposed architected material can be programmed by the width-to-length ratio w/l of the columns. According to Figure 5.2C, the materials with low w/l show no energy dissipation if the number of layers n is not large enough. We built an 8-layered architected material with 5 × 5 identical columns of w/l = 0.14 in each layer (Appendix A3.2 and A3.3). This material is expected to have zero energy dissipation based on our theory (Figure 5.5B). We conducted a displacement-controlled loading and unloading test for this sample (Appendix A3.2 and A3.3), and found that the loading and unloading curves are very close, resulting in very small energy dissipation $E_{\mathrm{dis}}/\mu AL = 0.0087$ (Figure 5.5A and Appendix Video 3.3). This energy dissipation is negligible compared to the energy dissipated in the 8-layered architected material with columns of w/l = 0.30 (Appendix Figure 3.9). The small energy dissipation observed is potentially caused by the adhesion in the self-contact region as the columns are fully folded.

Besides, the critical force for buckling of each layer and the ratio of dissipated energy to returned energy can be tuned by preloads. We hung some weight balances to the sample shown in Figure 5.3B as a preload (Appendix Figure 3.10). As the preload increases, both the critical force and the returned energy are reduced, but the dissipated energy is maintained (Figure 5.5C, D and Appendix Video 3.4). Hence, the ratio of the dissipated energy to the returned energy is increased.

Remarkably, when the preload is large enough such that the unloading path is shifted below the zero force, this material can be transformed from monostable to bistable. As shown by our experiment and theory (Figure 5.5E, F), instead of recovering to its original configuration, this material retains its deformed but stable configuration after unloading (Appendix Video 3.5), resulting in part of input energy trapped in the material.

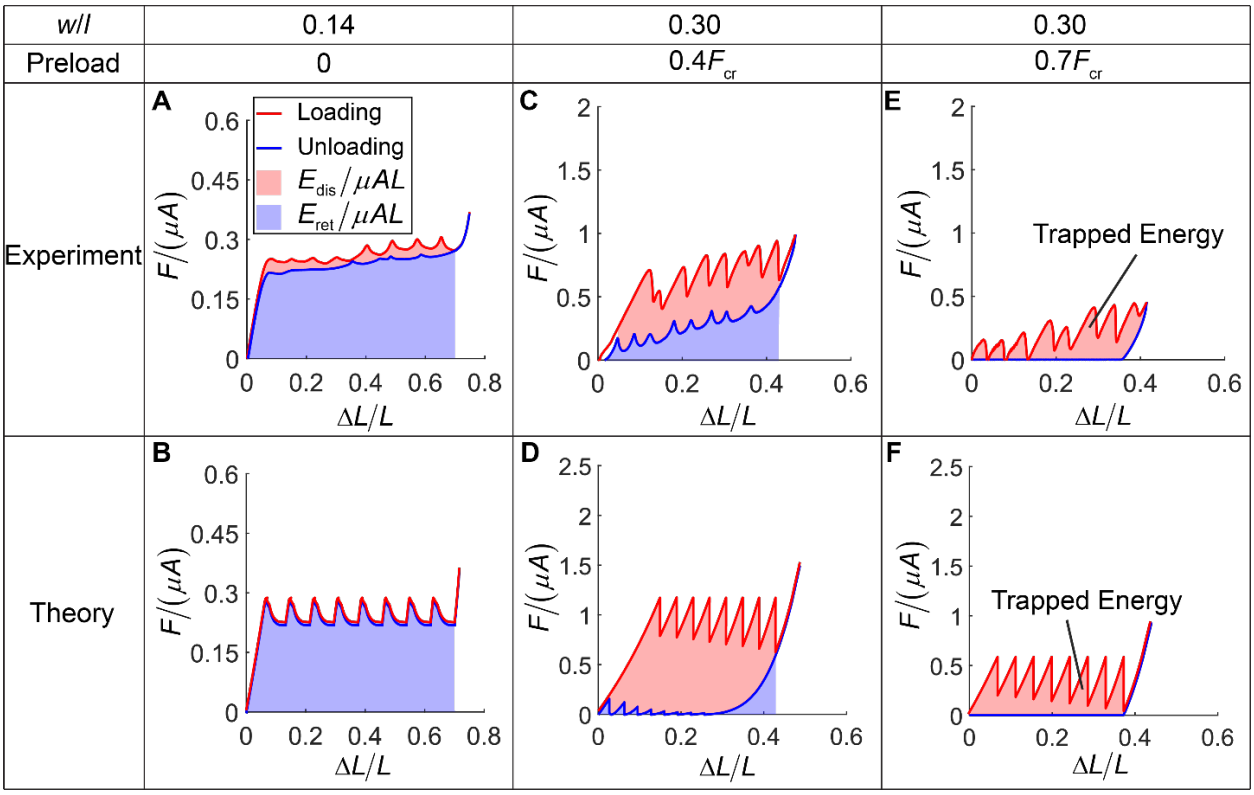

Figure 5.5 Influence of the width-to-length ratio w/l and the preloads on the performance of the proposed architected material. (A and B) The displacement-controlled force-displacement response of an 8-layered architected material with columns of $w/l = 0.14$ from the experiment (A) and the theory (B). Each column has a width w = 1.4 mm, length l = 10 mm, and out-of-plane thickness b = 9 mm. (C-F) The displacement-controlled force-displacement response of the sample shown in Figure 2B with a preload $0.4F_{cr}$ (C and D) and preload $0.7F_{cr}$ (E and F), with F_{cr}

corresponding to the first peak force on the force-displacement loading curve when no preload is applied. The results from the experiments (A, C, E) and theory (B, D, F) agree well with each other.

5.4 Summary

In summary, we combine FE simulations, theoretical analysis and experiments to develop a reusable energy-absorbing architected material harnessing the snapping-back buckling of wide hyperelastic columns. The quasi-static cyclic loading tests confirm that the proposed material is capable of dissipating energy while keeping the force nearly constant with a long working distance in a reusable, self-recoverable, and highly predictable manner, while the drop tests at high strain rates show the feature of rate-independency and the capability of force attenuation in a broad range of input energy. Moreover, we have demonstrated that the mechanical responses of the proposed energy-absorbing material can be widely tuned by the geometry and preloads. Compared to a multi-layered material harnessing the snapping-through buckling, ours harnessing the snapping-back buckling has higher maximum dissipation energy, and requires much less layers to achieve the maximum dissipation energy, which can dramatically reduce the volume and mass of the material for the same energy-absorbing performance. Due to the high local strain during the snapping-back buckling, our design of wide columns is limited to hyperelastic elastomers. Our findings broaden the design strategies for reusable energy-absorbing materials in applications including crashworthiness improvement of vehicles and aircrafts, protective packaging in goods transportation, and personal safety devices in sports.

Chapter 6 Blueprinting Photothermal Shape-Morphing of Liquid Crystal Elastomers

Shape morphing of flat thin sheets to well-defined 3D shapes is an effective method to fabricate complex 3D structures, and Liquid crystal elastomers (LCEs) are an attractive platform for shape morphing due to their ability to rapidly undergo large deformations. While recent work has focused on patterning the director orientation field to achieve desired target shapes, this strategy cannot be generalized to material systems where high-resolution surface alignment is impractical. Instead of programming the local orientation of anisotropic deformation, we develop here an alternative strategy for prescribed shape morphing by programming the magnitude of stretch ratio in a thin LCE sheet with constant director orientation. By spatially patterning the concentration of gold nanoparticles (AuNPs), uniform illumination leads to gradients in photothermal heat generation and therefore spatially-nonuniform deformation profiles that drive out-of-plane buckling of planar films into predictable three-dimensional (3D) shapes. Experimentally realized shapes are shown to agree closely with both finite element simulations and theoretical predictions for systems with unidirectional variation in deformation magnitude.

6.1 Introduction

Shape transition from an initially flat sheet to a desired 3D shape triggered by a stimulus is an effective approach for the design of complex 3D structures with advanced functionalities. With numerous 2D patterning techniques (lithography, inkjet printing, laser cutting, etc.), researchers have introduced spatial inhomogeneity to many types of flat stimuli-responsive materials such as hydrogels [16,17,164,165], Liquid Crystal Elastomers (LCE) [89,91,93,166–168], and Shape Memory Polymers (SMP) [169,170]. Upon activation by different stimuli, the

programmed flat active materials can deform into well-defined 3D shapes. This shape transitions from 2D to 3D shapes have been used in a wide range of applications including biomedical devices [171], soft actuators and sensors [172,173], and mechanical metamaterials [174,175].

To transition a flat sheet to a desired 3D shape, it is necessary to have spatially nonuniform stresses generated inside the material. There are two types of stress variation in space that can induce shape transition [176]: through-thickness variation and in-plane variation. The through-thickness stress variation, which are caused by strain gradients along the thickness upon stimuli activation, generate out-of-plane bending moments and thus out-of-plane deformations. This bending-driven strategy of shape transition can only program Mean curvature but not Gaussian curvature, since change in Gaussian curvature requires nonuniform in-plane stretch or compression. The in-plane stress variation, which are caused by in-plane stretch gradients in response to stimuli, generate in-plane compressive forces, driving the out-of-plane buckling of the flat sheet into 3D shapes. This buckling-driven strategy of shape transition enables the access to programming both Mean and Gaussian curvature, broadening the 3D shapes achieved through the shape transformation from a flat sheet.

Recently, we demonstrated a method [93] to prescribe in-plane stretch profile on a flat LCE sheet with constant director orientation by spatially patterning the concentration of gold nanoparticles. Under uniform illumination, the nonuniform distribution of gold nanoparticles causes gradients in photothermal heat generation and therefore nonuniform in-plane stretches, yielding out-of-plane buckling of the flat sheet. Compared to spatially programming the director orientation [88,89,91,177–179] on a flat LCE sheets, this method can be widely generalized to all LCE systems with simple fabrication process. The shape transition of a flat LCE sheet with prescribed in-plane stretch profile can be predicted by non-Euclidean plate theory [22,23] which,

like the Föppl-von Kármán (FvK) theory [180], takes into account both bending and stretching energies. The strains in this theory are measured with respect to the reference metric tensor, which is defined by the prescribed in-plane stretch profile and is not necessarily immersible in 3D Euclidean space.

In this chapter, we explore the utility of this method to blueprint shape changes of thin LCE nanocomposite (LCENC) sheets with unidirectional in-plane director fields in response to flood illumination. Specifically, we show that discrete patterns of photothermal inclusions can generate a rich array of dynamic shape changes due to buckling driven by nearly discontinuous changes of in-plane deformation. Furthermore, smooth variations in deformation can be programmed via grayscale patterning of AuNP absorbance to yield more complex shape changes. Finite element method (FEM) simulations are used to help understand the shapes selected by these materials, in concert with an analytical model based on the non-Euclidean plate theory [22,23] that provides a general approach to the design of axisymmetric shapes through unidirectionally varying stretch profiles.

6.2 Theory

In this section, we will analytically link the in-plane strain distributions to the 3D shapes transitioned from a flat LCE thin sheet. We start with a general model which considers both stretching and bending energies. We then simplify this model by neglecting the stretching energy for a LCE sheet with a very small thickness. This simplified model enables us to solve an inverse problem, in which we obtain the required in-plane strain distributions for a targeted 3D shape. In the end, we address the shape morphing of LCE sheets with finite thicknesses, in which the final 3D shape is determined by the interplay between the stretching and bending energies.

6.2.1 Modeling of LCE thin sheets

We model a rectangular LCE thin sheet with length L, width w, and thickness h using the reduced 2D non-Euclidean plate theory [22,23], in which the sheet is represented by its mid-surface and the intrinsic metric tensor $\bar{\boldsymbol{a}}$ of this mid-surface may not be immersible in the 3D Euclidean space. The intrinsic metric tensor $\bar{\boldsymbol{a}}$ of the sheet is determined by the following prescribed in-plane stretch profiles,

$$\bar{\boldsymbol{a}} = \begin{bmatrix} \lambda_u^2 & 0 \\ 0 & \lambda_v^2 \end{bmatrix}, \tag{6.1}$$

where u and v are the two curvilinear coordinates of the mid-surface, and λ_u and λ_v are the prescribed in-plane stretches in the u and v directions, respectively. Here we limit ourselves to the stretch distributions that are only functions of v. For incompressible LCE sheets, the λ_v can be obtained by

$$\lambda_v = \frac{1}{\sqrt{\lambda_u}}. \tag{6.2}$$

The elastic energy of the LCE sheet is given by

$$E_{\text{total}} = E_{\text{stretch}} + E_{\text{bend}}, \tag{6.3}$$

where E_{stretch} is the stretching energy,

$$E_{\text{stretch}} = \frac{\mu h}{4} \int_0^L \int_0^W \left(\bar{a}^{\alpha\beta}\bar{a}^{\gamma\eta} + \bar{a}^{\alpha\gamma}\bar{a}^{\beta\eta}\right)(a-\bar{a})_{\alpha\beta}(a-\bar{a})_{\gamma\eta}\sqrt{|\bar{\boldsymbol{a}}|}\,dv\,du, \tag{6.4}$$

and E_{bend} is the bending energy

$$E_{\text{bend}} = \frac{\mu h^3}{12} \int_0^L \int_0^W \left(\bar{a}^{\alpha\beta}\bar{a}^{\gamma\eta} + \bar{a}^{\alpha\gamma}\bar{a}^{\beta\eta}\right)b_{\alpha\beta}b_{\gamma\eta}\sqrt{|\bar{\boldsymbol{a}}|}\,dv\,du. \tag{6.5}$$

In Equations (6.4) and (6.5), $\boldsymbol{a}$ is the first fundamental form or metric tensor of the mid-surface and $\boldsymbol{b}$ is the second fundamental form or curvature tensor of the mid-surface. The stretching energy

in Equation (6.4) is associated with changes of distances in the mid-surface from its intrinsic metric tensor $\bar{\boldsymbol{a}}$, and the bending energy in Equation (6.5) is associated with changes of curvatures from the flat configuration. Once the two fundamental forms are obtained, the mid-surface of the sheet can be uniquely determined.

Note that the stretching energy scales linearly with h, whereas the bending energy scales with h^3. When the sheet is extremely thin, it prefers obeying its intrinsic metric tensor $\bar{\boldsymbol{a}}$ such that the stretching energy equals zero and all the energies go with bending energy. We call this condition as thin limit or isometric immersion. When the sheet is extremely thick, it prefers being flat such that the bending energy equals zero and all the energies go with stretching energy. We call this condition as thick limit. Within these two limits, the 3D shape of the sheet is determined by the interplay between the stretching energy and the bending energy.

6.2.2 Thin limit

We consider an extremely thin LCE sheet and predict its 3D shape produced by the intrinsic metric tensor shown in Equation (6.1). The Gaussian curvature K of this surface can be computed by [181]

$$-EK = (\Gamma_{12}^2)_{,u} - (\Gamma_{11}^2)_{,v} + \Gamma_{12}^1\Gamma_{11}^2 + \Gamma_{12}^2\Gamma_{12}^2 - \Gamma_{11}^2\Gamma_{22}^2 - \Gamma_{11}^1\Gamma_{12}^2, \tag{6.6}$$

where $E = g_{11} = \lambda^2$, $(\ \ )_{,u}$ and $(\ \ )_{,v}$ are partial derivatives with respect to u and v, $\Gamma_{\beta\gamma}^{\alpha}$ $(\alpha, \beta, \gamma = 1, 2)$ are the Christoffel symbols, which equal

$$\Gamma_{11}^1 = 0, \Gamma_{12}^1 = \Gamma_{21}^1 = \lambda'/\lambda, \Gamma_{22}^1 = 0, \Gamma_{11}^2 = -\lambda^2\lambda', \Gamma_{12}^2 = \Gamma_{21}^2 = 0, \Gamma_{22}^2 = -\frac{1}{2}\lambda'/\lambda. \tag{6.7}$$

Here $(\quad)'$ denotes differentiation with respect to v. With Equations (6.6) and (6.7), we can obtain the dependence of Gaussian curvature K on stretch profile $\lambda(v)$, as shown below

$$K = -\frac{1}{\sqrt{\lambda}}\left(\sqrt{\lambda}\lambda'\right)' = -\frac{2}{3\sqrt{\lambda}}\left(\lambda^{3/2}\right)''. \tag{6.8}$$

We assume that the 3D shape is axisymmetric about the v axis and thus the map $\boldsymbol{\chi}$: $\omega \subset \mathbb{R}^2 \longrightarrow \hat{\omega} \subset \boldsymbol{E}^3$ is given by

$$\boldsymbol{\chi}(u,v) = \left[r(v)\cos\left(\frac{u}{R_0}+\psi(v)\right) \quad r(v)\sin\left(\frac{u}{R_0}+\psi(v)\right) \quad z(v)\right], u \in [0,l], v \in [0,w], \tag{6.9}$$

where functions r, ψ and z depend only on v, and R_0 is a positive constant that will be determined later. The metric tensor of the surface $\hat{\omega}$ is given by

$$\boldsymbol{g}_{\hat{\omega}} = \boldsymbol{\nabla}\boldsymbol{\chi}^{\mathrm{T}}\boldsymbol{\nabla}\boldsymbol{\chi} = \begin{bmatrix} \left(\frac{r}{R_0}\right)^2 & \frac{r^2\psi'}{R_0} \\ \frac{r^2\psi'}{R_0} & r'^2 + z'^2 + r^2\psi'^2 \end{bmatrix}. \tag{6.10}$$

Since the LCE sheets are very thin, it is reasonable to assume that their final configurations are essentially stress-free and their metric tensors given by Equation (6.10) match the target metric tensor shown in Equation (6.1), i.e.

$$\begin{bmatrix} \left(\frac{r}{R_0}\right)^2 & \frac{r^2\psi'}{R_0} \\ \frac{r^2\psi'}{R_0} & r'^2 + z'^2 + r^2\psi'^2 \end{bmatrix} = \begin{bmatrix} \lambda(v)^2 & 0 \\ 0 & \frac{1}{\lambda(v)} \end{bmatrix}. \tag{6.11}$$

From the equation above, we obtain

$$r(v) = \lambda(v)R_0, \tag{6.12}$$

$$\psi'(v) = 0, \tag{6.13}$$

$$z'(v) = \pm\frac{1}{\sqrt{\lambda(v)}}\sqrt{1-\left(R_0\sqrt{\lambda(v)}\lambda'(v)\right)^2}, R_0 \leq \frac{1}{\sqrt{\lambda(v)}|\lambda'(v)|}. \tag{6.14}$$

Given a stretch profile $\lambda(v)$,we can obtain $r(v)$ from Equation (6.12) and $z(v)$ by evaluating numerically the integral on the right-hand side of Equation (6.14). In addition, we set $\psi = 0$. The 3D shape for this stretch profile can then be determined by Equation (6.9) with an appropriate R_0, which is selected such that the following bending energy is minimized

$$E_b = \int_0^l \int_0^w (4H^2 - K)dudv, \tag{6.15}$$

where H and K denote mean and Gaussian curvatures of the surface $\hat{\omega}$, respectively.

6.2.3 Finite thicknesses

When the thickness of the sheet is finite, the actual metric tensor $\boldsymbol{a}$ will deviate from the prescribed intrinsic metric tensor $\bar{\boldsymbol{a}}$, leading to non-zero stretching energy. Thus, minimizing solely the bending energy is not enough. The final 3D shape is determined by minimizing the total elastic energy.

Since the prescribed intrinsic metric tensor $\bar{\boldsymbol{a}}$ is a diagonal matrix and depends solely on v, it is reasonable to assume that the two fundamental forms $\boldsymbol{a}$ and $\boldsymbol{b}$ are functions of v and their off-diagonal terms are zero:

$$\boldsymbol{a} = \begin{bmatrix} E(v) & 0 \\ 0 & G(v) \end{bmatrix}, \boldsymbol{b} = \begin{bmatrix} e(v) & 0 \\ 0 & g(v) \end{bmatrix}. \tag{6.16}$$

Based on the Gauss formula and Mainardi-Codazzi equations [181,182], the terms $e(v)$ and $g(v)$ in $\boldsymbol{b}$ can be expressed in terms of $E(v)$ and $G(v)$:

$$e^2 = cE - \frac{E'^2}{4G}, \tag{6.17}$$

$$g^2 = \frac{\left(E'^2G + EE'G' - 2EE''G\right)^2}{4E^2G(4cEG - E'^2)}. \tag{6.18}$$

where $(\quad)'$ denotes the derivative of $(\quad)$ with respect to v, and c is the integration constant.

To determine the shape of the mid-surface, we need to find the $E(v)$, $G(v)$, and c such that the total elastic energy in Equation (6.3) is minimized. The process of the minimization is as follows. First, we uniformly discretize the domain of v into m points. Then $E(v)$, $G(v)$, $e(v)$, and $g(v)$ are also discretized. We use E_i, G_i, e_i, and g_i $(i = 1, \dots, m)$ to represent their values at point v_i $(0 \le v_i \le w)$, respectively. The discretized version of the stretching and bending energy can be written as

$$\begin{aligned} E_{\text{stretch}} = \frac{\mu h L}{2}\sum_{i=1}^{m}\Big[&\lambda_u^{-2}(v_i)\big(E_i - \lambda_u(v_i)\big)^2 + \lambda_v^{-2}(v_i)\big(G_i - \lambda_v(v_i)\big)^2 + \\ &\lambda_u^{-1}(v_i)\lambda_v^{-1}(v_i)\big(E_i - \lambda_u(v_i)\big)\big(G_i - \lambda_v(v_i)\big)\Big], \end{aligned} \tag{6.19}$$

$$E_{\text{bend}} = \frac{\mu h^3 L}{6}\sum_{i=1}^{m}[\lambda_u^{-2}(v_i)e_i^2 + \lambda_v^{-2}(v_i)g_i^2 + \lambda_u^{-1}(v_i)\lambda_v^{-1}(v_i)e_i g_i]. \tag{6.20}$$

Second, we express the e_i, and g_i in terms of E_i, G_i, and c using Equations (6.17) and (6.18), in which the derivative terms are approximated by the finite difference. Third, we use fminunc in Matlab to solve the following minimization problem

$$\min_{E_i, G_i, c} E_{\text{total}}, (i = 1, \dots, m), \tag{6.21}$$

where E_i, G_i, and c are to be determined. This minimization problem is solved iteratively, with increments in thicknesses h/w. We start from the case with an extremely small thickness: $h/w = 10^{-6}$, and use the solution of isometric immersion as the initial try, in which the first fundamental form fully obeys the intrinsic metric tensor and the second fundamental form is determined by

minimizing the bending energy. We gradually increase the thickness and use the solution of the previous step as an initial try of the current step. This iteration stops as the bending energy becomes negligible ($E_{\text{bend}}/E_{\text{total}} \leq 0.001$).

6.3 Experimental Setup

The fabrication of monodomain LCEs and the patterning of nanocomposites have been discussed in [93]. We summarize them in this section. The monodomain LCEs are synthesized following the work of Ahn and co-workers [183]. To incorporate photo-responsiveness into the LCEs, gold nanoparticles (AuNPs) are produced by photoreduction [184]. Because the degree of gold reduction is controlled by the dose of UV light, the distribution of the AuNP can be spatially programmed using grayscale photomasks [185]. Since the amount of AuNP determines the magnitude of temperature change upon photothermal heating, the transparency of the photomasks can be used to systematically program the resulting photothermal deformations. The stretch λ due to photothermal heating can be programmed from 0.77 – 0.92 by controlling the transparency of the photomask to UV light from 0% black (nearly transparent to UV light) and 100% black (nearly opaque) during patterning. This introduces the possibility to locally control in-plane photothermal strains and thus the shape morphing.

6.4 Finite element modeling

To numerically connect the patterned photothermal heat generation to shape morphing, we develop FEM simulations. In the FEM simulations, LCE sheets are modeled using the neo-classical free energy density [186,187] implemented into Abaqus as a user subroutine UMAT. A stretch-temperature relation, fit to the experimental measurement, is introduced into the free energy to describe the temperature-dependent anisotropy of LCEs (Appendix A4.1). Once a

temperature field corresponding to a specific design of photothermal patterning is prescribed, the equilibrium shape is solved by FEM in Abaqus.

6.5 Results

Using this patterning method, we first try discretely patterned deformation profiles to show how wide variety of 3D shapes we can obtain. Then we address the forward and inverse problems for the sheets with continuous in-plane stretch profiles under thin limit. Finally, we study the influence of thickness of the sheets with bistrip pattern on the shape morphing.

6.5.1 Discrete patterns

To probe the utility of this method to program a wider variety of shapes, a series of additional patterns are investigated. For example, illumination of a square sheet with a centered rectangular inclusion with the long axis oriented parallel to the director results in a saddle-like shape that is symmetric about the axes parallel and perpendicular to the director that bisect the center of the film (Figure 6.1A). Placement of a photothermal region in one quadrant of the film drives bending about an axis diagonally bisecting the sheet, resulting in a wrinkled hyperbolic surface (Figure 6.1B). Finally, inclusion of a large square in the center of the sheet drives rolling about an axis perpendicular to the director and wrinkling along the edges of the sheet (Figure 6.1C). These deformations are similar to those observed in nematic sheets with polydomain inclusions [188] and isotropic gels with local photothermal inclusions [189] and again result from a balance of stretching and bending energies as the films attempt to accommodate the discontinuous target metric.

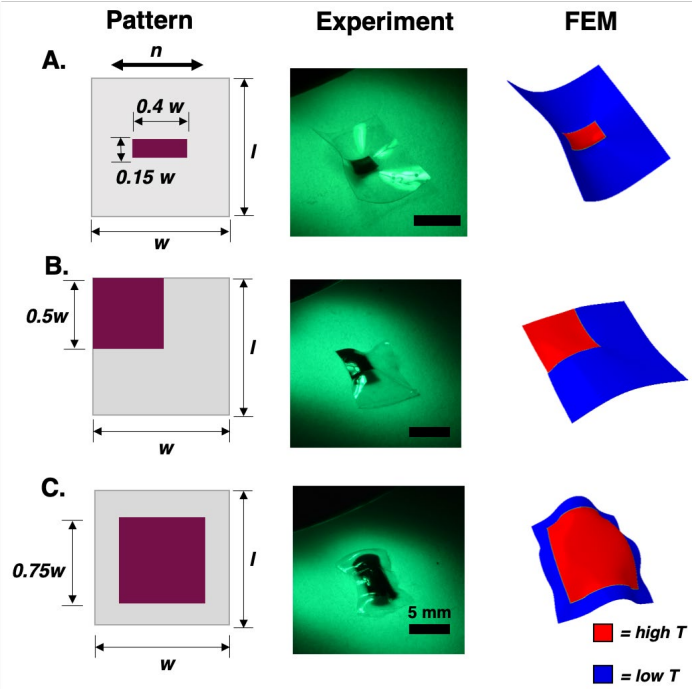

Figure 6.1 Shape transformation via localized photothermal inclusions. Buckling into different shapes in response to (A) rectangular and (B, C) square inclusion are demonstrated experimentally and the resulting shapes are predicted via FEM.

6.5.2 Continuous patterns under thin limit

Next, we explore the utility of smoothly-varying spatial gradients in absorption to introduce continuous in-plane stretch profiles into nematic sheets, which provides opportunities to program shapes with arbitrary Gaussian curvatures. As a proof-of-concept, we first investigate the 'forward' problem, i.e. defining a stretch profile and evaluating the match between experiments, FEM simulations, and geometric predictions for the resulting 3D shape. As a convenient test case, we use stretch profiles of the following form to program square sheets:

$$\lambda(\xi) = \lambda_{min} + (\lambda_{max} - \lambda_{min})\exp\left(-\frac{1}{2}\left(\frac{2\xi-1}{d}\right)^2\right), \tag{6.22}$$

where $\xi = \frac{v}{w} \in [0,1]$, λ_{min} and λ_{max} are the minimum and maximum experimentally accessible stretches, respectively, and d is a dimensionless parameter that controls the spatial extent of variations in λ (Figure 6.2A). Indeed, as predicted by Equation (6.8), as d is reduced, the resulting curvature increases in magnitude and becomes concentrated in a smaller region. Using the corresponding metric tensor, given by Equation (6.1), theory and FEM (Figure 6.2B-D) predict buckling into candy wrapper-like shapes, with a ridge of positive Gaussian curvature in the middle of the sheet that smoothly progresses along *v* to valley regions of negative Gaussian curvature that evolve to zero Gaussian curvature at the edges. To investigate these shape transformations experimentally, samples are patterned using photomasks generated in Matlab from a calibration curve of stretch versus percent black. Experimental results (Figure 6.2E,Appendix Figure 4.1) match the predicted deformations, with greater curvature and a tighter characteristic radius of curvature of the ridge as *d* decreases. We find that the Gaussian curvatures observed by FEM (Figure 6.2B) are in very good agreement with the ones predicted by Equation (6.8), and furthermore that the realized 3D shapes correspond closely to those from geometric predictions (see (Figure 6.2C)). This striking agreement demonstrates the robustness of the shape morphing concept developed here and suggests its potential for generalization to other chemistries and materials.

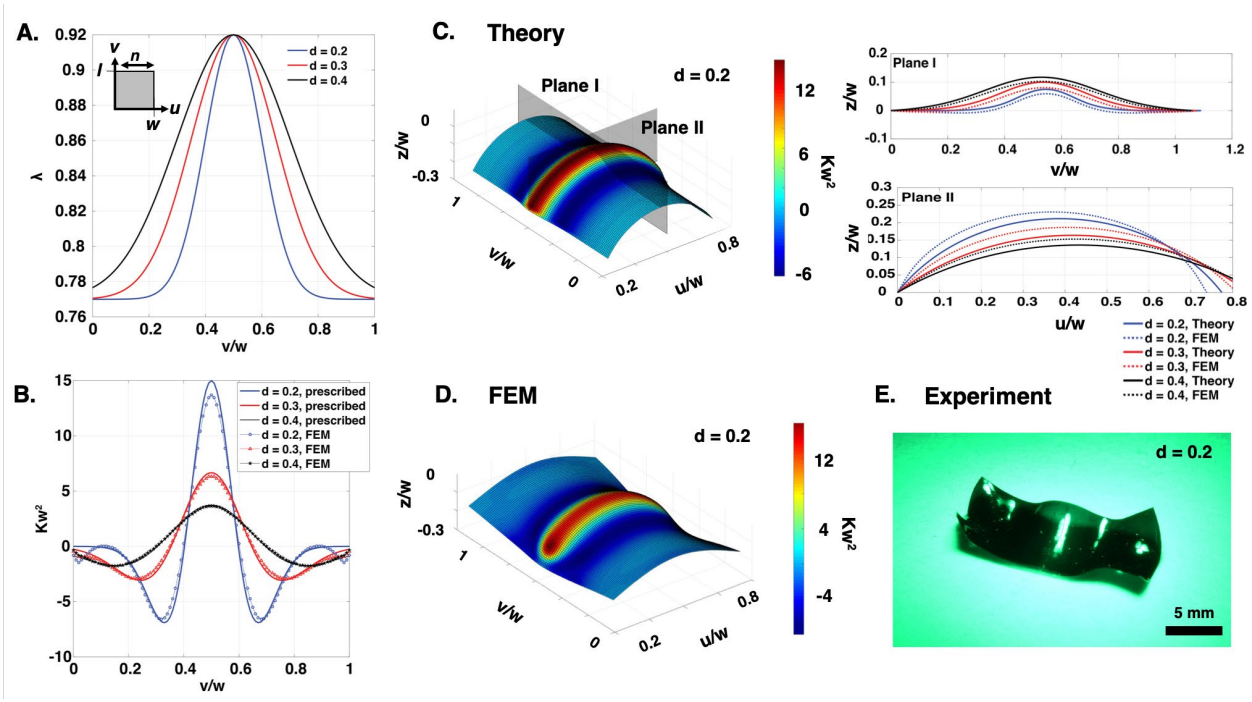

Figure 6.2 Patterning smoothly curved sheets with Gaussian stretch profiles. (A) Stretch profiles λ for different values of d for $w = l$ (inset). (B) Prescribed and FEM Gaussian curvature as a function of v at $u/w = 0.5$. (C) Shape prediction of $d = 0.2$ by theory (left) and comparison of theory to FEM simulations (right) for different values of d. (D) Shape prediction of $d = 0.2$ by FEM. (E) Experimental result for $d = 0.2$ demonstrates buckling into a candy wrapper-like shape due to regions of highly localized Gaussian curvature that closely matches the predicted shape by theory and FEM. Results for $d = 0.3$ and 0.4 are provided in the Supporting Information.

To truly program shape transformation, the inverse problem – i.e., computing the stretch profile $\lambda(v)$ that leads to a desired 3D shape upon actuation – needs to be solved. While the corresponding differential geometry has been developed for isotropic gels with differential swelling [16,17,24] and nematic sheets with varying director orientation [88,177], we are not aware of previous solutions for the anisotropic case of varying stretch magnitude with a

homogenous director orientation. As a first step, we focus here on shapes with constant negative and positive Gaussian curvature, with the appropriate stretch functions obtained by numerically solving Equation (6.8) within the constraint of the stretches achievable in our system and constructing a polynomial fit to the solution. The target negative and positive curvature, calculated stretch profiles, and simulated curvature generated by FEM are shown in Figure 6.3A, D. The calculated stretch profiles prescribe high deformation in the center of the sheet and low deformation at the edges parallel to the director field in the case of constant negative Gaussian curvature and the opposite – low deformation in the middle and high deformation at the edges – for the case of constant positive Gaussian curvature. The simulated curvatures from FEM match the target constant curvatures quite well in the center portions of the films but deviate at the edges, presumably reflecting an elastic 'boundary layer' [23] that lowers the bending energy for a non-zero thickness sheet. The corresponding samples are prepared using photomasks generated from the calculated stretch profiles and experiments show buckling of LCE sheets into a saddle-like shape and a shallow spherical cap-like shape for negative and positive Gaussian curvature, respectively, matching the predictions of the accompanying FEM simulations and geometric models (Figure 6.3B-C, E-F and Appendix Figure 4.2). Interestingly, FEM predicts that a non-axisymmetric saddle shape should be lower energy than the observed axisymmetric shape in the case of constant negative Gaussian curvature (Appendix Figure 4.3). However, the non-axisymmetric shape is not observed experimentally, possibly due to imperfections in sample fabrication or kinetic selection of the axisymmetric shape. We note that the observed shapes are analogous to those experimentally realized in LCEs with patterned axisymmetric director fields about a +1 defect [179].

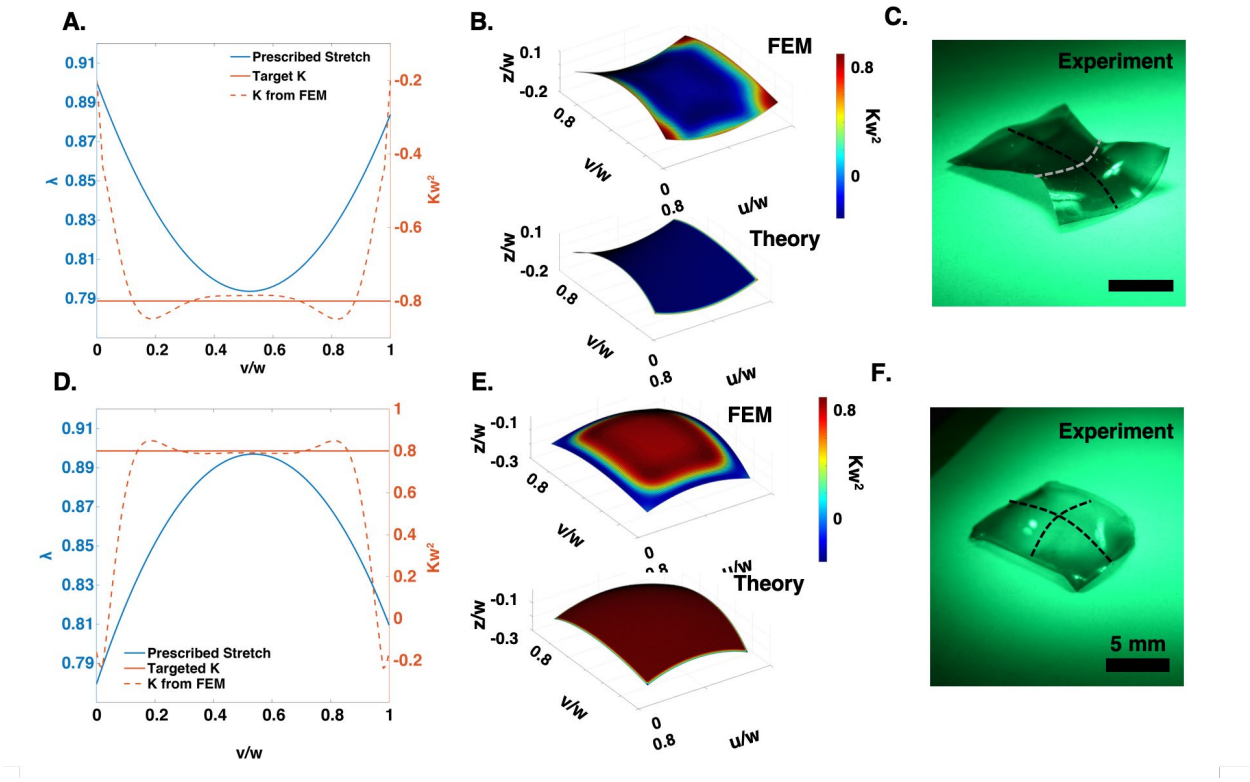

Figure 6.3 Programmed constant negative and positive Gaussian curvature via ninth-order polynomial stretch profiles. (A) Prescribed and predicted Gaussian curvature, (B) FEM simulation (top) and theory (bottom) and (C) experiment for negative Gaussian curvature. (D) Prescribed and predicted Gaussian curvature, (E) FEM simulation and (F) experiment for positive Gaussian curvature. White and black lines are drawn as guides to the eyes, with black and white denoting positive and negative curvature, respectively.

6.5.3 Bistrip patterns with finite thicknesses

In this section, we will study the effect of the thickness on the shape programming of the LCE sheets. We choose a very simple geometry called “bistrip”, where a rectangular sheet is divided into two strips: the photoactive strip and non-photoactive strip. The photoactive strip containing gold nanoparticles can generate more photothermal heats upon illumination than the

non-photoactive strip which contains no gold nanoparticles, leading to a single step change in temperature (Figure 6.4A) and thus a discretely patterned in-plane stretch profile. We found in both experiment (Figure 6.4B) and Finite Element (FE) simulation (Figure 6.4C) that upon illumination the bistrip deforms into a rolling shape, which consists of two nearly cylindrical regions smoothly connected via a transitional region.

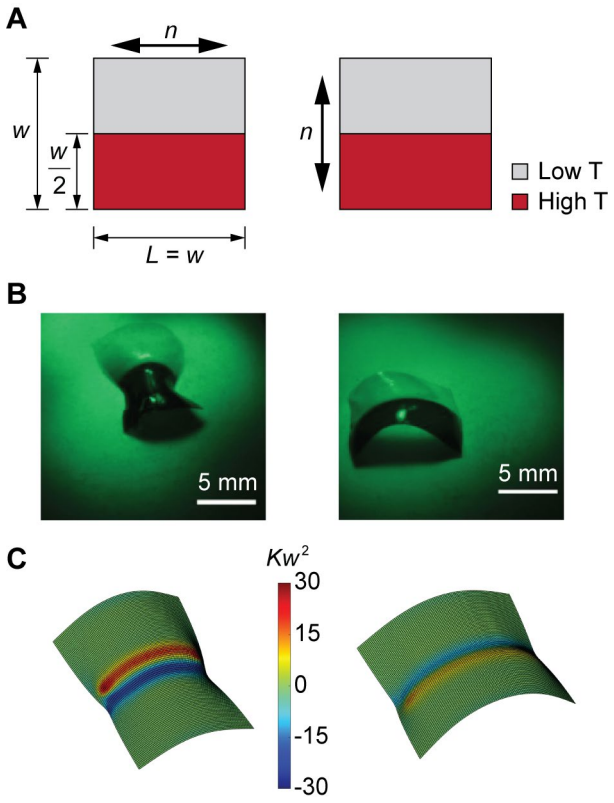

Figure 6.4 Rolling shape formation of LCE bistrips induced by discretely patterned in-plane strain profiles. (A) An initially flat rectangular LCE thin sheet is equally divided into photoactive and non-photoactive strips. Upon illumination, a rolling shape is observed in experiments (B) and predicted by FE simulation (C). The contour in (C) denotes the distribution of normalized Gaussian curvatures. The initial director is parallel (left) or orthogonal (right) to the interface between the photoactive and non-photoactive regions.

To demonstrate the process of minimizing the total elastic energy, we take the bistrip with $L/w = 2.0$ and the initial director parallel to the interface between photoactive and non-photoactive region as an example. In this example, the stretch distribution in u direction λ_u is given by

$$\lambda_u(v) = 0.92 - \frac{\Delta}{1+e^{-\frac{v/w-\rho}{\delta/w}}}, \tag{6.23}$$

where $\Delta = 0.15$, $\rho = 0.5$, and $\delta/w = 0.02$ (Figure 6.5A). the stretch distribution in v direction λ_v can be obtained based on incompressibility. In Figure 6.5B and C, we plot the total elastic energy E_{total}/h (black dots), bending energy E_{bend}/h (blue dots), and stretching energy E_{stretch}/h (red dots) as functions of thickness h/w. When the thickness h/w is very small, the majority of the total elastic energy is the bending energy. As the thickness h/w increases, the bending energy first increases and then reduces to nearly zero, whereas the stretching energy increases monotonically and becomes dominant. After the thickness is beyond its critical threshold h_{cr}/w , the stretching energy merges into the total energy, indicating no out-of-plane buckling of the bistrips. This is because the stretching energy scales with h and the bending energy scales with h^3. For the thin bistrips, the bending energy is less inexpensive, and thus the metric tensor $\boldsymbol{a}$ tends to obey the intrinsic metric tensor $\bar{\boldsymbol{a}}$, leading to nearly zero stretching energy. For the thick bistrips, the stretching energy is less inexpensive, thus the curvature tensor $\boldsymbol{b}$ tends to be zero, leading to nearly zero bending energy.

Figure 6.5C shows the following scaling relations when the thickness h/w is very small,

$$E_{\text{stretch}}/h \sim h^4, E_{\text{bend}}/h \sim h^2. \tag{6.24}$$

Equation (6.4) shows that the E_{stretch}/h is quadratic in the differences between the metric tensor $\boldsymbol{a}$ and the intrinsic metric tensor $\bar{\boldsymbol{a}}$. In Figure 6.5D, we plot the distributions of metric differences in *u* (Figure 6.5 up) and *v* (Figure 6.5 down) directions for the bistrips with very small thicknesses. We find that the metric tensor $\boldsymbol{a}$ obey the intrinsic metric tensor $\bar{\boldsymbol{a}}$ except the transition regions, and that the range of non-zero metric difference is unaffected by the thicknesses. In Figure 6.5E, we also plot the maximum magnitude of the metric differences in both *u* and *v* directions as the thickness increases, and find that this magnitude scales with h^2 when the thickness h/w is very small. Therefore, the increase of the thicknesses has no effect on the range of non-zero metric differences, but can quadratically increase the magnitude of the metric differences, resulting in the fourth power of scaling law between E_{stretch}/h and h. Equation (6.5) shows that the E_{bend}/h is not only quadratic in the curvature tensor $\boldsymbol{b}$, but also scales with h^2. In Figure 6.5F, we plot the distributions of curvature tensor in *u* (Figure 6.5F up) and *v* (Figure 6.5F down) directions for the bistrips with very small thicknesses, and find that the curvature tensor is independent of the thickness. Thus, the increase of the thickness can quadratically increase the E_{bend}/h, leading to the second power of scaling law between E_{bend}/h and h.

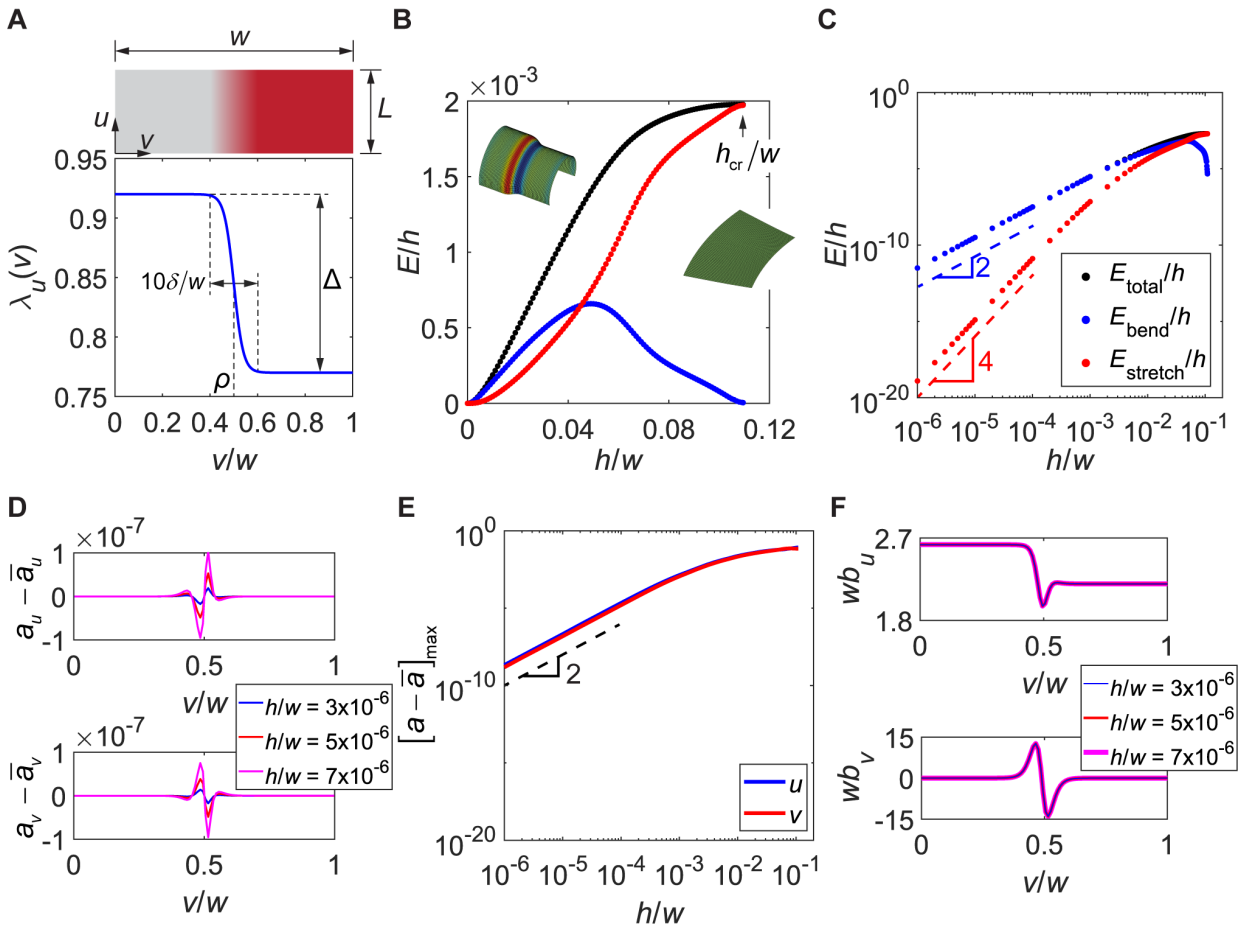

Figure 6.5 Determination of the rolling shapes. (A) Schematic overview of the LCE bistrip system. An initially flat LCE sheet of thickness h, width w, and length L is divided into the photoactive and non-photoactive regions. The width of the photoactive region is ρw. u and v are the two curvilinear coordinates with u parallel to the interface between the two regions. (B and C) The dependence of energy on thickness in linear (B) and logarithmic (C) scales for the case with ρ = 0.5, $L = 2w$, and initial director parallel to u. The dots in black, bule, and red colors represent the total, bending, and stretching elastic energies, respectively. (D) The distribution of the difference between the metric a and the reference metric $\bar{a}$ in u (upper) and v (lower) directions when h/w = $3\text{x}10^{-6}$ (blue), $5\text{x}10^{-6}$ (red), and $7\text{x}10^{-6}$ (magenta). (E) The relation between the maximum of a - $\bar{a}$

and h/w in u (blue) and v (red) directions. (F) The distribution of the normalized curvature tensor b in u (upper) and v (lower) directions when $h/w = 3\text{x}10^{-6}$ (blue), $5\text{x}10^{-6}$ (red), and $7\text{x}10^{-6}$ (magenta).

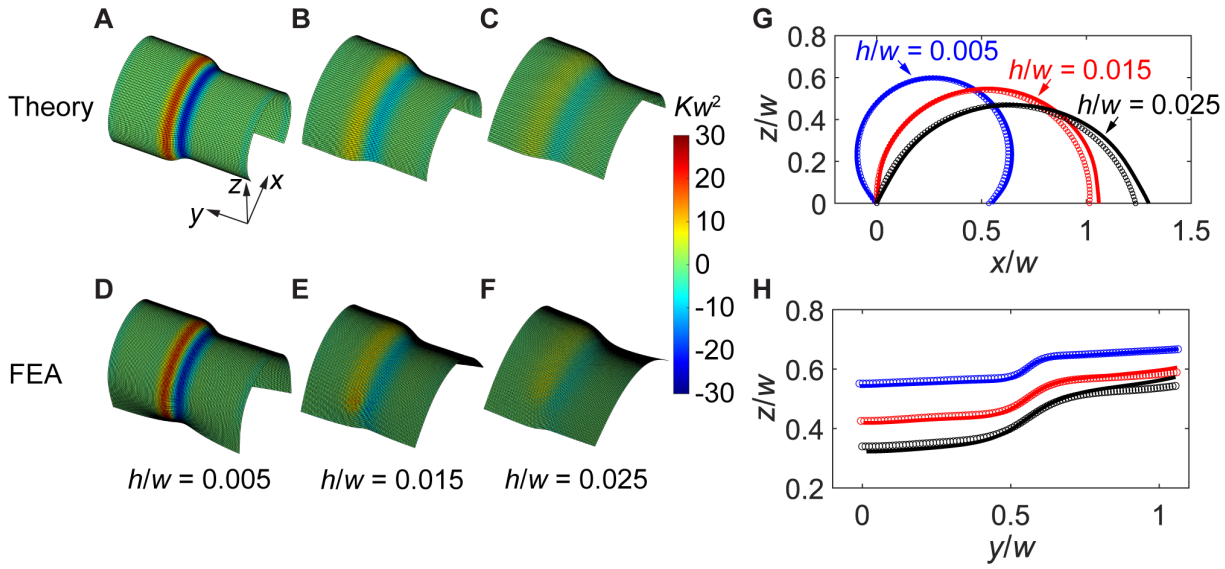

Figure 6.6 Quantitative Comparison between theory and FEA. (A-F) The rolling shapes obtained from theory (A-C) and FEA (D-F) when h/w = 0.005 (A and D), 0.015 (B and E), and 0.025 (C and F). (G and H) The profiles of the cross-section parallel (G) and orthogonal (H) to the photothermal interface. The circular dots represent theoretical results, whereas the solid lines represent the FEA results. The blue, red, and black colors denote h/w = 0.005, 0.015, and 0.025, respectively.

Once the two fundamental forms $\boldsymbol{a}$ and $\boldsymbol{b}$ are obtained from the process of minimization, the shape of the mid-surface of the bistrip is uniquely determined. In Figure 6.6, we plot the shapes of the mid-surfaces obtained from our model (Figure 6.6A-C) and compare them with the shapes obtained from FE simulations (Figure 6.6D-F) when h/w = 0.005 (A and D), 0.015 (B and E), and 0.025 (C and F). Both theory and FE simulations show that the bistrips deform into rolling shapes, and that the radius of curvature increases with the thickness. In Figure 6.6G and H, we plot the profiles of the cross-section parallel (G) and orthogonal (H) to the photothermal interface,

indicating that the theory (circular dots) and the FE simulations (solid lines) are in a quantitative agreement. To further validate our theory, we change the value of ρ from 0.2 to 0.8 for the bistrips with $L/w = 1.0$, $h/w = 0.005$, and initial director parallel to the u direction, and plot the shapes obtained from theory, FE simulations and experiments, as shown in Figure 6.7. They agree with each other very well.

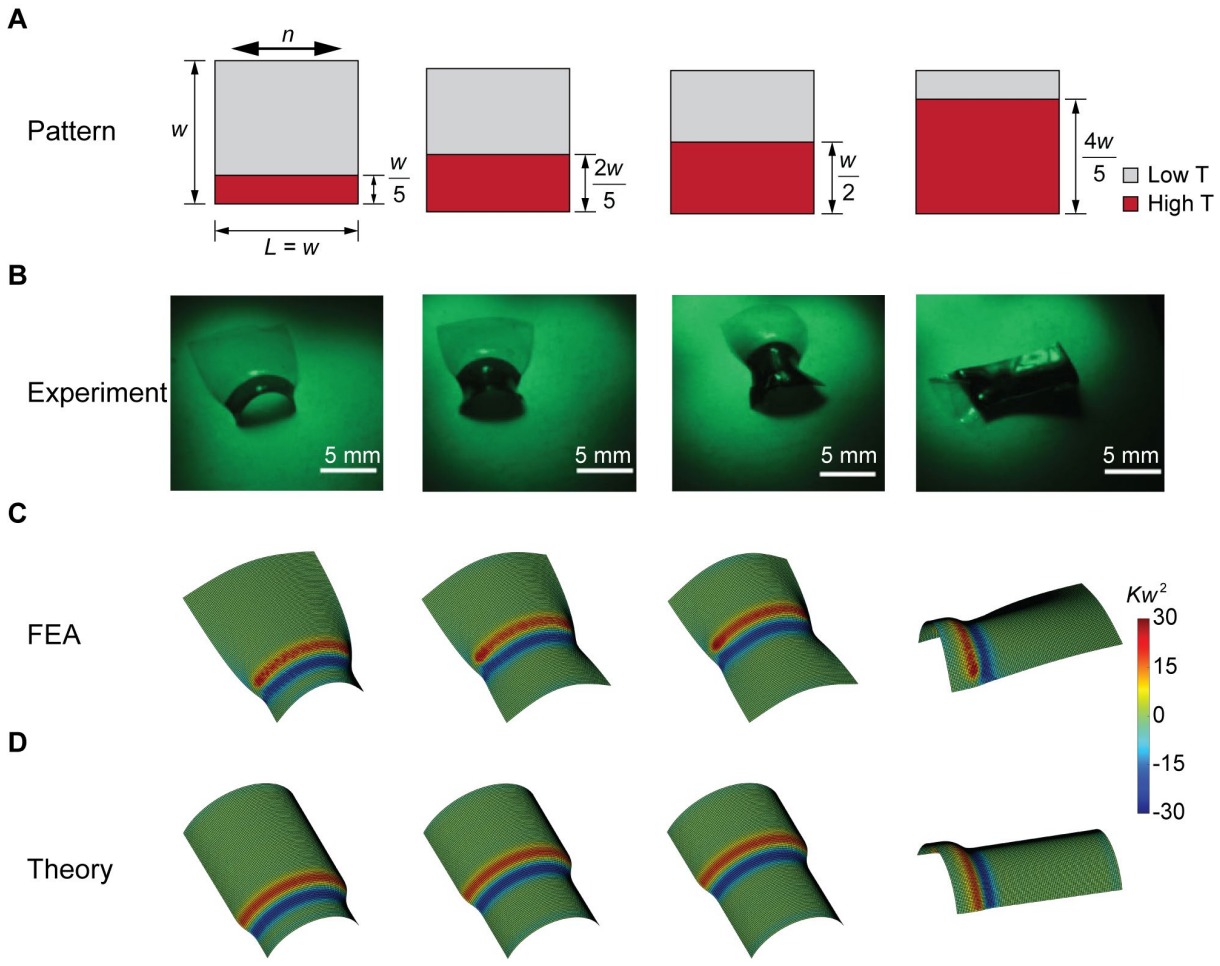

Figure 6.7 Comparison among experiment, FEA, and theory as ρ varies. (A) Patterns with ρ = 0.2 (1st column), 0.4 (2nd column), 0.5 (3rd column), and 0.8 (4th column). (B-D) The corresponding 3D shapes obtained from experiment (B), FEA (C), and Theory (D). All the square LCE sheets have thickness h/w = 0.005 and initial director parallel to the photothermal interface.

6.6 Summary

In summary, we have demonstrated a method combining experiments, FEM simulations, and theoretical predictions to program photoactive shape morphing from monodomain LCE sheets with a unidirectional director by spatially controlling photothermal heat generation. Discontinuous metrics introduced via localized photothermal inclusions are shown to drive buckling into many complex 3D shapes. Furthermore, we established an analytical model based on the non-Euclidean plate theory to encode smoothly-varying stretch profiles to rationally approach the design of targeted shapes. We anticipate that this fabrication method is generalizable to a variety of chemistries that are incompatible with methods to spatially pattern in-plane director fields, opening up new opportunities for shape morphing in a variety of liquid crystalline polymer materials. Our analysis provides an analytical tool for the design of shape morphing of LCE thin sheets.

Chapter 7 Conclusion and Outlook

7.1 Conclusion

In this dissertation, we have studied buckling instabilities of columns and thin films, and harnessed these buckling instabilities to design pneumatically actuated pattern-transforming metamaterials, design reusable energy-absorbing architected materials, and achieve complex 3D morphing of LCE thin films. The main results of each chapter are summarized as follows:

In Chapter 2, we propose a class of pneumatically actuated pattern-transforming metamaterials. We reveal the mechanism of its pattern transformation and investigate the geometric effects on the pattern transformation numerically, analytically, and experimentally. We find that the critical pressure for the onset of the pattern transformation is governed by the slenderest wall thickness of the metamaterial, and that the transformation strain is controlled by the pattern of the holes. Our analytical model reveals the mechanics of the pattern transformation and shows good agreement with the finite element analysis. The experimental results confirm our theoretical predictions. This study provides design guidelines for the metamaterial and facilitates its real-world applications in soft actuators.

In Chapter 3, we numerically discover a new buckling mode for straight columns with high width-to-length ratios under axial compression: snapping-back buckling mode. To understand the mechanism of snapping-back buckling, we have established an analytical discrete model, and unraveled that snapping-back buckling results from strong coupling between stretching and bending, similar to that of snapping-back buckling in shells. A phase diagram is constructed to demarcate the different buckling modes of axially compressed columns.

In Chapter 4, we analytically show that for a straight hyperelastic column, the increase of its width-to-length ratio can fundamentally alter its buckling mode, from continuous to snapping-through, and to snapping-back. Correspondingly, the initial post-buckling slope flips its sign from positive to negative, and eventually back to positive. By applying a continuum mechanics-based asymptotic analysis, we determine the initial post-buckling slope as a function of the width-to-length ratio, and then identify the critical width-to-length ratios for the transitions of the buckling modes, which perfectly match the FEA results. Furthermore, we find that as the shear-to-bulk modulus ratio, which represents the material compressibility, increases, the transition between snapping-through and snapping-back buckling is postponed to a higher critical width-to-length ratio. A phase diagram of the buckling modes with respect to the width-to-length ratio and shear-to-bulk modulus ratio is constructed. The framework proposed in this chapter can be applied to other constitutive laws to study the effect of different material nonlinearities on post-buckling behavior.

In Chapter 5, we develop a reusable energy-absorbing architected material harnessing the snapping-back buckling of wide hyperelastic columns. The quasi-static cyclic loading tests confirm that the proposed material is capable of dissipating energy while keeping the force nearly constant with a long working distance in a reusable, self-recoverable, and highly predictable manner, while the drop tests at high strain rates show the feature of rate-independency and the capability of force attenuation in a broad range of input energy. Moreover, we have demonstrated that the mechanical responses of the proposed energy-absorbing material can be widely tuned by the geometry and preloads. Compared to a multi-layered material harnessing the snapping-through buckling, ours harnessing the snapping-back buckling has higher maximum dissipation energy,

and requires much less layers to achieve the maximum dissipation energy, which can dramatically reduce the volume and mass of the material for the same energy-absorbing performance.

In Chapter 6, we demonstrate a method combining experiments, FEM simulations, and analytical modeling to program photoactive shape morphing from monodomain LCE sheets with a unidirectional director by spatially controlling photothermal heat generation. Discontinuous metrics introduced via localized photothermal inclusions are shown to drive buckling into many complex 3D shapes. Furthermore, we established an analytical model based on the non-Euclidean plate theory to encode smoothly-varying stretch profiles to rationally approach the design of targeted shapes. Our analysis opens up new opportunities for shape morphing in a variety of liquid crystalline polymer materials.

7.2 Outlook

There are still many exciting opportunities of finding new types of buckling instabilities and exploiting these buckling instabilities for function. Below are several possible extensions of the current work that may lead to novel functional materials.

First, the design of pattern-transforming metamaterials could be extended from periodic to aperiodic structures, from perfect structures to structures with defects, which may result in complex pattern transformations like patterns with multiple domains. The rapid development in additive manufacturing allows us to fabricate amazingly intricate and precisely defined structures. How to achieve rational design of aperiodic structures or structures with purposely introduced defects is still an open question. We believe complexity in structures would open the door to more programmable pattern-transforming metamaterials.

Second, we can embed additional timescales into our pattern-transforming metamaterials, leading to time-dependent pattern transformations. For example, the air flow can be replaced by other flows with high viscosity. The interplay between buckling instabilities and viscous timescales may cause novel buckling modes related to loading rates, and spatial-temporal pattern transformations, potentially leading to functionalities such as logic gates or information storage and retrieval.

Third, we have thoroughly studied the buckling behavior of columns made of a single hyperelastic material. More complex but controllable buckling behaviors could be obtained if we incorporate multiple materials with different properties into one column. For example, multi-layered columns can potentially exhibit programmable wavelength and post-buckling behaviors by tuning the layer numbers and modulus ratios among different layers. Embedding stimuli-responsive particles such as magnetic particles into parts of the columns can lead to buckling behaviors controlled by external stimuli. Those columns with peculiar but well-controlled buckling behaviors could be used as building blocks to design architected structures with advanced functionalities.

Fourth, our current shape morphing in LCE thin sheets can be programmed to deform into a target geometry under activation, but the actuation paths are not considered. To achieve more complex 3D shapes without self-collisions, it is essential to program spatially-temporal shape morphing into the LCE flat thin sheets. How to encode different timescales into the sheet and how to achieve an inverse design for a targeted 3D shapes with prescribed shape evolution-time relation are still challenging.

Appendix 1 Supplementary Materials for Pneumatically Actuated Pattern-transforming Metamaterials

A1.1 Verification of the Simplified Structures

Here we conduct finite element simulations to verify if the simplified structures shown in Figure 2.5b exhibit the similar pattern transformation and strain-pressure curves as their corresponding metamaterials. We convert the three metamaterials in Figure 2.3 into their simplified structures with the geometric parameters determined by Eqs. (2.2)-(2.5). We simulate the pattern transformation of the three simplified structures under the same pressure load and boundary conditions as shown in Figure 2.2b. We model both the deformable beams and rigid rectangles as linear elastic solids, and assign the modulus of the rigid rectangles five order of magnitudes higher than that of the deformable beams so that the deformation in the rigid rectangles is negligible. Eight-node, quadratic, hybrid, plane strain elements (ABAQUS element type CPE8H) are used for the simulation. The results shown in Appendix Figure 1.1 agree very well with those in Figure 2.3 on the critical pressure and the transformation strains.

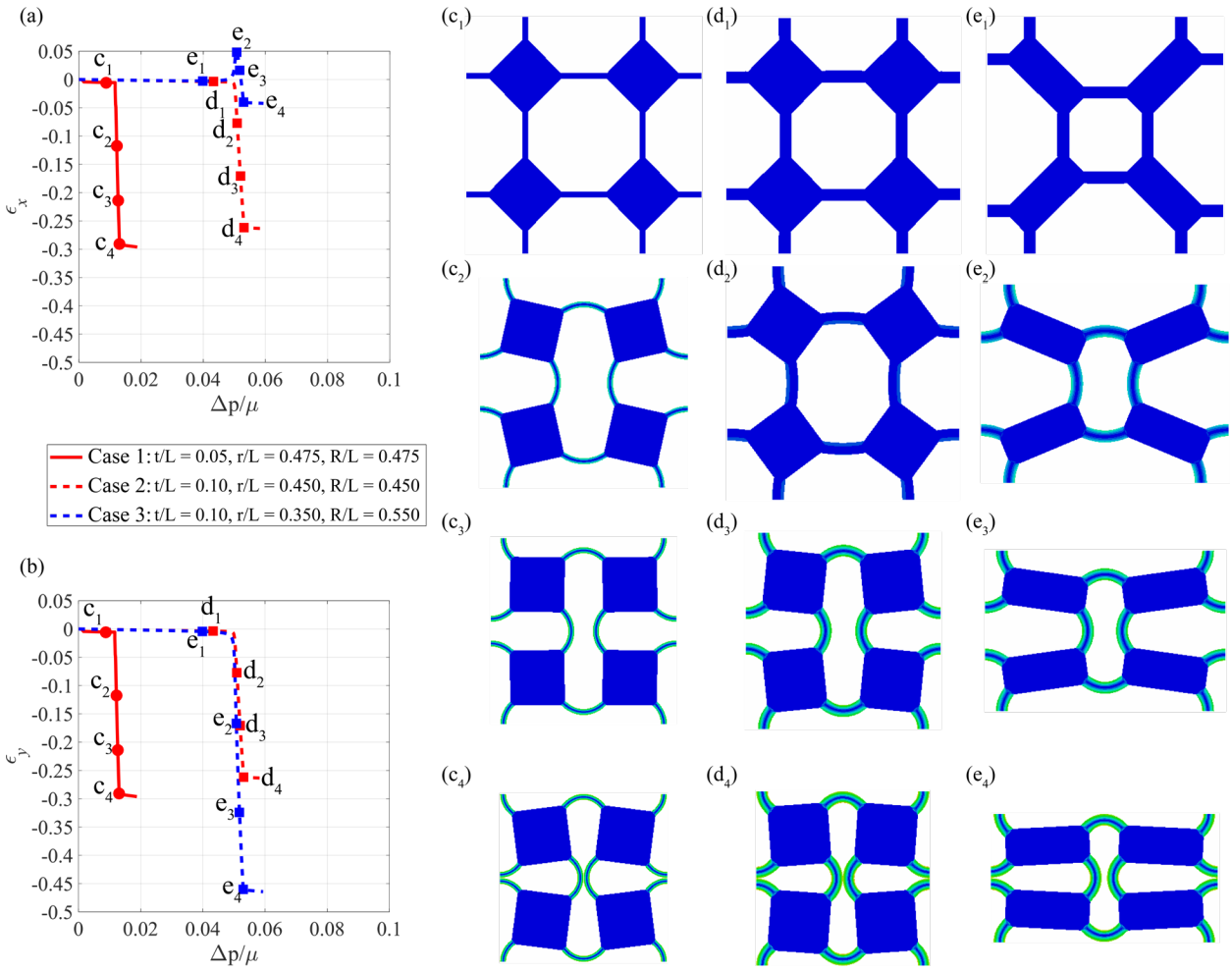

Appendix Figure 1.1 The results of finite element simulations to verifying the simplified structures. The dependence of the strains in the (a) *x* and (b) *y* directions on the pressure. (c) - (e) The deformed shapes of four unit cells of the three metamaterials: (c) uniformly large holes ($r/L = R/L = 0.475$, $t/L = 0.05$), (d) uniformly small holes ($r/L = R/L = 0.450$, $t/L = 0.10$), and (e) alternatingly large and small holes ($r/L = 0.350$, $R/L = 0.550$, $t/L = 0.10$). For each case, the states of deformation correspond to the four selected points on its strain-pressure curves.

A1.2 Buckling and Post-buckling Analysis of the Equivalent Beam Structure

Here we briefly derive the buckling condition and the post-buckling process of a beam fixed to two rigid bars under an axial load (Figure 2.6a), according to Euler's elastica and the

theory of elastic stability [118]. Consider the beam to be inextensible and linearly elastic. The lengths of the beam and each rigid bar are respectively $l_s = 2h$ and $l_r = (L - l_s)/2$. The whole structure is simply supported at the two ends and axially compressed by a force N under the plane strain condition. When the force is large enough, the beam will buckle and deflect from its straight position. The potential energy of this system is given by

$$P[v;N] = \int_0^{l_s} \frac{1}{2} K \varphi'^2 dx - N\Delta L = \int_0^{l_s} \frac{1}{2} K \frac{v''^2}{1-v'^2} dx - N\Delta L, \tag{A1.1}$$

where v denotes the deflection of the beam, φ denotes the bending angle, φ' denotes the curvature of the beam, ΔL denotes the length change of the whole structure in the vertical direction, and $K = Ew^3/[12(1-\tilde{\nu}^2)]$ is the bending stiffness of the beam under the plain strain condition with E the Young's modulus and $\tilde{\nu}$ the Poisson's ratio. The coordinate x is chosen to be along the tangential direction of the beam (Figure 2.6a), and $v'=dv/dx$ and $v''=d^2v/dx^2$ are the first and second derivatives of v with respect to x. The length change of the whole structure in the vertical direction ΔL involves the contributions from the beam and the rigid bars, which yields

$$\Delta L = \int_0^{l_s} \left(1 - \sqrt{1-v'^2}\right) dx + l_r \left(1 - \sqrt{1-v'(0)^2}\right) + l_r \left(1 - \sqrt{1-v'(l_s)^2}\right). \tag{A1.2}$$

Taylor expanding Eq. (A1.1) and neglecting the higher-order terms, we may rewrite the equation as

$$P[v;N] = P_2[v;N] + P_3[v;N] + P_4[v;N], \tag{A1.3}$$

where

$$P_2[v;N] = \int_0^{l_s} \left(\frac{1}{2} K v''^2 - \frac{1}{2} N v'^2\right) dx - \frac{1}{2} N l_r v'(0)^2 - \frac{1}{2} N l_r v'(l_s)^2, \tag{A1.4a}$$

$$P_3[v;N] = 0, \tag{A1.4b}$$

$$P_4[v;N] = \int_0^{l_s}\left(\frac{1}{2}Kv''^2v'^2 - \frac{1}{8}Nv'^4\right)dx - \frac{1}{8}Nl_rv'(0)^4 - \frac{1}{8}Nl_rv'(l_s)^4, \tag{A1.4c}$$

are the second, third and fourth order terms, respectively.

To establish the governing equations of buckling behavior, the total potential energy P [v; N] must be minimized under the given boundary conditions. It is usually sufficient to minimize only P_2 [v; N]. Computing the first variation of P_2 [v; N] and setting $\delta P_2 = 0$ yields

$$\delta P_2 = 0 = \int_0^{l_s}(Kv''\delta v'' - Nv'\delta v')dx - Nl_r\big(v'(0)\delta v'(0) + v'(l_s)\delta v'(l_s)\big). \tag{A1.5}$$

Integration by parts yields

$$\int_0^{l_s}\big(Kv^{(iv)} + Nv''\big)\delta v dx + Kv''\delta v'\Big|_0^{l_s} - (Kv''' + Nv')\delta v\Big|_0^{l_s} - Nl_r\big(v'(0)\delta v'(0) + v'(l_s)\delta v'(l_s)\big) = 0, \tag{A1.6}$$

from the first term of which we get the Euler-Lagrange equation

$$Kv^{(iv)} + Nv'' = 0. \tag{A1.7}$$

Inserting the kinematic boundary conditions, which correspond to the equal bending angles of the beam and the rigid bars at the fixed boundaries (Appendix Figure 1.2)

$$\begin{cases} \dfrac{v(0)}{l_r} = v'(0), \\ \dfrac{v(l_s)}{l_r} = -v'(l_s), \end{cases} \tag{A1.8}$$

into the boundary terms in Eq. (A1.6), we can further obtain the static boundary conditions

$$\begin{cases} Kv''(0) = Kv'''(0)l_r, \\ Kv''(l_s) + Kv'''(l_s)l_r = 0. \end{cases} \tag{A1.9}$$

These static boundary conditions correspond to the moment balance about the two pinned joints at the end of the structure (Appendix Figure 1.2a, c-d),

$$\begin{cases} M(0) - V(0)l_r\cos[\varphi(0)] - Nv(0) = 0, \\ -M(l_s) - V(l_s)l_r\cos[\varphi(0)] + Nv(l_s) = 0, \end{cases} \tag{A1.10}$$

where M and V are the bending moment and shear force, respectively. Using the relation between M and V obtained by the moment equilibrium of an infinitesimal segment (Appendix Figure 1.2c):

$$M' - Nv' = V\cos\varphi, \tag{A1.11}$$

and the relation between the moment and curvature $M = -Kv''/\sqrt{1-v'^2}$, Eq. S10 can recover Eq. (A1.9) with the terms higher than the second order neglected.

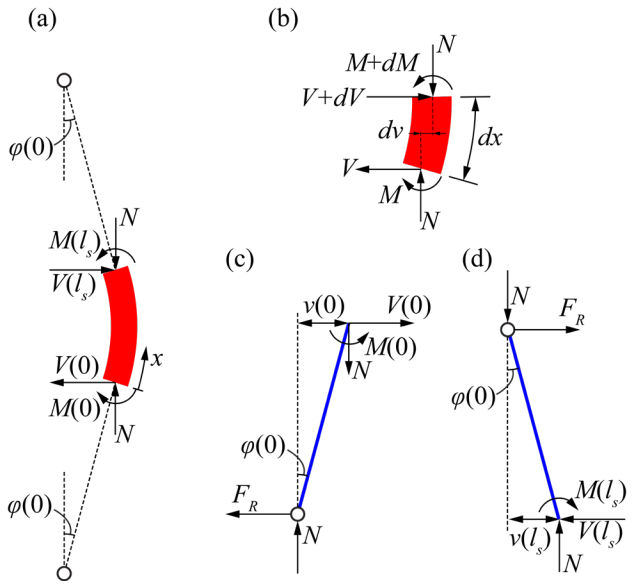

Appendix Figure 1.2 Free body diagrams of (a) the beam, (b) an infinitesimal segment of the beam, and (c, d) the two rigid bars.

The general solution to Eq. (A1.7) is

$$v(x) = A\sin kx + B\cos kx + Cx + D, \tag{A1.12}$$

in which A, B, C, and D are arbitrary constants and k^2 equals N/K. Plug the general solution, Eq. (A1.12), into the boundary conditions, Eqs. (A1.8) and (A1.9), and we get

$$\begin{cases} kl_r A - B + l_r C - D = 0, \\ (\sin kl_s + kl_r \cos kl_s)A + (\cos kl_s - kl_r \sin kl_s)B + (l_s + l_r)C + D = 0, \\ kl_r A - B = 0, \\ (\sin kl_s + kl_r \cos kl_s)A + (\cos kl_s - kl_r \sin kl_s)B = 0. \end{cases} \tag{A1.13}$$

This algebraic equation system can be rewritten as $\mathbf{M}[A \quad B \quad C \quad D]^{\mathrm{T}} = 0$. The constants A, B, C, and D have nonzero solutions only when the determinant of the coefficient matrix $\mathbf{M}$ vanishes, $\det(\mathbf{M}) = 0$, which yields

$$2kl_r \cos kl_s = (k^2 l_r^2 - 1)\sin kl_s. \tag{A1.14}$$

Eq. (A1.14) can be numerically solved, and the smallest positive root k_{cr} corresponds to the smallest critical load $N_{cr} = k_{cr}^2 K$. Note that the critical force N_{cr} recovers that of a simply supported beam when l_r=0. A non-zero l_r can significantly reduce the critical buckling force of this equivalent structure of a beam fixed to two rigid bars. The deflections of the buckled beam can be obtained by eliminating B, C and D in Eq. (A1.12), which yields

$$v(x) = a\sin(k_{cr}x + \gamma), \tag{A1.15}$$

where $a = A\sqrt{k_{cr}^2 l_r^2 + 1}$ is the amplitude of the first buckling mode, and $\tan\gamma = k_{cr} l_r$.

Next, let us consider the post-buckling behavior of the beam when the load N slightly exceeds the critical load N_{cr}. We expand the potential energy P [v; N] in Eq. (A1.1) with respect to the load N near $N = N_{cr}$,

$$P[v;N] = P_2[v;N_{cr}] + (N - N_{cr})\dot{P}_2[v;N_{cr}] + P_4[v;N_{cr}], \tag{A1.16}$$

where $\dot{(\,)} = \partial/\partial N$ and the terms higher than the fourth order have been neglected. The first term on the right-hand side of Eq. (A1.16) vanishes due to the equilibrium, and the potential energy now becomes

$$P[v;N] = (N - N_{cr})\dot{P}_2[v;N_{cr}] + P_4[v;N_{cr}]. \tag{A1.17}$$

Using Eqs. (A1.15) and (A1.4), we can express $\dot{P}_2[v;N_{cr}]$ and $P_4[v;N_{cr}]$ as

$$\dot{P}_2[a;N_{cr}] = -\frac{a^2k_{cr}^2[l_s(1+k_{cr}^2l_r^2)+2l_r]}{4(1+k_{cr}^2l_r^2)}, \tag{A1.18a}$$

$$P_4[a;N_{cr}] = a^4k_{cr}^4N_{cr}\frac{l_s(1+k_{cr}^2l_r^2)^2+2l_r(1-k_{cr}^2l_r^2)}{64(1+k_{cr}^2l_r^2)^2}. \tag{A1.18b}$$

The amplitude of the first buckling mode a can be achieved by minimizing the potential energy with respect to a, $\partial P/\partial a = 0$,

$$a = \frac{1}{2k_{cr}}\sqrt{\frac{N-N_{cr}}{N_{cr}}\frac{32l_s(1+k_{cr}^2l_r^2)^2+64l_r(1+k_{cr}^2l_r^2)}{l_s(1+k_{cr}^2l_r^2)^2+2l_r(1-k_{cr}^2l_r^2)}}. \tag{A1.19}$$

The axial displacement of the beam Δl_s can be calculated as

$$\Delta l_s = \int_0^{l_s}\left(1-\sqrt{1-v'^2}\right)dx \approx \int_0^{l_s}\frac{1}{2}v'^2dx = \frac{a^2k_{cr}^2(l_s+k_{cr}^2l_r^2l_s-2l_r)}{4(1+k_{cr}^2l_r^2)}. \tag{A1.20}$$

The bending angle $\varphi(x)$ can be calculated as

$$\varphi(x) = \sin^{-1}(v'(x)) = \sin^{-1}(ak_{cr}\cos(k_{cr}x+\gamma)). \tag{A1.21}$$

A1.3 Comparing Results from the Finite Element Simulations, Analytical Model and Experiments

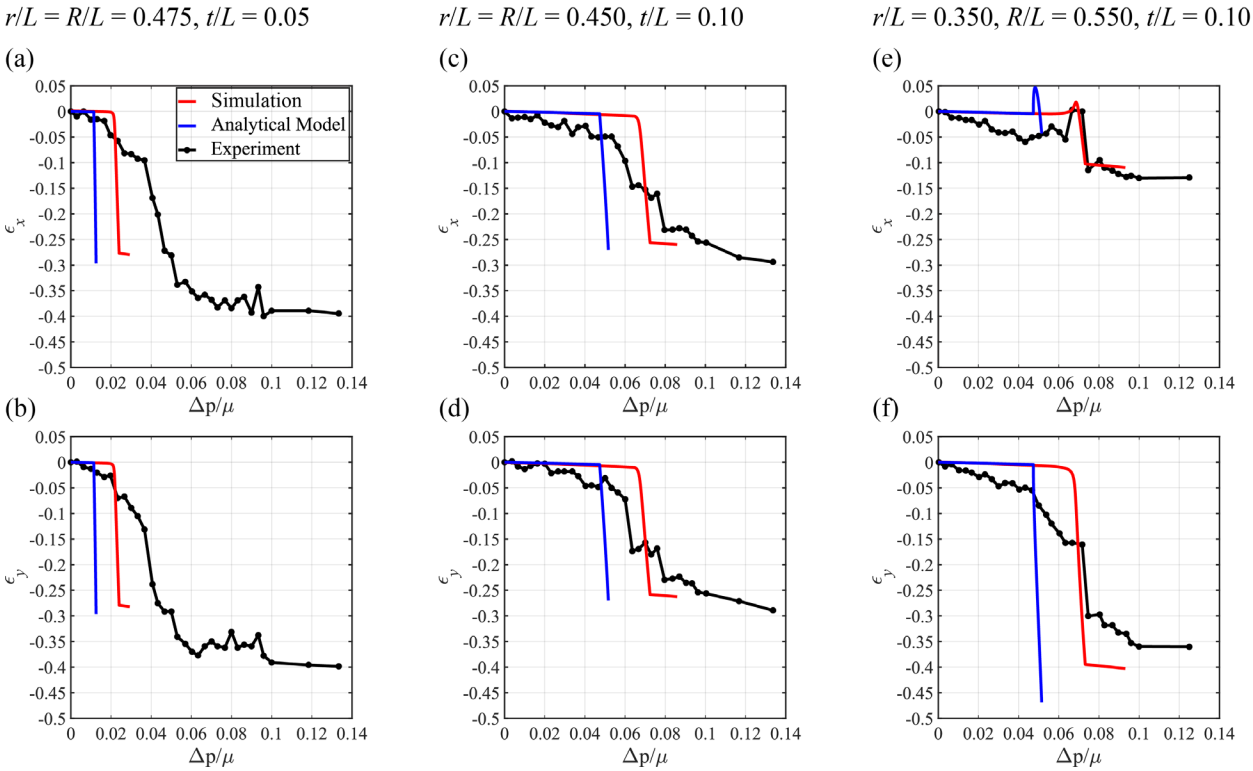

Appendix Figure 1.3 The dependence of the strains in the (a, c, e) *x* and (b, d, f) *y* directions on the pressure for three metamaterials with different geometric parameters: (a, b) uniformly large holes ($r/L = R/L = 0.475$, $t/L = 0.05$), (c, d) uniformly small holes ($r/L = R/L = 0.450$, $t/L = 0.10$), and (e, f) alternatingly large and small holes ($r/L = 0.350$, $R/L = 0.550$, $t/L = 0.10$). The results from the finite element simulations (red), analytical model (blue), and experiments (black) reveal the same effect of the geometric parameters on the pattern transformation of metamaterials.

A1.4 Videos

Appendix Video 1.1 Snapshots of the pattern transformation, and the corresponding strain-pressure curves in the *x* and *y* directions predicted by our analytical model for a metamaterial with the

geometric parameters t/L=0.05, and $r/L = R/L$ = 0.475 (same as Fig. 7c). In the left panel, the red dashed frames represent the initial boundaries of the lattice and the black dashed frames represent the current boundaries of the lattice. In the middle and the right panels, the red dots on the two curves depict the instantaneous values of the transformation strain and pressure that correspond to the deformed shape in the left panel.

Appendix Video 1.2 Snapshots of the pattern transformation, and the corresponding strain-pressure curves in the x and y directions predicted by our analytical model for a metamaterial with the geometric parameters t/L=0.10, and $r/L = R/L$ = 0.450 (same as Fig. 7d).

Appendix Video 1.3 Snapshots of the pattern transformation, and the corresponding strain-pressure curves in the x and y directions predicted by our analytical model for a metamaterial with the geometric parameters t/L=0.10, r/L = 0.350, and R/L = 0.550 (same as Fig. 7e).

Appendix 2 Supplementary Materials for Snapping-back Buckling of Wide hyperelastic Columns

A2.1 Finite Element Simulations

We used the commercial software Abaqus/Standard for our static finite element simulations. We modeled columns as an incompressible neo-Hookean material in plane strain conditions with hybrid quadratic rectangular elements (Abaqus type CPE8H). Defects with very small sizes were introduced to trigger buckling and creasing instabilities (Figure 3.1B). In all cases except $w/L = 0.24$, the size of the imperfection for buckling is $\Delta d/w = 0.001$, and the size of the imperfection for creasing is $r/w = 0.002$. Since the case with $w/L = 0.24$ approaches the boundary between negative and positive post-buckling slopes, a finer Δd is needed, which is $\Delta d/w = 0.0002$, an order of magnitude smaller than that in other cases. We performed a mesh refinement study to ensure the mesh size is at least one order of magnitude smaller than the dimension of the finest part of the samples. As a result, approximately from $6\text{x}10^4$ to $4\text{x}10^5$ rectangular elements are involved in each finite element model, depending on the width-to-length ratio of columns.

A2.2 Analytical Solution for the Onset Strains of Buckling and Barreling in Hyperelastic Columns

Consider an incompressible hyperelastic column of width w, length L and infinite in depth. This column is compressed by a load F between two flat frictionless plates (Appendix Figure 2.1A). Once the critical condition is reached, the column can exhibit either buckling (Appendix Figure 2.1B) or barreling (Appendix Figure 2.1C) instability [140]. In this section, we will derive the critical strain $\varepsilon_{cr} = |\Delta l_{cr}/L|$ for column buckling and barreling. We find for an incompressible neo-

Hookean column with an arbitrary width-to-length ratio *w/L*, buckling always occurs prior to barreling, because ε_{cr} for buckling is always lower than that for barreling.

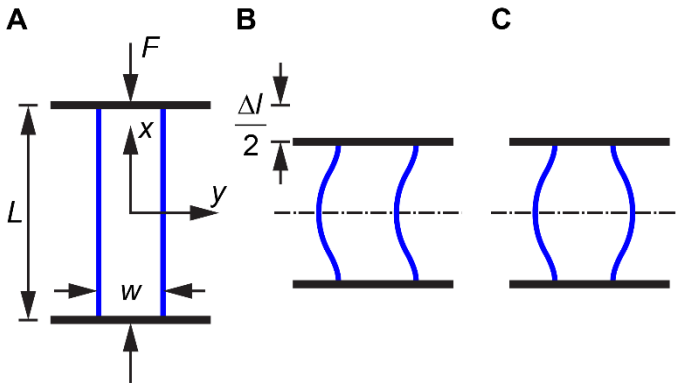

Appendix Figure 2.1 Schematic of a hyperelastic column forming buckling or barreling instability under an axial compression. (**A**) A hyperelastic column (in blue) of width *w*, length *L*, and infinite in depth is compressed by a load *F* between two flat smooth plates (in black). Schematics of the buckling (**B**) and barreling (**C**) modes.

Since both buckling and barreling are symmetric about the *y* axis (Appendix Figure 2.1), it is equivalent to only analyzing half of the column with symmetric boundary conditions. The deformation gradient tensor **F**, with the stress-free state as the reference configuration under the *x*-*y* coordinate, can be written as

$$\mathbf{F} = \begin{bmatrix} 1+u_{,x} & u_{,y} \\ v_{,x} & 1+v_{,y} \end{bmatrix}, \tag{A2.1}$$

where *u* and *v* are displacement fields in the *x* and *y* direction, and $(\ )_{,i} = \partial(\ )/\partial i$, $i = x, y$. By setting $|\mathbf{F}| = 1$ (| | denotes the determinant of a matrix), we can derive the incompressibility condition as

$$u_{,x} + v_{,y} + u_{,x}v_{,y} - u_{,y}v_{,x} = 0\,. \tag{A2.2}$$

The isotropic hyperelastic material models we adopt is incompressible neo-Hookean solid that has the following elastic energy density function in the plane strain condition:

$$W = \frac{\mu}{2}\left[tr\left(\mathbf{F}^{\mathrm{T}}\mathbf{F}\right) - 2\right], \tag{A2.3}$$

where μ is the shear modulus. The total potential energy of the top half of the column is given by

$$\phi = \int_0^{L/2}\int_{-w/2}^{w/2} W dy dx - F\int_0^{L/2} u_{,x} dx + \int_0^{L/2}\int_{-w/2}^{w/2} p\left(u_{,x} + v_{,y} + u_{,x}v_{,y} - u_{,y}v_{,x}\right) dy dx\,, \tag{A2.4}$$

where p is a Lagrangian multiplier and the load F can be further expressed as the integral of the first Piola-Kirchhoff stress S_{xx} through the top surface:

$$F = \int_{-w/2}^{w/2} S_{xx}\big|_{x=L/2}\, dy = \int_{-w/2}^{w/2} \left.\frac{\partial W}{\partial \mathrm{F}_{11}}\right|_{x=L/2} dy\,. \tag{A2.5}$$

With Eqs. (A2.1)-(A2.5), we rewrite the total potential energy

$$\phi = \int_0^{L/2}\int_{-w/2}^{w/2}\left[\frac{\mu}{2}\left(u_{,x}^2 + u_{,y}^2 + v_{,x}^2 + v_{,y}^2 + 2u_{,x} + 2v_{,y}\right) - S_{xx}\big|_{x=L/2}\, u_{,x} + p\left(u_{,x} + v_{,y} + u_{,x}v_{,y} - u_{,y}v_{,x}\right)\right] dy dx\,. \tag{A2.6}$$

Successive Frechet differentiation [139] of Eq. (A2.6) with respect to $V = \left[u, v, p\right]^{\mathrm{T}}$ gives

$$\phi' V_1 = \int_0^{L/2}\int_{-w/2}^{w/2}\begin{bmatrix} \mu\left(u_{,x}u_{1,x} + u_{,y}u_{1,y} + v_{,x}v_{1,x} + v_{,y}v_{1,y} + u_{1,x} + v_{1,y}\right) - S_{xx}\big|_{x=L/2}\, u_{1,x} + \\ p_1\left(u_{,x} + v_{,y} + u_{,x}v_{,y} - u_{,y}v_{,x}\right) + \\ p\left(u_{1,x} + v_{1,y} + v_{,y}u_{1,x} + u_{,x}v_{1,y} - v_{,x}u_{1,y} - u_{,y}v_{1,x}\right) \end{bmatrix} dy dx\,, \tag{A2.7}$$

$$\phi'' V_1 V_2 = \int_0^{L/2}\int_{-w/2}^{w/2}\begin{bmatrix} \mu\left(u_{1,x}u_{2,x} + u_{1,y}u_{2,y} + v_{1,x}v_{2,x} + v_{1,y}v_{2,y}\right) + \\ p_1\left(u_{2,x} + v_{2,y} + v_{,y}u_{2,x} + u_{,x}v_{2,y} - v_{,x}u_{2,y} - u_{,y}v_{2,x}\right) + \\ p_2\left(u_{1,x} + v_{1,y} + v_{,y}u_{1,x} + u_{,x}v_{1,y} - v_{,x}u_{1,y} - u_{,y}v_{1,x}\right) + \\ p\left(u_{1,x}v_{2,y} + v_{1,y}u_{2,x} - u_{1,y}v_{2,x} - v_{1,x}u_{2,y}\right) \end{bmatrix} dy dx\,. \tag{A2.8}$$

where $V_i = \left[u_i, v_i, p_i\right]^{\mathrm{T}}$ (i = 1, 2) denote the admissible vector field corresponding to the i-th order Frechet derivative of the total potential energy ϕ. The equilibrium vector field of V can be determined by extremizing the total potential energy given in Eq. (A2.6), which requires

$$\phi'\left[V(\varepsilon);\varepsilon\right]\delta V = 0\,. \tag{A2.9}$$

where ε is the absolute value of the shortening Δl in the x direction divided by the original length of the column L, i.e. $\varepsilon = \left|\Delta l/L\right|$. The fundamental solution V_0 to Eq. (A2.9), which corresponds to a uniform deformation, is given by

$$V_0 = \begin{bmatrix} u_0 \\ v_0 \\ p_0/\mu \end{bmatrix} = \begin{bmatrix} -\varepsilon x \\ \varepsilon y/(1-\varepsilon) \\ -1/(1-\varepsilon)^2 \end{bmatrix}. \tag{A2.10}$$

The buckling mode V_1 and its corresponding buckling condition ε_{cr} is given by

$$\phi''\left[V_0(\varepsilon_{cr});\varepsilon_{cr}\right]V_1\delta V = 0\,, \tag{A2.11}$$

which yields the following differential equations for V_1:

$$\begin{aligned} u_{1,xx} + u_{1,yy} + p_{1,x}/\left[\mu(1-\varepsilon_{cr})\right] &= 0 \\ v_{1,xx} + v_{1,yy} + (1-\varepsilon_{cr})\,p_{1,y}/\mu &= 0\,, \\ u_{1,x}/(1-\varepsilon_{cr}) + (1-\varepsilon_{cr})\,v_{1,y} &= 0 \end{aligned} \tag{A2.12}$$

with the boundary conditions

$$u_{1,y} + v_{1,x}/(1-\varepsilon_{cr})^2 = 0 \qquad \text{at } y = \pm w/2\,, \tag{A2.13}$$

$$v_{1,y} - u_{1,x}/(1-\varepsilon_{cr})^2 + (1-\varepsilon_{cr})\,p_1/\mu = 0 \qquad \text{at } y = \pm w/2\,, \tag{A2.14}$$

$$v_{1,x} + u_{1,y}/(1-\varepsilon_{cr})^2 = 0 \qquad \text{at } x = 0 \text{ and } x = L/2\,, \tag{A2.15}$$

$$u_{1,y} = 0 \qquad \text{at } x = 0 \text{ and } x = L/2 \,. \tag{A2.16}$$

where Eqs. (A2.13)-(A2.15) are natural boundary conditions, while Eq. (A2.16) is an essential boundary condition. The admissible displacement fields also need satisfy the following boundary conditions that eliminates the rigid body translations along the x and y directions

$$u_1\left(x = 0, y = 0\right) = 0,\ v_1\left(x = L/4, y = 0\right) = 0 \,. \tag{A2.17}$$

Here we restrict ourselves to the lowest critical condition and try the following solution

$$u_1\left(x, y\right) = A_u\left(y\right)\sin\frac{2\pi x}{L}, \tag{A2.18}$$

$$u_1\left(x, y\right) = A_u\left(y\right)\sin\frac{2\pi x}{L}, \tag{A2.19}$$

$$p_1\left(x, y\right) = A_p\left(y\right)\cos\frac{2\pi x}{L} \,. \tag{A2.20}$$

Substitution of these expressions into Eq. (A2.12) yields

$$\begin{aligned} A_u'' - \left(\frac{2\pi}{L}\right)^2 A_u - \frac{2\pi}{\mu L\left(1-\varepsilon_{cr}\right)} A_p &= 0 \\ A_v'' - \left(\frac{2\pi}{L}\right)^2 A_v + \frac{1-\varepsilon_{cr}}{\mu} A_p' &= 0 \,. \\ \frac{2\pi}{L\left(1-\varepsilon_{cr}\right)} A_u + \left(1-\varepsilon_{cr}\right) A_v' &= 0 \end{aligned} \tag{A2.21}$$

where $()' = d() / dy$. These three homogeneous ordinary differential equations can be solved by substituting

$$A_u\left(y\right) = \alpha e^{\rho y},\ A_v\left(y\right) = \beta e^{\rho y},\ A_p\left(y\right) = \gamma e^{\rho y} \tag{A2.22}$$

into Eq. (A2.21), which yields

$$\begin{bmatrix} \rho^2-\left(\frac{2\pi}{L}\right)^2 & 0 & -\frac{2\pi}{\mu L\left(1-\varepsilon_{cr}\right)} \\ 0 & \rho^2-\left(\frac{2\pi}{L}\right)^2 & \frac{\rho\left(1-\varepsilon_{cr}\right)}{\mu} \\ \frac{2\pi}{L\left(1-\varepsilon_{cr}\right)} & \rho\left(1-\varepsilon_{cr}\right) & 0 \end{bmatrix}\begin{bmatrix}\alpha\\ \beta\\ \gamma\end{bmatrix}=0. \tag{A2.23}$$

The nontrivial solution can be obtained if the determinant of the coefficient matrix vanishes, which yields

$$\left[\rho^2-\left(\frac{2\pi}{L}\right)^2\right]\left[\frac{1}{\left(1-\varepsilon_{cr}\right)^2}\left(\frac{2\pi}{L}\right)^2-\rho^2\left(1-\varepsilon_{cr}\right)^2\right]=0. \tag{A2.24}$$

The roots are thus

$$\rho_{1,2}=\pm\frac{2\pi}{L},\ \rho_{3,4}=\pm\frac{1}{\left(1-\varepsilon_{cr}\right)^2}\frac{2\pi}{L}. \tag{A2.25}$$

Thus, the solutions to Eq. (A2.21) can be expressed as the following hyperbolic functions

$$A_u=\alpha_1\sinh\left(\frac{2\pi}{L}y\right)+\alpha_2\sinh\left[\frac{1}{\left(1-\varepsilon_{cr}\right)^2}\frac{2\pi}{L}y\right]+\alpha_3\cosh\left(\frac{2\pi}{L}y\right)+\alpha_4\cosh\left[\frac{1}{\left(1-\varepsilon_{cr}\right)^2}\frac{2\pi}{L}y\right], \tag{A2.26}$$

$$A_v=\beta_1\sinh\left(\frac{2\pi}{L}y\right)+\beta_2\sinh\left[\frac{1}{\left(1-\varepsilon_{cr}\right)^2}\frac{2\pi}{L}y\right]+\beta_3\cosh\left(\frac{2\pi}{L}y\right)+\beta_4\cosh\left[\frac{1}{\left(1-\varepsilon_{cr}\right)^2}\frac{2\pi}{L}y\right], \tag{A2.27}$$

$$A_p=\gamma_1\sinh\left(\frac{2\pi}{L}y\right)+\gamma_2\sinh\left[\frac{1}{\left(1-\varepsilon_{cr}\right)^2}\frac{2\pi}{L}y\right]+\gamma_3\cosh\left(\frac{2\pi}{L}y\right)+\gamma_4\cosh\left[\frac{1}{\left(1-\varepsilon_{cr}\right)^2}\frac{2\pi}{L}y\right]. \tag{A2.28}$$

Substituting Eqs. (A2.26)-(A2.28) into Eq. (A2.21), we can express β_1, β_2, β_3, β_4, γ_1, γ_2, γ_3, γ_4 as functions of α_1, α_2, α_3 and α_4

$$\beta_1 = -\frac{1}{\left(1-\varepsilon_{cr}\right)^2}\alpha_3,\ \beta_2 = -\alpha_4,\ \beta_3 = -\frac{1}{\left(1-\varepsilon_{cr}\right)^2}\alpha_1,\ \beta_4 = -\alpha_2,$$
$$\gamma_1 = 0,\ \gamma_2 = \frac{2\pi\mu}{L}\left[\frac{1}{\left(1-\varepsilon_{cr}\right)^3} - \left(1-\varepsilon_{cr}\right)\right]\alpha_2,\ \gamma_3 = 0,\ \gamma_4 = \frac{2\pi\mu}{L}\left[\frac{1}{\left(1-\varepsilon_{cr}\right)^3} - \left(1-\varepsilon_{cr}\right)\right]\alpha_4 \quad \text{(A2.29)}$$

Further substituting Eqs. (A2.18)-(A2.20) and Eqs. (A2.26)-(A2.29) into the boundary conditions shown in Eqs. (A2.13)-(A2.14) (the boundary condition Eq. (A2.15) is satisfied automatically), we have

$$\begin{bmatrix} \mathbf{A}_{12} & \mathbf{0} \\ \mathbf{0} & \mathbf{A}_{34} \end{bmatrix} \begin{bmatrix} \alpha_1 \\ \alpha_2 \\ \alpha_3 \\ \alpha_4 \end{bmatrix} = 0, \quad \text{(A2.30)}$$

where $\mathbf{A}_{12}$ and $\mathbf{A}_{34}$ are both 2-by-2 matrices

$$\mathbf{A}_{12} = \begin{bmatrix} \left[1+\frac{1}{\left(1-\varepsilon_{cr}\right)^4}\right]\cosh\left(\frac{\pi w}{L}\right) & \frac{2}{\left(1-\varepsilon_{cr}\right)^2}\cosh\left[\frac{1}{\left(1-\varepsilon_{cr}\right)^2}\frac{\pi w}{L}\right] \\ \frac{2}{\left(1-\varepsilon_{cr}\right)^2}\sinh\left(\frac{\pi w}{L}\right) & \left[\left(1-\varepsilon_{cr}\right)^2+\frac{1}{\left(1-\varepsilon_{cr}\right)^2}\right]\sinh\left[\frac{1}{\left(1-\varepsilon_{cr}\right)^2}\frac{\pi w}{L}\right] \end{bmatrix}, \quad \text{(A2.31)}$$

$$\mathbf{A}_{34} = \begin{bmatrix} \left[1+\frac{1}{\left(1-\varepsilon_{cr}\right)^4}\right]\sinh\left(\frac{\pi w}{L}\right) & \frac{2}{\left(1-\varepsilon_{cr}\right)^2}\sinh\left[\frac{1}{\left(1-\varepsilon_{cr}\right)^2}\frac{\pi w}{L}\right] \\ \frac{2}{\left(1-\varepsilon_{cr}\right)^2}\cosh\left(\frac{\pi w}{L}\right) & \left[\left(1-\varepsilon_{cr}\right)^2+\frac{1}{\left(1-\varepsilon_{cr}\right)^2}\right]\cosh\left[\frac{1}{\left(1-\varepsilon_{cr}\right)^2}\frac{\pi w}{L}\right] \end{bmatrix}. \quad \text{(A2.32)}$$

A nontrivial solution to Eq. (A2.30) exists when the determinant of the coefficient matrix vanishes, which yields

$$\begin{vmatrix} \mathbf{A}_{12} & \mathbf{0} \\ \mathbf{0} & \mathbf{A}_{34} \end{vmatrix} = \left|\mathbf{A}_{12}\right|\left|\mathbf{A}_{34}\right| = 0. \quad \text{(A2.33)}$$

Eq. (A2.33) holds if

$$\left|\mathbf{A}_{12}\right| = 0 \text{ and } \left|\mathbf{A}_{34}\right| \neq 0\,, \tag{A2.34}$$

or

$$\left|\mathbf{A}_{12}\right| \neq 0 \text{ and } \left|\mathbf{A}_{34}\right| = 0\,, \tag{A2.35}$$

or

$$\left|\mathbf{A}_{12}\right| = 0 \text{ and } \left|\mathbf{A}_{34}\right| = 0\,. \tag{A2.36}$$

From Eq. (A2.34), we have $\alpha_3 = \alpha_4 = 0$ and

$$\left[1+\frac{1}{\left(1-\varepsilon_{cr}\right)^4}\right]^2 \tanh\left[\frac{1}{\left(1-\varepsilon_{cr}\right)^2}\frac{\pi w}{L}\right] = \frac{4}{\left(1-\varepsilon_{cr}\right)^6}\tanh\left(\frac{\pi w}{L}\right), \tag{A2.37}$$

which governs the critical strain ε_{cr} for column buckling. The solution to Eq. (A2.21) then becomes

$$A_u = \alpha_1 \sinh\left(\frac{2\pi}{L}y\right) + \alpha_2 \sinh\left[\frac{1}{\left(1-\varepsilon_{cr}\right)^2}\frac{2\pi}{L}y\right], \tag{A2.38}$$

$$A_v = \beta_3 \cosh\left(\frac{2\pi}{L}y\right) + \beta_4 \cosh\left[\frac{1}{\left(1-\varepsilon_{cr}\right)^2}\frac{2\pi}{L}y\right], \tag{A2.39}$$

$$A_p = \gamma_1 \sinh\left(\frac{2\pi}{L}y\right) + \gamma_2 \sinh\left[\frac{1}{\left(1-\varepsilon_{cr}\right)^2}\frac{2\pi}{L}y\right]. \tag{A2.40}$$

Similarly, Eq. (A2.35) yields $\alpha_1 = \alpha_2 = 0$ and

$$\left[1+\frac{1}{\left(1-\varepsilon_{cr}\right)^4}\right]^2 \tanh\left(\frac{\pi w}{L}\right) = \frac{4}{\left(1-\varepsilon_{cr}\right)^6}\tanh\left[\frac{1}{\left(1-\varepsilon_{cr}\right)^2}\frac{\pi w}{L}\right], \tag{A2.41}$$

which leads to the critical strain ε_{cr} for column barreling. The solution to Eq. (A2.21) is rewritten as

$$A_u = \alpha_3 \cosh\left(\frac{2\pi}{L}y\right) + \alpha_4 \cosh\left[\frac{1}{(1-\varepsilon_{cr})^2}\frac{2\pi}{L}y\right], \tag{A2.42}$$

$$A_v = \beta_1 \sinh\left(\frac{2\pi}{L}y\right) + \beta_2 \sinh\left[\frac{1}{(1-\varepsilon_{cr})^2}\frac{2\pi}{L}y\right], \tag{A2.43}$$

$$A_p = \gamma_3 \cosh\left(\frac{2\pi}{L}y\right) + \gamma_4 \cosh\left[\frac{1}{(1-\varepsilon_{cr})^2}\frac{2\pi}{L}y\right]. \tag{A2.44}$$

Eq. (A2.36) does not exists since there is no critical strain ε_{cr} that satisfies both Eq. (A2.37) and Eq. (A2.41).

With Eqs. (A2.37) and (A2.41), we are able to calculate the critical strains ε_{cr} for column buckling and barreling as functions of the width-to-length ratio w/L (Appendix Figure 2.2), from which, we conclude that column buckling occurs prior to barreling for any w/L lower than 1. Once the critical strain ε_{cr} is obtain, one may get the critical force F_{cr} from Eq. (A2.5), which yields

$$F_{cr} = \left[1 - \varepsilon_{cr} - \frac{1}{(1-\varepsilon_{cr})^3}\right]\mu w. \tag{A2.45}$$

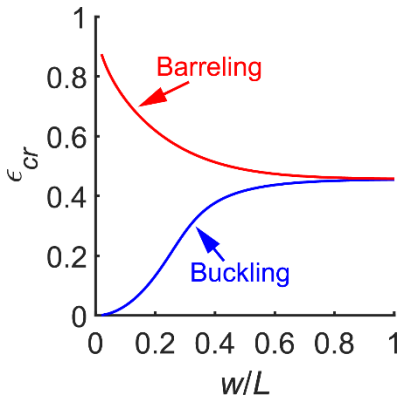

Appendix Figure 2.2 Critical strains for column buckling (blue line) and barreling (red line) as functions of the width-to-length ratio w/L.

A2.3 Sensitivity of the Snapping-back Buckling Modes to Imperfections

The relation between the imperfection r/w and the critical condition for the snapping-back buckling modes is plotted in Appendix Figure 2.3. This diagram shows that the impact of the imperfection used to trigger creases on the snapping-back buckling modes is limited.

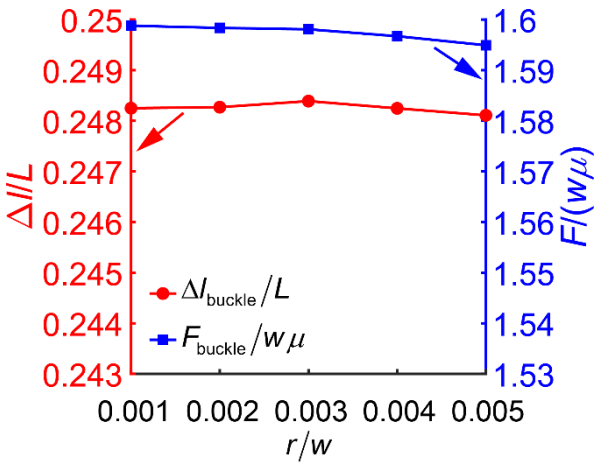

Appendix Figure 2.3 Critical strain $\Delta l_{buckle}/L$ and critical force $F_{buckle}/w\mu$ for buckling as functions of the imperfection r/w when $w/L = 0.28$ and $\Delta d/w = 0.001$.

A2.4 Experiments

We fabricated two identical wide columns with $w/L = 0.28$ (width $w = 14.6$ mm, length $L = 52.0$ mm, depth $b = 30.0$ mm) and one slender column with $w/L = 0.20$ (width $w = 10.4$ mm, length $L = 52.0$ mm, depth $b = 24.0$ mm) by molding silicone rubber (Ecoflex™ 00-30, shear modulus $\mu = 20$ KPa). We glued the columns onto acrylic plates and loaded the samples by a uniaxial testing machine (Instron 5966) equipped with a 500 N load cell. The measurement accuracy of a compressive force F is ± 0.5% of reading and the measurement accuracy of a displacement Δl is ± 0.01 mm. We conducted displacement-controlled and force-controlled tests

at loading/unloading rates ±5 mm/min and ±2 N/min, respectively. To avoid adhesion in the regions of self-contact, we put some silicone oil onto the surfaces of the columns.

A2.5 Experiment Results to Contrast the Snapping-back and Snapping-through Buckling Modes.

We conduct uniaxial loading and unloading tests for columns with width-to-length ratio w/L = 0.20 under displacement control at a ±0.1/min strain rate, and make a comparison between w/L = 0.20 and 0.28 (Appendix Figure 2.4). Unlike the sharp drop in the loading path of w/L = 0.28 (red color), which is identified as snapping-back buckling, the force declines more gently after the onset of buckling when w/L = 0.20 (magenta color), which is identified as snapping-through bucking. The kink in the loading path of w/L = 0.20 indicates the onset of crease. (See Appendix A2.4 and Appendix Video 2.3 for details.)

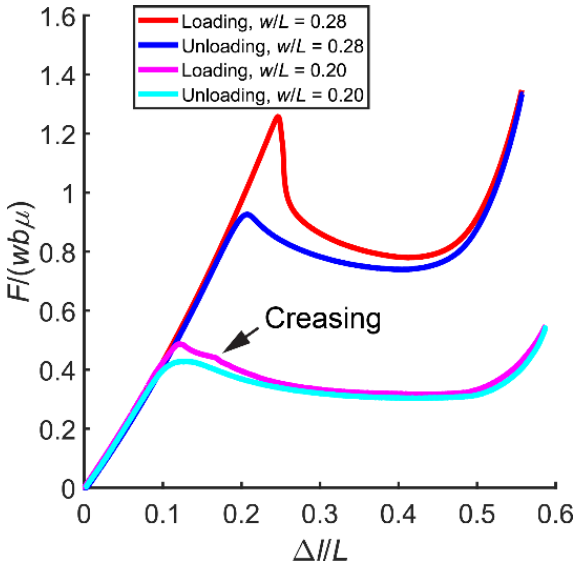

Appendix Figure 2.4 Normalized force $F/(wb\mu)$ and displacement $\Delta l/L$ relations for two columns with w/L = 0.20 (width w = 10.4 mm, length L = 52.0 mm, depth b = 24 mm) and w/L = 0.28 (width w = 14.6 mm, length L = 52.0 mm, depth b =30.0 mm)

A2.6 Discrete Model

To understand and capture the transitions between different buckling modes of a column as its width-to-length ratio w/L varies, we have developed a discrete model, which simplifies half of a column as a rigid bar supported by an extensional spring and a rotational spring (Figure 3.5A). This model accounts for coupling between stretching and bending, which stems from geometric nonlinearity and should not be neglected for wide columns since the pre-compression needed for buckling is nontrivial.

To correctly construct the elastic energies of the two springs, let us first derive the strain energy of a beam under both axial stretching and bending. Consider a prismatic Euler beam with width w, depth b and length l. Based on the Euler-Bernoulli beam theory, the displacement fields are

$$\begin{aligned} u_x &= u_s(x) - z\frac{dv(x)}{dx} = u_s(x) - z\varphi(x) \\ u_y &= 0 \\ u_z &= v(x) \end{aligned} \quad . \tag{A2.46}$$

where u_x, u_y and u_z are the total displacements in the axial (x) and the transverse (y and z) directions, $u_s(x)$ is the axial displacement in the neutral axis due to axial tensile/compressive loads, $v(x)$ is the deflection in the z direction and $\varphi(x)$ is the bending angle. The Green-Lagrange strain in the x direction with high order terms is

$$\begin{aligned} \varepsilon_{xx} &= \frac{1}{2}\left[2u_{x,x} + \left(u_{x,x}\right)^2 + \left(u_{y,x}\right)^2 + \left(u_{z,x}\right)^2\right] \\ &= u_{s,x} - z\varphi_{,x} + \frac{1}{2}\left[\left(u_{s,x} - z\varphi_{,x}\right)^2 + \left(v_{,x}\right)^2\right] \end{aligned} , \tag{A2.47}$$

where $(\ )_{,x} = \partial(\ )/\partial x$. The strain energy U of this beam with linear elastic behavior is given by

$$
\begin{aligned}
U &= \frac{b}{2}\int_0^l \int_{-w/2}^{w/2} \sigma_{xx}\varepsilon_{xx} dzdx \\
&= \frac{bE}{2}\int_0^l \int_{-w/2}^{w/2} \varepsilon_{xx}^2 dzdx \\
&= \frac{bE}{2}\int_0^l \int_{-w/2}^{w/2} \left\{ u_{s,x} - z\varphi_{,x} + \frac{1}{2}\left[\left(u_{s,x} - z\varphi_{,x}\right)^2 + \left(v_{,x}\right)^2 \right] \right\}^2 dzdx \\
&= \frac{Eb}{2}\int_0^l \int_{-w/2}^{w/2} \left(u_{s,x}^2 + u_{s,x}^3 + \frac{1}{4}u_{s,x}^4 + u_{s,x}v_{,x}^2 + \frac{1}{2}u_{s,x}^2 v_{,x}^2 + \frac{1}{4}v_{,x}^4 \right) dzdx + \quad , \\
&\quad \frac{Eb}{2}\int_0^l \int_{-w/2}^{w/2} \left[z^2 \left(\varphi_{,x}^2 + 3u_{s,x}\varphi_{,x}^2 + \frac{3}{2}u_{s,x}^2\varphi_{,x}^2 + \frac{1}{2}\varphi_{,x}^2 v_{,x}^2 \right) + \frac{1}{4}z^4\varphi_{,x}^4 \right] dzdx \\
&= \frac{EA}{2}\int_0^l \left(u_{s,x}^2 + u_{s,x}^3 + \frac{1}{4}u_{s,x}^4 + u_{s,x}v_{,x}^2 + \frac{1}{2}u_{s,x}^2 v_{,x}^2 + \frac{1}{4}v_{,x}^4 \right) dx + \\
&\quad \frac{EI}{2}\int_0^l \left(\varphi_{,x}^2 + 3u_{s,x}\varphi_{,x}^2 + \frac{3}{2}u_{s,x}^2\varphi_{,x}^2 + \frac{1}{2}\varphi_{,x}^2 v_{,x}^2 + \frac{3w^2}{80}\varphi_{,x}^4 \right) dx
\end{aligned}
\tag{A2.48}
$$

where E denotes the Young's modulus, $A = wb$ denotes the area of the cross section, $I = bw^3/12$ is the second moment of inertia about z axis. The first term is linearly proportional to the axial rigidity EA and can be viewed as the stretching energy U_s, and the second term is linearly proportional to the flexural rigidity EI and can be viewed as the bending energy U_b. Thus, the strain energy U in Eq. (A2.48) can be rewritten as

$$
U = U_s + U_b , \tag{A2.49}
$$

where

$$
U_s = \frac{EA}{2}\int_0^l \left(u_{s,x}^2 + u_{s,x}^3 + \frac{1}{4}u_{s,x}^4 + u_{s,x}v_{,x}^2 + \frac{1}{2}u_{s,x}^2 v_{,x}^2 + \frac{1}{4}v_{,x}^4 \right) dx , \tag{A2.50}
$$

$$
U_b = \frac{EI}{2}\int_0^l \left(\varphi_{,x}^2 + 3u_{s,x}\varphi_{,x}^2 + \frac{3}{2}u_{s,x}^2\varphi_{,x}^2 + \frac{1}{2}\varphi_{,x}^2 v_{,x}^2 + \frac{3w^2}{80}\varphi_{,x}^4 \right) dx . \tag{A2.51}
$$

Now we consider the vicinity of the buckling point where the bending angle φ and deflection v start to rise but are still extremely small. We rewrite the stretching energy U_s as

$$U_s = \frac{EA}{2}\int_0^l \left(u_{s,x}^2\right) dx, \tag{A2.52}$$

in which we have neglected the higher-order terms of $u_{s,x}$ and the terms related to the deflection v since the term of $u_{s,x}^2$ is dominant. In the bending energy U_b, we have neglected the last two terms because they are of order $O\left[\varphi_{,x}^4\right]$, which yields

$$U_b = \frac{EI}{2}\int_0^l \left(\varphi_{,x}^2 + 3u_{s,x}\varphi_{,x}^2 + \frac{3}{2}u_{s,x}^2\varphi_{,x}^2\right) dx. \tag{A2.53}$$

Here we keep the coupling terms between stretching u_s and bending φ in the bending energy U_b, which is absent in Euler's elastica. The strain energy U now becomes

$$U = U_s + U_b = \frac{EA}{2}\int_0^l \left(u_{s,x}^2\right) dx + \frac{EI}{2}\int_0^l \left(\varphi_{,x}^2 + 3u_{s,x}\varphi_{,x}^2 + \frac{3}{2}u_{s,x}^2\varphi_{,x}^2\right) dx. \tag{A2.54}$$

Inspired by the strain energy of an Euler beam, we construct the elastic energy of the discrete model (Figure 3.5A) as

$$U_{discrete} = \frac{1}{2}K_c q_c^2 + \frac{1}{2}K_b\left(q_b + \xi q_b q_c\right)^2, \tag{A2.55}$$

where the length of the rigid bar $L/2$ equates the length of the Euler beam l, the vertical displacement q_c at the base of the rigid bar corresponds to the total displacement of the Euler beam in the axial direction, and the inclination angle q_b of the rigid bar corresponds to the net bending angle of the Euler beam (Figure 3.5A), i.e.,

$$q_c = \int_0^{L/2} u_{s,x} dx,\ q_b = \int_0^{L/2} \varphi_{,x} dx. \tag{A2.56}$$

The first term in the elastic energy of the discrete model in Eq. (A2.55) is the stretching energy stored in the linear extensional spring with a stiffness $K_c = 2EA/L$. The second term in Eq. (A2.55) is the bending energy stored in the rotational spring with a stiffness $K_b = 2EI/L$. The bending energy

not only depends on the inclination angle q_b, but also the vertical displacement q_c, with ξ the coupling coefficient between stretching and bending.

Suppose the rigid bar in the discrete model is loaded vertically by F. The vertical displacement of the load $\Delta l/2$ depends on q_c and q_b following the geometric relation,

$$\frac{\Delta l}{2} = q_c + \frac{L}{2}\left(1-\cos q_b\right). \tag{A2.57}$$

The displacement q_c and inclination angle q_b can be determined by extremizing the following potential energy

$$\Pi = U_{\text{discrete}} - F\frac{\Delta l}{2} = \frac{1}{2}K_c q_c^2 + \frac{1}{2}K_b\left(q_b + \xi q_b q_c\right)^2 - F\frac{\Delta l}{2}, \tag{A2.58}$$

which yields two equilibrium equations

$$\Pi_{,c} = \frac{\partial \Pi}{\partial q_c} = K_c q_c + K_b \xi q_b\left(q_b + \xi q_b q_c\right) - F = 0, \tag{A2.59}$$

$$\Pi_{,b} = \frac{\partial \Pi}{\partial q_b} = K_b\left(q_b + \xi q_b q_c\right)\left(1 + \xi q_c\right) - \frac{L}{2}F\sin q_b = 0. \tag{A2.60}$$

By solving Eq. (A2.59) and (A2.60), we can obtain the relations between load F and displacement $\Delta l/2$.

We plot the normalized load-displacement curves for different width-to-length ratios w/L ranging from 0.1 to 0.34 (Figure 3.5B), from which one can observe the transitions from the continuous, snapping-through to snapping-back buckling mode as w/L increases. To highlight the role of coupling between stretching and bending in determining the buckling mode, we rewrite the elastic energy of the discrete model in Eq. (A2.55) as

$$U_{discrete} = U^{c}_{discrete} + U^{b}_{discrete} + U^{\xi}_{discrete}, \tag{A2.61}$$

where $U^{c}_{discrete}$, $U^{b}_{discrete}$ and $U^{\xi}_{discrete}$ represent the stretching, bending, and coupling energy components dependent on q_c, q_b, and both q_c and q_b, respectively, i.e.,

$$\begin{aligned} U^{c}_{discrete} &= \frac{1}{2} K_c q_c^2 \\ U^{b}_{discrete} &= \frac{1}{2} K_b q_b^2 \\ U^{\xi}_{discrete} &= \frac{1}{2} K_b \xi^2 q_b^2 q_c^2 + K_b \zeta q_b^2 q_c \end{aligned} \quad . \tag{A2.62}$$

We select three cases that exhibit distinctive buckling modes in Figure 3.5B: w/L = 0.10 (continuous buckling), w/L = 0.20 (snapping-through buckling) and w/L = 0.32 (snapping-back buckling), and plot each energy component of $U_{discrete}$ as a function of displacement (Appendix Figure 2.5). We note that when w/L = 0.10, $U^{\xi}_{discrete}$ is much smaller than $U^{c}_{discrete}$ and $U^{b}_{discrete}$ after the buckling; when w/L = 0.20, $U^{\xi}_{discrete}$ is on the same order of magnitude as $U^{c}_{discrete}$ and $U^{b}_{discrete}$ in the post-buckling; whereas $U^{\xi}_{discrete}$ in the case of w/L = 0.32 grows as fast as $U^{b}_{discrete}$ in the vicinity of the bifurcation point. This is because as w/L increases, the critical value of q_c for buckling increases, which leads to a significant contribution of the coupling energy $U^{\xi}_{discrete}$ to the total energy. Thus, we can conclude that the effect of the coupling between stretching and bending can be tuned by varying w/L, and a strong coupling effect results in the snapping-back buckling mode.

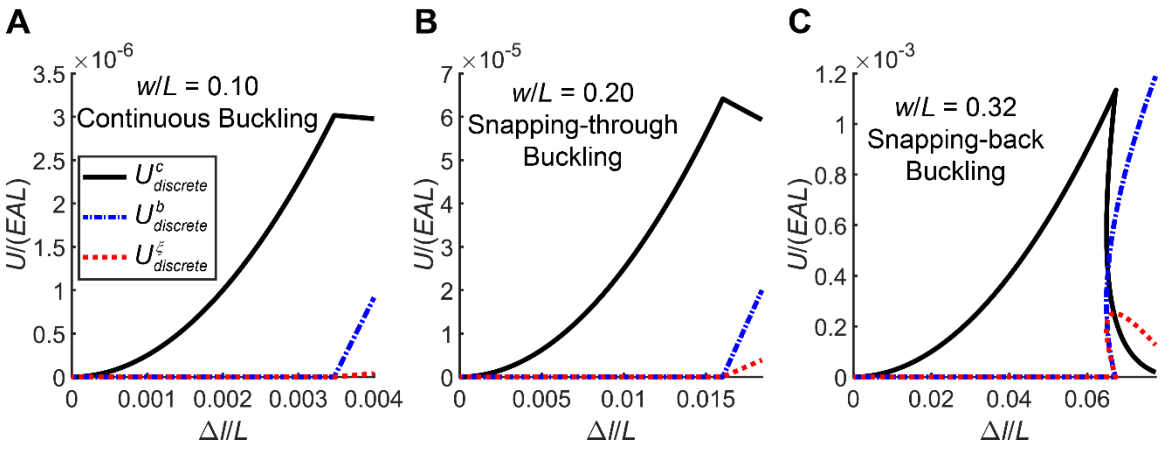

Appendix Figure 2.5 The role of coupling between stretching and bending in determining the buckling mode. The stretching $U^{c}_{discrete}$, bending $U^{b}_{discrete}$, and coupling $U^{\xi}_{discrete}$ energy components of total elastic energy $U_{discrete}$ in the discrete model as functions of $\Delta l/L$ when (**A**) w/L = 0.10, (**B**) w/L = 0.20 and (**C**) w/L = 0.32. (**A**-**C** have the same legend).

A2.7 Videos

Appendix Video 2.1 Uniaxial loading and unloading test for a column exhibiting a snapping-back buckling mode under displacement control. This column has a width-to-length ratio w/L = 0.28 (width w = 14.6 mm, length L = 52.0 mm, depth b =30.0 mm). The loading/unloading rate is ±5 mm/min.

Appendix Video 2.2 Uniaxial loading and unloading test for a column exhibiting a snapping-back buckling mode under force control. This column has a width-to-length ratio w/L = 0.28 (width w = 14.6 mm, length L = 52.0 mm, depth b =30.0 mm). The loading/unloading rate is ±2 N/min.

Appendix Video 2.3 Uniaxial loading and unloading test for a column exhibiting a snapping-through buckling mode under displacement control. This column has $w/L = 0.20$ (width $w = 10.4$ mm, length $L = 52.0$ mm, depth $b = 24$ mm) The loading/unloading rate is ± 5 mm/min.

Appendix 3 Supplementary Materials for Reusable Energy-absorbing Architected Materials

A3.1 Finite Element Modeling

We used the commercial software Abaqus/Standard for our static finite element simulations. The static Riks method was implemented to capture the unstable equilibrium force-displacement responses. We modeled columns as an incompressible neo-Hookean material in plane strain conditions with hybrid quadratic rectangular elements (Abaqus type CPE8H). Defects with very small sizes were introduced to trigger buckling and creasing instabilities (Appendix Figure 3.1). The size of the imperfection for buckling is $\Delta d/w$ = 0.001, and the size of the imperfection for creasing is r/w= 0.002. We performed a mesh refinement study to ensure the mesh size is at least one order of magnitude smaller than the dimension of the finest part of the samples. As a result, approximately from $6x10^4$ to $4x10^5$ quadrilateral elements are involved in each finite element model, depending on the width-to-length ratio of columns.

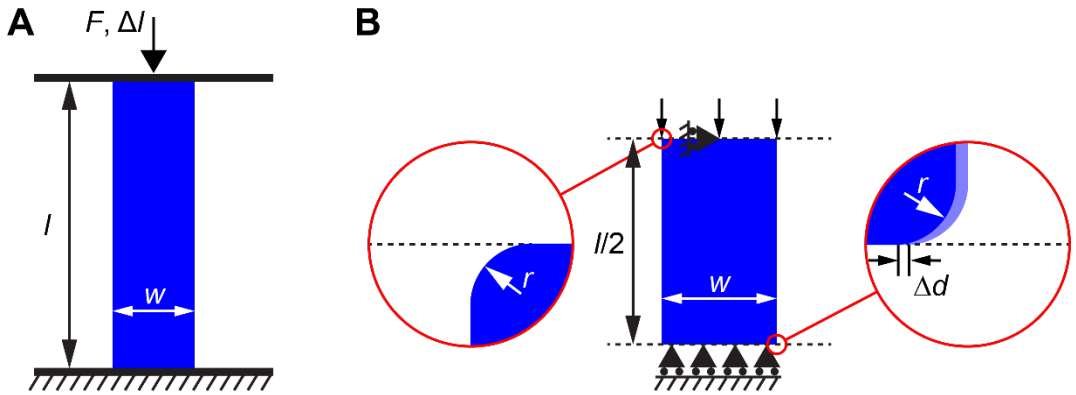

Appendix Figure 3.1 Setup of finite element (FE) modeling. (A) A 2D hyperelastic column with a width-to-length ratio w/l is subjected to a compressive force F or a displacement Δl that results in buckling of the column. (B) Due to symmetry, only the top half of the column in (A) is selected

for finite element modeling, where the bottom side is constrained by a symmetric boundary condition and the mid-point of the top side is restricted to moving vertically to eliminate rigid-body motions. A very small displacement defect Δd in the horizontal direction is introduced to the bottom side of the half column in its stress-free state (light blue) to trigger buckling. A quarter of a circle with a small radius r is introduced as a defect to trigger the initiation of a crease at both the bottom right and top left corners of the half column. A rigid frictionless surface (dashed line) abuts one of the quarter-circle defects to form a self-contacting fold.

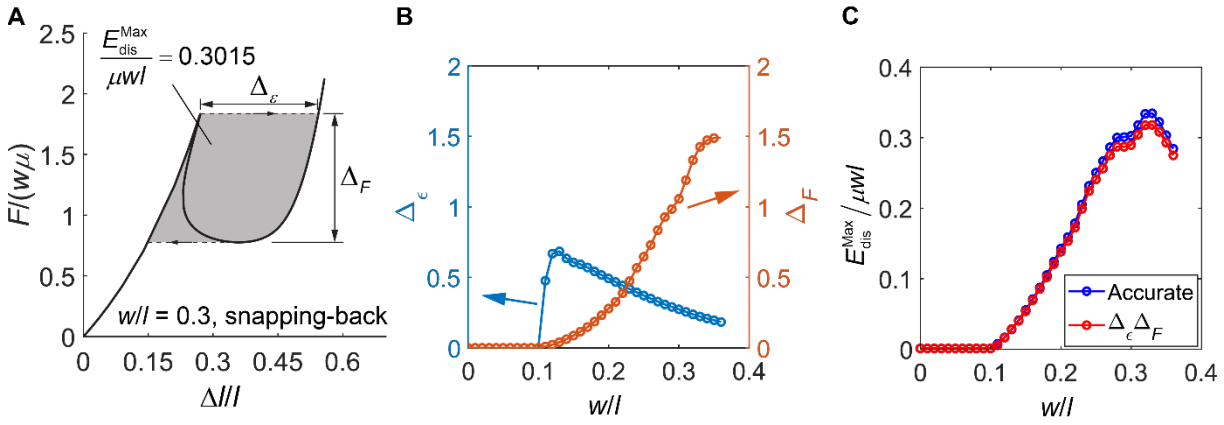

Appendix Figure 3.2 Non-monotonic change of $E_{\text{dis}}^{\text{Max}}/\mu wl$ with w/l. (A) Force-displacement equilibrium path for a wide column of w/l =0.3, with the definition of the width Δ_ε, height Δ_F, and area $E_{\text{dis}}^{\text{Max}}/\mu wl$ of the hysteresis under a force-controlled loading. (B) Δ_ε (left) and Δ_F (right) as functions of w/l. (C) Non-monotonic change of $E_{\text{dis}}^{\text{Max}}/\mu wl$ as w/l increases. Estimation of the hysteresis by the product of Δ_ε and Δ_F (red) agrees well with the accurate calculated area (blue).

A3.2 Fabrication

We fabricated the samples by molding silicone elastomers into the 3D printed molds. Ecoflex™ 00-30 was used for the samples containing columns with a width-to-length ratio w/l = 0.30, SORTA-Clear 40, which has a modulus over 10 times higher than the Ecoflex 00-30, was

used for the samples containing columns with w/l = 0.14. As a result, these samples with two different w/l have similar critical forces for column buckling. The characterization of the moduli of the two silicone elastomers is shown in Appendix A3.6.

A3.3 Static Tests

We used a uniaxial testing machine (Instron 5966) with a 500 N load cell to measure the displacement-controlled force-displacement relations of the proposed architected materials. The experimental results shown in Figure 3 and 5 were obtained at a strain rate of ±0.2 min^{-1} (16 mm/min). During the tests, the deformation of the samples was recorded by a Canon EOS 6D digital SLR camera. To investigate the effect of the number of loading cycles on the mechanical behavior of the samples, we conducted 50 loading and unloading compressive tests at a strain rate ±0.2 min^{-1} for the samples shown in Figure 3B. To explore whether the behavior is rate-dependent, we conducted the tests at strain rates ranging from ±0.05 min^{-1} to ±1 min^{-1}.

A3.4 Drop Tests

To explore the energy-absorbing performance of the proposed architected material, we dropped the sample from different heights to create impacts at its bottom, while measured the impact force at its top. The setup of the drop tests is shown in Figure S8. The sample together with some steel plates attached to its bottom was dropped from different heights h ranging from 1 cm to 20 cm. The total weight dropped is 1.142 kg. A slider on a rail was used to guide the fall of the sample. A piezoelectric accelerometer (PCB Piezotronics, Inc., model number: 352C23) was attached onto the top plate on the sample to record its acceleration. The impact force can be calculated by multiplying the acceleration by the mass of the top plate (m = 0.156 kg). The drop test was recorded using a Phantom V7.2 high speed camera at 6600 frames per second. The

Appendix Video 3.2 shows the deformation process of the sample during the impact. This movie is played at 100 frame per second, which is 66 times slower than the actual time scale. From this movie, we can see the strain rate is roughly 4000 min^{-1}, which is 20000 times higher than the strain rate in the static tests.

A3.5 Theory for the Force-displacement Response of a Snapping-back or Snapping-through Column Chain under Displacement Control.

In this section, we determine the force-displacement response of a column chain containing n number of identical snapping-back or snapping-through columns with a width-to-length ratio w/l under displacement control. A single column's equilibrium force-displacement path is obtained through a FE simulation, as shown in Figure 5.1. Based on the FE simulation result, we first determine all the equilibrium force-displacement branches of the column chain, and then identify the stability of each branch.

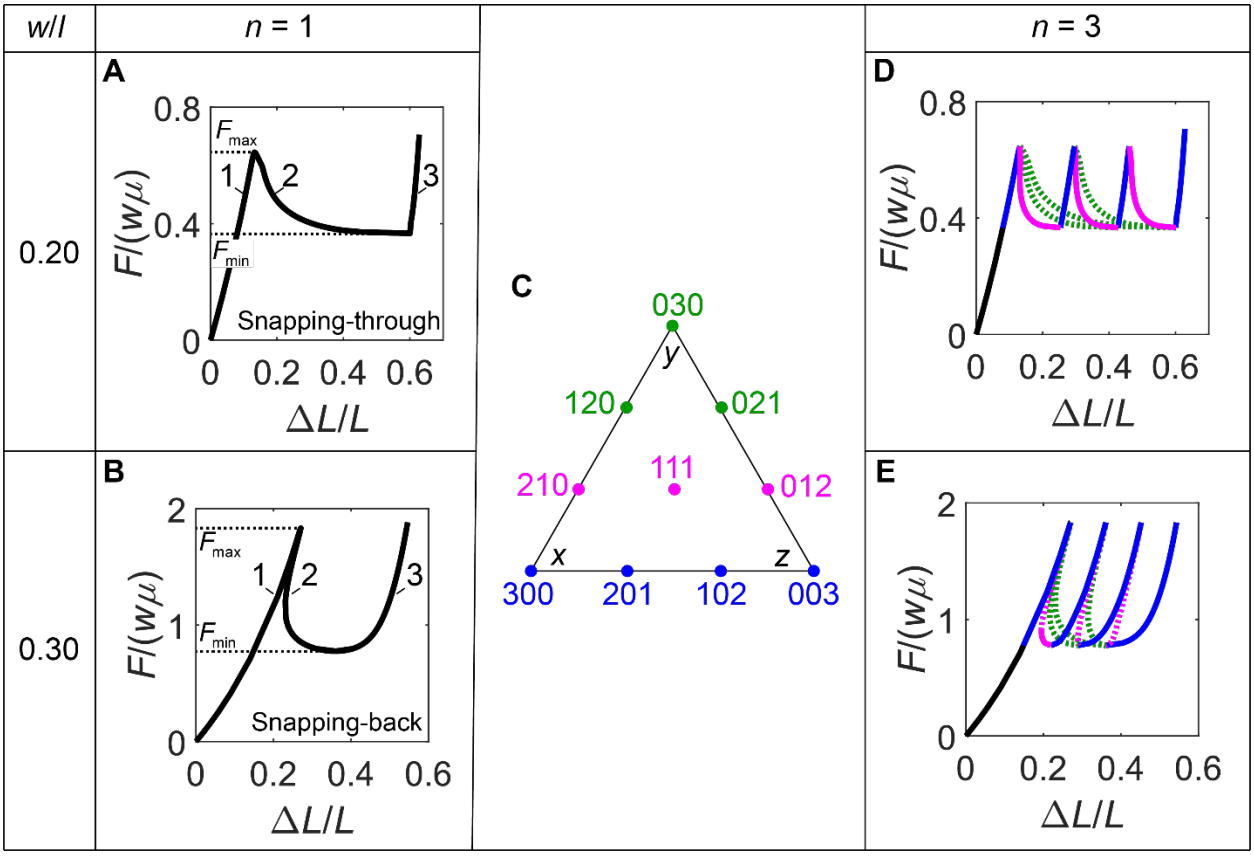

Appendix Figure 3.3 Determine the stable equilibrium force-displacement paths for a column chain. (A and B) The equilibrium force-displacement paths of a single column with a width-to-length ratio w/l = 0.20 (A) and 0.30 (B) from FE simulations. (C) Possible triples (x, y, z) for a column chain with n = 3 number of columns connected in series, where x, y, and z represent the numbers of columns whose displacements are on the branches 1, 2, and 3, respectively. The triples in blue, pink, and green denote the equilibrium configurations with y = 0, y = 1, and $y \geq 2$, respectively. (D and E) Equilibrium force-displacement paths for a column chain containing n = 3 number of columns with w/l = 0.20 (D) and 0.30 (E). The solid curves represent the stable equilibrium branches, whereas the dashed curves represent the unstable equilibrium branches when the displacement is controlled. The curves and the corresponding triples in (C) share the same colors.

Since the columns are connected in series (See Figure 5.2A), the total force F acting on the column chain equals the force F_i acting on each column, and the total displacement ΔL equals the sum of the displacement Δl_i of all the columns (i = 1, 2, …, n). When a column exhibits the snapping-through (Appendix Figure 3.3A) or snapping-back (Appendix Figure 3.3B) buckling mode, a given force F_i within the range of ($F_{\min}$, $F_{\max}$) corresponds to three different displacements Δl_i, which are on the three different branches 1, 2 and 3. For a column chain with n number of identical columns subjected to a force F_i ($F_{\min} < F_i < F_{\max}$), we define a triple ($x$, y, z), where x, y and z represent the number of columns whose displacements Δl_i are on the 1, 2, and 3 branches, respectively. Each triple leads to one equilibrium $F - \Delta L$ branch. Counting the total number of triples is a combinatorial problem: in how many ways the n identical columns can be divided into three distinct groups, in which empty groups are allowed. There are $C_{n+2}^2 = (n+1)(n+2)/2$ number of different triples, corresponding to the same number of equilibrium $F - \Delta L$ branches. Take n = 3 as an example. There are $C_{3+2}^2 = (3+1)(3+2)/2 = 10$ different triples, which can be displayed in the configurational space (Appendix Figure 3.3C) [74]. The equilibrium branch represented by the triple (x, y, z) has the following total displacement ΔL

$$\Delta L = x\Delta l^1 + y\Delta l^2 + z\Delta l^3, \tag{A3.1}$$

where Δl^1, Δl^2 and Δl^3 are the displacements corresponding to the force F on the branches 1, 2 and 3, respectively. In this way, we can identify all the equilibrium $F - \Delta L$ branches. Appendix Figure 3.3D and E are the examples of the 10 equilibrium $F - \Delta L$ branches for the column chains composed of n = 3 number of columns with w/l = 0.20 (Appendix Figure 3.3D) and 0.30 (Appendix Figure 3.3E).

Note that not all the equilibrium $F - \Delta L$ branches are stable when the displacement ΔL is controlled. A stable equilibrium $F - \Delta L$ branch requires the following Hessian matrix H_{ij} to be positive-definite

$$H_{ij} = \frac{\partial^2 G(q_1,\ldots,q_m;\lambda)}{\partial q_i \partial q_j} \quad (i,j = 1,\ldots,m), \tag{A3.2}$$

where G is the free energy, λ is the control parameter, and q_1, …, q_m are the generalized state variables. When the total displacement ΔL is specified ($\lambda = \Delta L$), the free energy is the total elastic energy of the column chain U.

Next, we determine the stable equilibrium $F - \Delta L$ branches under displacement control for a column chain composed of columns exhibiting the snapping-through buckling mode. The stability of the snapping-through elements connected in series has been well studied in the literature [74]. Here we briefly summarize how the stable equilibrium $F - \Delta L$ branches of the column chain are determined.

The elastic energy of this column chain depends only on the displacement of each column Δl_i,

$$U = \sum_{i=1}^{n} U_i(\Delta l_i), \tag{A3.3}$$

where U_i is the elastic energy of column i. Since ΔL is specified, we can eliminate the state variable Δl_n in Equation (A3.3) by $\Delta l_n = \Delta L - \sum_{i=1}^{n-1} \Delta l_i$. Then the total elastic energy U can be expressed as a function of state variables $\Delta l_1, \Delta l_2, \ldots, \Delta l_{n-1}$,

$$U(\Delta l_1, \Delta l_2, \ldots \Delta l_{n-1}; \Delta L) = U_1(\Delta l_1) + U_2(\Delta l_2) + \cdots + U_{n-1}(\Delta l_{n-1}) + U_n\left(\Delta L - \sum_{i=1}^{n-1} \Delta l_i\right). \tag{A3.4}$$

Substituting Equation (A3.4) into Equation (A3.2), we obtain a n-1 by n-1 Hessian matrix H_{ij}

$$H_{ij}=\frac{\partial^2 U\left(\Delta l_1,\ldots,\Delta l_{n-1};\Delta L\right)}{\partial\Delta l_i\partial\Delta l_j}=\begin{cases}k_i+k_n, & i=j\\ k_n, & i\neq j\end{cases}\quad\left(i,j=1,2,\ldots,n-1\right), \tag{A3.5}$$

where $k_m=\partial^2 U_m/\partial(\Delta l_m)^2$ $(m=1,2,\ldots,n)$ represent the slope of the equilibrium force-displacement curve for column m at the displacement Δl_m. If the Hessian matrix in Equation (A3.5) is positive definite, the equilibrium $F-\Delta L$ branch is stable. Otherwise, the branch is unstable. The Hessian matrix H_{ij} is positive definite if and only if all of its principal minors are positive

$$A_j=\left(\prod_{i=1}^{j}k_i\right)\left(1+\sum_{l=1}^{j}\frac{k_n}{k_l}\right)>0, j=1,2,...,n-1\,. \tag{A3.6}$$

The sign of A_j depends on the number of columns whose displacements are on the branch 2 featuring a negative slope. When there is no column on the branch 2 ($y = 0$), all the k_m ($m = 1, 2, \ldots, n$) in Equation (A3.6) are positive and thus H_{ij} is positive definite. When there are no less than two columns on the branch 2 ($y \geq 2$), one can always reorganize the columns such that the first and the last columns have displacements on their branch 2, i.e. $k_1 < 0$ and $k_n < 0$. Thus, H_{ij} is not positive definite since $A_1 = k_1 + k_n < 0$. When there is exactly one column on its branch 2 ($y = 1$), we assume, without loss of generality, that the (n-1)th column has a displacement on its branch 2, then $k_{n-1} < 0$ and $k_m > 0$ ($m = 1, 2, \ldots, n$-2, n). Therefore, $A_j > 0$ ($j = 1, 2, \ldots, n$-2) and the positive definiteness of H_{ij} depends only on A_{n-1}

$$A_{n-1}=\left(\prod_{i=1}^{n}k_i\right)\left(\sum_{l=1}^{n}\frac{1}{k_l}\right). \tag{A3.7}$$

Note that $\prod_{i=1}^{n}k_i<0$ and

$$\frac{dF}{d\left(\Delta L\right)}=\left(\sum_{l=1}^{n}\frac{1}{k_l}\right)^{-1}. \tag{A3.8}$$

$A_{n-1} > 0$ if the slope of the equilibrium $F-\Delta L$ branch is negative.

In summary, the equilibrium $F - \Delta L$ branches are stable if either (i) there is no column on the branch 2, or (ii) there is exactly one column on the branch 2 while the overall equilibrium $F - \Delta L$ curve of the column chain has a negative slope. Otherwise, the equilibrium branches are unstable. Appendix Figure 3.3D shows the stable (solid lines) and unstable (dashed lines) equilibrium $F - \Delta L$ branches when ΔL is controlled for a column chain composed of $n = 3$ number of columns with $w/l = 0.20$, which exhibit the snapping-through buckling mode.

For a column chain composed of columns exhibiting the snapping-back buckling mode, the stable equilibrium $F - \Delta L$ branches can be determined by the following. Note that the force-displacement curve featuring the snapping-back buckling (Appendix Figure 3.4A) can be mathematically separated into a monotonic force-displacement curve (Appendix Figure 3.4B) and a force-displacement curve featuring the snapping-through buckling (Appendix Figure 3.4C). The monotonic force-displacement curve (Appendix Figure 3.4B) is selected such that the branch 2 (purple) shown in Appendix Figure 3.4A corresponds to the negative slope part (the purple branch in Appendix Figure 3.4B) of the force-displacement curve featuring the snapping-through buckling. The column exhibiting the snapping-back buckling mode can be regarded as a nonlinear spring connected in series to a snapping-through element. A column chain containing n columns can then be viewed as a system containing n nonlinear springs and n snapping-through elements connected in series. The n nonlinear springs can be merged into a single spring with the equivalent force-displacement behavior. Therefore, the column chain containing n columns exhibiting the snapping-back buckling mode is equivalent to a serial combination of n snapping-through elements and a single nonlinear spring.

Following the previous procedure, the Hessian matrix H_{ij} for this column chain is

$$\mathbf{H}=\begin{bmatrix} \tilde{k}_1+\tilde{k}_n & \tilde{k}_n & \cdots & \tilde{k}_n & \tilde{k}_n \\ \tilde{k}_n & \tilde{k}_2+\tilde{k}_n & \cdots & \tilde{k}_n & \tilde{k}_n \\ \vdots & \vdots & \ddots & \vdots & \vdots \\ \tilde{k}_n & \tilde{k}_n & \cdots & \tilde{k}_{n-1}+\tilde{k}_n & \tilde{k}_n \\ \tilde{k}_n & \tilde{k}_n & \cdots & \tilde{k}_n & \tilde{k}_{\text{spring}}+\tilde{k}_n \end{bmatrix}, \tag{A3.9}$$

where $\tilde{k}_m$ $(m = 1, 2, \ldots, n)$ and $\tilde{k}_{\text{spring}}$ represent the slope of the equilibrium force-displacement curve of the snapping-through elements and the nonlinear spring, respectively. $\tilde{k}_{\text{spring}}$ is always positive. **H** is positive definite if and only if its principal minors are all positive

$$A_j=\begin{cases} \left(\prod_{i=1}^{j}\tilde{k}_i\right)\left(1+\sum_{l=1}^{j}\frac{\tilde{k}_n}{\tilde{k}_l}\right), j=1,2,\ldots,n-1 \\ \tilde{k}_{\text{spring}}\left(\prod_{i=1}^{j-1}\tilde{k}_i\right)\left(1+\frac{\tilde{k}_n}{\tilde{k}_{\text{spring}}}+\sum_{l=1}^{j-1}\frac{\tilde{k}_n}{\tilde{k}_l}\right), j=n \end{cases}. \tag{A3.10}$$

Since $\tilde{k}_{\text{spring}}$ is positive, it does not affect the stability. The conclusion made for the column chain with columns exhibiting the snapping-through buckling mode can be applied here. Take the column chain composed of $n = 3$ number of columns with $w/l = 0.30$, which exhibit snapping-back buckling mode, as an example. Among its 10 equilibrium $F - \Delta L$ branches (Appendix Figure 3.3E), the branches (blue curves) that correspond to zero column on its branch 2 are stable. The reason is that the equivalent system contains no snapping-through element on its branch 2. Thus, $\tilde{k}_m$ $(m = 1, 2, \ldots, n)$ in Equation(A3.10) are greater than zero, leading to a positive definite Hessian matrix. The branches (green curves) that correspond to no less than two columns on their branch 2 are unstable. The reason is the following. We assume, without loss of generality, that the first and the last columns have displacements on their branch 2. Thus the two corresponding snapping-through elements are also on their branch 2, i.e. $\tilde{k}_1 < 0$ and $\tilde{k}_m < 0$, yielding $A_1 = \tilde{k}_1 + \tilde{k}_m < 0$. Therefore, the Hessian matrix is not positive definite. The stability of the branches (pink

curves) that have exactly one column on its branch 2 depends solely on the slope of the equilibrium $F - \Delta L$ branches. The branches are stable if and only if the overall slope is negative. The reason is the following. We assume, without loss of generality, that the (n-1)th column has a displacement on its branch 2. Correspondingly, the snapping-through element of this column also has a displacement on its branch 2, i.e. $\tilde{k}_{n-1} < 0$. Note that $\tilde{k}_m$ $(m = 1, 2, \ldots, n-2, n)$ are positive, we get

$$A_j = \left(\prod_{i=1}^{j} \tilde{k}_i \right) \left(1 + \sum_{l=1}^{j} \frac{\tilde{k}_n}{\tilde{k}_l} \right) > 0, j = 1, 2, \ldots, n-2 . \tag{A3.11}$$

Then the equilibrium $F - \Delta L$ branches are stable if

$$\begin{aligned} A_{n-1} &= \left(\prod_{i=1}^{n-1} \tilde{k}_i \right) \left(1 + \sum_{l=1}^{n-1} \frac{\tilde{k}_n}{\tilde{k}_l} \right) = \left(\prod_{i=1}^{n} \tilde{k}_i \right) \left(\sum_{l=1}^{n} \frac{1}{\tilde{k}_l} \right) > 0, \text{ and} \\ A_n &= \tilde{k}_{\text{spring}} \left(\prod_{i=1}^{n-1} \tilde{k}_i \right) \left(1 + \frac{\tilde{k}_n}{\tilde{k}_{\text{spring}}} + \sum_{l=1}^{n-1} \frac{\tilde{k}_n}{\tilde{k}_l} \right) = \tilde{k}_{\text{spring}} \left(\prod_{i=1}^{n} \tilde{k}_i \right) \left(\frac{1}{\tilde{k}_{\text{spring}}} + \sum_{l=1}^{n} \frac{1}{\tilde{k}_l} \right) > 0 \end{aligned} . \tag{A3.12}$$

Note that $\prod_{i=1}^{n} \tilde{k}_i < 0$ and $\tilde{k}_{\text{spring}} > 0$, and

$$\frac{dF}{d(\Delta L)} = \left(\frac{1}{\tilde{k}_{\text{spring}}} + \sum_{l=1}^{n} \frac{1}{\tilde{k}_l} \right)^{-1} . \tag{A3.13}$$

Therefore, $A_{n\text{-}1} > 0$ and $A_n > 0$ if the slope of the equilibrium $F - \Delta L$ branch is negative.

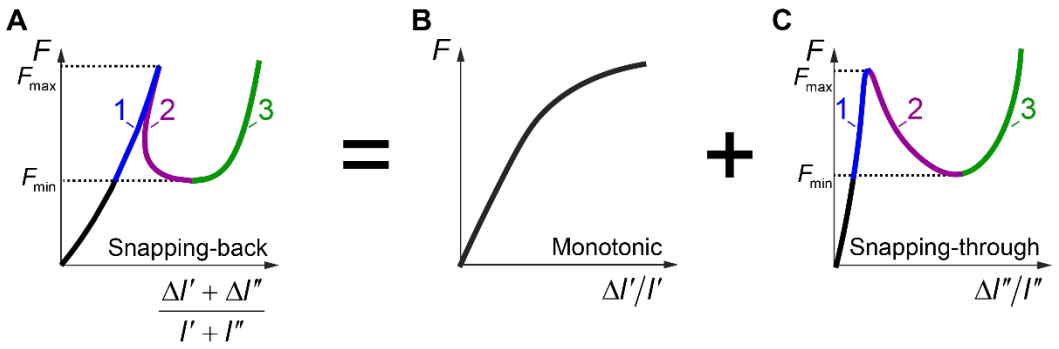

Appendix Figure 3.4 Schematic of equivalence between a column exhibiting the snapping-back buckling mode and a nonlinear spring connected in series to a snapping-through element. A force-displacement curve featuring the snapping-back buckling (A) is equivalent to a superposition of a monotonic force-displacement curve (B) and a force-displacement curve featuring the snapping-through buckling (C). The branches 1 (blue), 2 (purple), and 3 (green) in (A) correspond to the branches 1 (blue), 2 (purple), and 3 (green) in (**C**), respectively.

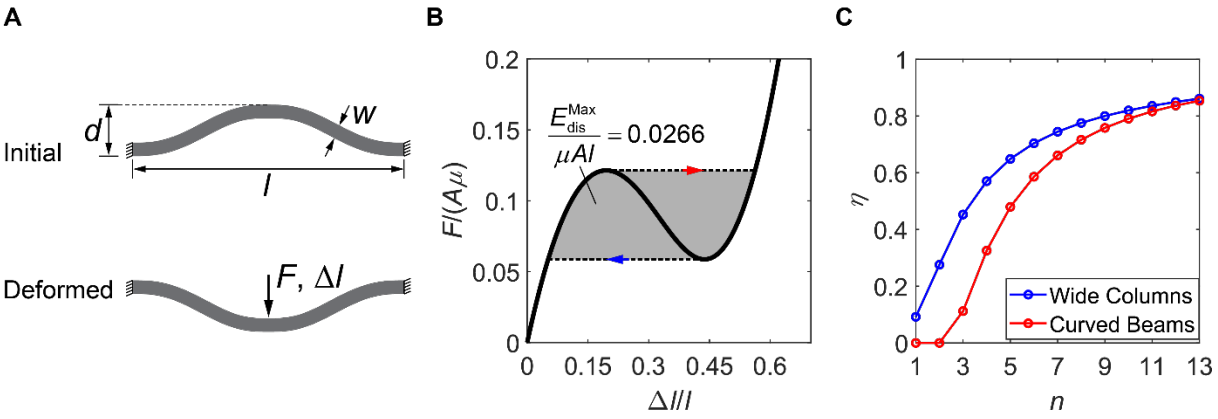

Appendix Figure 3.5 Energy dissipation of curved beams stacked in series. (A) Schematic of one curved beam in its initial (upper) and deformed (lower) states. This beam has a circular cross section with a diameter *w*. (B) Normalized force-displacement equilibrium path obtained from FE analysis. This curved beam exhibits a snapping-through buckling mode. The shaded area indicates the maximum normalized dissipated energy under force-controlled loading, $E_{\mathrm{dis}}^{\mathrm{Max}}/\mu Al$, where A

denotes the area of the cross section. The geometric parameters of this curved beam are: $w/l = 0.1$, $d/l = 0.28$. (C) The energy dissipation efficiency η as a function of the number of layers n for the curved beams (red), compared with that of wide columns with $w/l = 0.30$ (blue).

A3.6 Characterization of Silicone Elastomers

Next, we conducted uniaxial compression tests to characterize the initial shear modulus of the two silicone rubbers. We molded two solid cubes of length 50 mm, depth 50 mm and width 50 mm out of Ecoflex 00-30 and SORTA-Clear 40. The cubes sandwiched between two acrylic plates were loaded by a uniaxial testing machine (Instron 5966) equipped with a 500 N load cell. The nominal stress-strain relations for the two silicone rubbers at a strain rate of 0.3 min^{-1} were obtained and plotted in Appendix Figure 3.6. We modeled both materials by the following incompressible neo-Hookean model

$$W = \frac{\mu}{2}\left[\operatorname{tr}\left(\mathbf{F}\mathbf{F}^{\mathrm{T}}\right) - 3\right] + p\left[\det\left(\mathbf{F}\right) - 1\right], \tag{A3.14}$$

where W is the strain energy density function, μ is the initial shear modulus, $\mathbf{F}$ is the deformation gradient tensor and p is the hydrostatic pressure. The nominal (first Piola-Kirchoff) stress under uniaxial compression is then given by

$$S_{11} = \mu\left[\frac{1}{\left(1-\varepsilon_{11}\right)^2} - \left(1-\varepsilon_{11}\right)\right], \tag{A3.15}$$

where S_{11} and ε_{11} represent the nominal stress and strain along the loading direction, respectively. We fitted Equation (A3.15) to the experimental data using the linear least-square method, yielding $\mu = 16.461$ kPa for Ecoflex 00-30 and 288.147 kPa for SORTA-Clear 40. In Appendix Figure 3.6, we can see that the incompressible neo-Hookean model can capture the stress-strain behavior up to 10% strain very well.

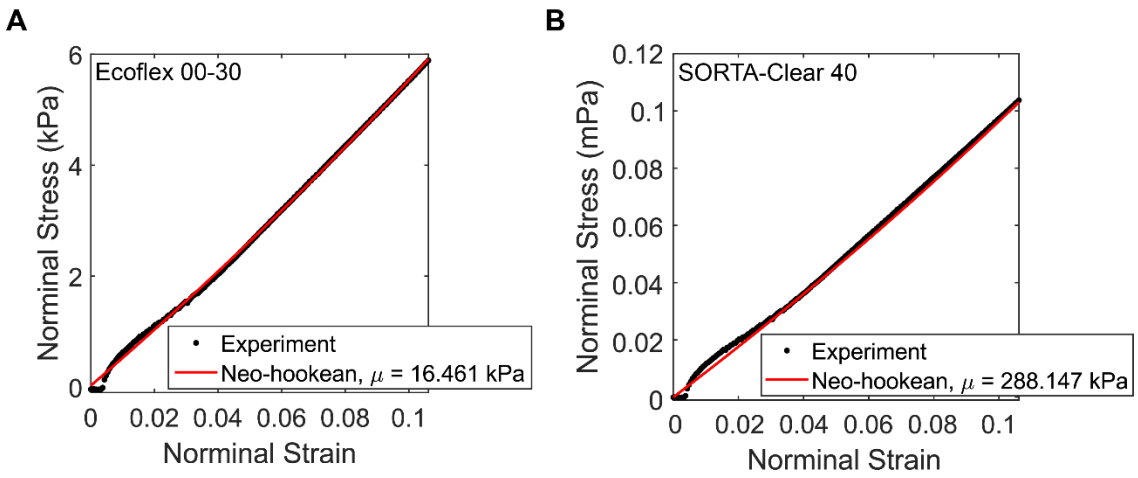

Appendix Figure 3.6 Characterization of the initial shear modulus for the silicone rubbers. (A and B) The relation between nominal stress and nominal strain in uniaxial compression tests for Ecoflex 00-30 (A) and SORTA-Clear (B). The black dots represent the experimental data, while the red lines represent the prediction of incompressible neo-Hookean model.

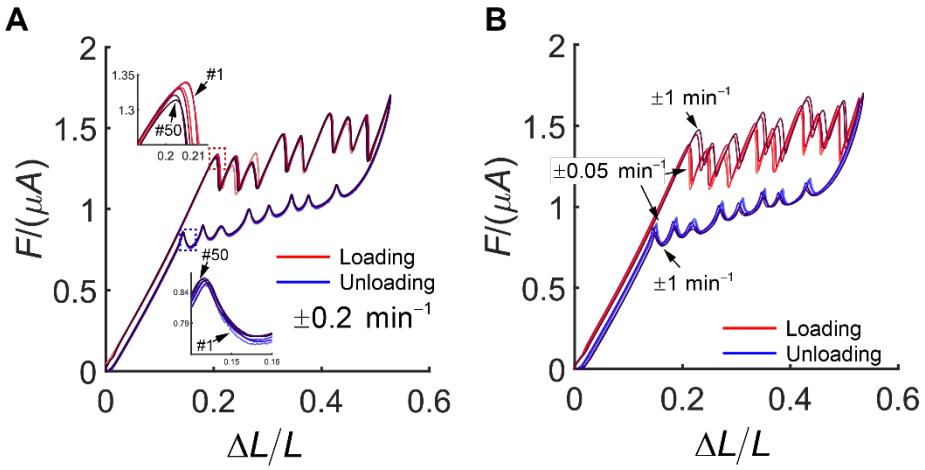

Appendix Figure 3.7 The effect of the number of loading cycles and the strain rates on the force-displacement relation of the sample when the displacement is controlled. (A) Every tenth of the 50 force-displacement measurements with strain rate ±0.2 min^{-1} is plotted. The force-displacement behavior is barely affected by the number of the loading cycles. (B) The force-displacement

measurements under different strain rates ranging from ±0.05 min^{-1} to ±1 min^{-1}. The strain rate has a very limited effect on the force-displacement behavior

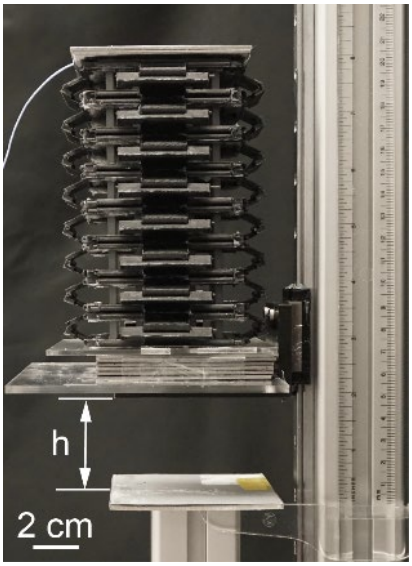

Appendix Figure 3.8 Setup of the drop test. The sample together with some steel plates attached to its bottom was dropped from different heights *h* ranging from 1 cm to 20 cm. The total weight dropped is 1.142 kg. A slider on a rail was used to guide the fall of the sample. A piezoelectric accelerometer was attached onto the top plate of the sample to record its acceleration.

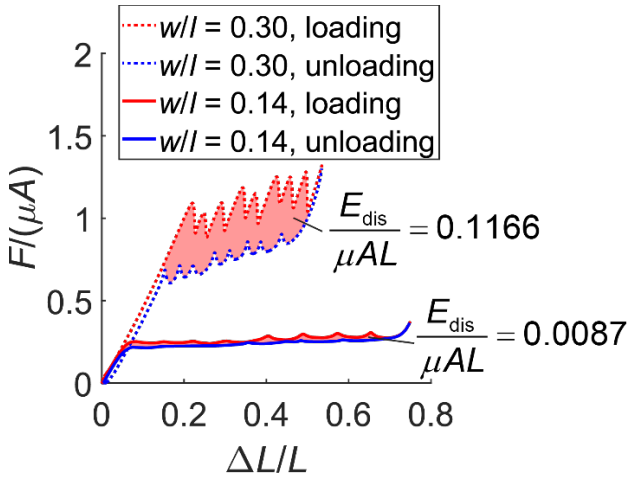

Appendix Figure 3.9 The loading (red) and unloading (blue) curves of 8-layered architected materials with columns of w/l = 0.30 (dashed) and 0.14 (solid). The shaded areas enclosed by the loading and unloading curves denote the normalized dissipated energy $E_{\mathrm{dis}}/\mu AL$.

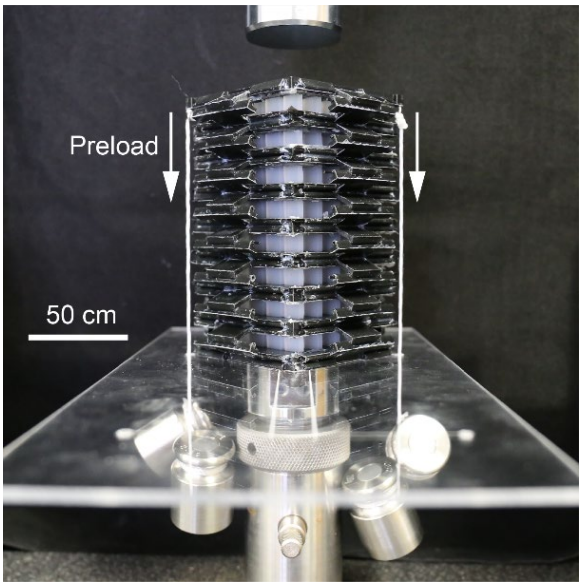

Appendix Figure 3.10 The method of applying preloads on the proposed architected materials. As preloads, some weight balances are hung on the two sides of the top layer of the material.

A3.7 Videos

Appendix Video 3.1 The displacement-controlled force-displacement response of the 8-layered architected material with columns of $w/l = 0.30$.

Appendix Video 3.2 Drop test for the proposed architected material when the energy input E_{inp} = 1.8 J.

Appendix Video 3.3 The displacement-controlled force-displacement response of the 8-layered architected material with columns of $w/l = 0.14$.

Appendix Video 3.4 The displacement-controlled force-displacement response of the 8-layered architected material with columns of $w/l = 0.30$ when a preload $0.4F_{cr}$ is applied.

Appendix Video 3.5 The displacement-controlled force-displacement response of the 8-layered architected material with columns of $w/l = 0.30$ when a preload $0.7F_{cr}$ is applied.

Appendix 4 Supplementary Materials for Blueprinting Photothermal Shape-morphing of Liquid Crystal Elastomers

A4.1 Constitutive Model of LCEs for FEM Simulations

We use the commercial software Abaqus/Standard for our finite element simulations. We implemented the following neo-classical free energy density [187] for LCEs in Abaqus by writing a user-defined material subroutine (UMAT)

$$\psi = \frac{\mu}{2}[\mathrm{Tr}(\tilde{\boldsymbol{g}}^{-1}\mathbf{F}\tilde{\boldsymbol{g}}_0\mathbf{F}^{\mathrm{T}}) - 3] + \frac{K}{2}(J-1)^2 - \mu \ln J, \tag{A4.1}$$

where μ is the shear modulus, K is the bulk modulus, $\mathbf{F}$ is the deformation gradient and $J = \det(\mathbf{F})$, $\tilde{\boldsymbol{g}}$ is a temperature-dependent three-dimensional metric tensor that describes the anisotropy of LCEs with respect to the isotropic phase in the current configuration [186], and $\tilde{\boldsymbol{g}}_0$ denotes $\tilde{\boldsymbol{g}}$ in the reference configuration which is selected as the nematic phase at temperature T = 60℃. The metric tensor $\tilde{\boldsymbol{g}}$ can be expressed as

$$\tilde{\boldsymbol{g}} = \tilde{g}_\perp \left[\mathbf{I} + \left(\frac{\tilde{g}_\parallel}{\tilde{g}_\perp} - 1\right)\boldsymbol{n}\otimes\boldsymbol{n}\right], \boldsymbol{n} = \frac{\mathbf{F}\boldsymbol{n}_0}{|\mathbf{F}\boldsymbol{n}_0|}, \tag{A4.2}$$

where $\tilde{g}_\parallel$ and $\tilde{g}_\perp$ are eigenvalues of $\tilde{\boldsymbol{g}}$ parallel and orthogonal to the director and $\tilde{g}_\parallel \tilde{g}_\perp^2 = 1$, $\boldsymbol{I}$ is a 3-by-3 identity matrix, $\boldsymbol{n}$ is a unit vector along the director, and $\boldsymbol{n}_0$ denotes $\boldsymbol{n}$ in the reference configuration. The stretch λ relates to the metric tensors by

$$\lambda = \sqrt{\tilde{g}_\parallel / \tilde{g}_{0\parallel}}, \tag{A4.3}$$

where $\tilde{g}_{0\parallel}$ is the eigenvalue of $\tilde{\boldsymbol{g}}_0$ parallel to the director. To determine the dependence of $\tilde{g}_\parallel$ and $\tilde{g}_\perp$ on temperature, we fit the stretch-temperature relation to the experimental data (Figure 6.1C) and obtain

$$\lambda = 0.6\sqrt{1 + 1.778\frac{120-T}{60}}, \tag{A4.4}$$

where T denotes temperature within the range of 60℃ to 120 ℃. The stretch $\lambda_\perp$ perpendicular to the director (Figure 6.1C) can be calculated based on incompressibility

$$\lambda_\perp = \sqrt{1/\lambda}. \tag{A4.5}$$

Equations (A4.4) and (A4.5) indicate that upon heating, LCEs transition from the nematic phase (T = 60℃) to the isotropic phase (T = 120℃), yielding a contractive stretch of 0.6 and a tensile stretch of 1.29 parallel and orthogonal to the director, respectively. From the definition of the metric tensor, we know that $\tilde{g}_\parallel(T = 120℃) = 1$, and therefore, according to Equation (A4.3), we have $\tilde{g}_{0\parallel} = 1/\lambda^2(T = 120℃)$ = 2.778. Based on Equations (A4.3) and (A4.4), the dependence of $\tilde{g}_\parallel$ on temperature can be expressed as

$$\tilde{g}_\parallel = 1 + 1.778\frac{120-T}{60}, \tag{A4.6}$$

and $\tilde{g}_\perp$ can be obtained by $\tilde{g}_\perp = \sqrt{1/\tilde{g}_\parallel}$.

A4.2 Stretch Profiles for Given Constant Gaussian Curvature

We obtain the stretch profiles giving constant Gaussian curvature by numerically solving Equation (6.8). The target constant (non-dimensional) Gaussian curvature Kw^2 is ± 0.8. Equation (6.8) can be solved using Matlab ODE45 solver with a relative error tolerance of $1\text{x}10^{-10}$. The initial conditions are adjusted such that the stretches are experimentally accessible in our system. To define a stretch profile yielding the same Gaussian curvature as the target one, we fit a 9^{th}-order polynomial to the solution such that the relative error of the obtained Gaussian curvature is less than $1\text{x}10^{-6}$. As a result, the stretch profile corresponding to positive Gaussian curvature 0.8 is

$$\lambda(v) = 0.0008016v^9 - 0.008048v^8 + 0.02585v^7 - 0.05128v^6 + 0.07006v^5 - 0.09382v^4 + 0.1015v^3 - 0.4649v^2 + 0.45v + 0.78, \quad \text{(A4.7)}$$

and the stretch profile corresponding to negative Gaussian curvature -0.8 is

$$\lambda(v) = -0.0003549v^9 - 0.002021v^8 + 0.01206v^7 - 0.01331v^6 - 0.007834v^5 - 0.00651v^4 + 0.04632v^3 + 0.3555v^2 - 0.4v + 0.9. \quad \text{(A4.8)}$$

A4.3 Supplementary Figures

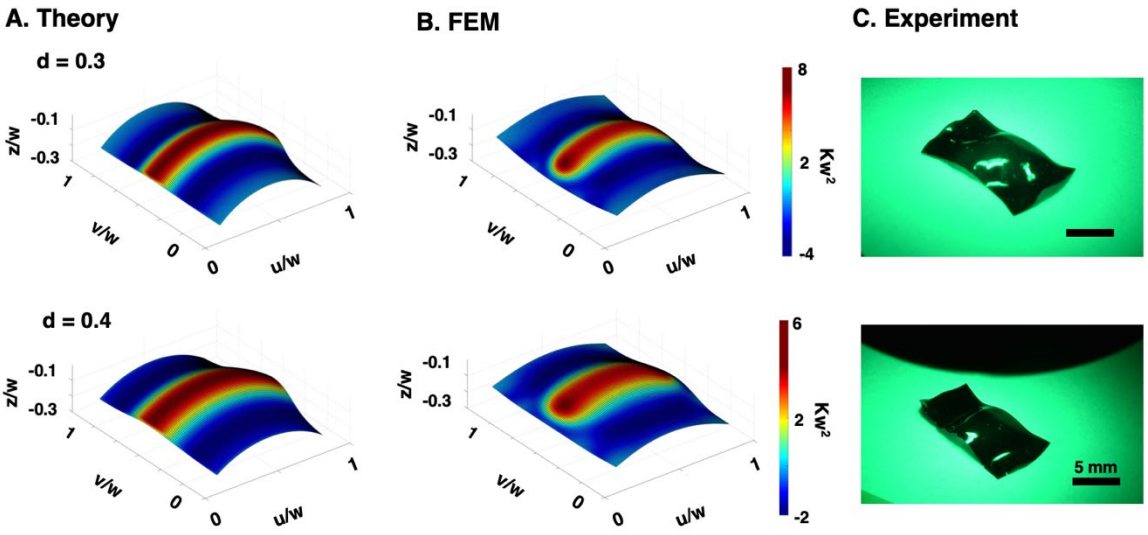

Appendix Figure 4.1 Shape predicted by (A) Theory and (B) FEM for Gaussian stretch profiles with $d = 0.3$ (top row) and $d = 0.4$ (bottom row). (C) Experiments match the predicted shape.

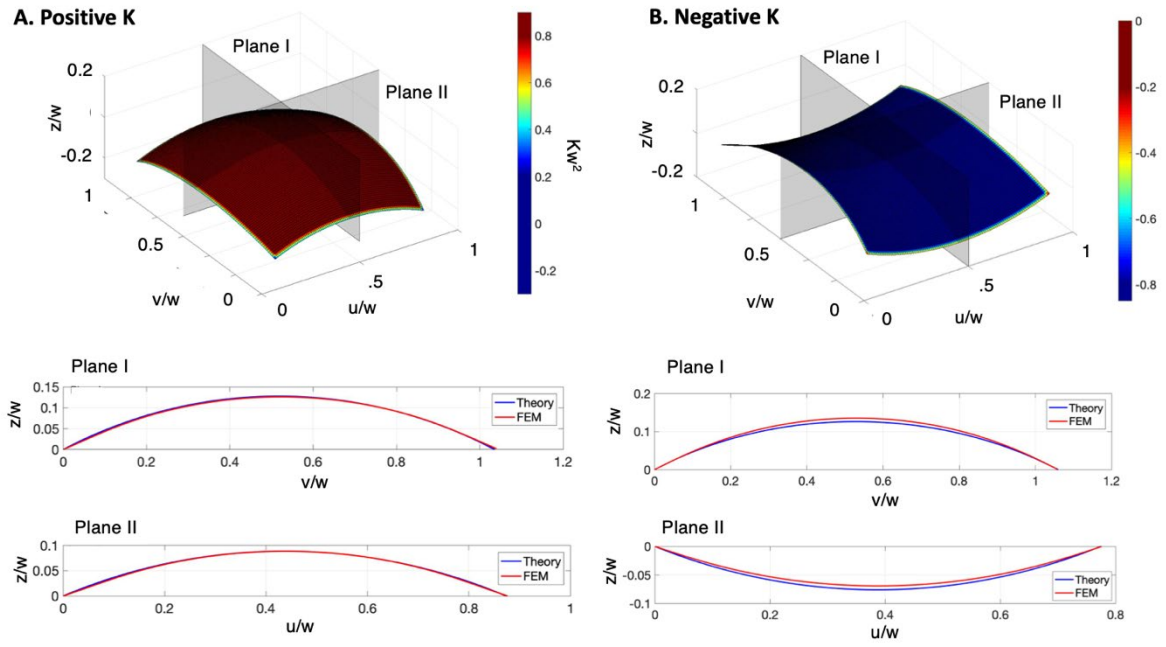

Appendix Figure 4.2 Comparison of curvature predicted by theory and FEM for (A) positive Gaussian curvature and (B) negative Gaussian curvature.

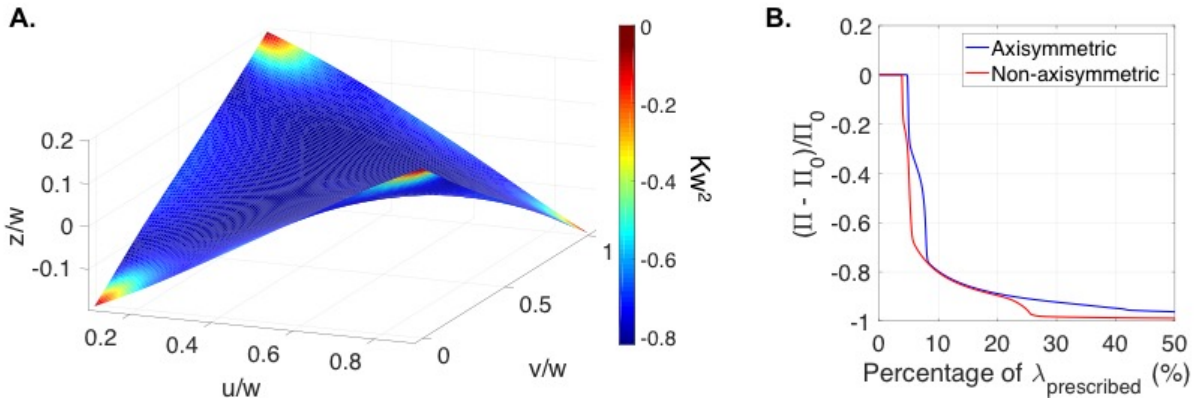

Appendix Figure 4.3 (A) Non-axisymmetric mode predicted by the FEM for the prescribed constant negative Gaussian curvature via the stretch profile shown in Figure 4A. (B) Normalized free energy difference between the curved states Π and the flat state Π_0 as a function of percentage of prescribed stretches $\lambda_{prescribed}$. The non-axisymmetric mode bifurcates from the flat state at a

lower stretch and is energetically preferred. To achieve the axisymmetric mode in the FEM simulations, a symmetric boundary condition about $u/w = 0.5$ is applied. The non-axisymmetric mode, however, has free boundary conditions in the FEM simulations.

Reference

[1] Z.P. Bažant, L. Cedolin, Stability of structures: elastic, inelastic, fracture and damage theories, World Scientific ed, World Scientific Pub, Hackensack, NJ ; London, 2010.

[2] D. Restrepo, N.D. Mankame, P.D. Zavattieri, Phase transforming cellular materials, Extreme Mech. Lett. 4 (2015) 52–60.

[3] T. Frenzel, C. Findeisen, M. Kadic, P. Gumbsch, M. Wegener, Tailored Buckling Microlattices as Reusable Light-Weight Shock Absorbers, Adv. Mater. 28 (2016) 5865–5870. https://doi.org/10.1002/adma.201600610.

[4] S. Shan, S.H. Kang, J.R. Raney, P. Wang, L. Fang, F. Candido, J.A. Lewis, K. Bertoldi, Multistable architected materials for trapping elastic strain energy, Adv. Mater. 27 (2015) 4296–4301.

[5] A. Rafsanjani, A. Akbarzadeh, D. Pasini, Snapping Mechanical Metamaterials under Tension, Adv. Mater. 27 (2015) 5931–5935. https://doi.org/10.1002/adma.201502809.

[6] D.P. Holmes, A.J. Crosby, Snapping Surfaces, Adv Mater. (2007) 5.

[7] A. Pandey, D.E. Moulton, D. Vella, D.P. Holmes, Dynamics of snapping beams and jumping poppers, (n.d.) 7.

[8] R.H. Plaut, Snap-through of arches and buckled beams under unilateral displacement control, Int. J. Solids Struct. (2015) 5.

[9] J. Hutchinson, Buckling and initial postbuckling behavior of oval cylindrical shells under axial compression, (1968).

[10] R.M. Neville, R.M. Groh, A. Pirrera, M. Schenk, Shape control for experimental continuation, Phys. Rev. Lett. 120 (2018) 254101.

[11] K.A. Serikawa, D.F. Mandoli, An analysis of morphogenesis of the reproductive whorl of Acetabularia acetabulum, Planta. 207 (1998) 96–104.

[12] H. Liang, L. Mahadevan, Growth, geometry, and mechanics of a blooming lily, Comput. Biol. (n.d.) 6.

[13] S. Armon, E. Efrati, R. Kupferman, E. Sharon, Geometry and Mechanics in the Opening of Chiral Seed Pods, 333 (2011) 6.

[14] S. Armon, H. Aharoni, M. Moshe, E. Sharon, Shape selection in chiral ribbons: from seed pods to supramolecular assemblies, Soft Matter. 10 (2014) 2733. https://doi.org/10.1039/c3sm52313f.

[15] F. Xu, C. Fu, Y. Yang, Water Affects Morphogenesis of Growing Aquatic Plant Leaves, Phys. Rev. Lett. (2020) 6.

[16] Y. Klein, E. Efrati, E. Sharon, Shaping of elastic sheets by prescription of non-Euclidean metrics, Science. 315 (2007) 1116–1120.

[17] J. Kim, J.A. Hanna, M. Byun, C.D. Santangelo, R.C. Hayward, Designing responsive buckled surfaces by halftone gel lithography, Science. 335 (2012) 1201–1205.

[18] J. Kim, J.A. Hanna, R.C. Hayward, C.D. Santangelo, Thermally responsive rolling of thin gel strips with discrete variations in swelling, Soft Matter. 8 (2012) 2375. https://doi.org/10.1039/c2sm06681e.

[19] Z.L. Wu, M. Moshe, J. Greener, H. Therien-Aubin, Z. Nie, E. Sharon, E. Kumacheva, Three-dimensional shape transformations of hydrogel sheets induced by small-scale modulation of internal stresses, Nat. Commun. 4 (2013) 1–7.

[20] T. Savin, On the growth and form of the gut, (n.d.) 7.

[21] J.W. Boley, W.M. van Rees, C. Lissandrello, M.N. Horenstein, R.L. Truby, A. Kotikian, J.A. Lewis, L. Mahadevan, Shape-shifting structured lattices via multimaterial 4D printing, Proc. Natl. Acad. Sci. 116 (2019) 20856–20862.

[22] E. Efrati, E. Sharon, R. Kupferman, Elastic theory of unconstrained non-Euclidean plates, J. Mech. Phys. Solids. 57 (2009) 762–775. https://doi.org/10.1016/j.jmps.2008.12.004.

[23] E. Efrati, E. Sharon, R. Kupferman, Buckling transition and boundary layer in non-Euclidean plates, Phys. Rev. E. 80 (2009) 016602. https://doi.org/10.1103/PhysRevE.80.016602.

[24] E. Sharon, E. Efrati, The mechanics of non-Euclidean plates, Soft Matter. 6 (2010) 5693. https://doi.org/10.1039/c0sm00479k.

[25] E. Efrati, E. Sharon, R. Kupferman, The metric description of elasticity in residually stressed soft materials, Soft Matter. 9 (2013) 8187. https://doi.org/10.1039/c3sm50660f.

[26] C.M. Soukoulis, Past achievements and future challenges in the development of three-dimensional photonic metamaterials, Nat. Photonics. 5 (2011) 8.

[27] O.R. Bilal, A. Foehr, C. Daraio, Bistable metamaterial for switching and cascading elastic vibrations, (n.d.) 4.

[28] K. Bertoldi, P.M. Reis, S. Willshaw, T. Mullin, Negative Poisson's ratio behavior induced by an elastic instability, Adv. Mater. 22 (2010) 361–366.

[29] J. Shim, C. Perdigou, E.R. Chen, K. Bertoldi, P.M. Reis, Buckling-induced encapsulation of structured elastic shells under pressure, Proc. Natl. Acad. Sci. 109 (2012) 5978–5983.

[30] S.H. Kang, S. Shan, A. Košmrlj, W.L. Noorduin, S. Shian, J.C. Weaver, D.R. Clarke, K. Bertoldi, Complex Ordered Patterns in Mechanical Instability Induced Geometrically Frustrated Triangular Cellular Structures, Phys. Rev. Lett. 112 (2014) 098701. https://doi.org/10.1103/PhysRevLett.112.098701.

[31] J.T. Overvelde, K. Bertoldi, Relating pore shape to the non-linear response of periodic elastomeric structures, J. Mech. Phys. Solids. 64 (2014) 351–366.

[32] S.H. Kang, S. Shan, W.L. Noorduin, M. Khan, J. Aizenberg, K. Bertoldi, Buckling-Induced Reversible Symmetry Breaking and Amplification of Chirality Using Supported Cellular Structures, Adv Mater. (2013) 6.

[33] S. Singamaneni, K. Bertoldi, S. Chang, J.-H. Jang, L. Young, E.L. Thomas, M.C. Boyce, V.V. Tsukruk, Bifurcated Mechanical Behavior of Deformed Periodic Porous Solids, Adv Funct Mater. (2009) 12.

[34] K. Bertoldi, M.C. Boyce, S. Deschanel, S. Prange, T. Mullin, Mechanics of deformation-triggered pattern transformations and superelastic behavior in periodic elastomeric structures, J. Mech. Phys. Solids. 56 (2008) 2642–2668.

[35] T. Mullin, S. Deschanel, K. Bertoldi, M.C. Boyce, Pattern transformation triggered by deformation, Phys. Rev. Lett. 99 (2007) 084301.

[36] G. Wang, M. Li, J. Zhou, Switching of deformation modes in soft mechanical metamaterials, Soft Mater. 14 (2016) 180–186.

[37] K.-I. Jang, Soft network composite materials with deterministic and bio-inspired designs, Nat. Commun. (2015) 11.

[38] A. Rafsanjani, D. Pasini, Bistable auxetic mechanical metamaterials inspired by ancient geometric motifs, Extreme Mech. Lett. 9 (2016) 291–296. https://doi.org/10.1016/j.eml.2016.09.001.

[39] C. Coulais, E. Teomy, K. De Reus, Y. Shokef, M. Van Hecke, Combinatorial design of textured mechanical metamaterials, Nature. 535 (2016) 529–532.

[40] O. Mesa, S. Norman, Non-Linear Matters: Auxetic Surfaces, (2017) 13.

[41] D. Yang, L. Jin, R.V. Martinez, K. Bertoldi, G.M. Whitesides, Z. Suo, Phase-transforming and switchable metamaterials, Extreme Mech. Lett. 6 (2016) 1–9.

[42] B. Florijn, C. Coulais, M. van Hecke, Programmable mechanical metamaterials: the role of geometry, Soft Matter. 12 (2016) 8736–8743.

[43] B. Florijn, C. Coulais, M. van Hecke, Programmable mechanical metamaterials, Phys. Rev. Lett. 113 (2014) 175503.

[44] J.L. Silverberg, A.A. Evans, L. McLeod, R.C. Hayward, T. Hull, C.D. Santangelo, I. Cohen, Using origami design principles to fold reprogrammable mechanical metamaterials, (n.d.) 5.

[45] D. Okumura, Effect of prestrains on swelling-induced buckling patterns in gel films with a square lattice of holes, Int. J. Solids Struct. (2015) 13.

[46] A. Rafsanjani, K. Bertoldi, Buckling-Induced Kirigami, Phys. Rev. Lett. (2017) 5.

[47] K. Otsuka, C.M. Wayman, Shape memory materials, Cambridge university press, 1999.

[48] A. Pal, D. Goswami, R.V. Martinez, Elastic Energy Storage Enables Rapid and Programmable Actuation in Soft Machines, Adv. Funct. Mater. 30 (2020) 1906603. https://doi.org/10.1002/adfm.201906603.

[49] T. Chen, O.R. Bilal, K. Shea, C. Daraio, Harnessing bistability for directional propulsion of soft, untethered robots, Proc. Natl. Acad. Sci. 115 (2018) 5698–5702. https://doi.org/10.1073/pnas.1800386115.

[50] Y. Tang, Y. Chi, J. Sun, T.-H. Huang, O.H. Maghsoudi, A. Spence, J. Zhao, H. Su, J. Yin, Leveraging elastic instabilities for amplified performance: Spine-inspired high-speed and high-force soft robots, Sci. Adv. 6 (2020) eaaz6912.

[51] L.J. Gibson, M.F. Ashby, Cellular solids: structure and properties, Cambridge university press, 1999.

[52] L. Salari-Sharif, T.A. Schaedler, L. Valdevit, Energy dissipation mechanisms in hollow metallic microlattices, J. Mater. Res. 29 (2014) 1755–1770. https://doi.org/10.1557/jmr.2014.226.

[53] G. Lu, T.X. Yu, Energy absorption of structures and materials, CRC Press ; Woodhead Pub. Ltd, Boca Raton : Cambridge, England, 2003.

[54] M.C. Constantinou, M. Symans, Experimental and analytical investigation of seismic response of structures with supplemental fluid viscous dampers, National Center for earthquake engineering research Buffalo, NY, 1992.

[55] L. Wang, J. Lau, E.L. Thomas, M.C. Boyce, Co-Continuous Composite Materials for Stiffness, Strength, and Energy Dissipation, Adv. Mater. 23 (2011) 1524–1529. https://doi.org/10.1002/adma.201003956.

[56] P. Zhang, M.A. Heyne, A.C. To, Biomimetic staggered composites with highly enhanced energy dissipation: Modeling, 3D printing, and testing, J. Mech. Phys. Solids. 83 (2015) 285–300. https://doi.org/10.1016/j.jmps.2015.06.015.

[57] R. Wang, J. Shang, X. Li, Z. Luo, W. Wu, Vibration and damping characteristics of 3D printed Kagome lattice with viscoelastic material filling, Sci. Rep. 8 (2018) 9604. https://doi.org/10.1038/s41598-018-27963-4.

[58] J.M. Bajkowski, B. Dyniewicz, C.I. Bajer, Semi-active damping strategy for beams system with pneumatically controlled granular structure, Mech. Syst. Signal Process. 70–71 (2016) 387–396. https://doi.org/10.1016/j.ymssp.2015.09.026.

[59] K. Fu, Z. Zhao, L. Jin, Programmable Granular Metamaterials for Reusable Energy Absorption, Adv. Funct. Mater. 29 (2019) 1901258. https://doi.org/10.1002/adfm.201901258.

[60] Y. Wang, B. Ramirez, K. Carpenter, C. Naify, D.C. Hofmann, C. Daraio, Architected lattices with adaptive energy absorption, Extreme Mech. Lett. 33 (2019) 100557. https://doi.org/10.1016/j.eml.2019.100557.

[61] D.M. Correa, T. Klatt, S. Cortes, M. Haberman, D. Kovar, C. Seepersad, Negative stiffness honeycombs for recoverable shock isolation, Rapid Prototyp. J. 21 (2015) 193–200. https://doi.org/10.1108/RPJ-12-2014-0182.

[62] B. Haghpanah, L. Salari-Sharif, P. Pourrajab, J. Hopkins, L. Valdevit, Multistable Shape-Reconfigurable Architected Materials, Adv. Mater. 28 (2016) 7915–7920. https://doi.org/10.1002/adma.201601650.

[63] N. Kidambi, R.L. Harne, K.W. Wang, Energy capture and storage in asymmetrically multistable modular structures inspired by skeletal muscle, Smart Mater. Struct. 26 (2017) 085011. https://doi.org/10.1088/1361-665X/aa721a.

[64] C.S. Ha, R.S. Lakes, M.E. Plesha, Design, fabrication, and analysis of lattice exhibiting energy absorption via snap-through behavior, Mater. Des. 141 (2018) 426–437. https://doi.org/10.1016/j.matdes.2017.12.050.

[65] H. Yang, L. Ma, Multi-stable mechanical metamaterials with shape-reconfiguration and zero Poisson's ratio, Mater. Des. 152 (2018) 181–190. https://doi.org/10.1016/j.matdes.2018.04.064.

[66] F. Pan, Y. Li, Z. Li, J. Yang, B. Liu, Y. Chen, 3D Pixel Mechanical Metamaterials, Adv. Mater. 31 (2019) 1900548. https://doi.org/10.1002/adma.201900548.

[67] C. Morris, L. Bekker, C. Spadaccini, M. Haberman, C. Seepersad, Tunable Mechanical Metamaterial with Constrained Negative Stiffness for Improved Quasi-Static and Dynamic Energy Dissipation, Adv. Eng. Mater. 21 (2019) 1900163. https://doi.org/10.1002/adem.201900163.

[68] H. Yang, L. Ma, Multi-stable mechanical metamaterials by elastic buckling instability, J. Mater. Sci. 54 (2019) 3509–3526. https://doi.org/10.1007/s10853-018-3065-y.

[69] Y. Zhang, D. Restrepo, M. Velay-Lizancos, N.D. Mankame, P.D. Zavattieri, Energy dissipation in functionally two-dimensional phase transforming cellular materials, Sci. Rep. 9 (2019) 12581. https://doi.org/10.1038/s41598-019-48581-8.

[70] Y. Zhang, Q. Wang, M. Tichem, F. van Keulen, Design and characterization of multi-stable mechanical metastructures with level and tilted stable configurations, Extreme Mech. Lett. 34 (2020) 100593. https://doi.org/10.1016/j.eml.2019.100593.

[71] E.G. Karpov, D. Ozevin, M. Mahamid, L.A. Danso, On the comprehensive stability analysis of axially loaded bistable and tristable metastructures, Int. J. Solids Struct. 199 (2020) 158–168. https://doi.org/10.1016/j.ijsolstr.2020.04.032.

[72] Z. Vangelatos, A. Micheletti, C.P. Grigoropoulos, F. Fraternali, Design and Testing of Bistable Lattices with Tensegrity Architecture and Nanoscale Features Fabricated by Multiphoton Lithography, Nanomaterials. 10 (2020) 652. https://doi.org/10.3390/nano10040652.

[73] S. Sun, N. An, G. Wang, M. Li, J. Zhou, Snap-back induced hysteresis in an elastic mechanical metamaterial under tension, Appl. Phys. Lett. 115 (2019) 091901. https://doi.org/10.1063/1.5119275.

[74] G. Puglisi, L. Truskinovsky, Mechanics of a discrete chain with bi-stable elements, J. Mech. Phys. Solids. 48 (2000) 1–27.

[75] M. Warner, E.M. Terentjev, Liquid crystal elastomers, Oxford University Press, Oxford, 2003.

[76] S. Krause, F. Zander, G. Bergmann, H. Brandt, H. Wertmer, H. Finkelmann, Nematic main-chain elastomers: Coupling and orientational behavior, Comptes Rendus Chim. 12 (2009) 85–104. https://doi.org/10.1016/j.crci.2008.08.003.

[77] H.K. Bisoyi, Q. Li, Light-Driven Liquid Crystalline Materials: From Photo-Induced Phase Transitions and Property Modulations to Applications, Chem. Rev. 116 (2016) 15089–15166. https://doi.org/10.1021/acs.chemrev.6b00415.

[78] Y. Yu, M. Nakano, T. Ikeda, Directed bending of a polymer film by light, Nature. 425 (2003) 145–145. https://doi.org/10.1038/425145a.

[79] C.M. Spillmann, J. Naciri, B.D. Martin, W. Farahat, H. Herr, B.R. Ratna, Stacking nematic elastomers for artificial muscle applications, Sens. Actuators Phys. 133 (2007) 500–505. https://doi.org/10.1016/j.sna.2006.04.045.

[80] Q. He, Z. Wang, Z. Song, S. Cai, Bioinspired Design of Vascular Artificial Muscle, Adv. Mater. Technol. 4 (2019) 1800244. https://doi.org/10.1002/admt.201800244.

[81] M. Rogóż, H. Zeng, C. Xuan, D.S. Wiersma, P. Wasylczyk, Light-Driven Soft Robot Mimics Caterpillar Locomotion in Natural Scale, Adv. Opt. Mater. 4 (2016) 1689–1694. https://doi.org/10.1002/adom.201600503.

[82] A.W. Hauser, D. Liu, K.C. Bryson, R.C. Hayward, D.J. Broer, Reconfiguring nanocomposite liquid crystal polymer films with visible light, Macromolecules. 49 (2016) 1575–1581.

[83] M. Lahikainen, H. Zeng, A. Priimagi, Reconfigurable photoactuator through synergistic use of photochemical and photothermal effects, Nat. Commun. 9 (2018) 1–8.

[84] J. Lv, Y. Liu, J. Wei, E. Chen, L. Qin, Y. Yu, Photocontrol of fluid slugs in liquid crystal polymer microactuators, Nature. 537 (2016) 179–184.

[85] M.K. McBride, M. Hendrikx, D. Liu, B.T. Worrell, D.J. Broer, C.N. Bowman, Photoinduced Plasticity in Cross-Linked Liquid Crystalline Networks, Adv. Mater. 29 (2017) 1606509.

[86] S. Ahn, T.H. Ware, K.M. Lee, V.P. Tondiglia, T.J. White, Photoinduced topographical feature development in blueprinted azobenzene-functionalized liquid crystalline elastomers, Adv. Funct. Mater. 26 (2016) 5819–5826.

[87] A.H. Gelebart, G. Vantomme, E. Meijer, D.J. Broer, Mastering the photothermal effect in liquid crystal networks: a general approach for self-sustained mechanical oscillators, Adv. Mater. 29 (2017) 1606712.

[88] H. Aharoni, Y. Xia, X. Zhang, R.D. Kamien, S. Yang, Universal inverse design of surfaces with thin nematic elastomer sheets, Proc. Natl. Acad. Sci. 115 (2018) 7206–7211.

[89] Y. Xia, G. Cedillo-Servin, R.D. Kamien, S. Yang, Guided folding of nematic liquid crystal elastomer sheets into 3D via patterned 1D microchannels, Adv. Mater. 28 (2016) 9637–9643.

[90] Z. Wang, Z. Wang, Y. Zheng, Q. He, Y. Wang, S. Cai, Three-dimensional printing of functionally graded liquid crystal elastomer, Sci. Adv. 6 (2020) eabc0034. https://doi.org/10.1126/sciadv.abc0034.

[91] T.H. Ware, M.E. McConney, J.J. Wie, V.P. Tondiglia, T.J. White, Voxelated liquid crystal elastomers, Science. 347 (2015) 982–984.

[92] A. Kotikian, R.L. Truby, J.W. Boley, T.J. White, J.A. Lewis, 3D printing of liquid crystal elastomeric actuators with spatially programed nematic order, Adv. Mater. 30 (2018) 1706164.

[93] A.S. Kuenstler, Y. Chen, P. Bui, H. Kim, A. DeSimone, L. Jin, R.C. Hayward, Blueprinting Photothermal Shape-Morphing of Liquid Crystal Elastomers, Adv. Mater. 32 (2020) 2000609. https://doi.org/10.1002/adma.202000609.

[94] X. Yu, J. Zhou, H. Liang, Z. Jiang, L. Wu, Mechanical metamaterials associated with stiffness, rigidity and compressibility: A brief review, Prog. Mater. Sci. 94 (2018) 114–173.

[95] A.A. Zadpoor, Mechanical meta-materials, Mater. Horiz. 3 (2016) 371–381.

[96] X. Zheng, H. Lee, T.H. Weisgraber, M. Shusteff, J. DeOtte, E.B. Duoss, J.D. Kuntz, M.M. Biener, Q. Ge, J.A. Jackson, Ultralight, ultrastiff mechanical metamaterials, Science. 344 (2014) 1373–1377.

[97] L.R. Meza, S. Das, J.R. Greer, Strong, lightweight, and recoverable three-dimensional ceramic nanolattices, Science. 345 (2014) 1322–1326. https://doi.org/10.1126/science.1255908.

[98] M. Kadic, T. Bückmann, N. Stenger, M. Thiel, M. Wegener, On the practicability of pentamode mechanical metamaterials, Appl. Phys. Lett. 100 (2012) 191901.

[99] A.V. Cherkaev, Which elasticity tensors are realizable, J Eng Mater Technol. 117 (1995) 483–493.

[100] T. Bückmann, M. Kadic, R. Schittny, M. Wegener, Mechanical metamaterials with anisotropic and negative effective mass-density tensor made from one constituent material, Phys. Status Solidi B. 252 (2015) 1671–1674.

[101] R. Lakes, Foam structures with a negative Poisson's ratio, Science. 235 (1987) 1038–1041.

[102] G.W. Milton, Composite materials with Poisson's ratios close to—1, J. Mech. Phys. Solids. 40 (1992) 1105–1137.

[103] J.N. Grima, K.E. Evans, Auxetic behavior from rotating squares, (2000).

[104] G.N. Greaves, A. Greer, R.S. Lakes, T. Rouxel, Poisson's ratio and modern materials, Nat. Mater. 10 (2011) 823–837.

[105] K. Sun, A. Souslov, X. Mao, T. Lubensky, Isostaticity, auxetic response, surface modes, and conformal invariance in twisted kagome lattices, ArXiv Prepr. ArXiv11121109. (2011).

[106] L. Mizzi, K.M. Azzopardi, D. Attard, J.N. Grima, R. Gatt, Auxetic metamaterials exhibiting giant negative Poisson's ratios, Phys. Status Solidi RRL–Rapid Res. Lett. 9 (2015) 425–430.

[107] H. Yasuda, J. Yang, Reentrant origami-based metamaterials with negative Poisson's ratio and bistability, Phys. Rev. Lett. 114 (2015) 185502.

[108] T. Frenzel, M. Kadic, M. Wegener, Three-dimensional mechanical metamaterials with a twist, Science. 358 (2017) 1072–1074.

[109] J. Shim, S. Shan, A. Košmrlj, S.H. Kang, E.R. Chen, J.C. Weaver, K. Bertoldi, Harnessing instabilities for design of soft reconfigurable auxetic/chiral materials, Soft Matter. 9 (2013) 8198. https://doi.org/10.1039/c3sm51148k.

[110] D. Yang, B. Mosadegh, A. Ainla, B. Lee, F. Khashai, Z. Suo, K. Bertoldi, G.M. Whitesides, Buckling of elastomeric beams enables actuation of soft machines, Adv. Mater. 27 (2015) 6323–6327.

[111] K. Bertoldi, M. Boyce, Mechanically triggered transformations of phononic band gaps in periodic elastomeric structures, Phys. Rev. B. 77 (2008) 052105.

[112] K. Bertoldi, Harnessing Instabilities to Design Tunable Architected Cellular Materials, Annu. Rev. Mater. Res. 47 (2017) 51–61. https://doi.org/10.1146/annurev-matsci-070616-123908.

[113] C.G. Johnson, U. Jain, A.L. Hazel, D. Pihler-Puzović, T. Mullin, On the buckling of an elastic holey column, Proc. R. Soc. Math. Phys. Eng. Sci. 473 (2017) 20170477.

[114] Y. He, Y. Zhou, Z. Liu, K. Liew, Pattern transformation of single-material and composite periodic cellular structures, Mater. Des. 132 (2017) 375–384.

[115] P. Wang, J. Shim, K. Bertoldi, Effects of geometric and material nonlinearities on tunable band gaps and low-frequency directionality of phononic crystals, Phys. Rev. B. 88 (2013) 014304.

[116] R.W. Ogden, Non-linear elastic deformations, Courier Corporation, 1997.

[117] M.C. Boyce, E.M. Arruda, Constitutive models of rubber elasticity: a review, Rubber Chem. Technol. 73 (2000) 504–523.

[118] W. Koiter, Elastic Stability of Solids and Structures, Cambridge university press, Cambridge, 2009.

[119] C. Coulais, J.T. Overvelde, L.A. Lubbers, K. Bertoldi, M. van Hecke, Discontinuous buckling of wide beams and metabeams, Phys. Rev. Lett. 115 (2015) 044301.

[120] R.V. Martinez, J.L. Branch, C.R. Fish, L. Jin, R.F. Shepherd, R.M. Nunes, Z. Suo, G.M. Whitesides, Robotic tentacles with three-dimensional mobility based on flexible elastomers, Adv. Mater. 25 (2013) 205–212.

[121] J.T.B. Overvelde, S. Shan, K. Bertoldi, Compaction through buckling in 2D periodic, soft and porous structures: effect of pore shape, Adv. Mater. 24 (2012) 2337–2342.

[122] C. Coulais, A. Sabbadini, F. Vink, M. van Hecke, Multi-step self-guided pathways for shape-changing metamaterials, Nature. 561 (2018) 512–515.

[123] H. Niknam, A. Akbarzadeh, In-plane and out-of-plane buckling of architected cellular plates: Numerical and experimental study, Compos. Struct. 206 (2018) 739–749.

[124] A.G. Mark, S. Palagi, T. Qiu, P. Fischer, Auxetic metamaterial simplifies soft robot design, in: Ieee, 2016: pp. 4951–4956.

[125] P. Rothemund, A. Ainla, L. Belding, D.J. Preston, S. Kurihara, Z. Suo, G.M. Whitesides, A soft, bistable valve for autonomous control of soft actuators, Sci. Robot. 3 (2018).

[126] L.A. Lubbers, M. van Hecke, C. Coulais, A nonlinear beam model to describe the postbuckling of wide neo-Hookean beams, J. Mech. Phys. Solids. 106 (2017) 191–206.

[127] A. Gent, I. Cho, Surface instabilities in compressed or bent rubber blocks, Rubber Chem. Technol. 72 (1999) 253–262.

[128] A. Ghatak, A.L. Das, Kink instability of a highly deformable elastic cylinder, Phys. Rev. Lett. 99 (2007) 076101.

[129] E. Hohlfeld, L. Mahadevan, Unfolding the sulcus, Phys. Rev. Lett. 106 (2011) 105702.

[130] S. Cai, D. Chen, Z. Suo, R.C. Hayward, Creasing instability of elastomer films, Soft Matter. 8 (2012) 1301–1304.

[131] E. Hohlfeld, L. Mahadevan, Scale and nature of sulcification patterns, Phys. Rev. Lett. 109 (2012) 025701.

[132] D. Chen, L. Jin, Z. Suo, R.C. Hayward, Controlled formation and disappearance of creases, Mater. Horiz. 1 (2014) 207–213.

[133] L. Jin, Z. Suo, Smoothening creases on surfaces of strain-stiffening materials, J. Mech. Phys. Solids. 74 (2015) 68–79.

[134] C. Armanini, F. Dal Corso, D. Misseroni, D. Bigoni, From the elastica compass to the elastica catapult: an essay on the mechanics of soft robot arm, Proc. R. Soc. Math. Phys. Eng. Sci. 473 (2017) 20160870.

[135] A. Cazzolli, F. Dal Corso, Snapping of elastic strips with controlled ends, Int. J. Solids Struct. 162 (2019) 285–303.

[136] A. Humer, Exact solutions for the buckling and postbuckling of shear-deformable beams, Acta Mech. 224 (2013) 1493–1525.

[137] H. Irschik, J. Gerstmayr, A continuum mechanics based derivation of Reissner's large-displacement finite-strain beam theory: the case of plane deformations of originally straight Bernoulli–Euler beams, Acta Mech. 206 (2009) 1–21.

[138] D. Chen, S. Cai, Z. Suo, R.C. Hayward, Surface energy as a barrier to creasing of elastomer films: An elastic analogy to classical nucleation, Phys. Rev. Lett. 109 (2012) 038001.

[139] B. Budiansky, Theory of buckling and post-buckling behavior of elastic structures, in: Adv. Appl. Mech., Elsevier, 1974: pp. 1–65.

[140] N. Triantafyllidis, W. Scherzinger, H.-J. Huang, Post-bifurcation equilibria in the plane-strain test of a hyperelastic rectangular block, Int. J. Solids Struct. 44 (2007) 3700–3719.

[141] M. Golubitsky, I. Stewart, D.G. Schaeffer, Singularities and Groups in Bifurcation Theory: Volume II, Springer Science & Business Media, 2012.

[142] T. Poston, I. Stewart, Catastrophe theory and its applications, Courier Corporation, 2014.

[143] K. Bertoldi, V. Vitelli, J. Christensen, M. Van Hecke, Flexible mechanical metamaterials, Nat. Rev. Mater. 2 (2017) 1–11.

[144] H. Qiu, Y. Li, T.F. Guo, X. Guo, S. Tang, Deformation and pattern transformation of porous soft solids under biaxial loading: Experiments and simulations, Extreme Mech. Lett. 20 (2018) 81–90.

[145] C. Yuan, X. Mu, C.K. Dunn, J. Haidar, T. Wang, H. Jerry Qi, Thermomechanically triggered two-stage pattern switching of 2D lattices for adaptive structures, Adv. Funct. Mater. 28 (2018) 1705727.

[146] P. Celli, C. McMahan, B. Ramirez, A. Bauhofer, C. Naify, D. Hofmann, B. Audoly, C. Daraio, Shape-morphing architected sheets with non-periodic cut patterns, Soft Matter. 14 (2018) 9744–9749.

[147] E. Reissner, On one-dimensional large-displacement finite-strain beam theory, Stud. Appl. Math. 52 (1973) 87–95.

[148] G. Yoshiaki, Y. Tomoo, O. Makoto, Elliptic integral solutions of plane elastica with axial and shear deformations, Int. J. Solids Struct. 26 (1990) 375–390.

[149] S.P. Timoshenko, J.M. Gere, Theory of elastic stability, Courier Corporation, 2009.

[150] M.A. Biot, Exact theory of buckling of a thick slab, Appl. Sci. Res. Sect. A. 12 (1963) 183–198.

[151] M. Levinson, Stability of a compressed neo-Hookean rectangular parallelepiped, J. Mech. Phys. Solids. 16 (1968) 403–408.

[152] K. Sawyers, R. Rivlin, Bifurcation conditions for a thick elastic plate under thrust, Int. J. Solids Struct. 10 (1974) 483–501.

[153] N. Young, Bifurcation phenomena in the plane compression test, J. Mech. Phys. Solids. 24 (1976) 77–91.

[154] R. Ogden, D. Roxburgh, The effect of pre-stress on the vibration and stability of elastic plates, Int. J. Eng. Sci. 31 (1993) 1611–1639.

[155] D. Roxburgh, R. Ogden, Stability and vibration of pre-stressed compressible elastic plates, Int. J. Eng. Sci. 32 (1994) 427–454.

[156] Y. Cao, J.W. Hutchinson, From wrinkles to creases in elastomers: the instability and imperfection-sensitivity of wrinkling, Proc. R. Soc. Math. Phys. Eng. Sci. 468 (2012) 94–115.

[157] H.-H. Dai, Y. Wang, F.-F. Wang, Primary and secondary bifurcations of a compressible hyperelastic layer: Asymptotic model equations and solutions, Int. J. Non-Linear Mech. 52 (2013) 58–72.

[158] H.-H. Dai, F.-F. Wang, J. Wang, J. Xu, Pitchfork and octopus bifurcations in a hyperelastic tube subjected to compression: Analytical post-bifurcation solutions and imperfection sensitivity, Math. Mech. Solids. 20 (2015) 25–52.

[159] A.A. Almet, H.M. Byrne, P.K. Maini, D.E. Moulton, Post-buckling behaviour of a growing elastic rod, J. Math. Biol. 78 (2019) 777–814.

[160] W. Hong, X. Zhao, Z. Suo, Formation of creases on the surfaces of elastomers and gels, Appl. Phys. Lett. 95 (2009) 111901.

[161] W. Hong, F. Gao, Crease instability on the surface of a solid, in: Mech. Self-Assem., Springer, 2013: pp. 111–130.

[162] B. Haghpanah, A. Shirazi, L. Salari-Sharif, A.G. Izard, L. Valdevit, Elastic architected materials with extreme damping capacity, Extreme Mech. Lett. 17 (2017) 56–61.

[163] I. Benichou, S. Givli, Structures undergoing discrete phase transformation, J. Mech. Phys. Solids. 61 (2013) 94–113. https://doi.org/10.1016/j.jmps.2012.08.009.

[164] A.S. Gladman, E.A. Matsumoto, R.G. Nuzzo, L. Mahadevan, J.A. Lewis, Biomimetic 4D printing, Nat. Mater. 15 (2016) 413–418.

[165] S.-J. Jeon, A.W. Hauser, R.C. Hayward, Shape-Morphing Materials from Stimuli-Responsive Hydrogel Hybrids, Acc. Chem. Res. 50 (2017) 161–169. https://doi.org/10.1021/acs.accounts.6b00570.

[166] T.J. White, D.J. Broer, Programmable and adaptive mechanics with liquid crystal polymer networks and elastomers, Nat. Mater. 14 (2015) 1087–1098.

[167] R.S. Kularatne, H. Kim, J.M. Boothby, T.H. Ware, Liquid crystal elastomer actuators: Synthesis, alignment, and applications, J. Polym. Sci. Part B Polym. Phys. 55 (2017) 395–411.

[168] B.A. Kowalski, V.P. Tondiglia, T. Guin, T.J. White, Voxel resolution in the directed self-assembly of liquid crystal polymer networks and elastomers, Soft Matter. 13 (2017) 4335–4340.

[169] Q. Zhao, H.J. Qi, T. Xie, Recent progress in shape memory polymer: New behavior, enabling materials, and mechanistic understanding, Prog. Polym. Sci. 49–50 (2015) 79–120. https://doi.org/10.1016/j.progpolymsci.2015.04.001.

[170] A. Lendlein, O.E. Gould, Reprogrammable recovery and actuation behaviour of shape-memory polymers, Nat. Rev. Mater. 4 (2019) 116–133.

[171] C.L. Randall, E. Gultepe, D.H. Gracias, Self-folding devices and materials for biomedical applications, Trends Biotechnol. 30 (2012) 138–146. https://doi.org/10.1016/j.tibtech.2011.06.013.

[172] L. Ionov, Polymeric Actuators, Langmuir. 31 (2015) 5015–5024. https://doi.org/10.1021/la503407z.

[173] C. Ohm, M. Brehmer, R. Zentel, Liquid Crystalline Elastomers as Actuators and Sensors, Adv. Mater. 22 (2010) 3366–3387. https://doi.org/10.1002/adma.200904059.

[174] J.L. Silverberg, J.-H. Na, A.A. Evans, B. Liu, T.C. Hull, C.D. Santangelo, R.J. Lang, R.C. Hayward, I. Cohen, Origami structures with a critical transition to bistability arising from hidden degrees of freedom, Nat. Mater. 14 (2015) 389–393. https://doi.org/10.1038/nmat4232.

[175] Y. Tang, Y. Li, Y. Hong, S. Yang, J. Yin, Programmable active kirigami metasheets with more freedom of actuation, Proc. Natl. Acad. Sci. 116 (2019) 26407–26413. https://doi.org/10.1073/pnas.1906435116.

[176] T. van Manen, S. Janbaz, A.A. Zadpoor, Programming the shape-shifting of flat soft matter, Mater. Today. 21 (2018) 144–163. https://doi.org/10.1016/j.mattod.2017.08.026.

[177] H. Aharoni, E. Sharon, R. Kupferman, Geometry of thin nematic elastomer sheets, Phys. Rev. Lett. 113 (2014) 257801.

[178] P. Plucinsky, B.A. Kowalski, T.J. White, K. Bhattacharya, Patterning nonisometric origami in nematic elastomer sheets, Soft Matter. 14 (2018) 3127–3134.

[179] B.A. Kowalski, C. Mostajeran, N.P. Godman, M. Warner, T.J. White, Curvature by design and on demand in liquid crystal elastomers, Phys. Rev. E. 97 (2018) 012504.

[180] B. Audoly, Y. Pomeau, Elasticity and geometry: from hair curls to the non-linear response of shells, Oxford university press, 2010.

[181] M.P. Do Carmo, Differential geometry of curves and surfaces: revised and updated second edition, Courier Dover Publications, 2016.

[182] M. Moshe, E. Sharon, R. Kupferman, Pattern selection and multiscale behaviour in metrically discontinuous non-Euclidean plates, Nonlinearity. 26 (2013) 3247–3258. https://doi.org/10.1088/0951-7715/26/12/3247.

[183] H.-H. Yoon, D.-Y. Kim, K.-U. Jeong, S. Ahn, Surface aligned main-chain liquid crystalline elastomers: Tailored properties by the choice of amine chain extenders, Macromolecules. 51 (2018) 1141–1149.

[184] A.S. Kuenstler, H. Kim, R.C. Hayward, Liquid crystal elastomer waveguide actuators, Adv. Mater. 31 (2019) 1901216.

[185] J.-H. Na, N.P. Bende, J. Bae, C.D. Santangelo, R.C. Hayward, Grayscale gel lithography for programmed buckling of non-Euclidean hydrogel plates, Soft Matter. 12 (2016) 4985–4990.

[186] L. Jin, Z. Zeng, Y. Huo, Thermomechanical modeling of the thermo-order–mechanical coupling behaviors in liquid crystal elastomers, J. Mech. Phys. Solids. 58 (2010) 1907–1927.

[187] P. Bladon, E. Terentjev, M. Warner, Transitions and instabilities in liquid crystal elastomers, Phys. Rev. E. 47 (1993) R3838.

[188] C. Ahn, X. Liang, S. Cai, Inhomogeneous stretch induced patterning of molecular orientation in liquid crystal elastomers, Extreme Mech. Lett. 5 (2015) 30–36.

[189] H. Kim, J. Kang, Y. Zhou, A.S. Kuenstler, Y. Kim, C. Chen, T. Emrick, R.C. Hayward, Light-Driven Shape Morphing, Assembly, and Motion of Nanocomposite Gel Surfers, Adv. Mater. 31 (2019) 1900932.